Underground gas storage thermodynamics : from laboratory to salt caverns

Firas Tayeb

PSL UNIVERSITÉ PARIS

THÈSE DE DOCTORAT
DE L'UNIVERSITÉ PSL

Préparée à Mines Paris-PSL

Thermodynamique de stockage souterrain de gaz : du laboratoire aux cavités salines

Soutenue par
Firas TAYEB
Le 29/02/2024

Ecole doctorale n° 398
Géosciences, ressources naturelles et environnement

Spécialité
Géosciences et géoingénierie

Composition du jury :

Laurent DE WINDT Directeur de recherche, MINES Paris	*Président*
Pascale BENEZETH Directrice de Recherche, CNRS	*Rapportrice*
Christophe COQUELET Professeur, MINES-Albi	*Rapporteur*
Grégoire HEVIN Docteur, Storengy	*Examinateur*
Nicolas GATELIER Docteur, Géostock	*Examinateur*
Murad ABUAISHA Chargé de recherche, MINES Paris	*Co-encadrant*
Ahmed ROUABHI Maître de recherche, MINES Paris	*Directeur de thèse*

MINES PARIS | PSL

Acknowledgements

Je commence cette section des remerciements en exprimant ma sincère gratitude à ceux qui m'ont soutenu, conseillé, et accompagné tout au long de ce parcours académique. Je souhaite particulièrement reconnaître l'apport fondamental d'Ahmed Rouabhi, mon directeur de thèse, dont l'encadrement avisé, les orientations précises, l'aide inestimable, et les conseils judicieux ont constitué la base de mon succès académique. Grâce à son accompagnement, j'ai pu développer des compétences et une expérience essentielles, indispensables à l'accomplissement de ce travail. Mes remerciements vont également à mon encadrant Murad Abuasha pour sa disponibilité continue, son suivi rigoureux, et son dévouement sans relâche, qui ont grandement contribué à enrichir ma recherche. Son soutien quotidien et son implication ont joué un rôle clé dans la progression de mes travaux. Je tiens aussi à exprimer ma reconnaissance à Faouzi Hadj Hassen pour ses conseils éclairés, ses idées novatrices, et le partage généreux de son expérience.

Je tiens à exprimer ma gratitude envers le personnel permanent de l'école, dont l'intervention, qu'elle ait été ponctuelle m'a été précieuse. Mon remerciement s'adresse particulièrement à Laurent Gerbaud pour son encouragement, particulièrement dans les moments cruciaux vers la fin de ma thèse. Ma reconnaissance s'étend à Alain Valtz pour son soutien considérable lors de mes travaux expérimentaux et je lui adresse mes meilleurs vœux pour sa retraite. Je remercie aussi chaleureusement le personnel technique du CTP pour leur aide et les solutions apportées à mes problématiques expérimentales.

En étendant ma reconnaissance, je tiens également à remercier l'ensemble du personnel de l'école pour leur bienveillance constante. Leur support, que ce soit à travers des conseils avisés, un recul réfléchi ou simplement un sourire encourageant, a été un véritable atout dans les moments les plus éprouvants. Ma gratitude s'étend spécifiquement aux enseignants-chercheurs tels que Laura, Joël, Emad, Isabelle, et Hedi, aux membres du service informatique comme Alain, Christophe, et Patrice, ainsi qu'aux assistantes dévouées, Véronique, Catherine, Sandrine, Sylvie, Sarojinee, et Jenifer, pour avoir facilité nos recherches en s'occupant de toutes les tâches administratives.

Mes remerciements vont également à l'ensemble du jury, pour leur examen attentif de mon travail et leurs recommandations constructives. Un immense merci est adressé à Laurent De Windt pour avoir accepté de présider le jury et d'être un membre dévoué du comité de suivi, offrant une évaluation continue de mes recherches, leurs encouragements, et pour les discussions enrichissantes que nous avons eues. Une gratitude particulière est réservée à Christophe Coquelet

et Pascal Bénézeth pour leur approche méticuleuse et leur précision dans la révision de mon manuscrit, ce qui a grandement contribué à en affiner le contenu. Pour finir, un grand merci à Nicolas Gatelier et Grégoire Hevin pour avoir été examinateurs et pour avoir partagé leur savoir et leur expérience, ce qui a rendu ma soutenance encore meilleure.

Ma reconnaissance va à tous mes collègues, tant passés que présents - Houssem, Mejda, Massi, Alain, Aurélien, Naveen, Marwa, Fabien, Zainab, Mariam - pour les précieux moments que nous avons partagés. Mon soutien et mes encouragements vont spécialement à ceux qui sont en phase finale de leur parcours, tels que Léo, Antoine, Diana, se préparant avec assiduité à leur soutenance. Je souhaite également exprimer ma gratitude à tous mes amis - Aymen, Sofiene, Ahmed, Kilani, Riadh, Badis, Milou, Kamel, Maroine - et à ceux non mentionnés ici, pour leur appui continu et leur amitié indéfectible.

Ma profonde appréciation est réservée à mes parents, Fethi et Houda, dont l'amour sans limite, le soutien sans faille et les encouragements ont été le fondement de tout ce que j'ai entrepris. Leur engagement total dans mon éducation et ma carrière est quelque chose que je chéris profondément. Ils ont été le pilier sur lequel j'ai pu compter à chaque étape de mon parcours. Un remerciement spécial est également dû à ma sœur Feten et à mon frère Chaker, dont les accomplissements personnels et professionnels ne cessent de nous inspirer et de remplir notre famille de fierté. Leur soutien, bien que souvent en coulisses, a été crucial et source d'inspiration constante.

Enfin, mes pensées les plus chaleureuses se tournent vers ma fiancée Ons. Sa présence dans ma vie est survenue à un moment décisif, marquant le début d'une période de transformation profonde. Son soutien sans réserve tout au long de ma thèse, et tout particulièrement durant cette dernière année critique, s'est avéré inestimable. Ons a été ma source de réconfort dans les moments de doute, ma joie dans les moments de réussite, et son amour, sa tendresse et sa générosité ont été le fondement de mon équilibre et de mon bonheur quotidien.

Table des matières

List of figures

List of tables

Introduction en français

Dans le contexte actuel, le secteur énergétique mondial connaît une transformation notable, principalement motivée par une prise de conscience accrue des conséquences négatives liées à l'utilisation des combustibles fossiles et des préoccupations concernant l'épuisement des ressources. Historiquement, les combustibles fossiles ont joué un rôle dominant dans le mix énergétique mondial, principalement en raison de leur viabilité économique [Ediger, 2019 ; Kalair, 2021]. Cependant, ils ont également présenté des problèmes significatifs, notamment d'importantes émissions de gaz à effet de serre et leurs conséquences sur le changement climatique [Ediger, 2019 ; Kalair, 2021]. En conséquence, il y a eu une transition notable vers l'utilisation de ressources énergétiques renouvelables au sein de l'infrastructure énergétique mondiale. Ces ressources renouvelables, obtenues à partir de processus naturels tels que la lumière du soleil, le vent et l'énergie géothermique, offrent une alternative écologiquement durable aux combustibles fossiles. De plus, la nature presque illimitée de ces ressources surmonte les contraintes liées à leur disponibilité. L'Agence internationale de l'énergie [IEA, 2020] prédit une augmentation significative de 75 % de la capacité énergétique renouvelable mondiale de 2022 à 2027. Cependant, l'expansion anticipée de l'énergie renouvelable soulève également le problème de l'intermittence des énergies. En fait, la production d'énergie renouvelable est influencée par des conditions environnementales fluctuantes [Kumi, 2023]. Par exemple, l'énergie solaire est limitée pendant la nuit, tandis que la production d'énergie éolienne est affectée par les variations de vitesse du vent. Ces variables conduisent à une alimentation électrique inconsistante.

Dans ce contexte, l'importance des solutions de stockage d'énergie devient primordiale, car elles aident à équilibrer la production intermittente de ressources renouvelables avec les demandes énergétiques fluctuantes. Ces systèmes permettent de stocker l'énergie excédentaire pendant les périodes de haute production, permettant sa transformation en une forme stockée et accessible pendant les périodes de faible production. En fait, au sein de la structure complexe du stockage d'énergie, le stockage souterrain est devenu un élément clé pour faire face à la nature intermittente des ressources énergétiques renouvelables. Bien que le stockage souterrain soit une utilisation spécialisée dans l'industrie pétrolière, il offre de nombreux avantages importants. Parmi les diverses solutions de stockage souterrain, les cavités salines présentent des avantages uniques, en particulier en termes de capacité et d'impact environnemental. Les cavités salines sont considérées comme une option particulièrement avantageuse pour les opérations de stockage à grande échelle par rapport à d'autres choix de stockage géologique tels que les aquifères.

La raison de cela peut être attribuée non seulement aux mesures de sécurité renforcées, mais aussi à la capacité de ces installations de stockage à contenir des gaz à haute pression comme l'hydrogène (H_2) et le dioxyde de carbone (CO_2), ainsi qu'aux propriétés imperméables de la roche saline. Le sel agit comme une barrière efficace qui isole de manière optimale le gaz stocké de l'environnement extérieur, prévenant ainsi toute contamination possible et assurant la préservation de la qualité et de l'intégrité du gaz.

Suite à la création des cavités salines, une certaine quantité de saumure demeure inévitablement au fond, engageant des échanges de masse avec les gaz stockés. Ces échanges de masse entre la saumure résiduelle et les gaz stockés constituent un point central dans notre étude.

Dans ce contexte, l'étude du comportement des gaz et des échanges de masse entre les phases liquide et gazeuse dans les stockages souterrains revêt une importance considérable. Historiquement, diverses industries ont accumulé une connaissance significative concernant le stockage de certains fluides, tels que le gaz naturel et les hydrocarbures, dans les cavités souterraines. Cependant, avec l'évolution des techniques de stockage, il devient impératif de comprendre les propriétés de stockage de gaz plus récents, notamment l'hydrogène et le dioxyde de carbone.

En outre, les effets de la dissolution des gaz dans la saumure résiduelle ont été négligés dans la plupart des études existantes traitant le stockage souterrain de gaz. Il est couramment admis que la cavité est remplie du gaz stocké en négligeant le volume de saumure résiduelle [Zhang, 2022 ; Li, 2022] ; cependant, la saumure résiduelle peut occuper jusqu'à 10 % du volume de la cavité. Notamment, le CO_2 montre une solubilité supérieure dans la saumure par rapport à d'autres gaz tels que le CH_4 [Soubeyran, 2019]. Il est donc impératif de quantifier la perte de gaz due à la dissolution pour une bonne gestion des quantités cyclées. Par ailleurs, la cinétique de dissolution des gaz dans la saumure, souvent supposée suivre un équilibre thermodynamique instantané, reste un sujet peu étudié dans les travaux existants.

Toutefois, il est essentiel de souligner que, même si la dissolution du CO_2 dans l'eau pure a été largement traitée [Belgodere, 2015 ; Cadogan, 2014 ; Lu, 2013], l'effet de la salinité sur la diffusion du CO_2 et H_2 dans la saumure sous des conditions de stockage n'a pas été suffisamment étudié. Il est donc primordial de mener des études complémentaires pour approfondir notre compréhension de l'influence de la salinité sur la dissolution du CO_2 et H_2 dans le cadre spécifique du stockage souterrain de gaz [Lankof, 2023].

Cette thèse vise à explorer ces échanges de masse entre les phases gazeuses (H_2 et CO_2) et liquide, en se concentrant sur la cinétique de dissolution des gaz dans la saumure et le comportement des gaz humides.

En fait, l'étude de ces échanges de masse est importante pour garantir un suivi précis de la masse de gaz stocké durant les opérations de cyclage de gaz et pour optimiser l'efficacité du stockage dans les infrastructures souterraines. En effet, l'étude de la cinétique de dissolution des gaz fournit des informations précieuses sur la durée à laquelle des gaz tels que le CO_2 et le H_2 peuvent se dissoudre dans la saumure résiduelle présente au fond des cavités salines. La perte de masse du gaz et la capacité totale de stockage sont toutes deux influencées par cette cinétique de dissolution.

De plus, le comportement du gaz humide est un facteur important à considérer tout au long

de la procédure de stockage. La vapeur d'eau dans le gaz stocké peut causer la corrosion de l'infrastructure, affecter les propriétés thermodynamiques du gaz et rendre la procédure d'extraction plus compliquée. De plus, le coût des installations de déshumidification en surface est élevé. Comprendre les interactions entre le gaz, la vapeur d'eau et la saumure est essentiel pour prédire le comportement du gaz dans différentes conditions de stockage.

Dans le cadre de ce travail, une étude à la fois expérimentale et numérique des phénomènes en question sera menée. L'approche expérimentale, conduite dans des conditions de laboratoire contrôlées, est destinée à fournir des données essentielles concernant la cinétique de dissolution des gaz et le comportement des gaz humides. Ensuite, les modèles mathématiques et numériques développés peuvent étendre ces résultats pour prédire le comportement des gaz à l'échelle de cavités salines.

L'étude présentée dans cette thèse comprend deux chapitres principaux. Le premier chapitre se focalise sur la dissolution des gaz et examine le comportement des gaz humides à l'échelle du laboratoire, tandis que le second étend l'étude à l'échelle de la cavité. Pour la première chapitre, deux expériences ont été menées. La première expérience a porté sur la cinétique de dissolution du CO_2 et du H_2 dans l'eau pure et la saumure, en utilisant la méthode de Pressure-Decay. L'expérience suivante a utilisé un pilote de stockage de laboratoire novateur pour déterminer l'humidité dans le gaz, en utilisant l'hélium comme cas d'étude.

Pour reproduire les échanges de masse observés expérimentalement, des modèles mathématiques et numériques ont été développés. Ces modèles ont servi à étudier la cinétique de dissolution des gaz dans la saumure et les processus d'humidification des gaz. Le premier modèle, traitant de la dissolution des gaz, a été formulé sous forme non dimensionnelle, le rendant adapté à l'analyse de la cinétique de dissolution à l'échelle de la cavité dans le deuxième chapitre. Le modèle de gaz humide, conçu pour prédire la teneur en eau dans la phase gazeuse et les propriétés du gaz humide, repose sur l'hypothèse d'un état thermodynamique homogène. Cette hypothèse facilite la transition de l'échelle du laboratoire à celle de la cavité tout en négligeant les dimensions du modèle.

Dans le deuxième chapitre, les modèles développés avec les paramètres ajustés expérimentalement sont utilisés pour quantifier la dissolution du gaz dans la saumure et examiner le comportement du gaz humide dans des cavités salines. En effet, le modèle non dimensionnel de dissolution des gaz intègre les différents phénomènes physiques telles que le transfert de chaleur et de masse, la cinétique de dissolution et les effets de convection pour étudier la dissolution des gaz dans les cavités salines. Le modèle de gaz humide a été utilisé pour étudier la teneur en eau dans la phase riche en gaz lors de différents scénarios de stockage de gaz.

Introduction

Currently, there is a notable transformation occurring in the global energy sector. This transition is largely motivated by an increased awareness of the negative consequences linked to the use of fossil fuels, along with concerns over resource depletion. Throughout history, fossil fuels have played a dominant role in the global energy mix, mostly owing to their economic viability [Ediger, 2019 ; Kalair, 2021]. However, they have also presented significant problems. These issues include substantial emissions of greenhouse gases and their resulting consequences on climate change [Wuebbles, 2001 ; Johnsson, 2019 ; Soeder, 2021]. As a result, there has been a noticeable transition towards the use of renewable energy resources within the global energy infrastructure. These renewable resources, obtained from natural processes such as sunlight, wind, and geothermal energy, provide an ecologically sustainable alternative to fossil fuels. Furthermore, the almost unlimited nature of these sources overcomes constraints related to the availability of resources. The International Energy Agency [IEA, 2020] predicts a significant 75% increase in global renewable energy capacity from 2022 to 2027, and renewable energy is expected to surpass coal as the main source of electricity production by 2030. However, the anticipated expansion of renewable energy also brings up the significant issue of supply intermittency. The production of renewable energy is influenced by fluctuating environmental conditions [Kumi, 2023]. For example, solar energy supply is limited during the night and in cloudy conditions, while wind energy production is affected by changing wind speeds. These variables lead to an inconsistent power supply.

In this context, the importance of energy storage solutions becomes crucial, as they help to balance the intermittent production of renewable resources with the fluctuating energy demands. These systems provide a method to store surplus energy during periods of high production, enabling its transformation into a stored and accessible form during periods of low production. In fact, underground storage has become a key element in dealing with the intermittent nature of renewable energy resources within the intricate structure of energy storage. Although underground storage is a specialized use in the oil and gas industry, it offers numerous significant benefits. Underground storage, especially in salt caverns, is well-suited for the renewable energy industry since it effectively addresses the intermittent nature of renewable energy by providing flexible storage options that are not constrained by surface limits. This has great importance for the long-term sustainability of renewable energy operations. Among various energy storage solutions, salt caverns offer unique advantages, particularly in terms of capacity and environmental

impact. Salt caverns are considered to be a more attractive choice for large-scale storage operations when compared to other geological storage choices such as depleted hydrocarbon reservoirs or aquifers. The reason for this may be attributed not only to the enhanced safety measures but also to the ability of these storage facilities to contain high-pressure gases like hydrogen and CO_2, as well as the impermeable properties of salt rock. Salt serves as an effective barrier that effectively isolates the stored contents from the external environment, preventing any potential contamination and ensuring the preservation of gas quality and integrity [Lankof, 2023].

Salt caverns, created by solution mining, have remarkable capacities for holding both liquids and gases, ranging from between 6 and 35 million barrels [Liu, 2023]. This may be attributed to their large dimensions which might vary considerably depending on economic demands. The depth (ranging from 500 to 1500 m in the case of hydrocarbons storage [Zhao, 2022]) provides a consistent thermal environment, which is an important condition for certain storage requirements, and significantly decreases contamination hazards to the surrounding ecosystem in the rare case of leaks. The safe storage of various fluids is ensured by the structural integrity of these caverns, which is defined by their impermeability and self-sealing properties, thereby sustaining high pressure levels. Their rapid response capability, which allows fluid to be easily and quickly injected or withdrawn, is another positive feature that surface storage facilities generally lack. This is especially advantageous when managing gases used for energy supply, since it guarantees a prompt response to fluctuations in demand. From an economic perspective, the establishment of these underground caverns demonstrates more cost-effectiveness compared to the construction of similar storage facilities on the surface.

To comprehend the gas storage in salt caverns, it is essential to understand the process by which they are formed. In fact, a salt cavern is created in a controlled process, typically inside an extensive underground layer of salt known as a salt dome. Initially, a borehole is drilled from the surface level to penetrate the deep salt layer, and then two layered tubes are inserted into this borehole. When the required depth is attained, water is pumped into the salt layer via the inner tube. This results in the dissolution of the salt ; this is known as leaching. The saline solution produced (brine) is then extracted back up through the outer tube. The process of continuously injecting water and extracting brine leads to the gradual expansion of the void within the salt layer. The procedure is repeated until the void reaches the required size, which might take months or even years, depending on the size of the cavern. Once the necessary dimensions have been attained and the majority of the brine is replaced with the stored fluid, it is important to note that a quantity of brine will inevitably remain at the bottom of the cavern. This residual brine will have mass exchanges with the stored gases. Finally, the cavern is sealed in order to prevent any further dissolution of salt. Consequently, the cavern is ready for use. This complicated process transforms resilient layers of underground salt into a cavern that offers safe and efficient storage solutions.

The investigation of gas behavior and mass exchanges between the liquid and gas phases in underground storage has considerable importance in light of the increasing requirements of energy storage efforts. Over the years, several industries have built up a significant body of knowledge related to the storage of certain fluids, such as natural gas and hydrocarbons, inside

underground caverns. Nevertheless, as the energy environment changes, there is a rising need to understand the storage properties of more recent gases, notably hydrogen (H_2) and carbon dioxide (CO_2). Furthermore, the majority of previous studies on underground gas storage assume that the cavern is filled with the stored gas, overlooking the volume of residual brine [Zhang, 2022 ; Li, 2022] ; however, the brine can occupy up to 10% of the cavern volume [Soubeyran, 2019]. In fact, certain gases, particularly CO_2, are highly soluble in brine. This leads to a massive mass exchange between the stored gas and brine in the salt cavern which influences the thermodynamic properties of the gas. In addition, the humidity introduced by this mass transfer can affect the storage conditions and necessitate the use of additional surface apparatus to control the humidity of the extracted gas. Moreover, the kinetics of gas dissolution in brine have frequently been overlooked in the literature, with the thermodynamic equilibrium assumed in almost all studies of gas dissolution in salt caverns. It is also noteworthy that, while the process of CO_2 dissolution in pure water has been widely addressed [Belgodere, 2015 ; Cadogan, 2014 ; Lu, 2013], the impact of salinity on the diffusion of CO_2 and H_2 in brine under storage conditions has not received adequate attention. Hence, further experimental studies is needed to enhance our understanding the kinetics of dissolution of CO_2 and H_2 in saturated brine within the specific setting of storage conditions.

Hydrogen has unique challenges and properties that make it a subject of significant investigation. Safety is a primary concern when it comes to hydrogen storage. The small molecular size of the hydrogen makes it vulnerable to leaking through both the salt rock of the cavern and the surface infrastructure. In addition, hydrogen has a low density, which requires the use of immense storage volumes in order to store an amount of energy comparable to that of fossil fuels [Navaid, 2023]. Due to the scarcity of comprehensive storage data related to hydrogen in the operational caverns, we have had to depend on general thermodynamic information and knowledge obtained from its storage in other geological reservoirs to further our understanding of its behavior.

This research aims to explore the mass exchanges between the gas (H_2 and CO_2) and liquid phases in the salt caverns, focusing on the kinetics of gas dissolution in brine and the behavior of the humid gases. These aspects are particularly important to have an accurate track of the cycled quantities and to enhance the effectiveness and reliability of gas storage in underground structures. In fact, the gas dissolution kinetics study provides valuable information on the rate at which gases such as carbon dioxide (CO_2) and hydrogen (H_2) may be dissolved into the brine solution located at the bottom of salt caverns. Mass loss of gas and total storage capacity are both influenced by this dissolution rate.

The behavior of humid gas is an important factor to consider throughout the storage procedure. Water vapor in the stored gas may cause corrosion of the infrastructure, affect the thermodynamic properties of the gas, and make the extraction procedure more complicated. Furthermore, the price of dehumidification surface installations is expensive. Understanding the interactions between the gas, water vapor, and brine is essential for predicting gas behavior under different storage conditions.

Hence, a comprehensive experimental and theoretical investigation of these phenomena will

be studied in this work. Experimental research provides valuable data on the kinetics of gas dissolution and the behavior of humid gases in controlled environments. Then, the developed mathematical and numerical models can extend these findings to predict the behavior of gases in actual cavern environments. By combining experimental data with model predictions, a thorough comprehension of gas and brine interactions in salt caverns may be accomplished, thereby improving the efficiency of these caverns.

The study presented in this dissertation comprises two primary chapters. The first chapter delves into gas dissolution and examines humid gas on laboratory scale, while the second extends the study to the cavern scale. In the first chapter, the research undertook two experimental studies. The initial experiment focused on the dissolution kinetics of CO_2 and H_2 in water and brine, employing the pressure decay method. The subsequent experiment used a novel laboratory storage pilot to ascertain the humidity levels in gas, using helium as a case of study, and simulated a cycling process that replicated real cavern conditions to determine mass transfer from brine to gas.

The experimental study established the basis for the creation of mathematical and numerical models that replicate the observed mass exchanges. These models served to investigate the dissolution kinetics of gases in brine and the humidification processes of gases. These models were thoroughly validated, including adjustments of the studied parameters. The first model, addressing gas dissolution, was formulated in non-dimensional form, making it suitable for the second chapter analysis of dissolution kinetics on cavern scale environment. The humid gas model (known as HGM model) aims to predict the water content in the gas phase and the properties of humid gas. It is important to note that in the development of this model, a homogeneous thermodynamic state was assumed. This assumption facilitates the transition from the laboratory to the cavern scale while disregarding model dimensions.

In the second chapter, the study scales up these models to cavern dimensions to quantify gas dissolution in brine and scrutinize the behavior of humid gas within a salt cavern. The non-dimensional model of gas dissolution integrates variables such as heat and mass transfer, dissolution kinetics, and convective effects to determine the dissolution rate in a cavern setting. The HGM model was used to investigate the water content in the gas-rich phase during different scenarios of gas storage in salt caverns.

Chapitre 1

Study of gas-brine mass exchange on the laboratory scale

Objectifs

The primary objective of the first chapter is to replicate the mass transfer phenomena between stored gases and an aqueous solution under defined storage conditions within a laboratory environment, as well as the study of humid gas behavior. This chapter is structured into two main sections :

— The first section delineates the experimental investigation conducted to understand the dissolution kinetics of CO_2 and H_2 in pure water and brine. Additionally, this section includes a thorough evaluation of the humidification processes of helium gas, conducted using an innovative laboratory storage pilot apparatus.

— The second section outlines the developed mathematical and numerical models to simulate the kinetics of gas dissolution and the behavior of humid gas and to determine the studied parameters.

Contents

Introduction du premier chapitre en français

L'intégration des processus de dissolution et d'humidification des gaz dans la modélisation des cavités, souvent négligée, est abordée dans ce chapitre de manière approfondie. L'objectif principal de cette partie est de reproduire, dans un environnement de laboratoire soigneusement contrôlé, les phénomènes de transfert de masse entre les gaz étudiés et les solutions aqueuses (eau pure ou saumure), ainsi que d'étudier le comportement des gaz humides. Ce chapitre, structuré en deux sections principales, vise à approfondir notre compréhension de ces processus.

La première section de ce chapitre se focalise sur une étude expérimentale visant à comprendre la cinétique de dissolution du CO_2 et du H_2 dans l'eau pure et dans la saumure. Cette partie inclut également une évaluation détaillée des processus d'humidification de l'hélium, réalisée à l'aide d'un dispositif expérimental de stockage innovant.

La deuxième section est dédiée au développement de modèles numériques pour simuler la cinétique de dissolution des gaz et le comportement des gaz humides. Cette démarche permet d'aller au-delà des résultats expérimentaux, en fournissant un cadre théorique et numérique pour la compréhension et la prédiction des phénomènes observés. Les modèles développés, basés sur des paramètres ajustés, jouent un rôle essentiel dans l'explication des interactions complexes entre les gaz et les solutions aqueuses, offrant ainsi une base solide pour une application à l'échelle des cavités.

Introduction of the first chapter

The integration of gas dissolution and humidification processes within cavern models is usually disregarded. Yet, gases, notably CO_2, demonstrate a solubility in brine that surpasses that of many regularly stored fluids in these caverns. Hence, the influence of these processes on storage thermodynamics cannot be deemed insignificant. It is, therefore, imperative to elucidate this influence to either verify or challenge the traditional methodology adopted for the quantification of fluid storage. That's why we start by investigating gas dissolution and humidification on the laboratory scale in order to build comprehensive and robust models to be applied on the cavern scale in the second chapter.

This first chapter focuses on exploring the transfer of mass between gaseous and liquid domains under controlled laboratory conditions. This encompasses the process of gas dissolution in pure water or brine and the quantification of water content in the gas-rich domain. Initially, we introduce the experimental results obtained from the mass exchange experiments. Here, CO_2 and H_2 are chosen as a case study for gas dissolution analysis, while further exploration is directed towards the moisture concentration in the gas (He, H_2)-rich domain. Subsequently, a discussion on our numerical and mathematical models concerning the kinetics of gas dissolution in water and brine and gas humidification will be presented. The developed models using the adjusted parameters will be used in the second chapter, where we delve into the mass transfer between gases and brine at the cavern dimension.

1 Laboratory investigation

In the forthcoming section, the objective is to reproduce the mass transfer phenomena observed between the stored gases and the aqueous solution under specific storage conditions within a controlled laboratory setting. To elucidate the structure of this section, it is imperative to note that it will be divided into two distinct subsections. Initially, an experimental study relevant to the dissolution kinetics of CO_2 and H_2 in both pure water and brine will be presented. Subsequent to this, the laboratory investigation of helium gas humidification using an innovative storage pilot apparatus will be described.

1.1 Experimental study of gas dissolution in an aqueous solution

In this subsection, a rigorous experimental examination concerning the dissolution kinetics of CO_2 and H_2 in both brine and pure water will be systematically described. To begin, a comprehensive overview of the current advancements in experimental techniques used to investigate the kinetics of gas dissolution in aqueous solutions will be presented. Furthermore, a description of the laboratory apparatus and its configuration will be provided. This part will conclude with a thorough discussion about the obtained results.

1.1.1 Overview of experimental research

Kinetics is the branch of chemistry that delves into the temporal changes in reactant concentrations during chemical reactions, influenced by both physical processes such as species diffusion and chemical dynamics. Most studies often overlook dissolution kinetics by assuming equilibrium, thus eliminating time as a factor. Other research, on the other hand, relate the evolution of the system over time to the mass transfer that has occurred in order to forecast the evolution of the parameters of interest.

Historically, varied experimental approaches have been established to evaluate gas diffusion in pure water and brine, with prior studies focusing on mass transfer by molecular diffusion. These methods typically allow the system to reach equilibrium naturally. Experimental methods can be divided into conventional, direct, and non-conventional, or indirect categories.

In direct methods, compositional analysis is conducted on several fluid samples, which are commonly collected at different times and locations during the diffusion experiment [Sigmund, 1976 ; Nguyen, 1998]. The determination of gas diffusivity involves doing chromatographic analysis to measure the concentration distribution of each sample. In order to measure gas diffusion in liquid systems, the use of a pressure-volume-temperature (PVT) cell is necessary [Sheikha, 2005]. Pioneering contributions by researchers such as [Gubbins, 1966 ; Witherspoon, 1965] have used direct methods to measure the diffusion coefficients of hydrocarbons in water and gases like hydrogen and methane in electrolytes for different temperature ranges. Moreover, laboratory equipment was constructed by [Islas-Juárez, 2004] to evaluate the nitrogen effective diffusion coefficient in sand-pack models. In their porous model, they designed a unique configuration to analyze crude oil dissolved with nitrogen.

Although direct methods provide a direct assessment of the gas concentration distribution in a liquid phase, their operation is complex, and obtaining samples can be challenging under high pressures and temperatures. Furthermore, these techniques necessitate costly experimental apparatus and are incapable of detecting minor changes in concentration.

On the other hand, indirect methods, also known as non-conventional methods, offer a more straightforward and reliable approach to measuring gas diffusivity in a gas-liquid system as compared to direct methods, including simpler operation, cost-effectiveness, and the capacity to detect even minor changes in concentration. These techniques quantify a characteristic of the system that is connected to the rate of diffusion during the mass transfer test. Moreover, these techniques have been employed in numerous research investigations to measure the diffusion coefficient of various gases, such as carbon dioxide and hydrogen. The diffusion process modifies several properties of gas-fluid systems, which, based on the measured parameter, divide these methods into separate experimental procedures, all performed under constant temperatures. These methods include the constant pressure method [Renner, 1988], the dynamic pendant drop shape and volume analysis method [Yang, 2006 ; Yang, 2008], and the pressure decay method [Riazi, 1996 ; Zhang, 2000] :

— **Constant pressure method :** This method quantifies the volume change of a gas phase while preserving system pressure, which is achieved by continuous gas delivery to the diffusion cell. The total amount of gas extracted from the supply cell is measured at the end of the test. In fact, the variation in volume of the gaseous phase correlates directly with the mass transferred, given that the density, pressure, and temperature remain constant. The main advantage of this technique is the fixed boundary condition at the interface between the gas and liquid phases, which simplifies the mathematical model used for interpreting experimental findings [Etminan, 2010 ; Renner, 1988] effectively employed this technique to quantify the diffusivity of CO_2 in brine and decane.

— **Dynamic pendant drop shape :** This method involves suspending a liquid droplet, usually a heavy oil or brine, in a gaseous phase. The process entails a meticulous study of the droplet shape and volume change over time. These changes indicate the transfer of the solute from the gas to the liquid phase, which naturally affects the interfacial tension between the phases. Through systematic recording of the droplet's shape and volume changes, we can deduce the diffusion coefficients. [Yang, 2006 ; Yang, 2008] successfully identified the mass transfer characteristics of CO_2 gas in CO_2-crude oil by establishing a connection between the changing interfacial tension and the time-dependent distribution of CO_2 concentration within the oil phase. The DPDSA approach necessitates a minimal quantity of liquid, such as oil or brine, and may be performed quickly.

— **Pressure decay method :** This method is the most effective indirect approach for monitoring the diffusion of gas in liquids. The system includes gas and liquid confined within a PVT cell. When the gas comes into direct contact with a liquid, it will dissolve into the liquid until a state of equilibrium is reached. In a hermetically sealed system with pre-established volumes of liquid and gas at a specified pressure, the gas dissolution into the liquid causes a noticeable decrease in the pressure of the system. This decline in pressure

is meticulously recorded over time, thereby quantifying the rate of gas dissolution. The pressure decay approach in a gas-liquid system has been enhanced by employing the pulse-echo method, which uses an acoustic pulse echo technique to detect changes in pressure and volume [Janiga, 2020]. The pulse-echo approach provides the advantage of accurately identifying the location of the interface between gas and liquid with distinct densities, enabling the simple observation of volume changes resulting from gas diffusion into the underlying liquid. The pressure decay approach is easily employed in the laboratory and can be applied to several gas types, including solvents and other liquids.

Techniques like Pressure-Decay offer a simplified method for investigating fluid behavior in geological formations, avoiding the need for complex sampling or analysis equipment. This technique can reproduce the interaction between liquid and gas phases in an underground storage conditions, making it a suitable method for studying the kinetics of the dissolution of the gas in the brine. Nevertheless, due to the lack of detailed data on the various phases, it is required to use some assumptions while developing the Pressure-Decay device. Moreover, this method is highly vulnerable to impurities, which can have an impact on the accuracy of equilibrium pressure measurements [Zhang, 2015], highlighting the need to use pure substances before the injection into the PVT cell.

In order to reproduce underground storage conditions, we will use CO_2 or H_2 as the gaseous phase and brine as the liquid phase. While CO_2 diffusivity in pure water is extensively studied [Civan, 2001 ; Belgodere, 2015 ; Hirai, 1997], impact of salinity on CO_2 diffusion in formation water is less explored. There are a few studies that have specifically examined the diffusion rate of CO_2 in brine under specific pressure and temperature conditions [Moghaddam, 2012 ; Bahar, 2008 ; Sell, 2013]. Additional investigation is required to develop a more comprehensive understanding of the impact of salinity on the rate of CO_2 diffusion.

The study described in [Azin, 2013] and [Jafari Raad, 2015] investigates the solubility of CO_2 in saturated brines. The experimental apparatus encompassed cells containing 120 ml of brine under initial pressures between 5.9 MPa and 6.9 MPa, maintaining continuous temperatures from 32°C to 50°C. Despite the experiments lasting for about 20 hours, equilibrium was not definitively reached. The lack of specific data regarding the quantity of gas introduced makes it difficult to reproduce and use these findings. Another investigation conducted by [Bahar, 2008] examined the process of dissolution of CO_2 in a brine solution containing approximately 6% salt mass fraction, which is far from saturated brine. The experimental apparatus consisted of a capsule with a volume of 1.5 liters, with the volume of brine (800 cm^3) representing over half of the capsule's total volume. The experiments were conducted using CO_2 under the conditions of 17.8 MPa pressure and a high temperature of 83 °C temperature. The system required around 20 hours to achieve equilibrium.

To sum up, the majority of experimental findings reported in the literature diverge from the specific conditions of underground storage. In the next section, we will present our experimental investigation of the dissolution kinetics of CO_2 and H_2 in aqueous solutions, encompassing both pure water and brine, across various initial pressures and temperatures.

1.1.2 Laboratory set-up

The methodological approach adopted in this study is the pressure decay method in order to investigate the diffusion coefficient using a PVT cell. This technique is straightforward and does not require sampling or phase analysis. Furthermore, using a PVT cell ensures a highly controlled environment, hence enhancing the accuracy of the obtained findings. In fact, the pressure decay method is based on analyzing the observed drop in pressure resulting from the diffusion of gas into the water/brine [Riazi, 1996].

The experimental substances consisted of gases (H_2, CO_2) with a purity of 99.999% (Appendix A), pure deionized water, and sodium chloride with a purity of 99.6%. The process included the dissolution of sodium chloride in distilled water to create the brine solution. The study aims to examine the kinetics of gas mass transfer in pure water/brine at a constant temperature and measure the duration needed to achieve the saturation concentration of gas in the aqueous solution. To achieve these goals, an experimental setup was established, as shown in Figure 1.1. The technique used in this study is the pressure decay approach, which involves monitoring the pressure changes after the introduction of gaseous and liquid phases inside a constant-volume PVT cell. The system is then allowed to spontaneously attain thermodynamic equilibrium. The experiments were conducted using two cylindrical PVT cells with respective total volumes of 96.48 cm^3 and 131.64 cm^3. A bath is used to keep each cell at a constant temperature. Experiments were conducted using three distinct salinities and varied brine volumes, as delineated in Table 1.1. The purpose is to elucidate the effects of salt concentration, temperature, and liquid volume variations on the mass transfer of H_2 and CO_2 in the aqueous solution.

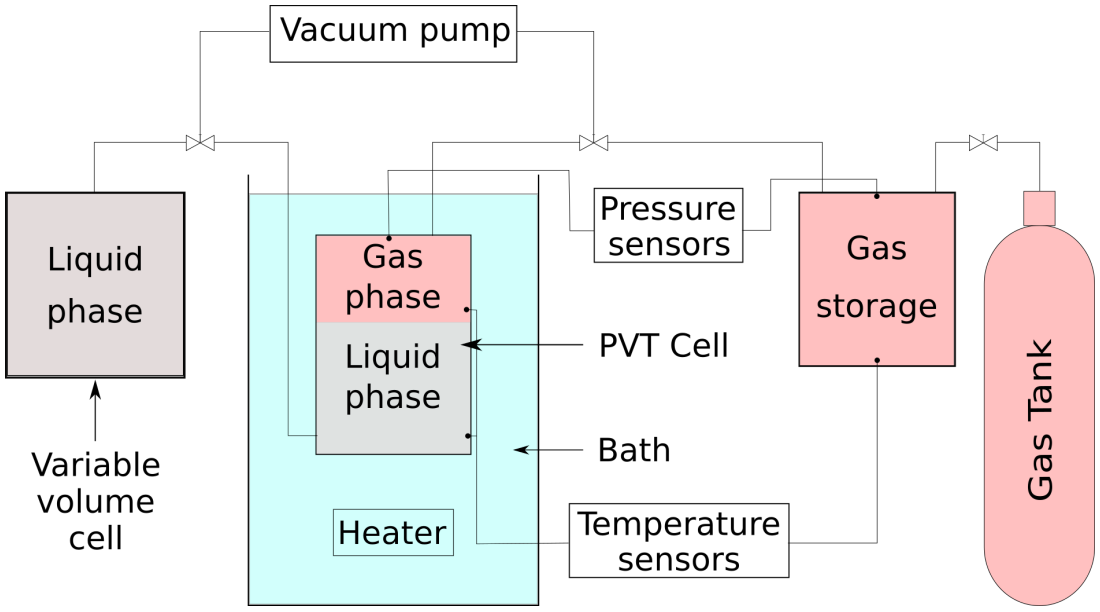

FIGURE 1.1 – The pressure decay method : A schematic representation of the gas dissolution experiment.

During the tests, two platinum temperature probes were set in the top and the bottom of the cell to confirm the minimal temperature difference within the cell. Additionally, pressure

sensors were placed at the top to measure the gas pressure. The uncertainties associated with these measurement instruments are presented in Appendix A. The upper port of the PVT cell is linked to a gas reservoir with a volume of 100 cm^3, enabling the measurement of pressure and temperature. Therefore, it is possible to determine the density and the exact mass of the gas that is inserted into the cell. The lower port is linked to a variable-volume cell that contains the liquid phase. This allows for the precise injection of a liquid volume into the PVT cell (refer to Figure 1.2).

A vacuum pump was employed to evacuate the PVT cell prior to the start of the experiment. The liquid is the initial phase that is introduced into the cell. Subsequently, the gaseous phase is rapidly introduced until the desired pressure is attained. After attaining this pressure, the cell is hermetically sealed, and the system is allowed to develop freely while temperature and pressure measurements are taken every 5 seconds. The thermodynamic equilibrium is achieved when there is no longer any variation in the pressure of the system.

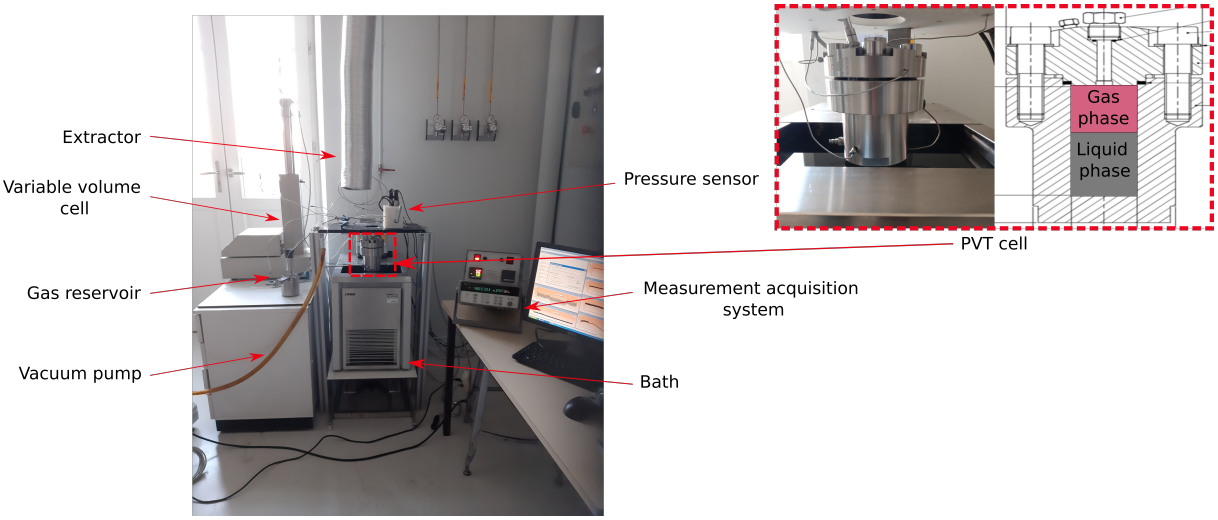

FIGURE 1.2 – Overview of the experimental device of gas dissolution and its components.

To investigate the kinetics of dissolution, we performed experiments using two gases : carbon dioxide (CO_2) and hydrogen (H_2). Initially, our attention was directed towards conducting experiments involving CO_2. These experiments were conducted under different conditions of temperature, salinity, and brine volume. The main goal was to evaluate how the volume and salinity of the brine affect the kinetics of CO_2 dissolution. Then, we conducted similar experiments using H_2, a gas well-known for its low solubility in water and brine.

1.1.3 Experimental investigation of the carbon dioxide dissolution kinetics in aqueous solution

This section explores the experimental analysis of the dissolution kinetics of CO_2 in aqueous solutions. The study evaluates the impact of salinity, gas-liquid volume ratio, gas initial pressure, and temperature on different laboratory conditions. This section is divided into two parts : the

first delineates the experimental procedure, while the second part provides a detailed discussion of the experimental outcomes.

1.1.3.1 Carbon dioxide dissolution in aqueous solution : Experimental procedure

We have thoroughly examined several factors that may be varied in our experimental set-up, such as the ratio of gas to liquid volume, concentration of salt, gas pressure, and temperature. The range of temperature variation was limited to underground storage conditions. Table 1.1 presents a summary of all the tests conducted at two distinct temperatures (T_0 = {30, 40} °C). Given the constant temperature of the system throughout the experiments, the changes in CO_2 pressure were solely attributed to the transfer of CO_2 into the liquid phase. In order to determine the effect of varying the pressure on the kinetics of CO_2 mass transfer in the pure water, Tests 1, 2, and 3 were conducted at 30 °C with the same volume of the liquid phase ϑ_λ in the cell and three distinct pressures $p_{\gamma 0} = \{10, 41.5, 48.8\}$ bar. The experiments conducted between 4 and 12 were performed at a temperature of $T_0 = 40$ °C. Various salinities ($c_{\text{salt}} = \{11, 22.5\}\%$) and varied liquid volumes were used to investigate the impact of these factors on the dissolution kinetics. In addition, we conducted two experiments (Tests 11 and 12) in which we used a saturated brine with a salinity of c_{salt}= 22.5 % and high initial pressures of CO_2 ($p_{\gamma 0}$ = {129, 168.7} bar) in order to study the impact of high pressures on the CO_2 dissolution kinetics in the saturated brine.

Table 1.1 – Experimental parameters and conditions of all the performed tests : A comprehensive laboratory study.

Test number	Temperature T_0 (°C)	Initial pressure $p_{\gamma 0}$ (bar)	Liquid volume ϑ_λ (cm^3)	Gas volume ϑ_γ (cm^3)	Salinity c_{salt} (%)
1	30	10	30.39	101.25	0
2	30	41.5	30.39	101.25	0
3	30	48.8	30.39	101.25	0
4	40	10.5	28.45	68.03	0
5	40	10.5	48.24	48.24	0
6	40	10	90.5	41.14	0
7	40	10.5	28.45	68.03	11
8	40	10.5	48.24	48.24	11
9	40	10.5	28.45	68.03	22.5
10	40	10.5	48.24	48.24	22.5
11	40	129	105.31	26.32	22.5
12	40	168.7	105.31	26.32	22.5

1.1.3.2 Carbon dioxide dissolution in aqueous solution : Experimental findings

The kinetics of CO_2 mass transfer in the pure water/brine is measured by analyzing the temporal changes in CO_2 pressure during pressure decay experiments. Figure 1.3 illustrates the 12 experimental findings of the measured pressures from the various performed tests described in Table 1.1. The gas pressure decreases significantly at the start of each experiment until it stabilizes at the end, when the thermodynamic equilibrium is established. It implies that the rate at which CO_2 is transferred in the aqueous solution is high during the early phases of the tests, but gradually decreases as time progresses. Furthermore, the kinetics of dissolution are affected by changes in salinity, CO_2 initial pressure, and liquid volume. The following paragraphs will address these implications.

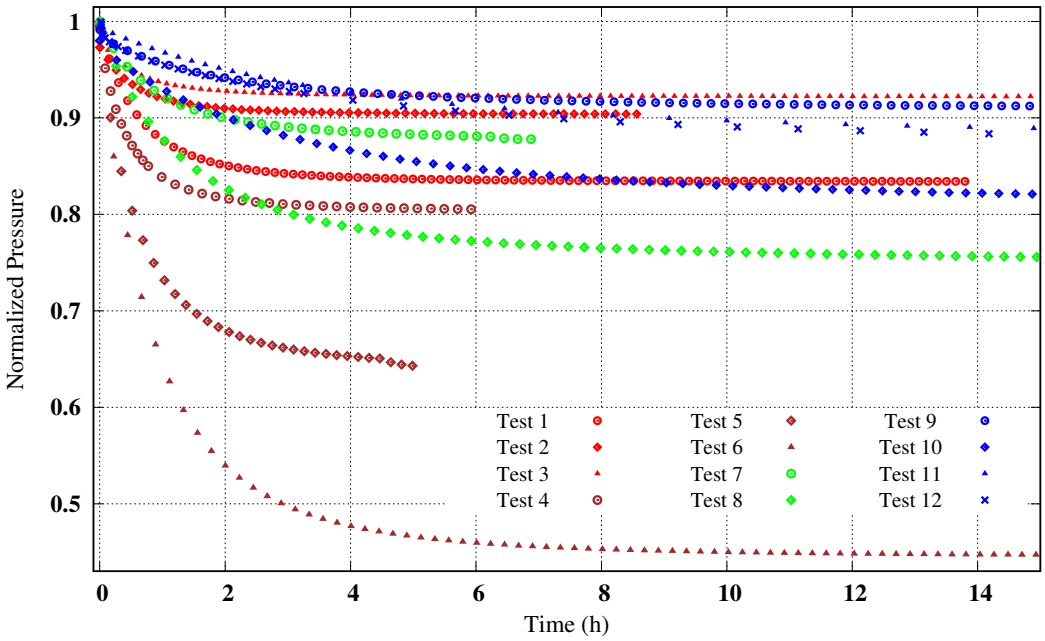

FIGURE 1.3 – Experimental results of the CO_2 pressure profiles over time of all the performed tests presented in Table 1.1.

Remark 1 : Impact of salinity on the carbon dioxide mass transfer rate

The effect of salinity on the rate of CO_2 mass transfer over time was examined in tests 4, 7, and 9, as shown in Table 1.1. These tests used a liquid volume ϑ_λ of 28.45 cm^3, incorporating pure water and two different NaCl mass concentrations, $c_{salt} = \{11, 22.5\}\%$ at a temperature of 40 °C. It was observed, as depicted in Figure 1.3, that the solubility of CO_2 is inversely related to the presence of salt within the solution, with a quicker dissolution rate in pure water compared to brine. The equilibrium state is attained within 4 hours in pure water, 7 hours at 11% c_{salt}, and 15 hours at 22.5% c_{salt}. A similar pattern appears for tests 5, 8, and 10, which were carried out with a liquid volume ϑ_λ of 48.24 cm^3 at a constant temperature of 40 °C and different salinities $c_{salt} = \{0, 11, 22.5\}\%$.

The addition of NaCl not only decreases the solubility of CO_2, but also impacts the rate of mass transfer towards the end of the experiment, when diffusion becomes more significant

than convection. The observed behavior may be explained by the higher viscosity of the solution caused by the presence of salt. This increased viscosity restricts the movement of CO_2 molecules, resulting in a slower diffusion rate [Zarghami, 2017].

Remark 2 : Initial gas pressure and liquid phase volume effects on the carbon dioxide mass transfer rate

Experiments 1 to 3, as shown in Table 1.1, were carried out to investigate the impact of the initial CO_2 gas pressure on the decrease of gas pressure at equilibrium. These experiments were performed at a constant temperature of 30 °C. The findings, shown in Figure 1.3, demonstrate a less significant decrease in gas pressure in tests 2 and 3, which used greater initial pressures of 41.5 and 48.8 bar respectively, in contrast to test 1 with a lower initial pressure of 10 bar. Therefore, the solubility of CO_2 is clearly dependent on the initial gas pressure. Moreover, tests 4 to 6, executed with pure water, were aimed at assessing the volume of liquid's influence on the kinetics of CO_2 mass transfer. The equilibrium pressure decreases as the volume of the liquid phase introduced increases, as illustrated in Figure 1.3. This decrease in gas pressure is caused by a change in the mass of the gas phase : dissolved CO_2 has a lower mass when the volume of the liquid phase is small. In addition, an increase in the volume of the liquid phase in the experiments results in a greater duration of dissolution. Due to the constant section of the cell, the volume of the liquid phase is proportional to the height of the cell. An increased volume of the aqueous solution causes more distance between the interface and the bottom of the cell, which extends the diffusion time of the dissolved gas [Tayeb, 2023].

1.1.4 Experimental investigation of the hydrogen dissolution kinetics in aqueous solution

In the previous section, we discussed the dissolution of CO_2 in aqueous solutions. The present work is mainly focused on studying the kinetics of hydrogen dissolution in water and brine using the same pressure decay method. Actually, the significant decreases in pressure observed in our experimental results indicate a possible leakage, which brings an element of inaccuracy into the experimental findings. The purpose of this section is to provide a clear presentation of the findings on the dissolution of H_2 in aqueous solutions and to explore the potential for correcting the detected leakage in the experimental outcomes.

1.1.4.1 Hydrogen dissolution in aqueous solution : Experimental procedure

The kinetics of H_2 dissolution in water and brine were examined through two distinct experiments, using the pressure decay method (See section 1.1.2) . In the first experiment, pure water was used as the solvent, however in the second, brine with a salinity content of 22.5 % was used. The experiments were carried out at a constant temperature of 40 °C, as seen in Figures 1.4 and 1.5. Initial pressures $p_{\gamma 0}$ were set at 10.2 bar for the water experiment and 54.1 bar for the brine experiment. The detailed experimental conditions (the initial pressure, temperature, volumes of liquid and gas, and salinity) are encapsulated in Table 1.2.

It is important to mention that, in order to ensure safety due to the flammable nature of hydrogen, the pressure was limited to a maximum of 60 bar in the laboratory. This restriction limits this study from using high initial pressures.

TABLE 1.2 – Experimental parameters and conditions of the two performed H_2 dissolution experiments in pure water and brine.

Test numbers	Temperature T_0 (°C)	Initial pressure $p_{\gamma 0}$ (bar)	Liquid volume ϑ_λ (cm^3)	Gas volume ϑ_γ (cm^3)	Salinity c_{salt} (%)
1	40	10.2	105.31	26.32	0
2	40	54.1	90.45	41.19	22.5

The following sections will provide a comprehensive analysis of the experimental findings, with a primary focus on elucidating the kinetics of hydrogen dissolution in aqueous solutions and the impact of the system leakage on the results.

1.1.4.2 Hydrogen dissolution in aqueous solution : Experimental findings

This section provides a description of the results obtained from two experimental tests that focused on the kinetics of hydrogen dissolution in aqueous solutions (pure water and saturated brine). As presented in the previous section for CO_2 dissolution, the findings are expressed in terms of the temporal variations in the pressure of H_2 for each experiment.

In the first test, the dissolution kinetics of H_2 in pure water were evaluated by measuring the temporal changes in hydrogen pressure p_γ.

The data shown in Figure 1.4 clearly shows a drop of gas pressure over time, suggesting the dissolution of hydrogen in the water. For the thermodynamic equilibrium, we calculated the final pressure of the H_2 using the hydrogen solubility measurement in pure water reported by [Chabab, 2020]. According to these data from the literature, the thermodynamic equilibrium pressure for H_2 is approximately 9.6 bar. The hydrogen pressure decreased from 10.1 bar to 9.6 bar over the first five days, indicating that the hydrogen is dissolving into the water. However, a persistent decrease in pressure suggested a potential system leak. This deviation from the determined equilibrium pressure is explained by a leakage in the system occurring after the fifth day.

The collected data may be used to measure the kinetics of H_2 dissolution in pure water. However, it is crucial to interpret the results cautiously due to the identified leak. Thus, in section 2.1.3.2, we will provide the analysis of the experimental findings using our developed model, while considering the presence of a leak in the system.

The second experiment investigated the dissolution kinetics of hydrogen in brine. Under these circumstances, the initial pressure was considerably elevated compared to the first test, hence increasing the probability of system leakage. Referring to the same work conducted by [Chabab, 2020], the expected final pressure in the thermodynamic equilibrium is around 53.4

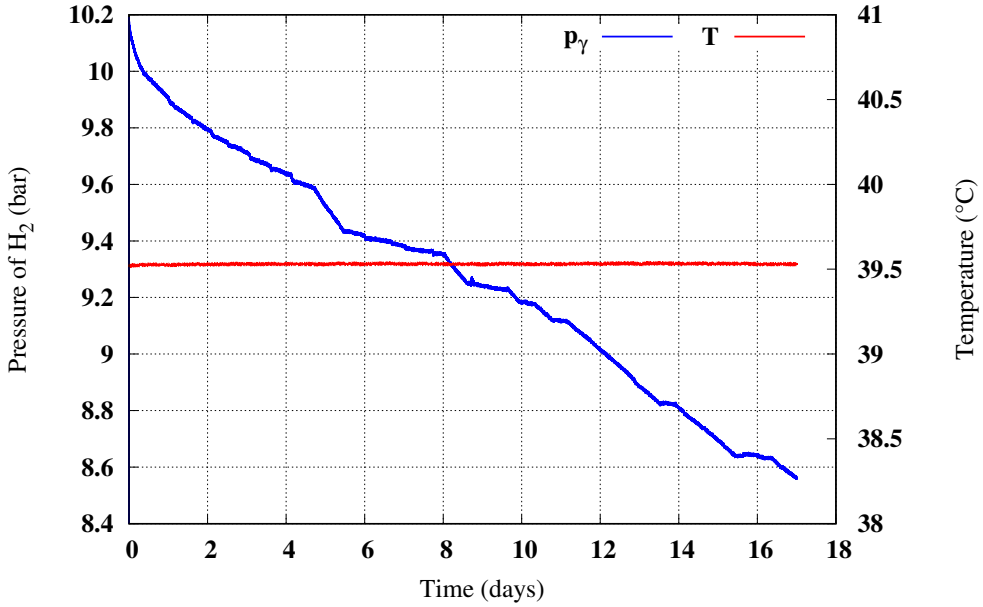

FIGURE 1.4 – Pure water experiment : H_2 pressure decay profile. The figure presents both the pressure of H_2 (p_γ) and the temperature (T) over the course of the experiment.

bar. During a period of 3.5 days, the pressure decreased from 54.2 bar to 51.8 bar, as shown in Figure 1.5. Hence, the final pressure recorded was much below the expected one, indicating a possible leakage of hydrogen gas from the system. The decrease in pressure in this case may be attributed to both the hydrogen dissolution in the water and a possible system leak. The rate of pressure decline in the second experiment was much faster than in the first, suggesting that the higher initial pressure may have contributed to the increased leakage in the system.

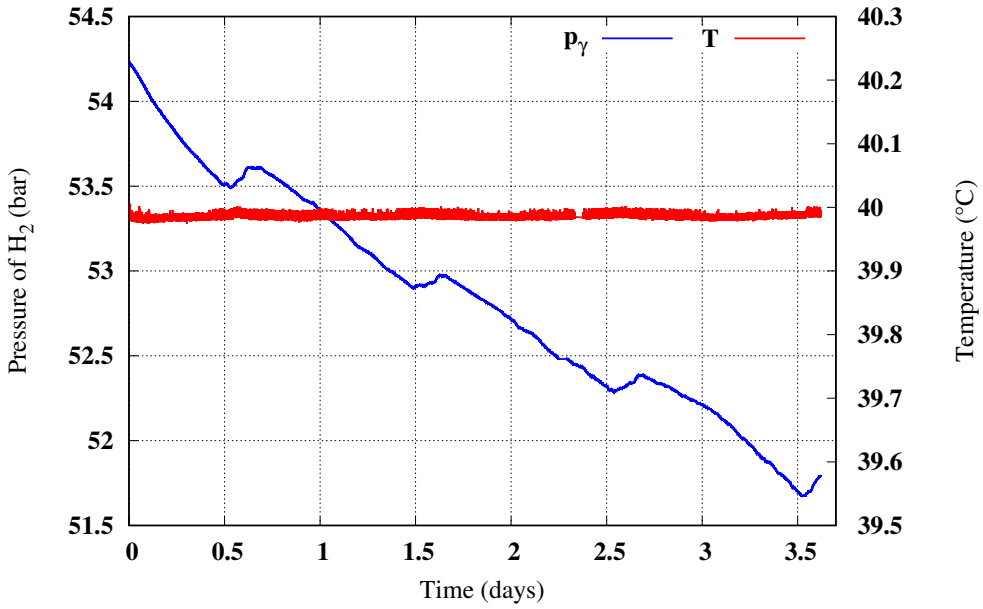

FIGURE 1.5 – Brine experiment : H_2 pressure decay profile.The figure presents both the pressure of H_2 (p_γ) and the temperature (T) over the course of the experiment.

The kinetics of hydrogen dissolution in brine and water were investigated in this analysis via two experiments in pure water and brine. A leak in the system was identified in these two tests. The leakage is a result of the challenges associated with handling hydrogen due to its tiny size. The data collected from these studies need careful analysis, especially considering the possibility of system leaks, in order to ensure correct interpretation and use of the results, which will be the purpose of section 2.1.3.2.

1.2 Experimental study of gas humidification

This section focuses on studying the water content in the gaseous phase which indicates the amount of water present in the gas-rich phase. For this purpose, an innovative storage pilot is used to conduct a laboratory-scale gas storage scenario. The helium gas is used as a case of study. In fact, we will perform a cycling experiment of the helium in this laboratory pilot that initially contains saturated brine. The purpose is to accurately quantify the water content in the helium-rich phase.

The investigation starts with a comprehensive justification for selecting helium gas as the main study case. Subsequently, a rigorous review of the most recent scientific literature on the topic is conducted. Following this, we provide a detailed description of the laboratory setup used in this investigation. Finally, we present and analyze the findings of our study.

1.2.1 Helium as an alternative to hydrogen in the experimental work

The general purpose of our work primarily concerns hydrogen. However, due to its complex operating features, helium is used as an alternative in our experimental investigation. In fact, dealing with hydrogen in laboratory investigations poses several difficulties mainly because of its distinct physico-chemical properties. Due to its low molecular weight and tiny size, hydrogen has a natural tendency to escape or leak through surfaces. This is worsened by its low viscosity and molecular weight, resulting in a notable rate of escape from confinement, which may be up to 50 times higher than water and 10 times higher than liquid nitrogen [Ministry of ecology and energy, 2009]. The gas easily permeates through porous surfaces and tiny gaps, possibly leaking from hermetically sealed equipment as we noticed in the previous section 1.1.4. Furthermore, hydrogen is classified as an extremely flammable substance [Skjold, 2017]. Its wide flammability range of 4 to 75 % in air, coupled with a very low ignition energy, poses a high risk of fire or explosion. Indeed, these two outcomes are responsible for 84% of recorded accidents involving hydrogen. Its low ignition energy means that even minimal energy sources can trigger combustion, which poses a significant risk during laboratory handling [Ministry of ecology and energy, 2009].

To reduce the challenges associated with hydrogen manipulation during experimental procedures, it is preferable to replace it with helium, an inert and non-flammable gas. This significantly reduces the risk of chemical reactivity during experiments and addresses the safety concerns associated with hydrogen's high flammability specially at high pressures [Kouremenos, 1988]. In addition, helium and hydrogen have comparable thermal characteristics, as seen in Figure 1.6. The specific heat at constant volume C_v (1.6c) and at constant pressure C_p (1.6d) of hydrogen

and helium gases show a relative variation of less than 2% within a temperature range of [20, 50] °C and at pressures ranging from 10 MPa to 20 MPa. Figures 1.6a and 1.6b demonstrate that helium and hydrogen exhibit similar values for the isobaric thermal expansivity (α) and the isothermal compressibility factor (β) under different temperature and pressure conditions. The relative variations of α and β are less than 18% [Kunz, 2012].

In our experimental investigation, we will use helium rather than hydrogen to avoid safety risks and possible leakage linked to high-pressure hydrogen in the laboratory setting. In the next subsection, we will present an overview of the water content determination methods in the literature.

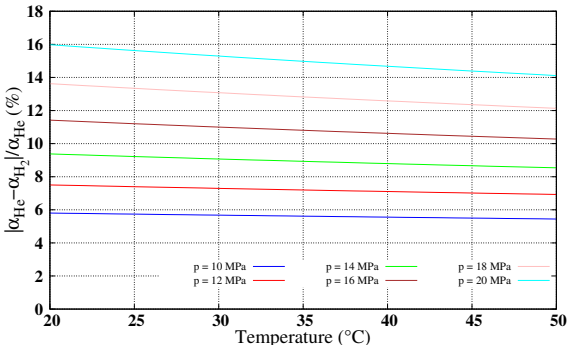

(a) Isobaric thermal expansivity α

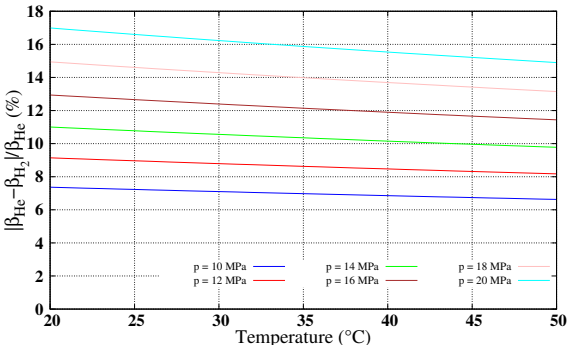

(b) Isothermal compressibility factor β

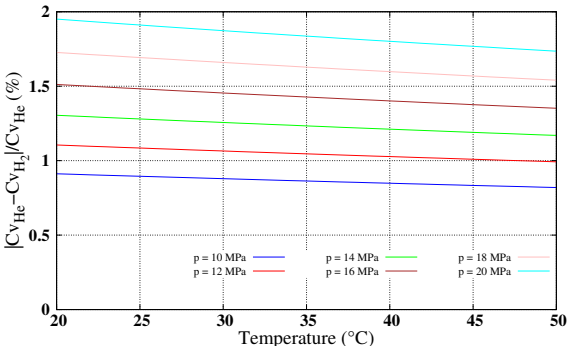

(c) Specific heat at constant volume C_v

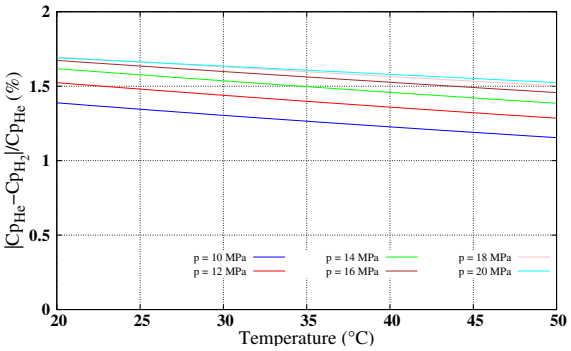

(d) Specific heat at constant pressure C_p

FIGURE 1.6 – Comparative analysis between the proprieties of He and H_2 gases [Kunz, 2012].

1.2.2 Literature review : Experimental methods for determining water content in gas-rich phase

The assessment of water content in the gas-rich phase is a critical aspect of this study. It is important to outline the common experimental methods described in the literature for measuring the amount of water content in the gaseous phase. This review summarizes the existing techniques, which can be broadly classified as direct and indirect methods [Mohammadi, 2004] :

- **Direct Methods** : Usually referred to as absolute methods, these methods rely on a direct relation between the evaluated quantity and the water content in the gas. These measurement techniques are included in such methods :

- Karl Fischer Titration : This method is a widely adopted experimental method that quantifies water content within various samples through a chemical reaction involving water, iodine, and sulfur dioxide [Connors, 1988]. The quantity of iodine used in the reaction is directly proportional to the amount of water content in the sample. The Karl Fischer Titration process requires introducing a standardized iodine solution to the sample and quantifying the electrical current generated throughout the reaction. By using the current measurement, it is possible to determine the water content of the sample, thereby obtaining a comprehensive insight into its composition. This method has a high level of precision and is suitable for quantifying water content within the low parts per million (ppm) range [Davies, 1975 ; Archer, 1974 ; Scholz, 2012].
- Gravimetric Hygrometer : This technique is used to determine the amount of water in a gas sample by removing the moisture and measuring the mass of the remaining dry gas. This is achieved by exposing the sample to a desiccant, commonly silica gel, to absorb the water [Wilke, 1993 ; Visscher, 1999]. Subsequently, the mass of the dry gas is meticulously measured with a high-precision balance. This approach is highly precise, however it may be time-consuming and necessitates a meticulously well controlled balance as reported in the work of [Bell, 1995].

- **Indirect Methods** : These methods rely on a secondary parameter that correlates with the amount of water present in the gas phase. Instead of directly measuring the water content, these techniques estimate the water content by evaluating a specific property of the sample that is influenced by the presence of water. The advantages of indirect methods are numerous, including the convenience and simplicity in analysis, cost-effectiveness, and the flexibility to be applied to a wider range of sample types. Despite the advantages mentioned, the approaches have certain limitations, such as reduced accuracy and vulnerability to interference from other compounds present in the sample. Some of the most known indirect techniques are presented below :

  - Laser spectroscopy : This method uses the principle of light absorption or transmission as it passes through a sample. Through the precise determination of the amount of light that is either absorbed or transmitted at specific wavelengths, it is possible to calculate the water concentration in the sample [Funke, 2003 ; Berezin, 2008]. As reported by [Bulatov, 1982], this technique is especially valuable for examining small quantities of water in gases, as water's light absorption is extremely sensitive. However, the equipment is often costly and necessitates meticulous calibration and maintenance [Crocombe, 2018].
  - Gas chromatography : It is a technique used to separate compounds in a mixture of gases. The separation takes place when the volatile components traverse a column containing a stationary phase, therefore classifying compounds depending on their retention duration. As explained by [McNair, 2019], gas chromatography method is well known for its capacity to detect and measure substances at very low concentrations, producing detailed data that is useful for studying complex mixtures. However, its use is limited to volatile substances.

— Capacitance : This method is based on the principle that the dielectric constant of a material varies with its moisture content. This method offers a quick and non destructive way to determine water content in different materials by measuring their capacitance, which refers to their ability to store an electric charge. However, [Lstiburek, 1996] elucidated that the precision of the measurements can be affected by variables such as temperature and density which may require frequent calibration.

We have thoroughly reviewed the experimental methods described in the literature for measuring the amount of water in gaseous systems. A summary of all methods employed for measuring water content in gases is presented in Table 1.3.In the next part, we will describe our innovative laboratory storage pilot, an indirect method that measures the water content in the gas-rich phase. This pilot is capable of reproducing underground storage conditions on a laboratory scale setting.

Table 1.3 – Summary of methods for measuring water content in gas.

Method Type	**Technique**	**Description**	**Advantages**	**Drawbacks**
Direct	Karl Fischer Titration	Quantification of water content through a chemical reaction involving water, iodine, and sulfur dioxide.	High precision, suitable for low ppm range.	Requires standardized iodine solution, meticulous current measurement.
	Gravimetric Hygrometer	Measures water by removing moisture and weighing dry gas.	Highly precise, wide applicability.	Time-consuming, requires precise balance control.
Indirect	Laser Spectroscopy	Light absorption or transmission through a sample to calculate water concentration.	Sensitive for small quantities, rapid, non-destructive.	Costly equipment, requires calibration and maintenance.
	Gas Chromatography	Separates compounds in gas mixture using retention time in a stationary phase column.	Detects low concentrations.	Limited to volatile substances.
	Capacitance	Measures dielectric constant changes with moisture content.	Rapid, non-destructive.	Affected by temperature and density, requires frequent calibration.

1.2.3 Experimental set-up : Laboratory storage pilot

The experimental set-up presented in this work, depicted in Figure 1.7, is designed to replicate a salt cavern environment within a controlled laboratory setting, with the primary objective of examining the influence of humidity on the thermodynamics of gas stored in such conditions.

FIGURE 1.7 – Overview of the laboratory storage pilot and its components.

The core of this set-up is a high-pressure cylindrical tank constructed from stainless steel, with dimensions specified as height $L = 50.0$ cm and radius $R = 9.0$ cm, resulting in a total volume of $V = 12.3$ litres (see Figure 1.8). The experimental apparatus includes a reservoir situated at the base, measuring 6 cm in height and 5.65 cm in diameter, which is designed to contain brine. It is equipped with a heating system that regulates the temperature at the top and a heat transfer fluid that controls the temperature at the bottom. The pilot is insulated by a thermal envelope that surrounds its sides. This insulation helps create a temperature difference between the lower and upper sections of the set-up. Figure 1.8 illustrates the axes used for measuring vertical temperature profiles. Each axis is equipped with five sensors : sensors C (86 mm from the wall), M (46 mm from the wall), and W (6 mm from the wall). These sensors are separated along the axis, with a vertical interval of 28 mm between each sensor. Additionally, seven humidity sensors, labeled H_1 to H_7, are installed throughout the storage pilot to track the water content in the gas phase (see Figure 1.8). It is important to mention that these sensors also measure the temperature. The uncertainties associated with these measurement instruments are presented in Appendix A.

1.2.4 Water content in helium gas-rich phase : Experimental procedure

Two laboratory tests were conducted to evaluate the behavior of Helium as a stored gas under different conditions : one with saturated brine ($c_{\text{salt}} = 22.5\%$) present in the brine reservoir (the

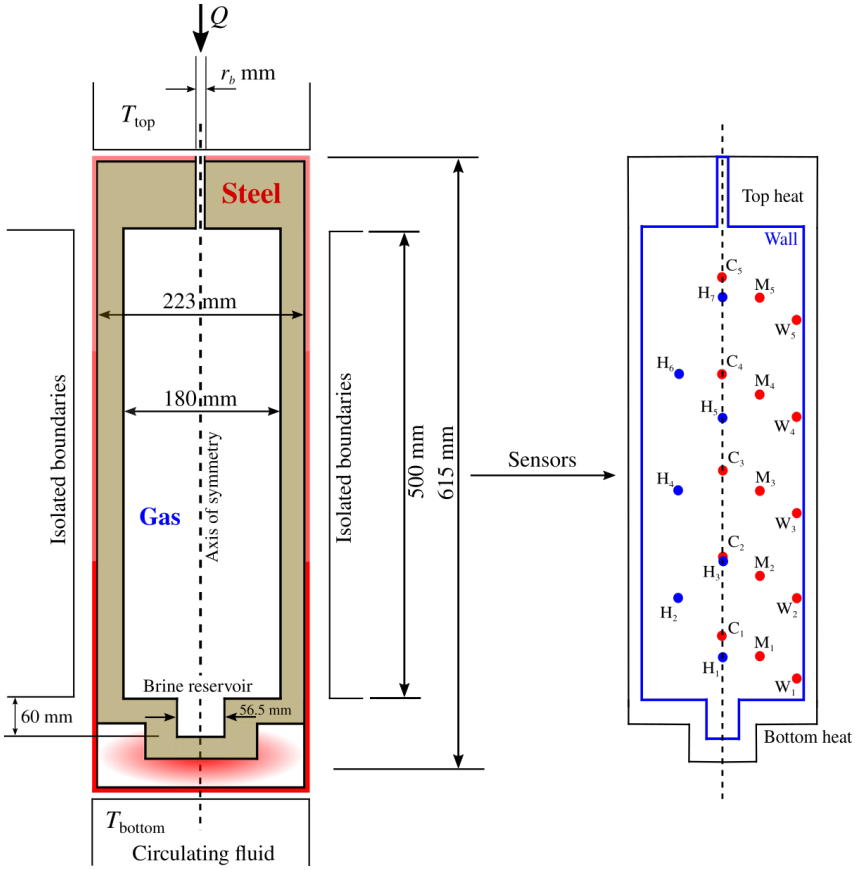

FIGURE 1.8 – Schematic diagram of the laboratory storage pilot and the placement of sensors.

humid test), and the other with an empty reservoir (the dry test). The temperatures at the upper and lower sections of the storage pilot were set at 43°C and 46°C, respectively, with the sides of the set-up being isolated. Prior to each test, a helium flush was carried out. The apparatus was filled with helium, increasing the pressure from atmospheric to the desired initial pressure of 12 MPa. The system is kept at this pressure for a duration of 2.5 days in order to establish stability in both temperature and pressure. This period is referred to as the stabilization phase. Following this phase, the acquisition system is given the mass variation program shown in Figure 1.9.

The program starts with a slow filling phase of 2.26 hours, followed by a rest phase of 30 minutes (see Figure 1.9). Cycling begins after this rest phase and consists of three cycles. Each cycle lasts 16.3 minutes and contains four phases : a withdrawal phase (5.4 minutes), a rest phase (2.7 minutes), an injection phase (5.4 minutes), and a rest phase (2.7 minutes). The cycling leads to relative mass variations ranging from 16.9% to 35.4% (see Figure 1.9). At the end, an intense withdrawal phase for 19.9 minutes is conducted.

1.2.5 Water content in helium gas-rich phase : Experimental findings

This section is divided into two separate subsections, delineating the outcomes of the dry and humid tests. Initially, we conducted a comprehensive comparison analysis of these two tests.

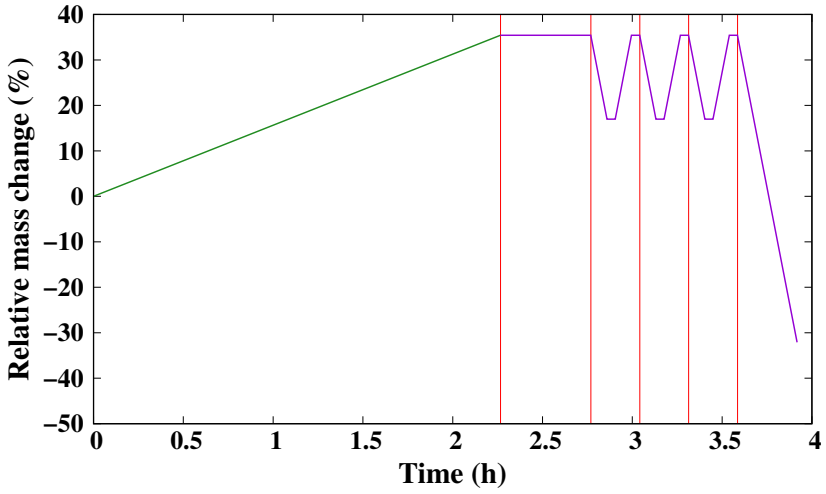

FIGURE 1.9 – Relative mass exchange during filling and cycling phases.

Following this,the second part delves into the detailed experimental results of the humid test, presenting the results of the temperature, pressure, and relative humidity during the stabilization and cycling phases. The experimental data obtained from this part will subsequently be used in the latter section of this study for numerical modeling.

Comparison between the dry and humid tests

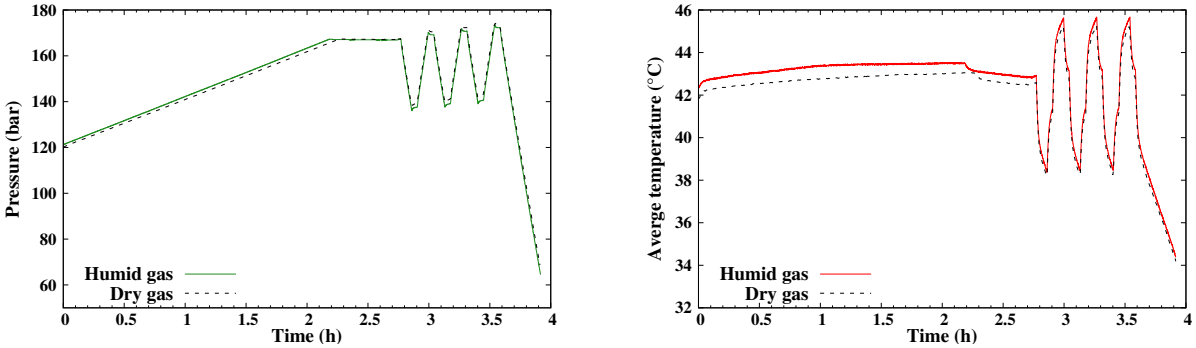

(a) Pressure

(b) Average temperature

FIGURE 1.10 – Pressure and average temperature evolution over time during the two experimental humid and dry tests.

Figure 1.10a displays the evolution of helium pressure throughout the dry and humid tests. The pressure data from both tests exhibits a strong correlation, with minimal differences observed.

Moreover, Figure 1.10b illustrates the average temperature evolution (average of all the temperature sensors presented in Figure 1.8) during these two tests, highlighting the little differences seen between them, which are limited to a maximum of 0.7 °C. To further clarify the differences between the two tests, we present the temperature profiles of the the bottom sensors, which are W_1, M_1, C_1 and the sensors on the top of the pilot, W_5, M_5, C_5 (see figures 1.11). These profiles

show a strong correlation across all observed temperatures in the storage pilot, with minimal discrepancies. The differences are more apparent in the upper section of the pilot compared to the lower section, which is primarily affected by the heating at its bottom.

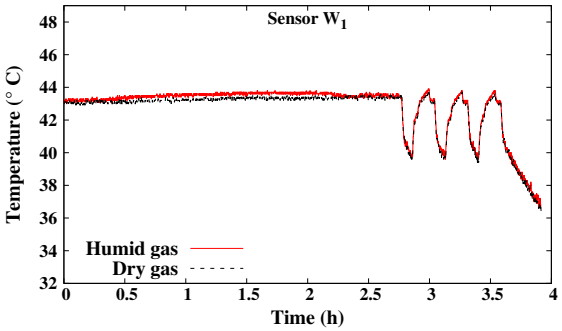

(a) Sensor W1 (The well sensor at the bottom)

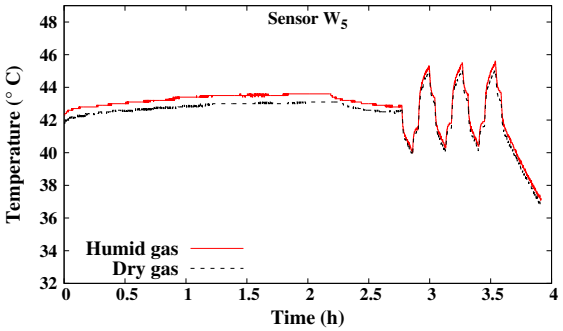

(b) Sensor W5 (The well sensor at the top)

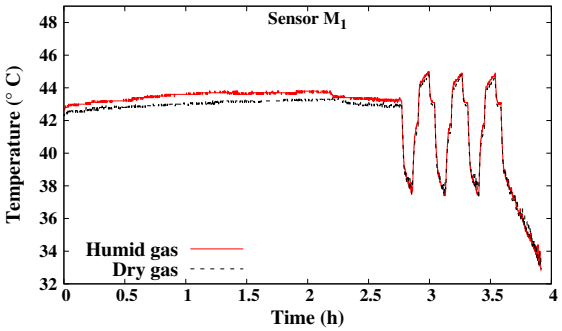

(c) Sensor M1 (The sensor located at the bottom middle of the pilot)

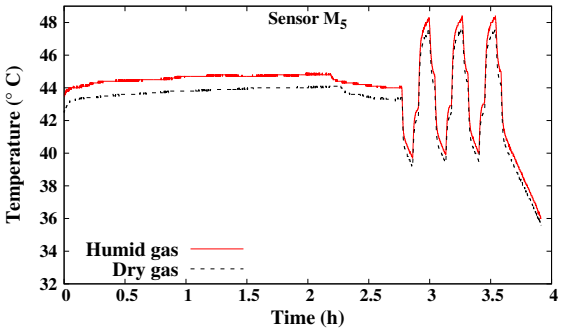

(d) Sensor M5 (The sensor located at the top middle of the pilot)

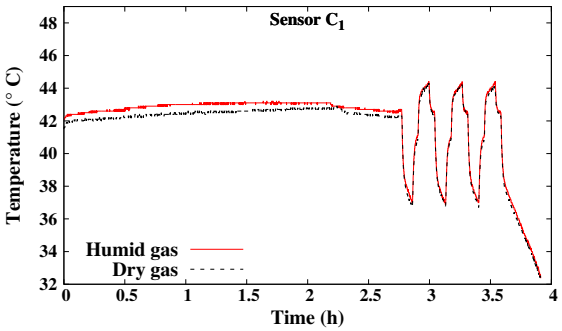

(e) Sensor C1 (The bottom axial sensor)

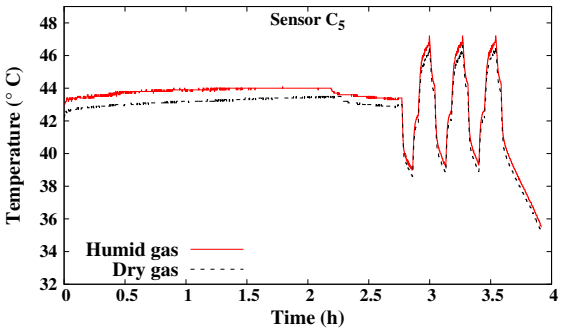

(f) Sensor C5 (The top axial sensor)

FIGURE 1.11 – Temperature evolution over time in the pilot : sensors $\{W_1,M_1,C_1\}$ (at the bottom) and sensors $\{W_5,M_5,C_5\}$ (at the top) as shown in Figure 1.8. The figures compare the results from the humid test (solid lines) and the dry test (dashed lines).

Experimental results of the humid test

In the following part of this investigation, our primary focus will be directed towards a comprehensive examination of the humid test.

During the stabilization phase, the average temperature of all the sensors increased from 30 °C to reach the desired temperature of 42 °C, which caused an increase in pressure. Figure 1.12b shows that the helium pressure increased from 12 MPa to 12.5 MPa. After this phase,

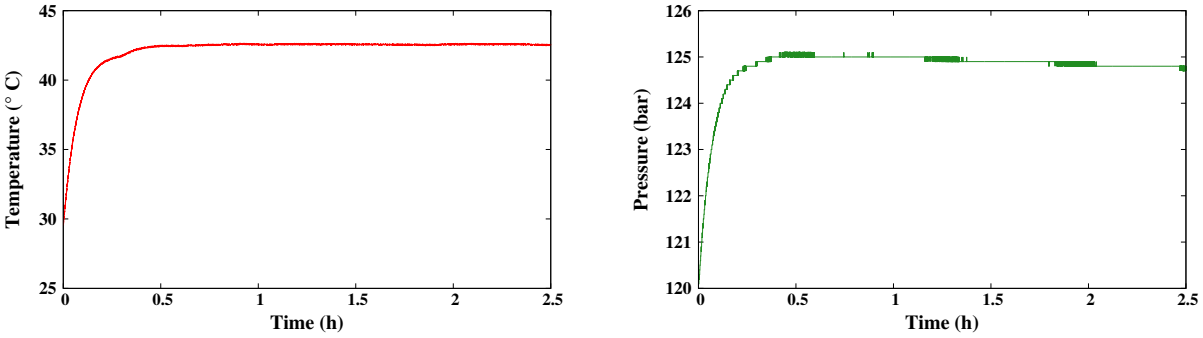

(a) Average temperature (b) Pressure

FIGURE 1.12 – Pressure and average temperature evolution over time during the stabilization phase.

the gradual filling and cycling of helium are initiated, as previously shown in Figures 1.10a and 1.10b (solid lines). These figures delineate the temporal evolution of the average temperature and pressure during the slow fill and cycling phases of the humid test. The initial slow introduction of helium elevates the pressure from 12 MPa to 17.2 MPa, while the average temperature remains relatively stable at 43.5°C. Throughout the cycling phase, there was a decrease in the average temperature and pressure when helium was withdrawn and a rise when helium was injected.

Figure 1.13 illustrates the relative humidity levels recorded by the seven humidity sensors, designated from H_1 to H_7 (as previously depicted in figure 1.8). It is observed that sensor H_1, positioned at the lowest point of the pilot, consistently measures a higher moisture level since it is closer to the reservoir. In contrast, sensor H_7, located at the top of the pilot, registers the minimal relative humidity readings due to its location far from the moisture reservoir. Moreover, the data shows that sensor H_2 does not delineate the cycling phase nor the relative humidity fluctuations with the same clarity as the other sensors. This observation highlights the possibility of irregularities in the functioning of this sensor. In fact, Figure 1.14 represents the average relative humidity of the sensors, which remains constant during the slow filling phase and experiences a gradual reduction throughout the cycling ; it drops from 89% to 44%.

To sum up, the experimental findings provided in this work show a decrease in the average relative humidity values during the cycling phase, which can be explained by the effect of introducing dry gas into the pilot during the injection and the removal of humid gas during the withdrawal. Furthermore, this decrease may be attributed to the gas humidification kinetics, which will be clarified in the numerical analysis of this experiment.

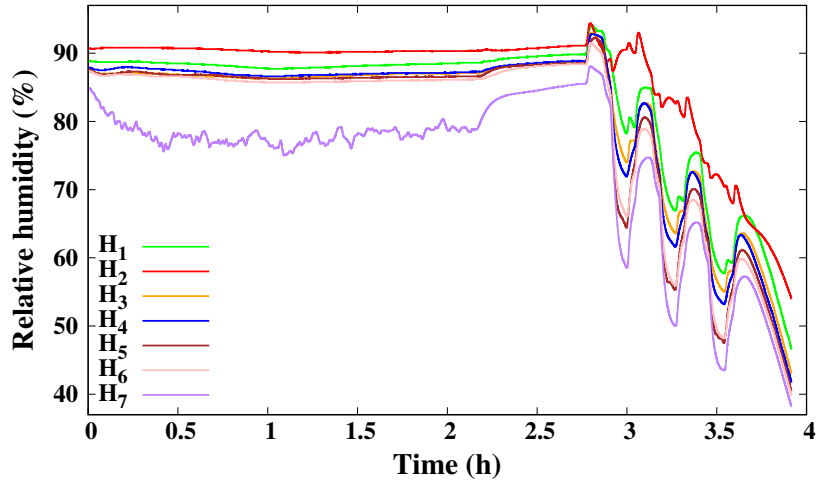

FIGURE 1.13 – Relative humidity evolution over time during cycling of the humid test for all the sensors H_1 - H_7 (as shown in Figure 1.8).

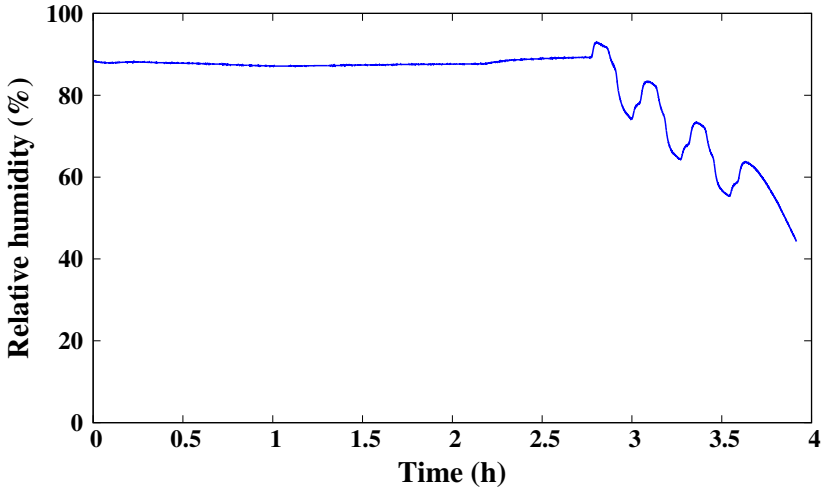

FIGURE 1.14 – Average relative humidity evolution over time during cycling of the humid test.

2 Comprehensive study of gas dissolution kinetics and humidity models : Numerical validation and comparison with the literature

Understanding the behavior of gases in aqueous solutions and the influence of water content in the gas-rich phase is imperative for the optimization of underground storage systems. Specifically, the kinetics of gas dissolution and the solubility of water in gases are critical parameters for efficient design and operation. This section aims to present a comprehensive explanation of these subjects, which are explored in two separate but interconnected subsections : the study of how gases dissolve in water and brine during pressure decay experiments (Section 2.1), and the verification of the accuracy of the humid gas model for different gases (Section 2.2). In the first subsection, a thorough examination is conducted on the kinetics of CO_2 and H_2 dissolution in

aqueous solutions. Using the PVT cell experiments and the numerical methods, the objective is to make connections between laboratory-scale data and large-scale implementations in underground storage caverns. Therefore, a non-dimensional model is developed, aiming to ensure that laboratory-based findings can be accurately extended to real-world conditions.

On the other hand, the second subsection is primarily oriented towards the validation of the proposed humid gas model. This model aims to elucidate the solubility of water in hydrogen and helium, which is an essential variable in the efficiency and safety of gas storage systems. The validation process involves a comparison between the predictions of the model and existing experimental data, offering rigorous scrutiny of its applicability and accuracy. This model, which assumes a homogeneous thermodynamic state and is unaffected by model dimension, thereby maintains validity when applied on the large scale of salt caverns.

Indeed, the focus of this section is predominantly on the numerical approach to the problem. The findings herein will serve as foundational elements for the second chapter of this dissertation, which aims to extend the study to actual salt cavern conditions.

2.1 Study of the kinetics of gas dissolution in pure water and brine during pressure decay experiments

As delineated in Section 1.1, the experimental results of gas dissolution in aqueous solutions have been previously presented. Building upon this foundation, the primary objective of this subsection is to examine the kinetics of gas dissolution, specifically CO_2 and H_2, in both pure water and brine under pressure decay conditions. Utilizing a PVT (Pressure-Volume-Temperature) cell, this study aims to simulate the dissolution processes at a laboratory scale, providing a foundational basis for applications in underground storage caverns. Two numerical models are employed to characterize the mass transfer phenomena : firstly, a diffusion model informed by Fick's law and Henry's law, and secondly, a more comprehensive model that accounts for density-driven natural convection.

In addressing the challenges posed by scale disparities between laboratory setups and large-scale underground storage conditions, this subsection focuses on model validation at the laboratory scale for future application in expansive environments. To this end, the development and calibration of a numerical model are critical, with a special emphasis on the diffusion coefficient. Consequently, the governing equations are presented in a non-dimensional form to allow for reliable scaling and comparison with real salt cavern conditions.

To achieve a comprehensive understanding, this subsection is structured to provide a sequential presentation of relevant topics. Initially, it offers a review of existing models that describe diffusion and dissolution kinetics, followed by a presentation of the modeling framework developed for this study. This encompasses the governing equations, boundary conditions, and their non-dimensional forms, which are crucial for parameter calibration. Subsequently, results from numerical simulations are detailed, focusing on the impact of natural convection and varying brine salinities on the dissolution processes of CO_2 and H_2. These results are compared with the experimental data from Section 1.1 to evaluate the validity and accuracy of the model.

Through this approach, this subsection aims to further our understanding of gas dissolution

kinetics, particularly in the context of underground storage, and sets the stage for the next chapter that will examine this subject on a storage site scale.

2.1.1 Literature review on diffusion coefficients data and the existing numerical models

Investigating the dissolution kinetics of gases is crucial for understanding their behavior in underground storage. While extensive research has been performed on the thermodynamic equilibrium of gas dissolution in water/brine, data on gas diffusivity remain scarce [Chabab, 2020 ; Akinfiev, 2003]. This study aims to quantify the gas mass transfer kinetics into the aqueous solution over time. When gas comes into contact with the liquid phase, it starts to dissolve along the interface between the two phases. Therefore, a gradient of concentration occurs, leading to a change in density within the brine. The presence of this gradient causes the generation of the natural convection process, which significantly accelerates the gas dissolution kinetics. Hence, it is essential to have a more thorough understanding of the mass exchange process in order to accurately estimate the duration of gas dissolution under storage conditions. The dissolution kinetics will be modeled using experimental data, which will provide essential parameters for the salt cavern model.

Diffusion coefficient of CO_2 in water and brine

The diffusion coefficient (D) is the most important parameter in this study. In fact, numerous studies in the literature have investigated the influence of pressure and temperature on the dissolution kinetics of CO_2 into pure water [Belgodere, 2015 ; Lu, 2013 ; Hirai, 1997 ; Tamimi, 1994]. However, even though there are a few studies [Cadogan, 2014 ; Hirai, 1997] that have investigated high-pressure environments, the experimental conditions within these works still deviate significantly from those of underground storage conditions due to their use of pure water rather than saturated brine. For instance, [Tamimi, 1994] conducted a study on the diffusion coefficient of CO_2 in pure water by assessing the rate of CO_2 dissolution under atmospheric conditions and elevated temperatures (up to 95°C). Similarly, [Tan, 1992] employed a quiescent approach to determine the diffusion coefficients of carbon dioxide in water and various fluids. In addition, [Hirai, 1997] used laser-induced fluorescence to analyze the dissolution rate of a liquid CO_2 droplet, thereby estimating the diffusion coefficient of CO_2 in formation water at high pressures (up to 392 bar). Furthermore, a theoretical model for calculating the diffusivity of CO_2 and water mixtures across a large range of pressures was proposed [Mutoru, 2011].

However, only a select number of works in the literature have focused on the dissolution kinetics of CO_2 in saline solutions. [Bahar, 2008] explored the diffusivity of CO_2 in a 2% NaCl brine, separating the steady and unsteady states of diffusion. Their results revealed a higher diffusion coefficient in the unsteady state compared to the steady state. In a comparative study, [Shi, 2018] investigated the temporal mass transfer of CO_2 in both pure water and brine under reservoir conditions noting a 30% pressure reduction in pure water and a 15% decrease in brine at equilibrium compared to the initial pressures. Furthermore, [Yang, 2006] conducted a study on the rate of CO_2 into brine at high temperatures (up to 58 °C) within a PVT cell using

the pressure decay method. Using a modified diffusion equation, this study applied an effective diffusion coefficient that is two orders of magnitude greater than the molecular diffusivity. In addition, [Azin, 2013] conducted a study on the diffusion of CO_2 in brine, examining a pressure interval between 59 and 69 bar.

To sum up, the CO_2 diffusion coefficient can be influenced by various factors, including substances purities, and laboratory methods. However, the used mathematical model and assumptions have the most significant impact on the observed D. Table 1.4 presents a summary of the diffusion coefficients of CO_2 in pure water and brine, as reported in the literature. The experimental data on the effect of salt on the dissolution kinetics of CO_2 in brine are still very scarce. Further elucidation, particularly regarding saturated brine and elevated gas pressures, is required to get a more comprehensive understanding of the rate of CO_2 mass transfer in the brine under storage conditions.

TABLE 1.4 – Summary of the measured diffusion coefficient of CO_2 in pure water/brine in the literature.

Temperature (°C)	Pressure (bar)	Diffusion coefficient D (10^{-9} $\frac{m^2}{s}$)	References
		Brine	
50	60	1.25-82	[Shi, 2018]
50-75	17.45	3.6-8.2	[Zarghami, 2017]
25	5-11.7	1.2-1.91	[Zhang, 2015]
32-50	59-69	3.52-6.16	[Azin, 2013]
27-58	17.86-56.47	170.7-269.8	[Yang, 2006]
38	15.4-58.3	1.92	[Renner, 1988]
		Pure Water	
21	40	0.92-1.71	[Belgodere, 2015]
25-150	142-493	2.218-12.33	[Cadogan, 2014]
-5 – 200	200	0.76-16.1	[Lu, 2013]
45	34.3-80.2	238.2-251.3	[Wang, 2013]
26	5-50	1.86	[Sell, 2013]
25-30	10-50	2-280	[Farajzadeh, 2009]
13	294-392	1.35-1.45	[Hirai, 1997]
25-55	1	1.97-3.67	[Frank, 1996]
20-95	1	1.76-8.2	[Tamimi, 1994]

Models of gas diffusion

The accuracy of the mathematical model describing the diffusion process is crucial in determining the measured value of the gas diffusion coefficient. This value D is mostly dependent on the assumed conditions required for developing the diffusion model. Typically, the models used to study the mass transfer process are established from a set of governing partial differential

equations by introducing certain boundary conditions [Rezk, 2022].

Two main approaches have been largely used for resolving the issue of gas dissolution in brine [Tayeb, 2023]. The first approach, based on pure diffusion, is interesting because it only considers Fickian diffusion and disregards the complications of natural convection [Farajzadeh, 2007 ; Upreti, 2000 ; Zhang, 2015]. This approach uses simplified assumptions that have a significant impact on the obtained outcomes, resulting in large differences in the reported gas diffusion coefficients across similar systems, as we can see in Table 1.4.

On the other hand, a more intricate method is proposed to integrate the different physical processes involved in the gas dissolution process. This sophisticated approach is devised to evaluate the impact of natural convection on the kinetics of mass transfer. This sophisticated approach was developed to include the phenomenon of natural convection in the study of gas dissolution kinetics. In fact, when the gas in question comes into contact with the brine, its dissolution into the brine starts via a molecular diffusion process. As a result, a concentration gradient occurs, which generates a density variation within the brine. This density gradient accelerates the homogenization of the liquid phase. Natural convection is expected to play an important role in the transport of dissolved gas due to its influence on gas dissolution kinetics. Few published works, [Hassanzadeh, 2007 ; Farajzadeh, 2009 ; Soubeyran, 2019], included natural convection into their dissolution model.

The assumption of boundary conditions at the gas-liquid interface is a crucial factor in the study of gas dissolution in aqueous solutions, affecting the accuracy of the model. Typically, three categories of boundary conditions are assumed at the interface between the liquid and gas phases. Firstly, equilibrium boundary conditions assume that the concentration of gas in the liquid is immediately in a state of equilibrium with the gas phase. This is described by Henry's Law, which states that $c = H \cdot p_\gamma$, where c represents the gas concentration at the interface, H is Henry's constant, and p_γ is the pressure of the gas [Renner, 1988 ; Rowley, 1997]. Secondly, the semi-equilibrium condition assumes that the gas concentration at the interface between liquid and gas is dependent on the time-varying pressure of the system [Zhang, 2000 ; Upreti, 2002]. Lastly, the Robin boundary condition is a non-equilibrium boundary condition. It is considered the most general and sophisticated boundary condition because it introduces an additional resistance at the interface $1/K$ where K is the mass transfer coefficient. It is often described as $J = K(c - c^s)$ with J is the flux at the boundary [Zhang, 2000 ; Upreti, 2002].

In conclusion, Table 1.5 summarizes the different boundary conditions for gas dissolution at the gas-liquid interface. It is required to carefully choose and implement suitable boundary conditions in order to ensure the accuracy of the gas diffusion coefficients.

2.1.2 Mathematical framework for modeling the gas dissolution tests

This study introduces a model that considers convective transport to elucidate mass transfer kinetics. It specifically integrates an ordinary differential equation at the liquid-gas boundary to precisely quantify the temporal decrease in gas pressure and calculate the dissolution rate within the liquid phase. The non-dimensional formulation of this model is delineated in section 2.1.2.2, facilitating its application across scales from laboratory experiments to underground caverns.

TABLE 1.5 – Boundary conditions for gas dissolution at the gas-liquid interface.

Boundary Condition	**Description**	**Equation**	**Advantages**	**Drawbacks**
Equilibrium Boundary	Assumes instant equilibrium between the gas and liquid phases at the interface.	$c = c^s$	Simplifies calculations, suitable for systems close to equilibrium.	Unrealistic for dynamic systems, neglects kinetic factors.
Quasi-Equilibrium Boundary	Considers a dynamic equilibrium that accounts for changes in gas concentration over time.	$c(t) = c(p_\gamma(t))$	More realistic for systems not at true equilibrium, allows for time-dependent study.	May not hold valid for longer periods
Robin-Type Boundary	Includes mass transfer resistance at the interface.	$J = K \cdot (c - c^s)$	General, sophisticated, accounts for both equilibrium and kinetic effects.	Can be difficult to determine the appropriate mass transfer coefficient K.

For clarity, subscripts signify specific quantities within this section. Greek letter subscripts (α, γ, λ) represent various phases ; α indicates a generic phase, γ the gaseous phase (for instance, CO_2 and H_2), and λ the aqueous phase (such as pure water or saline solution). The temperature is represented by T, p_α is the pressure, and ρ_α is the density.

The system being analyzed consists of a cell with a vertical height h and radius R (see Figure 1.15). This cell comprises two distinct phases, namely gas γ and liquid λ, which are separated by an interface denoted as $\Sigma_{\gamma\lambda}$. The interface is located at the abscissa $z = 0$. The gas phase is L_γ, whereas the liquid phase is L_λ. Each phase is located inside a domain Ω_α with a volume of ϑ_α and interacts with the other phase via the interface $\Sigma_{\gamma\lambda}$. This modeling technique offers a thorough representation of the kinetics of mass transfer, facilitating a more detailed comprehension of the system's behavior.

To model the experimental configuration illustrated in Figure 1.1, the problem is divided into three different stages. In the initial stage, for $t \leq 0$, the cell is comprised solely of the liquid phase λ. Under extremely low pressure, it is assumed that the λ–phase with mass $\mathcal{M}_\lambda$ is in hydrostatic equilibrium. The injection of the gas has a duration, denoted as t_0, that is so brief that no measurements are possible during this interval. For the subsequent stage, where $0 \leq t \leq t_0$, the γ–phase is introduced into the cell at a constant rate, with a mass denoted as $\mathcal{M}_\gamma$. The change in the overall mass of the fluid inside the system at any given time t may be mathematically represented as :

$$\mathcal{M}(t) = \mathcal{M}_\lambda + \mathcal{M}_\gamma \times (t/t_0).$$

In the third stage, when $t \geq t_0$, there is a transfer of mass between the two phases, and the

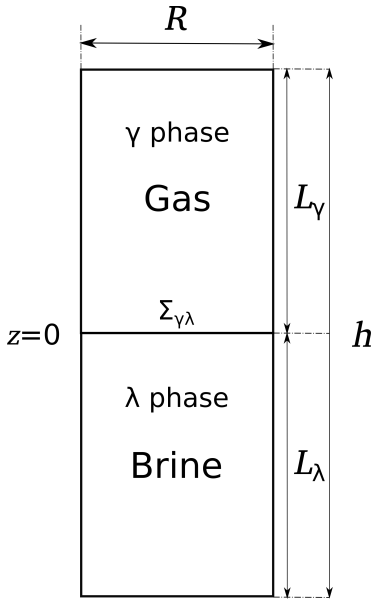

FIGURE 1.15 – Schematic representation of the gas - brine model inside a closed PVT cell

system gradually moves towards its equilibrium state. The principle of mass conservation states that :

$$\begin{cases} \mathcal{M}(t) = \mathcal{M}(t_0) = \mathcal{M}_\lambda + \mathcal{M}_\gamma; \\ \dot{\mathcal{M}} = 0. \end{cases}$$

To facilitate the modeling of pressure-decay experiments, certain assumptions are adopted. The volume of both phases ϑ_α is presumed invariant, with the interface $\Sigma_{\gamma\lambda}$ remaining static at an abscissa $z = 0$ and maintaining a constant section. The cell is considered impermeable, discounting any mass exchange from the λ–phase to the γ–phase. Consequently, any experimental pressure decrease is attributed exclusively to the mass transfer of the γ–phase into the λ–phase via the interface $\Sigma_{\gamma\lambda}$. Uniformity of temperature throughout the cell is presumed, with no fluctuation during the experiment. For the λ–phase, its density, ρ_λ, is considered dependent solely on the mass concentration of the dissolved gas, c, and the salt concentration of the brine, c_{salt}. The γ–phase is assumed to adhere to the real gas law, with its density, ρ_γ, expressed as follows :

$$\rho_\gamma = \frac{p_\gamma}{T_0 Z_\gamma}, \tag{1.1}$$

where the pressure of the γ–phase is denoted as p_γ, the constant temperature is by T_0, and the compressibility factor of the gas is denoted as Z_γ. It is assumed that Z_γ is a function of p_γ [Kunz, 2007].

2.1.2.1 Dimensional form of the equations

This section delineates the dimensional equations that form the foundation of our model for gas dissolution in an aqueous solution. It articulates the interplay between the gas and liquid phases, governed by a set of differential equations that describe the mass transfer process. The

equations presented herein are essential for understanding the kinetics of gas dissolution and will be explored in their dimensional form, providing the basis for subsequent non-dimensional analysis. For the sake of clarity, we shall proceed by assuming that for any given function φ, the material derivative can be represented as $\dot{\varphi} = \partial_t \varphi + \vec{v}_\lambda . \vec{\nabla} \varphi$ with $\vec{\nabla}$ being the gradient of a vector field.

Fick's law of diffusion

For the λ–phase, the barycentric movement can be mathematically represented as follows :

$$\rho_\lambda \vec{v}_\lambda = \rho_n \vec{v}_n + \rho_b \vec{v}_b. \tag{1.2}$$

The subscripts n and b refer to the dissolved gas and the solvent (either pure water or brine solution) with a mass concentration of $1-c$, where c represents the mass fraction of the dissolved gas. The density of the dissolved gas in the λ–phase is denoted as ρ_n, while the velocity of the dissolved gas in the λ–phase is represented by $\vec{v}_n$.

The diffusion flux vector $\vec{J}$ is defined as :

$$\begin{aligned} \vec{J} = \vec{J}_n = c(\vec{v}_n - \vec{v}_\lambda); \quad \text{or,} \\ -\vec{J} = \vec{J}_b = (1-c)(\vec{v}_b - \vec{v}_\lambda). \end{aligned} \tag{1.3}$$

By applying Fick's law, we can express the mass flux as :

$$\vec{J} = -D \vec{\nabla} c, \tag{1.4}$$

where D represents the diffusion coefficient.

Governing equations

The principle of mass conservation in the λ–phase can be expressed as :

$$\begin{cases} \dot{\rho_\lambda} + \rho_\lambda \vec{\nabla} . \vec{v_\lambda} & = 0; \\ \rho_\lambda \dot{c} + \vec{\nabla} . (\rho_\lambda \vec{J}) & = 0. \end{cases} \tag{1.5}$$

Although the temperature remains constant in our experimental modeling, we will include the entire model equations in this study as they will be used in the next chapter for the analysis on the cavern scale. Therefore, The energy equation of the λ–phase can be written in the following form :

$$\rho_\lambda C_{p\lambda} \partial_t T_\lambda + \rho_\lambda C_{p\lambda} \vec{v}_\lambda . \vec{\nabla} T_\lambda - \vec{\nabla} \cdot (\kappa_\lambda \vec{\nabla} T_\lambda) = 0, \tag{1.6}$$

where $C_{p\lambda}$ represents the heat capacity of the λ–phase, and κ_λ is the thermal conductivity of the aqueous solution.

The equation that describes the motion of fluid in the λ–phase, known as the Navier-Stokes momentum equation, is given by :

$$\rho_\lambda \dot{\vec{v}}_\lambda = -\vec{\nabla} p_\lambda + \vec{\nabla}.\underline{\underline{\xi_\lambda}} + \rho_\lambda \vec{g}. \tag{1.7}$$

The vector $\vec{g}$ is the gravitational acceleration vector and the fluid stress tensor, denoted by $\underline{\underline{\xi_\lambda}}$, is given by the equation $\underline{\underline{\xi_\lambda}} = \mu(\underline{\underline{\vec{\nabla}}}\vec{v_\lambda} + \underline{\underline{\vec{\nabla}}}\vec{v_\lambda}^T) - (2/3)(\vec{\nabla}\vec{v_\lambda})\underline{\underline{\delta}}$, where μ represents the dynamic viscosity of the λ–phase and $\underline{\underline{\delta}}$ is the second-order Kronecker delta.

If we assume that λ is initially at rest ($\vec{v}_\lambda = \vec{0}$ and $\underline{\underline{\xi_\lambda}} = \underline{\underline{0}}$), the pressure gradient ($p_\lambda(\vec{x}, t = 0) = p_{\lambda 0}(\vec{x})$) can be described by the following equation : $\vec{\nabla} p_{\lambda 0} = \rho_{\lambda 0}\vec{g}$. Thus, the Navier-Stokes momentum equation 1.7 can be written as follows, with $p = p_\lambda - p_{\lambda 0}$:

$$\rho_\lambda \dot{\vec{v}}_\lambda = -\vec{\nabla} p + \vec{\nabla}.\underline{\underline{\xi_\lambda}} + (\rho_\lambda - \rho_{\lambda 0})\vec{g}. \tag{1.8}$$

The impact of the dissolved gas and temperature variations on density is limited to the body force component of the Navier-Stokes momentum equation. The density ρ_λ is dependent on the concentration of the dissolved gas c and temperature T_λ. It can be written as :

$$\rho_\lambda = \rho_{\lambda 0}(1 - \alpha_T(T_\lambda - T_0) + \beta_c(c - c_0)), \tag{1.9}$$

with α_T being the thermal expansion coefficient and β_c being the volumetric expansion coefficient.

In the experimental modeling of the pressure decay experiments, the temperature $T_\lambda = T_{\lambda 0} = T_0$ which eliminates the temperature term in the equation 1.9 and cancels out the equation 1.6.

Initial and boundary conditions

This section outlines the initial and boundary conditions for the gas dissolution problem. These conditions are defined for the experimental model of gas dissolution in aqueous solutions using the pressure decay method.

In a controlled laboratory setting, as described in section 1.1, thermal regulation is accomplished by enclosing the dissolution apparatus in a basin that maintains a stable temperature. This ensures that all components remain at a consistent temperature, denoted as T_0.

The initial conditions of the system can be summarized as :

$$\text{Initial Conditions} \begin{cases} T_\lambda(\vec{x}, t = 0) = T_\lambda(\vec{x}, t) = T_0; \\ p(\vec{x}, t = 0) = p_0 = 0; \\ \vec{v}_\lambda(\vec{x}, t = 0) = \vec{0}; \\ c(\vec{x}, t = 0) = c_0 = 0. \end{cases} \tag{1.10}$$

We assume that there is no mass transfer from the λ–phase to the γ–phase across the interface $\Sigma_{\gamma\lambda}$. Thus, based on the Equations 1.3 and 1.4, we can write $\vec{v}_b = \vec{0}$ and $\vec{v}_\lambda$ can be expressed as :

$$\vec{v}_\lambda = \frac{\vec{J}}{1-c}, \quad \text{at } \Sigma_{\gamma\lambda}. \tag{1.11}$$

The mass rates of the two phases λ and γ at $\Sigma_{\gamma\lambda}$ can be written as :

$$\dot{\mathcal{M}}_\lambda = -\int_{\Sigma_{\gamma\lambda}} \rho_\lambda \vec{v}_\lambda . \vec{n}\, dA_{\gamma\lambda} = -\dot{\mathcal{M}}_\gamma. \tag{1.12}$$

The vector $\vec{n}$ is the outward unit vector, which is normal to Ω_λ. Various types of boundary conditions have been suggested in the literature for the interface $\Sigma_{\gamma\lambda}$, as explained in section 2.1.1.

In this study, we will employ the Robin-type boundary condition to describe the concentration of the dissolved gas. This boundary condition is considered the most comprehensive form as it incorporates essential parameters for mass transfer, including gas solubility, diffusion coefficient D , and interface resistance $(1/K)$. The Robin type boundary condition is expressed as $D\partial_z c(z=0,t) = K(c(z=0,t) - c^s)$, where c^s represents the saturation concentration of the dissolved gas. This approach has been previously used in studies by [Reza Etminan, 2013 ; Civan, 2001 ; Soubeyran, 2019].

In summary, the boundary conditions employed in this study at $\Sigma_{\gamma\lambda}$ can be described as :

$$\text{Boundary Conditions} \begin{cases} p_\lambda(z=0,t) = p_\gamma(t) \Rightarrow p(z=0,t) = 0; \\ \vec{v}_\lambda = \dfrac{-D\vec{\nabla}c}{1-c}; \\ \vec{J}.\vec{n} = K(c - \dfrac{p_\gamma(t)}{H}). \end{cases} \tag{1.13}$$

Henry's law defines the solubility of the γ–phase in λ–phase as $c^s = p_\gamma/H$, where H denotes the henry coefficient and is dependent on gas pressure p_γ, temperature, and salinity c_{salt}.

2.1.2.2 Non-dimensional form of the equations

This section provides a detailed description of the non-dimensional model equations. It elucidates the formulation of the field equations of the λ–phase in a non-dimensional form. To facilitate the translation of the mathematical model from laboratory scale to cavern scale, the preceding section field equations will be reformulated in a non-dimensional form.

To simplify the analysis, we introduce the following dimensionless quantities and operators, using L as a characteristic dimension of the studied geometry, L^2/D, D/L, and $\rho_{\lambda 0}D^2/L^2$ as scaling factors for time, velocity, and pressure :

$$\text{Scaling factors} \begin{cases} \tilde{t} & = t \times \dfrac{D}{L^2}; \\ \vec{\tilde{v}}_\lambda & = \vec{v}_\lambda \times \dfrac{L}{D}; \\ \tilde{p} & = p \times \dfrac{L^2}{\rho_{\lambda 0} D^2}; \\ \vec{\tilde{\nabla}}\phi & = \vec{\nabla}\phi \times L \quad \text{(for any variable } \phi\text{)}. \end{cases} \tag{1.14}$$

The equations presented in the section 2.1.2.1 can be transformed into a non-dimensional form by introducing the following non-dimensional variables :

$$\text{Non-dimensional variables} \begin{cases} \tilde{c} & = \dfrac{c}{c^s}; \\ \tilde{T_\lambda} & = \dfrac{T_\lambda - T_0}{T_0}. \end{cases} \tag{1.15}$$

Considering Equation 1.11, the non-dimensional velocity $\vec{v}_\lambda$ at the λ–phase surface is derived by applying the definitions in equation 1.14 and 1.15 :

$$\vec{v}_\lambda = \frac{\vec{\tilde{J}}}{1/c^s - \tilde{c}}, \tag{1.16}$$

where $\vec{\tilde{J}}$ is redefined as the non-dimensional mass flux into the λ–phase, such that $\vec{\tilde{J}} = L/(D\,c^s)\,\vec{J}$.

The body force term of the momentum equation is the only factor that accounts for the influence of dissolved gas and temperature changes on the density, under the assumption that the liquid phase is weakly compressible. Let us define the normalized λ–phase density as $\varepsilon_\lambda = \rho_\lambda/\rho_{\lambda 0}$. Thus, the density of the λ–phase, as given by Equation 1.9, can be expressed as :

$$\varepsilon_\lambda = \frac{\rho_\lambda}{\rho_{\lambda 0}} = 1 + \beta_c(c - c_0) - \alpha_T(T_\lambda - T_0). \tag{1.17}$$

The non-dimensional form of the principle of mass conservation 1.5 can be derived considering the Equation 1.17.

$$\begin{cases} c^s \dfrac{D}{L^2}\,\varepsilon_\lambda \partial_{\tilde{t}}\tilde{c} + c^s \dfrac{D}{L^2}\,\varepsilon_\lambda \vec{v}_\lambda \cdot \vec{\tilde{\nabla}}\tilde{c} - c^s \dfrac{D}{L^2}\,\vec{\tilde{\nabla}} \cdot (\varepsilon_\lambda \vec{\tilde{\nabla}}\tilde{c}) = 0; \\ \dfrac{D}{L^2}\,\partial_{\tilde{t}}\varepsilon_\lambda + \dfrac{D}{L^2}\,\vec{\tilde{\nabla}} \cdot (\varepsilon_\lambda \vec{v}_\lambda) = 0. \end{cases} \tag{1.18}$$

By dividing both sides of equation 1.18 by $(c^s\,D/L^2)$ and (D/L^2), the equation can be expressed as follows :

$$\begin{cases} \varepsilon_\lambda \partial_{\tilde{t}}\tilde{c} + \varepsilon_\lambda \vec{v}_\lambda \cdot \vec{\tilde{\nabla}}\tilde{c} - \vec{\tilde{\nabla}} \cdot (\varepsilon_\lambda \vec{\tilde{\nabla}}\tilde{c}) = 0; \\ \partial_{\tilde{t}}\varepsilon_\lambda + \vec{\tilde{\nabla}} \cdot (\varepsilon_\lambda \vec{v}_\lambda) = 0. \end{cases} \tag{1.19}$$

Using the definition $\tilde{T_\lambda}$ in the equation 1.15, the energy equation for the λ-phase (Equation 1.6) can be represented in its non-dimensional form as :

$$\varepsilon_\lambda \partial_{\tilde{t}}\tilde{T_\lambda} + \varepsilon_\lambda \vec{v}_\lambda \cdot \vec{\tilde{\nabla}}\tilde{T_\lambda} - \vec{\tilde{\nabla}} \cdot \left(\frac{\tilde{a}_\lambda}{D} \vec{\tilde{\nabla}}\tilde{T_\lambda} \right) = 0. \tag{1.20}$$

The non-dimensional brine thermal diffusivity, denoted as $\tilde{a}_\lambda$, is considered to have a constant value and it is described as $\tilde{a}_\lambda = \kappa_\lambda/\rho_{\lambda 0} C_{p\lambda}$.

The assumption is made that the dynamic viscosity of the λ–phase remains constant. Hence, the Prandtl and Rayleigh numbers may be precisely described as :

$$\begin{cases} \mathrm{Pr} = \dfrac{\mu}{\rho_{\lambda 0} D}; \\ \mathrm{Ra} = \dfrac{g(\varepsilon_\lambda - 1)\rho_{\lambda 0} L^3}{D\mu}, \end{cases} \tag{1.21}$$

where μ represents the dynamic viscosity of the λ–phase.

The diffusion coefficient of γ–phase (CO_2, H_2) in the λ–phase (pure water or brine) is notably minimal [Yan, 2011], leading to simulations presenting elevated Parndtl numbers ($\mathrm{Pr} \gg 1$), which suggests a predominance of momentum diffusivity over Fickian diffusivity. Conversely, the Rayleigh number delineates the flow regime of the gas within the λ–phase [Busse, 1971]. A low Rayleigh number, specifically $\mathrm{Ra} < 10^3$, indicates that the impact of natural convection is insignificant. In scenarios where buoyancy forces are significantly strong, characterized by $\mathrm{Ra} > 10^8$, a turbulent model becomes indispensable to accurately represent the velocity field [Sankar, 2011]. The numerical model used in this study is laminar flow, anticipating that the Rayleigh number will be between 10^3 and 10^8. Therefore, the non-dimensional form of the momentum balance equation is derived by dividing equation 1.8 by $\rho_{\lambda 0}$ and subsequently applying the scale factors from equation 1.14 :

$$\varepsilon_\lambda \partial_{\tilde{t}} \vec{\tilde{v}}_\lambda + \varepsilon_\lambda \vec{\tilde{v}}_\lambda \cdot \vec{\underline{\tilde{\nabla}}} \vec{\tilde{v}}_\lambda = -\vec{\tilde{\nabla}} \tilde{p} + \frac{L^2}{D^2 \, \rho_{\lambda 0}} \vec{\tilde{\nabla}} \cdot \underline{\tilde{\zeta}} + \frac{L^3}{D^2} (\varepsilon_\lambda - 1) \vec{g}, \tag{1.22}$$

where the viscous stress tensor $\underline{\zeta}$ must be expressed in its dimensionless form :

$$\underline{\tilde{\zeta}} = \left(\mu_\lambda \frac{D}{L^2} \right) \left(\vec{\underline{\tilde{\nabla}}} \vec{\tilde{v}}_\lambda + \vec{\underline{\tilde{\nabla}}} \vec{\tilde{v}}_\lambda{}^{\mathrm{T}} \right) - \frac{2}{3} \times \left(\mu_\lambda \frac{D}{L^2} \right) \times \vec{\tilde{\nabla}} . \vec{\tilde{v}}_\lambda \underline{\delta},$$

Hence, by applying the Prandtl formula and the Rayleigh number in Equation 1.21, we can derive the non-dimensional Navier-Stokes momentum equation (Equation 1.8) for the λ–phase :

$$\varepsilon_\lambda \partial_{\tilde{t}} \vec{\tilde{v}}_\lambda + \varepsilon_\lambda \vec{\tilde{v}}_\lambda \cdot \vec{\underline{\tilde{\nabla}}} \vec{\tilde{v}}_\lambda = -\vec{\tilde{\nabla}} \tilde{p} + \mathrm{Pr} \vec{\tilde{\nabla}} \cdot \underline{\tilde{\zeta}} + \mathrm{RaPr} \, \vec{e}_z. \tag{1.23}$$

Initial and boundary conditions

In this section, we will present the non-dimensional initial and boundary conditions at the laboratory scale. In fact, the initial conditions can be briefly described as follows :

$$\text{Initial Conditions} \begin{cases} \tilde{T}_\lambda(\tilde{x}, t = 0) = 0; \\ \vec{\tilde{v}}_\lambda(\tilde{x}, t = 0) = \vec{0}; \\ c(\tilde{x}, t = 0) = \dfrac{c_0}{c^s}. \end{cases} \tag{1.24}$$

The following non-dimensional definitions are used at the interface $\Sigma_{\gamma\lambda}$:

$$\begin{cases} \tilde{p}(\tilde{t}) = 0; \\ \vec{\tilde{J}} \cdot \vec{n} = \tilde{K}\left(\tilde{c} - \dfrac{p_\gamma}{H\, c^s}\right), \quad \text{with } \tilde{K} = K\,(L/D); \\ \vec{\tilde{v}}_\lambda \cdot \vec{n} = \dfrac{\vec{\tilde{J}} \cdot \vec{n}}{\dfrac{1}{c^s} - \tilde{c}} = \dfrac{\tilde{K}\left(\tilde{c} - \dfrac{p_\gamma}{H\, c^s}\right)}{\dfrac{1}{c^s} - \tilde{c}}; \\ \dfrac{\dot{\mathcal{M}}_\gamma L^2}{\mathcal{M}_\gamma D} = \dfrac{-\displaystyle\int_{\tilde{\Sigma}_{\gamma\lambda}} \varepsilon_\lambda \vec{\tilde{v}}_\lambda \cdot \vec{n}\, d\tilde{A}_{\gamma\lambda}}{\tilde{\vartheta}_\gamma\, \varepsilon_{\gamma\lambda}} = \dfrac{-\displaystyle\int_{\tilde{\Sigma}_{\gamma\lambda}} \varepsilon_\lambda \left[\dfrac{\tilde{K}(\tilde{c} - p_\gamma/(H \times c^s))}{1/c^s - \tilde{c}}\right] d\tilde{A}_{\gamma\lambda}}{\tilde{\vartheta}_\gamma\, \varepsilon_{\gamma\lambda}}, \end{cases} \tag{1.25}$$

where $\varepsilon_{\gamma\lambda} = \rho_\gamma/\rho_{\lambda 0}$, $\tilde{\vartheta}_\gamma$ is the non–dimensional gas volume, and $\tilde{A}_{\gamma\lambda}$ is the non–dimensional area of the gas–liquid interface, $\tilde{\Sigma}_{\gamma\lambda}$.

In summary, this dimensionless mathematical model will be used to simulate the Pressure decay tests in the next section, with the aim of determining the values of the mass transfer coefficient K and the gas dissolution coefficient D. In the next chapter, we will include the modeling of the γ–phase and the surrounding rock salt domain of the cavern. The experimentally determined values of K and D will be used at the cavern scale.

2.1.3 Numerical investigations of the kinetics of gas dissolution

The following subsection describes the numerical analyses conducted to explain the dissolution kinetics of CO_2 and H_2 in aqueous solutions using two distinct models : a pure diffusion model and a diffusion-convection model. The Comsol Multiphysics Finite Element Package was used for simulation and programming purposes. The field equations were solved using the transport of diluted species and laminar flow modules. An ordinary boundary differential equation was used at the interface. These simulations, based on the experimental findings described in section 1.1, seek to thoroughly clarify the kinetics of dissolution. Subsequent sections will analyze the numerical results and compare them with both experimental observations and works from literature. The initial focus will be on the simulated results related to the dissolution of CO_2, followed by an examination of the kinetics of H_2 dissolution.

2.1.3.1 Numerical Analysis of carbon dioxide dissolution in aqueous solution

This part focuses on the numerical analysis of CO_2 dissolution kinetics within aqueous solutions. The dissolution process is simulated using both the pure diffusion and diffusion-convection models. These models are carefully implemented to reproduce the experimental results described in section 1.1.3.2 and are compared to the results from the existing literature.

This section presents the numerical results obtained from the two developed models. The first model, known as the pure diffusion model, considers only Fick's law of diffusion. The second model combines a density-driven natural convection mechanism with Fickian diffusion to determine the diffusion coefficient with improved precision. The shared parameters between the models are listed in Table 1.6. The data concerning Henry's coefficient in CO_2 are obtained

from the thermodynamic model proposed by [Akinfiev, 2003], which is based on 362 experimental measurements of CO_2 solubility in water. Data for Henry's coefficient in saline solutions are interpolated from [Chabab, 2019], which defines CO_2 solubilities at various pressures and temperatures. The initial density of the aqueous solution, represented as $\rho_{\lambda 0}$, is determined based on the research conducted by [Archer, 2000], which takes into account both the salinity and temperature. The two models are employed to calibrate the parameters D and K, which represent the diffusion and mass transfer coefficients, respectively (Equations 1.26). These coefficients play a crucial role in determining the kinetics of the dissolution of CO_2 in the aqueous solution. In our analysis, we make the assumption of a constant mass transfer coefficient K, as specified in Table 1.6. However, we consider the diffusion coefficient to be dependent on the concentration of salinity, expressed as :

$$D = \frac{D_0}{\eta}, \tag{1.26}$$

where η is a coefficient dependent on the salinity c_{salt} and D_0 can be either the calibrated diffusion coefficient D_{diff} from the pure diffusion model in section 2.1.3.1, or the real diffusion coefficient D_{real} from the diffusion and convection model described in section 2.1.3.1. According to [Frank, 1996], the molecular diffusion coefficient of CO_2 in pure water ranges from 1.97×10^{-9} to 3.07×10^{-9} m^2/s for temperatures below 45 °C.

Table 1.6 – The used parameters for the two developed models.

T_0 (°C)	c_{salt} (%)	$p_{\gamma 0}$ (bar)	H (MPa/mass fraction)	$\rho_{\lambda 0}$ (kg/m^3)	K (m/s)
30	0	10	79.28	995.5	0.252
		41.5	97.29		
		48.8	102.93		
40	0	10.5	99.07	992	
	11	10.5	184.27	1070	
	22.5	10.5	287.81	1158	
		129	550.08		
		168.7	726.64		

When the two phases come into contact, CO_2 dissolves into the saline solution in order to reach equilibrium at the phase boundary. Nevertheless, the flow is restricted by the interface resistance, which is represented as $1/K$. Higher resistance leads to a decrease in flow, resulting in a reduced initial rise in the concentration of dissolved gas at the interface. Consequently, the slope of the pressure curve gradually decreases. Subsequently, the gas that is dissolved at the boundary begins to spread into the brine, resulting in a temporary decrease in concentration at the boundary. This decrease is then balanced out by the transfer of mass into the liquid phase. Physically, when diffusion is more significant, the dissolved gas quickly spreads throughout the liquid phase, which restricts the concentration changes at the interface [Reza Etminan, 2013]. However, the concentration at the interface rises quickly until it reaches saturation due to the greater resistance at the interface. It induces a significant variation in concentration between

the surface of the cell and its bottom. Subsequently, the concentration at the interface drops progressively until it reaches a state of equilibrium concentration at the end.

This section will provide a comprehensive analysis of the two numerical models by comparing their results with the experimental data and existing literature. To prevent repetition, Figures 1.16, 1.17, 1.18, and 1.19 illustrate the comparison of the normalized pressure $p_\gamma(t)/p_{\gamma 0}$ obtained from both models with the experimental data.

The Pure Diffusion Model

The initial interpretation of the measured pressure decay results (presented in section 1.1.3) is based on the pure diffusion model. This approach relies solely on Fick's law of diffusion to match the experimental data. It achieves this by selecting a calibrated diffusion coefficient for the varying salinity of the aqueous solution, as demonstrated in equation 1.26. Regardless of the volume of water or brine introduced into the cell, this model can reasonably predict the duration of CO_2 dissolution after the parameters have been calibrated using experimental data. The subsequent section presents the numerical normalized pressure obtained from this model, depicted by dashed lines. Figure 1.16 illustrates the normalized experimental pressure profiles (tests 1, 2, and 3 in Table 1.3) in comparison to the predicted pressure profiles for CO_2 in pure water. The predictions are based on different pressures and a constant temperature T= 30 °C. In addition, Figure 1.17 demonstrates that the numerically simulated pressures for CO_2 in pure water accurately anticipate the experimental pressure profiles (tests 4, 5, and 6 in Table 1.3) under different liquid volumes and a constant temperature of T= 40 °C. The diffusion coefficient is the primary factor that governs the rate at which the dissolution process occurs. The rate of mass transfer of the gas within the liquid phase is influenced by this coefficient. The pressure drop of CO_2 over time is used to determine this rate. The study determined that the diffusion coefficient in pure water, denoted as D_{diff}, is 1.1×10^{-7} m^2/s. This value remains constant regardless of the initial gas pressure, temperature, or the ratio between the liquid and gas volumes. The pure diffusion model yields a calibrated value for the diffusion coefficient that is two orders of magnitude greater than the molecular diffusivity of CO_2 in pure water. The same order of magnitude was found by other researchers [Farajzadeh, 2009 ; Wang, 2013 ; Yang, 2006]. In fact, the disparity between the molecular and calibrated diffusion coefficients arises from neglecting the phenomena related to the diffusion of dissolved gas in the liquid phase, despite their significance in the overall mass exchange process.

Conversely, the modified diffusion coefficient decreases as the salt concentration in the water increases. This coefficient is nearly divided by two for brine concentrations of c_{salt}=11% (tests 7, 8 in Table 1.3) and by four for brine concentrations of $c_{\text{salt}} = 22.5\%$ (tests 9, 10, 11, 12 in Table 1.3). Table 1.7 presents a concise overview of the determined values for the diffusion coefficient, which is dependent on the salinity as indicated in equation 1.26. The values correspond to the average of the adjustments applied to different volumes of tested brine and the initial gas pressure.

Moreover, at low and high initial gas pressures, the numerical pressure profiles obtained are in good agreement with almost all the experimental results, as shown in Figures 1.18 and

1.19. However, the pure diffusion model slightly underestimates the experimental data for Test 6 and overestimates the pressure drop for Test 11 during the initial phase of the experimental duration. This can be attributed, as previously elucidated, to the disregard of the influence of the dissolved gas concentration on the density-driven natural convection.

TABLE 1.7 – The calibrated parameters of the diffusion coefficient (as defined in equation 1.26) for the pure diffusion model.

c_{salt} (%)	D_{diff} (m^2/s)	η
0	1.1×10^{-7}	1
11		1.96
22.5		4

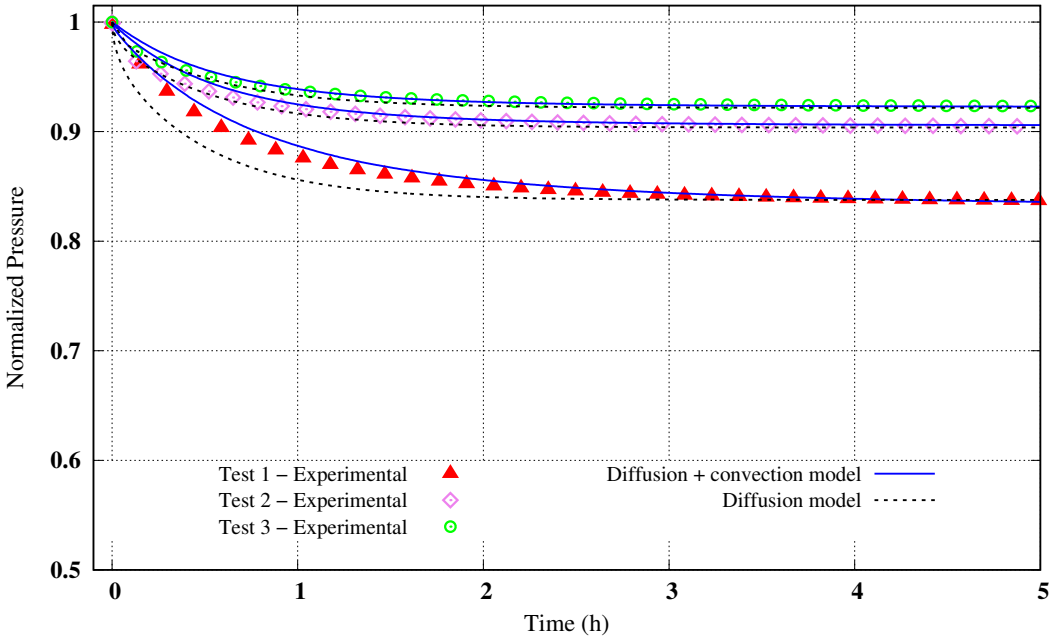

FIGURE 1.16 – Comparison between experimental CO_2 pressure data in pure water and the two numerical models at initial pressures of $p_{\gamma 0} = \{10, 41.5, 48.8\}$ bar and Temperature of 30 °C.

In summary, the pure diffusion model, which relies on numerous simplifications, proves to be interesting approach for modeling the CO_2 dissolution kinetics in both pure water and brine. The diffusion coefficient values (Table 1.7) are estimated to be approximately one hundred times greater than the molecular diffusion coefficient. This estimation is obtained by fitting the Pressure-Decay tests and numerical results.

In this study, a more intricate modeling approach will be suggested to provide a more accurate description of the mass transfer process. The objective is to incorporate various physical phenomena, such as natural convection, that occur during the dissolution of CO_2.

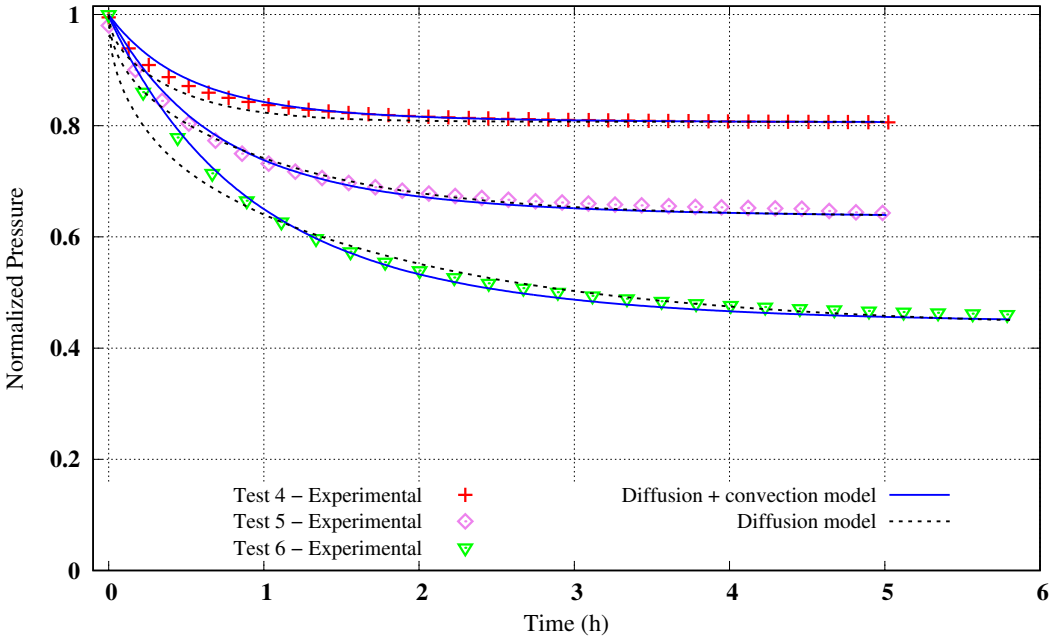

FIGURE 1.17 – Comparison between experimental CO_2 pressure data for different volumes of pure water $\vartheta_\lambda = \{28.45, 48.24, 90.5\}$ cm^3 and the two numerical models at T_0= 40 °C.

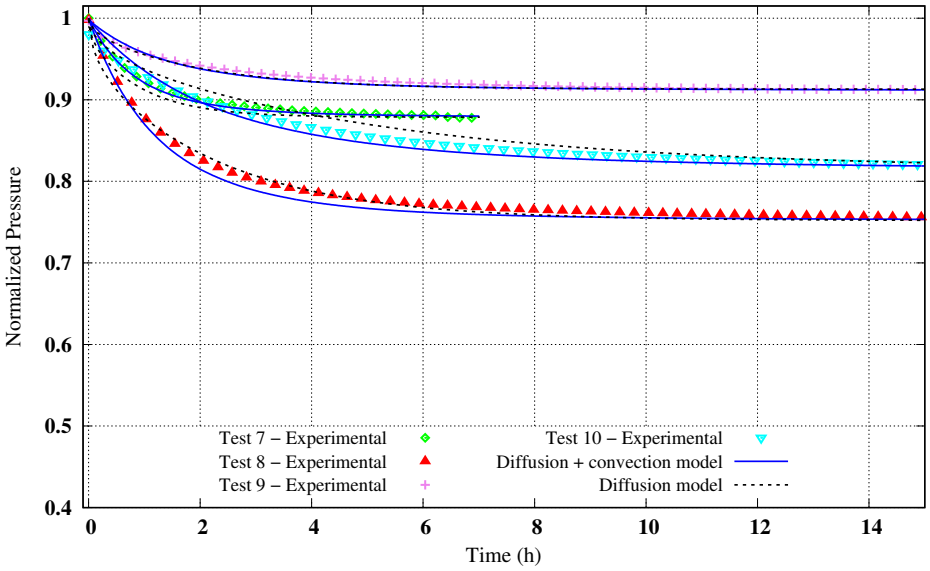

FIGURE 1.18 – Comparison between experimental CO_2 pressure data for different salinities $c_{\text{salt}} = \{11, 22.5\}$ % of the brine and the two numerical models at T_0= 40 °C.

The diffusion and convection model

This approach incorporates density-driven natural convection into the simulation by considering the Navier-Stokes momentum equation 1.8. The current model is more intricate than the pure diffusion model discussed in the previous section. However, it still employs the same initial and boundary conditions as presented in equations 1.24 and 1.25.

Natural convection plays a vital role in the dissolution of CO_2 in water and brine, as it leads

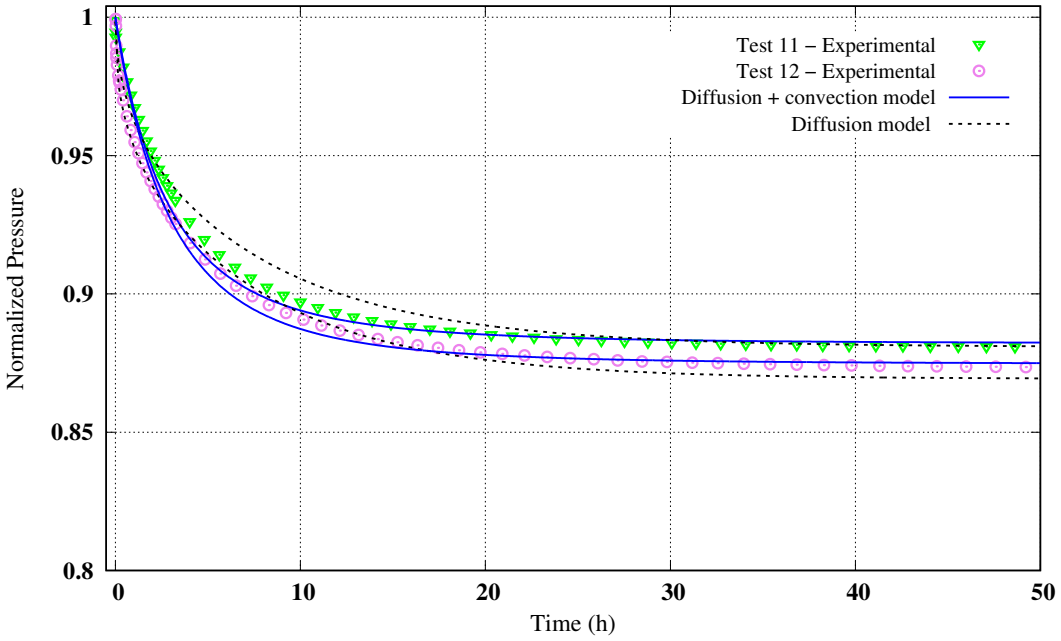

FIGURE 1.19 – Comparison between experimental CO_2 pressure data in saturated brine (c_{salt} = 22.5%) and the two numerical models using high initial pressures $p_{\gamma 0} = \{129, 168.7\}$ at T_0= 40 °C.

to rapid homogenization of the liquid phase. It is generated by the density gradient in the brine, resulting from the concentration gradient of the dissolved gas.

The density of the brine in this study is directly proportional to the concentration of the dissolved gas c, as indicated by equation 1.9. The values of β_c adopted in the different tests are described in Table 1.8, derived from the CO_2-saturated brine density measurements conducted by [Yan, 2011]. The dynamic viscosity μ is influenced by both the temperature and salinity of the brine. The values of dynamic viscosity were obtained from the work conducted by [Kestin, 1981], which provides viscosity data for different combinations of brine temperatures and salinities. This study only focused on the laminar regime due to the small value of the Reynolds number (Re < 2300) and the fact that the Rayleigh number Ra is below 10^5 [Bird, 2007]. The molecular diffusion coefficient of CO_2 in pure water, denoted as D_{real}, is equal to $D_{real} = 2 \times 10^{-9}$ m^2/s. The diffusion and convection model was employed to simulate the Pressure-decay tests (Table 1.1) under different temperature conditions, water volumes, and initial gas pressures. The figures 1.16 and 1.17 display the results derived from the CO_2 pressure profiles in pure water, represented by solid lines. Furthermore, the data presented in Table 1.8 demonstrates that the diffusion coefficient decreases as the concentration of NaCl increases, which aligns with the findings of the pure diffusion model in the previous analysis. In fact, using the equation 1.26, D_{real} is divided by a factor η. The value of η is determined and shown in Table 1.8. This factor increases as the salinity of the brine rises c_{salt}.

Figures 1.18 and 1.19 show the experimental data for pressure decline and the corresponding numerical results from the complete diffusion and convection model. This model accurately predicts the changes in the pressure of the dissolved gas over time, considering both low and

high initial pressures of CO_2 and varying brine salinities. Across all simulated experiments, the slope of the normalized gas pressure curve is initially high and gradually decreases over time. This indicates a significant reduction in the rate of mass transfer from the early stages of the experiments, which continues to decline as time goes on until reaching thermodynamic equilibrium. This model provides a more accurate estimation of the rate and duration of CO_2 dissolution in an aqueous solution compared to the previous model.

Figure 1.20 displays the spatial distribution of dissolved gas concentrations, the magnitude, and vectors of fluid velocity at various intervals. Specific illustrations from Test 4 are delineated. The dissolution of CO_2 begins immediately when the liquid and gas phases come into contact. The initial increase in mass transfer is caused by the convective process. The CO_2 concentration is primarily increased at the top of the cell, resulting in a difference in density within the liquid phase. As a result, convection has a tendency to homogenize the liquid phase rapidly. The Rayleigh number is relatively high to explain the formation of convective vortices in the liquid phase, regardless of volume. By examining the velocity vector of the liquid phase, the formation of these vortices is clearly depicted in Figure 1.20. After a duration of 5 hours, the process of homogenization in the aqueous solution leads to a decrease in the difference between the highest and lowest concentrations, as well as a reduction in the magnitude of velocity. Hence, the concentration gradient at the interface $\Sigma_{\gamma\lambda}$ and the bottom of the cell becomes very low, thereby reducing the instability between the upper and lower regions of the liquid phase. The observations can be attributed to the predominance of diffusion over convection in the process. Indeed, in all experiments, regardless of the initial pressure, volume, salinity, and liquid volume, the effect of convection diminishes with time until it disappears in the thermodynamic equilibrium.

TABLE 1.8 – The diffusion and convection model parameters : the density coefficients β_c, the dynamic viscosities, and the real diffusion coefficient expressed in 1.26 for the different salinities c_{salt} and at $T_0 = \{30, 40\}$ °C.

T_0 (°C)	c_{salt} (%)	β_c	μ (Micro Pa.s)	D_{real} (m^2/s)	η
30	0	0.18	796.5	2×10^{-9}	1
40		0.26	653.8		
	11	0.24	848		1.21
	22.5	0.22	1139.4		2.5

To sum up, the estimation of the diffusion coefficient values obtained from the Pressure-Decay tests using the complete diffusion and convection model (Table 1.8) is more precise than the pure diffusion model. Furthermore, these values are equivalent to the molecular diffusivity of CO_2 in water and brine. Hence, this proposed model is comprehensive and applicable for predicting the kinetics of CO_2 dissolution in water and brine under storage conditions.

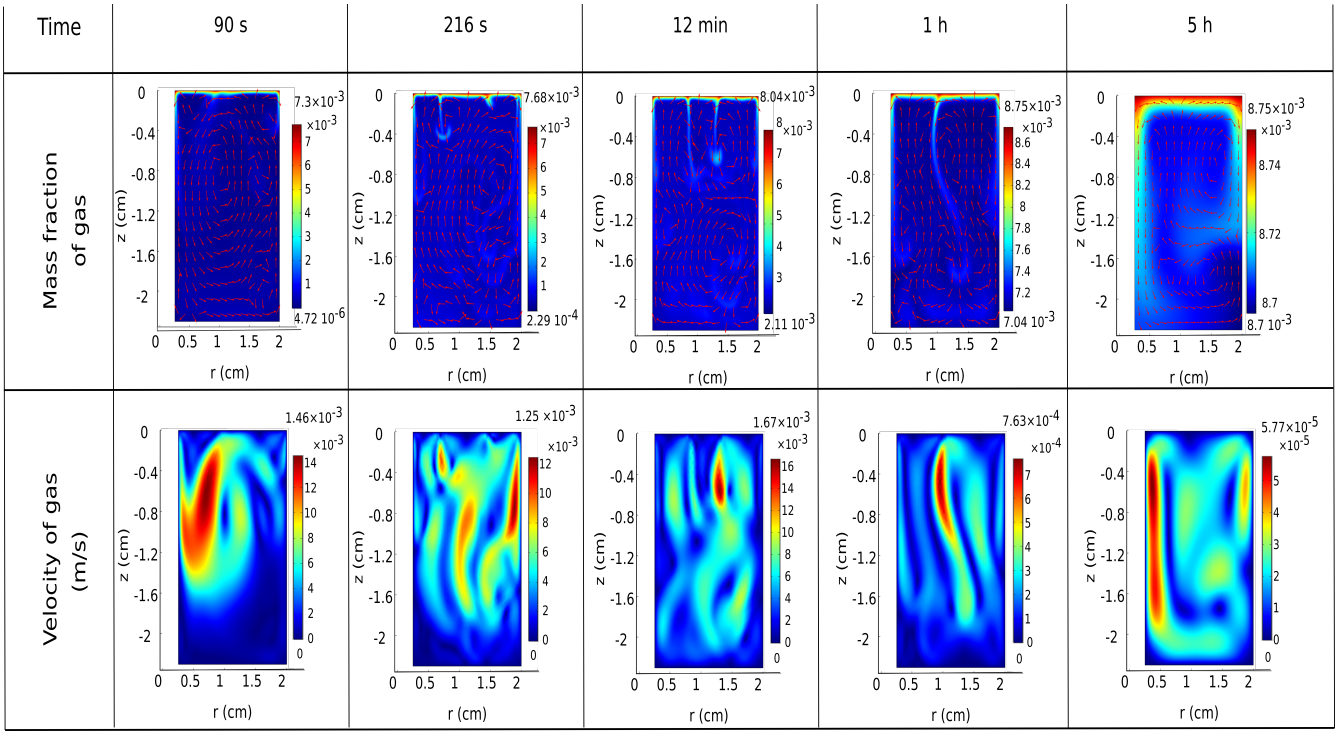

FIGURE 1.20 – Temporal evolution of CO_2 concentration and velocity profiles during Test 4 (Table 1.3).

Comparison between the two developed models with the literature

This section presents a comparative analysis of our obtained results and previous studies in the literature regarding the diffusion coefficient of CO_2 in water/brine. The literature reports calibrated values of the diffusion coefficient using the model of pure diffusion that are two orders of magnitude higher than the molecular diffusivity of CO_2 into pure water. [Farajzadeh, 2009] adjusted this parameter to be between 1.4×10^{-7} m^2/s to 2.8×10^{-7} m^2/s. The evaluations were conducted at pressures ranging from 1 to 5 MPa and a temperature of 30 °C. The study conducted by [Shi, 2018] determined the adjusted value to be 2.9×10^{-7} m^2/s at a pressure of 5.9 MPa and a temperature of 30 °C. However, only a limited number of works have incorporated the concept of natural convection in the examination of CO_2 mass transfer in water. [Gholami, 2015], for instance, emphasized the relevance of natural convection in the acceleration of the equilibrium in Pressure-Decay test models compared to those restricted to simple diffusion. Moreover, a study by [Farajzadeh, 2009] provided evidence that the diffusion coefficient adjustment using a convection-diffusion model approaches the molecular diffusion coefficient of CO_2 in water. Other researches focused on the critical time after which density gradient instabilities take precedence over CO_2 diffusion [Hassanzadeh, 2007 ; Riaz, 2014].

In order to corroborate the findings of our study, we conducted a comparative analysis between our two developed models and the experimental data on the dissolution of CO_2 in pure water, as reported by [Farajzadeh, 2009]. The initial gas pressures are denoted as $p_{\gamma 0}$ and have values of 10.1, 19.4, and 32.1 bar at a temperature of $T_0 = 30$ °C. Figure 1.21 illustrates the

normalized pressure drop of CO_2 obtained from the two models. The dashed lines represent the results from the pure diffusion model, which used a calibrated diffusion coefficient of 1.1×10^{-7} m^2/s (Table 1.7). On the other hand, the solid lines represent the results from the diffusion and convection model, which used a molecular diffusion coefficient of 2×10^{-9} m^2/s (Table 1.8). The pressure results obtained using the two developed models agree with the published experimental data for various initial gas pressures. Moreover, the diffusion coefficient values of CO_2 in pure water used in this work are comparable to those reported in the study of [Farajzadeh, 2009].

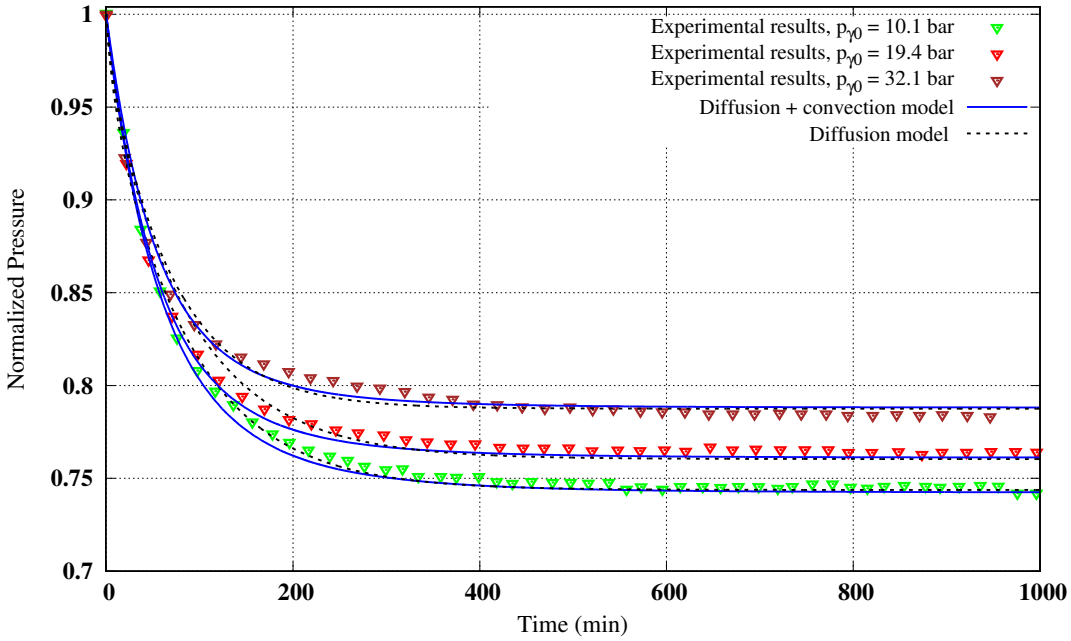

FIGURE 1.21 – Comparison between experimental CO_2 pressure data in pure water published by [Farajzadeh, 2009] and the two numerical models at initial pressures of $p_{\gamma 0} = \{10.1, 19.4, 32.1\}$ bar and Temperature of 30 °C.

In summary, the estimation of the diffusion coefficient values obtained from the pressure-decay tests using the diffusion and convection model (Table 1.8) is more precise than the pure diffusion model. Furthermore, these values are equivalent to the molecular diffusivity of CO_2 in water and brine.

2.1.3.2 Numerical Analysis of hydrogen dissolution in aqueous solutions

In this section, the attention shifts to simulating the dissolution of H_2 in water and brine, using the convection and diffusion model presented in section 2.1.3.1. Two experimental tests were conducted to quantify the H_2 dissolution in the aqueous solutions, as elucidated in section 1.1.4.1. The experimental observations revealed a leakage in the system for both water and brine experiments, attributed to the challenges associated with handling hydrogen due to its small molecular size.

Given this situation, it is essential to model these experiments while accounting for the leakage in the system. The diffusion and convection model is employed to simulate the obtained

results with a linear leakage integrated into the model. This model, which takes into account all the complexities related to gas dissolution in aqueous solutions, was validated for the CO_2 dissolution using the intrinsic diffusion coefficient. Since the model was developed to be applicable to all types of gases, we can therefore have confidence in its ability to accurately simulate the kinetics of H_2 dissolution.

The focal point of this study is to quantify the mass drop of hydrogen in the gas phase of the PVT cell. The quantification of the mass drop serves as a pivotal indicator, where it is either attributed to the gas being dissolved in the aqueous solution or due to the leakage in the system. This study aims to use our model to determine the contribution of the dissolution process and system leakage to the observed mass drop. By doing so, it will provide a more detailed understanding of the kinetics of H_2 dissolution under the specific experimental conditions.

First, we will introduce the parameters used to model the two experimental tests of H_2 dissolution in pure water and brine. In fact, the coefficient β_c is derived from the work of [Bignell, 1987], which measure the relative variation of density as a function of the H_2 concentration at various temperatures. Considering the constant temperature in our study, we can use the equation 1.9 and the data provided by [Bignell, 1987] to determine the value of β_c :

$$\beta_c = \frac{\Delta\rho_\lambda}{\rho_{\lambda 0}\Delta c}$$

The literature does not provide any available data for the mass transfer coefficient K. Therefore, we will use the value previously determined for the case of CO_2 dissolution in aqueous solution. Moreover, the initial density of pure water/brine $\rho_{\lambda 0}$ is derived from the work of [Archer, 2000]. The intrinsic diffusion coefficient of hydrogen in pure water, $D = 5.91 \times 10^{-9}\,\mathrm{m^2/s}$ is given by the work of [Ferrell, 1967]. The hydrogen diffusion coefficient in the saturated brine, $D = 2.36 \times 10^{-9}\,\mathrm{m^2/s}$, was determined using the same coefficient $\eta = 2.5$ found for the CO_2 (see Table 1.8).

Furthermore, it is necessary to know the solubility of H_2 in both pure water and brine, which will determine the maximum quantity that may be dissolve in it. Any mass above this level is considered leakage. Figures 1.22a and 1.22b illustrate the calculated values at the saturation obtained from the r-PR-CPA model, representing the molar fraction of the dissolved H_2 ($x^s_{\mathrm{H_2}}$) in pure water and brine as a function of pressure and salt mass fraction c_{salt} at a temperature of 40 °C [Chabab, 2020]. By using the molar fraction of H_2 and using the formula 1.27, the mass fraction at saturation ($c^s_{\mathrm{H_2}}$) of dissolved H_2 as a function of pressure can be calculated, as illustrated in the same Figures 1.22a and 1.22b.

$$c^s_{\mathrm{H_2}} \approx \frac{x^s_{\mathrm{H_2}}\left(\frac{1}{\mathrm{M}_w} + \left(\frac{1}{\mathrm{M}_{salt}} - \frac{1}{\mathrm{M}_w}\right)c_{\mathrm{salt}}\right)}{\frac{1}{\mathrm{M}_g} - \left(\frac{1}{\mathrm{M}_g} - \frac{1}{\mathrm{M}_w}\right)x^s_{\mathrm{H_2}}} \tag{1.27}$$

with M_w, M_{salt} and M_g being respectively the molar masses of water, salt, and gas.

The Henry's coefficient is interpreted from the determined solubility values which is equal to $H = 5.65 \times 10^5$ MPa for the dissolution of H_2 in pure water and $H = 25.6 \times 10^5$ MPa for the dissolution of H_2 in saturated brine at a temperature of 40 °C.

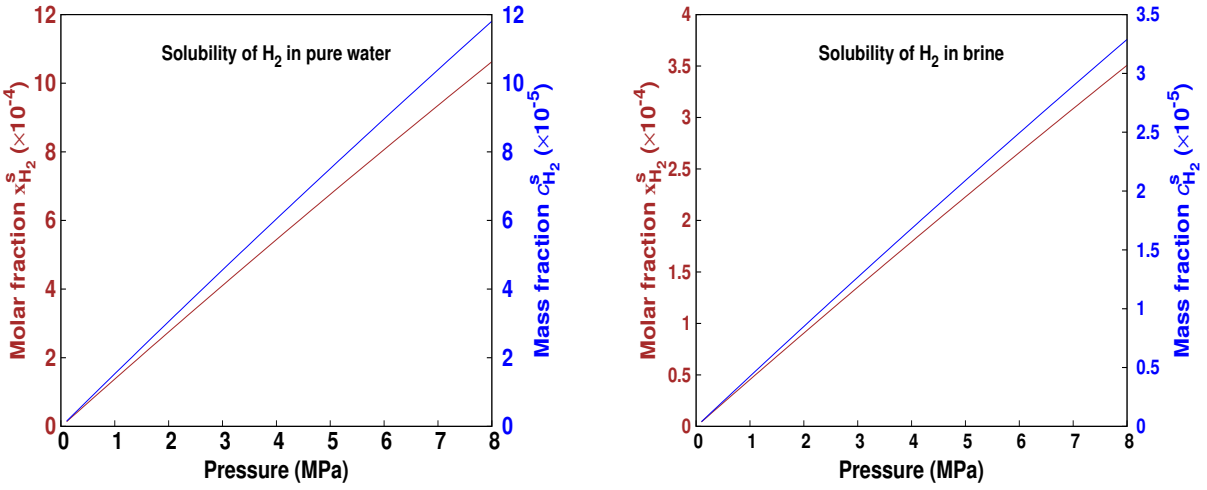

(a) Pure water (b) Brine

FIGURE 1.22 – Variation of mass fraction ($c^s_{H_2}$) and molar fraction ($x^s_{H_2}$) with pressure at T = 40 °C for the solubility of H_2 in the pure water and the saturated brine (c_{salt}= 22.5%), derived from [Chabab, 2020].

TABLE 1.9 – Summary of the used parameters in the model.

Test	c_{salt} (%)	$p_{\gamma 0}$ (bar)	β_c	K (m/s)	H (×10^4 MPa)	D (×10^{-9} m^2/s)	$\rho_{\lambda 0}$ (kg/m^3)
1	0	10.2	9.25	0.252	5.65	5.91	992
2	22.5	54.1			25.6	2.36	1158

A summary of the parameters employed in our model is provided in Table 1.9.

The analysis starts with the first dissolution test of hydrogen in pure water, as delineated in section 1.1.4.1. Figure 1.23 illustrates the comparison between the calculated mass of H_2 ($\mathcal{M}^{cal}_{H_2}$) using the diffusion and convection model (represented by the blue line) and the experimental data of the mass of H_2 ($\mathcal{M}^{exp}_{H_2}$) in the gas-rich phase (represented by the green line).

The numerical results of our model show that the system reaches thermodynamic equilibrium after $\sim$ 10 days, which corresponds to a decrease in $\mathcal{M}^{cal}_{H_2}$ to a value of $\sim$ 0.0192 g. However, the experimental data reveals a continued drop in mass $\mathcal{M}^{exp}_{H_2}$ even post the attainment of thermodynamic equilibrium, suggesting a leakage of hydrogen in the PVT cell. During the early stage, particularly prior to t_{corr} = 4.9 days, the calculated mass $\mathcal{M}^{cal}_{H_2}$ in the gas–rich phase is slightly less than the experimentally measured mass. These findings indicate that the estimated amount of H_2 dissolved in the water is greater than the measured mass of dissolved H_2. Therefore, there is no leakage in the system during this specific period. For $t > t_{corr}$, the model detects leakage in the system, which is characterized by a constant leakage rate. A correction for this leakage was applied by considering a linear adjustment over a time interval extending from 4.9 to 18 days, and then the mass $\mathcal{M}^{cal}_{H_2}(t)$ were corrected to obtain $\mathcal{M}^{corr}_{H_2}(t)$ (see red line in Figure 1.23) by applying a correction of the form :

$$\begin{cases} \mathcal{M}^{corr}_{H_2}(t) = \mathcal{M}^{cal}_{H_2}(t), & \text{if } t \leq t_{corr} \\ \mathcal{M}^{corr}_{H_2}(t) = \mathcal{M}^{cal}_{H_2}(t) - \varepsilon(t - t_{corr}), & \text{if } t > t_{corr} \end{cases} \tag{1.28}$$

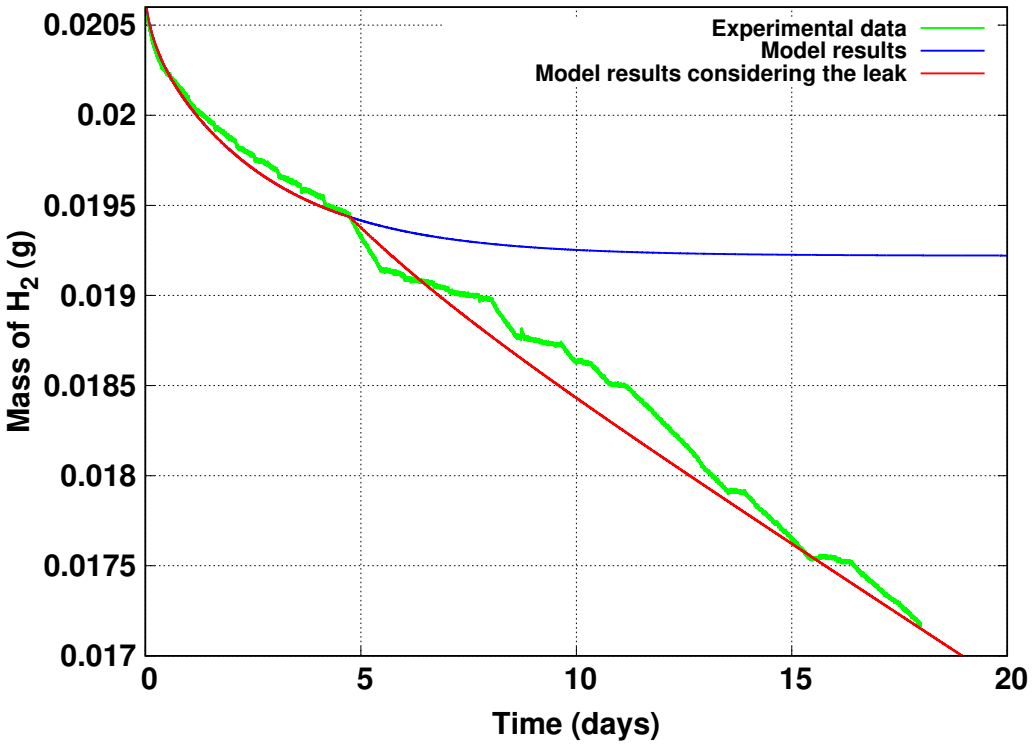

FIGURE 1.23 – Comparison between the measured mass data of H_2 in gas–rich phase and the numerical model in H_2–pure water system at $p_{\gamma 0} = 10.2\,\text{bar}$ and $T_0 = 40\,°C$.

with ε being the slope of the linear regression. In this test, ε is equal to 1.56×10^{-4}.

This adjustment serves to elucidate the observed discrepancies between the model findings and experimental data, thereby highlighting the need to consider potential leakages when interpreting the results. Therefore, this refined comprehension significantly contributes to a more accurate analysis of the dissolution kinetics of H_2 in pure water.

In a parallel investigation, the same analytical methodology is applied to study the dissolution kinetics of H_2 in saturated brine, as shown in Figure 1.24. The governing parameters for this model are detailed in Table 1.9. Unlike the case of pure water, a significant deviation is evident from the beginning of this test. Specifically, the experimentally measured mass of hydrogen in the gas phase rapidly declined and surpass $\mathcal{M}_{H_2} = 0.162\,\text{g}$, confirming that the brine had reached its saturation capacity for hydrogen dissolution. Therefore, the test was stopped after 3.6 days.

In contrast to the previous study, a leakage adjustment was applied right from the beginning of the experiment ($t_{\text{corr}} = 0$ day in the equation 1.28), as seen by the red line in Figure 1.24. The leakage rate was determined through a linear adjustment carried out from 0 to 3.6 days, offering a systematic clarification of the dissolution kinetics of H_2 in brine. As a result of the high initial pressure in this test, the observed leakage is more significant than in the previous test. Therefore, the value of ε is calibrated to 1.8×10^{-3}.

In conclusion, using modeling and experimental data, this work investigated the kinetics of H_2 dissolution in both pure water and brine. The diffusion and convection model, which included a linear leakage adjustment, was used to determine the experimental findings. The

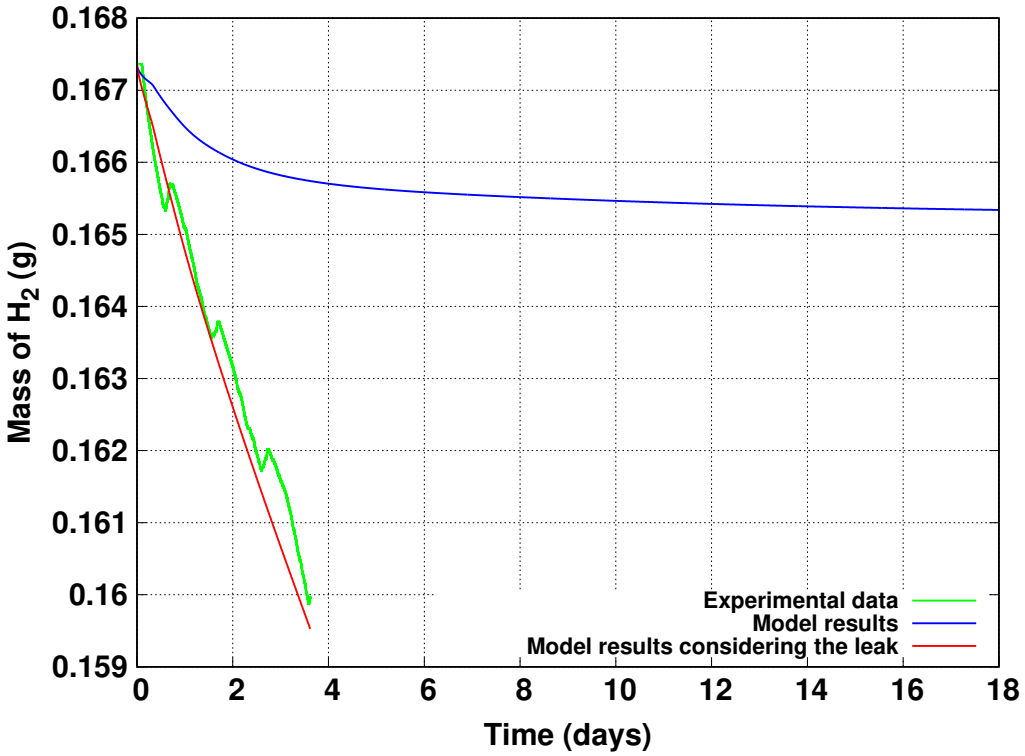

FIGURE 1.24 – Comparison between the measured mass data of H_2 in gas–rich phase and the numerical model in H_2–saturated brine system at $p_{\gamma 0} = 54.1\,\text{bar}$ and $T_0 = 40\,°C$.

model replicated the dissolution kinetics of pure water up to a particular time point, beyond which a leakage became visible. In brine, on the other hand, a large variation was immediately apparent, requiring immediately leakage correction. These results highlight the importance of accounting for system leakage when interpreting the tests of H_2 dissolution in water/brine.

2.2 Validation of the HGM model for hydrogen and helium

The primary aim of this part is to verify the accuracy of our Humid Gas Model, known as the HGM model, which is developed to measure the water content in gases. This model, developed to be generally applicable across a wide range of gases, is particularly used to study the water content in hydrogen and helium. The choice of these gases is motivated by the lack of numerical models that can fully describe the humidity of these gases under storage conditions. In fact, the study of the behavior of humid hydrogen is our primary focus. Helium, on the other hand, shares similarities with hydrogen and has been the subject of prior experimental work conducted in a laboratory storage pilot (see section 1.2).

It is worth noting that the findings of this section will serve as the foundation for the next chapter of this dissertation in order to model different scenarios of gas storage in actual salt caverns, offering a comprehensive understanding of humid gas behavior.

The section is organized as follows : First, the mathematical and theoretical model will be elucidated, including the state laws for pure water and the studied gases. Subsequently, the model will be applied to study humid hydrogen. Data concerning the water content in hydrogen

across a large range of temperatures and pressures will be collected from existing literature. This data will then be compared with the predictions of the model as a measure of validation. Next, the validated model will be applied to the case of the helium cycling experiment previously conducted. Finally, the thermodynamic properties of humid hydrogen and helium are presented using our model.

This section intends to validate the HGM model in a structured manner, thereby enhancing the understanding of water content under storage conditions.

2.2.1 State laws of pure water, helium and hydrogen

Among the most precise laws of state, the GERG-2004 [Kunz, 2007] and GERG-2008 [Kunz, 2012] equations have been meticulously adjusted using extensive experimental data. The thermodynamic potential is divided into two parts : an ideal part that describes the behavior of an ideal gas, and a residual part that accounts for deviations from this ideal behavior. In fact, the thermodynamic potential can be expressed as :

$$f(\rho, T) = \check{f}(\rho, T) + \tilde{f}(\rho, T) \tag{1.29}$$

In the case of low density ($\lim_{\rho \to 0} f = \check{f}(\rho \to 0, T)$), we obtain the behavior of an ideal gas. The general expression for the equation is :

$$\begin{cases} \check{f}(\rho, T) = \ln(\delta) + a_1 + a_2\tau + a_3 \ln(\tau) + a_4 \ln\left(1 - e^{-b_4\tau}\right); \\ \tilde{f}(\rho, T) = \sum_{i=1}^{N_1} n_i \tau^{t_i} \delta^{d_i} + \sum_{i=N_1+1}^{N_2} n_i \tau^{t_i} \delta^{d_i} e^{-\delta^{c_i}}. \end{cases} \tag{1.30}$$

with $\tau = T^c/T$ and $\delta = \rho/\rho^c$ are respectively the reduced parameters of temperature and density. The values T^c and ρ^c correspond to the thermodynamic coordinates of the critical point of the fluid. For each substance, the constants a_i, b_i, c_i, d_i, n_i are known.

Although the GERG equations are relatively simple compared to other state laws, they offer the advantages of precision and flexibility in fluid selection. These equations have been adjusted for water as well as all the studied fluids (H_2, Helium) in this work. Due to the uniformity of the structure of these equations of state across all fluids, changing the investigated fluid exclusively requires adjustments to the calibration parameters without the modification of the entire equation.

2.2.2 Theoretical development of the HGM model

The primary objective of this study is to investigate a binary mixture consisting of dry gas (H) and water (W). The study specifically focuses only on the gaseous phase. To facilitate the development of the model, a set of assumptions were used and may be delineated as follows :

— The studied gases are hydrogen (H_2) and helium (He), which have respective critical temperatures of 130 K and 150 K. In fact, these gases exist in their gaseous form when the temperature range is over their critical temperatures.

— The water included in the mixture appears in several states : as water vapor (V), as liquid water (L), or simultaneously in both gaseous and liquid phases.

— When the temperature exceeds the critical temperature of pure water ($T_c = 373.95°\mathrm{C}$), only the water vapor (V) occurs, therefore the mixtures are in the gaseous state.

— It is assumed that the dissolution of the dry gas in the liquid phase of water is negligible, thus the liquid contains only the water/brine.

— The coexistence of all three phases, namely dry gas, vapor, and liquid water, is only possible when the temperature $T \leq T_c$.

The total volume, denoted as ϑ, is defined as the sum of the separate volumes of the dry gas and water vapor (ϑ_G) and the volume of the liquid water (ϑ_L).

$$\vartheta = \vartheta_{\mathrm{G}} + \vartheta_L. \tag{1.31}$$

Let $\alpha = (H, V, L)$ be a set of constituents. The total mass $\mathcal{M}$ that occupies the volume ϑ of the mixture and its specific volume ν is defined as :

$$\begin{cases} \mathcal{M} = \sum \mathcal{M}_\alpha; \\ \nu = \dfrac{1}{\rho} = \dfrac{1}{\sum \rho_\alpha}. \end{cases} \tag{1.32}$$

The density of the mixture is represented by ρ and ρ_α is the apparent density of the α constituent per unit of total volume ϑ. The mass fraction c_α and the specific volume ν_α are introduced as :

$$\begin{cases} c_\alpha = \dfrac{\mathcal{M}_\alpha}{\mathcal{M}} = \dfrac{\rho_\alpha}{\rho}; \\ \nu_\alpha = \dfrac{1}{\rho_\alpha}. \end{cases} \tag{1.33}$$

Therefore, the specific volumes ν_α of each constituent (H, V, L) are defined in the following manner :

$$\nu_H = \frac{\vartheta_{\mathrm{G}}}{\mathcal{M}_H}, \nu_V = \frac{\vartheta_{\mathrm{G}}}{\mathcal{M}_V}, \nu_L = \frac{\vartheta_{\mathrm{L}}}{\mathcal{M}_L}. \tag{1.34}$$

The composition of the mixture, denoted as $\vec{c} = (c_H, c_V, c_L)$, can be described by the mass fractions $\gamma_G = \dfrac{\mathcal{M}_H}{\mathcal{M}_G}$ and $c = \dfrac{\mathcal{M}_H}{\mathcal{M}}$:

$$c_H = c, \quad c_V = \frac{c}{\gamma_G} - c, \quad c_L = 1 - \frac{c}{\gamma_G}. \tag{1.35}$$

The variable c represents the mass fraction of the gas, which describes the thermodynamic state. This mass fraction remains constant and is unaffected by variations in temperature or total volume. In contrast, the value of γ_G is influenced by the thermodynamic state of the mixture as a result of the mass transfer occurring between the two phases of water (V, L). Therefore, the composition of the mixture vector $\vec{c}$ may be reduced to a unique parameter c, while the coefficients c_V and c_L are transformed into state functions. In order to remain positive, these two coefficients must satisfy the condition $c \leq \gamma_G$. The saturation of the mixture, consisting of dry gas and water vapor, is represented by the equation :

$$\gamma_G(\nu, T, c) = c = c^s \tag{1.36}$$

with c^s is the concentration of the gas corresponding to the saturation. Any excess amount of water can only exist in the form of liquid.

The thermodynamic state, which is determined by the specific volume (ν), temperature (T), and concentration (c), plays a crucial role in determining all the thermodynamic functions of the mixture. Therefore, the thermodynamic potential f, which is the free energy of the mixture divided by $\mathcal{M}$, is dependent on the state functions $(\nu, T, \vec{c})$. f may be expressed as follows as it is an additive quantity :

$$f(\nu, T, \vec{c}) = \sum c_\alpha \bar{f}_\alpha(\nu, T, \vec{c}), \tag{1.37}$$

with $\bar{f}_\alpha$ represents the free energy of the α component in the mixture. In this study, we examine the thermodynamic potential $f(\nu, T, \vec{c})$ by considering the partial functions $\bar{f}_\alpha(\nu, T, \vec{c})$. These partial functions correspond to each of the components $f_\alpha(\nu_\alpha, T)$, where ν_α represents a function of the thermodynamic state $(\nu, T, \vec{c})$. Thus, f can be expressed as :

$$f(\nu, T, \vec{c}) = \sum c_\alpha f_\alpha\left(\nu_\alpha(\nu, T, \vec{c}), T\right). \tag{1.38}$$

This mixture is ideal because the equation contains no term that enables the interaction of the components. After the potential f has been defined, the unknown functions $\nu_\alpha(\nu, T, \vec{c})$ must be identified.

In fact, the dry gas and the water vapor possess identical volumes. This allows us to express the following relationship :

$$c_H \nu_H = c_V \nu_V. \tag{1.39}$$

Based on the equations 1.31, 1.34, 1.35 and 1.39, the following relations are derived :

$$\begin{cases} \nu = c_H \nu_H + c_L \nu_L = c_V \nu_V + c_L \nu_L; \\ \\ c_H \nu_H = \dfrac{\nu - (1 - \nu_H)\nu_L}{\nu_V - \nu_L} \nu_V. \end{cases} \tag{1.40}$$

These relationships show that a specific volume can be represented as a function of the other two. Consequently, two further equations are necessary. To begin, we determine the gradient of the thermodynamic potential $\vec{\nabla} f(\nu, T, c)$:

$$-\vec{\nabla} f = \begin{pmatrix} p \\ s \\ \mu \end{pmatrix} = \begin{pmatrix} \sum_{\mathrm{g}_V - \mathrm{g}_H}^{p_L} c_\alpha s_\alpha\left(\nu_\alpha, c\right) \end{pmatrix} + \left[p_H + p_V - p_L\right] \vec{\nabla}\left(c_H \nu_H\right) + \left[\mathrm{g}_V - \mathrm{g}_L\right] \vec{\nabla}\left(c_L\right), \tag{1.41}$$

where $p = -\partial f / \partial \nu$, $s = -\partial f / \partial T$ and $\mu = -\partial f / \partial c$ are respectively the pressure, the entropy, and the derivative of f with respect to c. Moreover, $p_\alpha = -\partial f_\alpha / \partial \nu_\alpha, s_\alpha = -\partial f_\alpha / \partial T$ and $\mathrm{g}_\alpha = f_\alpha + p_\alpha \nu_\alpha$ are the partial quantities, which are the pressure, the mass entropy and the free enthalpy of the constituent α, respectively.

To solve the relation 1.41, it is necessary to include the mechanical equilibrium condition and the thermodynamic equilibrium condition of both the vapor and liquid phases of water, as :

$$\begin{cases} \mathrm{g}_V\left(\nu_V, T\right) = \mathrm{g}_L\left(\nu_L, T\right); \\ p_H\left(\nu_H\left(\nu_L, \nu_V\right), T\right) + p_V\left(\nu_V, T\right) = p_L\left(\nu_L, T\right) = p. \end{cases} \tag{1.42}$$

Thus, a straightforward expression for the derivative of f is obtained :

$$-\vec{\nabla} f = \begin{pmatrix} p \\ s \\ \mu \end{pmatrix} = \begin{pmatrix} p_L \\ \sum c_\alpha s_\alpha\left(\nu_\alpha, c\right) \\ \mathrm{g}_V - \mathrm{g}_H \end{pmatrix}. \tag{1.43}$$

The study of the water thermodynamics delineates three distinct cases :

1. When the total pressure is beneath the saturation pressure $p_s(T)$, water is in the vapor phase. Consequently, the mixture consists of dry gas and water vapor.
2. When the total pressure surpasses a limit pressure $p_{\mathrm{lm}}(T)$, water is in the liquid phase. Thus, the mixture is composed of dry gas and liquid water.
3. For total pressures within the range $]p_s(T), p_{\mathrm{lm}}(T)[$, water is present in both phases (vapor and liquid), meaning the mixture includes dry gas, water vapor, and liquid water.

Only the third case necessitates numerically solving the system 1.42 through a Newton-Raphson-type iterative process. After calculating the specific volumes ν_α, the free energy of each constituent α is determined. Subsequently, the thermodynamic potential f is derived using Equation 1.37.

The thermodynamic properties of equilibrium are obtained from the function f. In order to compute these thermodynamic properties, higher-order derivatives of f are necessary, which in turn require the partial derivatives of ν_V and ν_L

The mass compressibility factor can be expressed as :

$$Z = -\left(\frac{\nu}{T}\right)\frac{\partial f(\nu, T, c)}{\partial T}. \tag{1.44}$$

We consider the function $\phi = f/T$. Based on this, we introduce the parameters X and Y :

$$\begin{cases} X = \dfrac{\partial p(\rho, T, c)/\partial \rho}{T} = \dfrac{\partial\left(\rho Z(\rho, T, c)\right)}{\partial \rho} = 2Z + \rho^2 \dfrac{\partial^2 \phi}{\partial^2 \rho}; \\ Y = \dfrac{\partial p(\rho, T, c)/\partial T}{\rho} = \dfrac{\partial\left(T Z(\rho, T, c)\right)}{\partial T} = Z + \rho T \dfrac{\partial^2 \phi}{\partial^2 \rho T}. \end{cases} \tag{1.45}$$

Using these parameters, we can further express the following key thermodynamic properties :

$$\begin{cases} \text{Thermal expansion coefficient :} & \alpha = \dfrac{Y}{TX}; \\ \text{Isothermal compressibility :} & \beta = \dfrac{1}{\rho TX}; \\ \text{Specific heat at constant volume :} & C_v = -2T\dfrac{\partial \phi}{\partial T} - T^2\dfrac{\partial^2 \phi}{\partial^2 T}; \\ \text{Specific heat at constant pressure :} & C_p = C_v + \dfrac{Y^2}{X}; \\ \text{Heat capacity ratio :} & \gamma = \dfrac{X + Y^2/C_v}{Z}; \\ \text{Joule - Thomson coefficient :} & \mu_{JT} = \dfrac{\alpha T - 1}{\rho C_p}. \end{cases} \tag{1.46}$$

In order to examine the rate of change of humidity in the gas, we included an extra equation in our model. This equation establishes a relationship between the rate at which the water concentration in the gas changes over time, represented as $\dot{c}_W$, and the saturation concentration of water in the gas-rich phase, c_W^s. The equation is expressed as :

$$\tau \dot{c}_W = c_W^s - c_W \tag{1.47}$$

where τ represents the time constant determining the rate of the process, and c_W and c_W^s are defined respectively as $c_W = 1 - c$ and $c_W^s = 1 - c^s$.

Given the above definitions, Equation 1.47 can be rewritten in terms of the gas concentration c as follows :

$$\tau \dot{c} = c^s - c \tag{1.48}$$

By incorporating the equation 1.48 into our model, we are able to investigate the kinetics of humidity in the gas. This enables us to gain a deeper understanding of the system dynamics under various thermodynamic conditions and improves the precision of our predictions by considering the system time-dependent behavior.

2.2.3 Validation of the model with hydrogen

The main objective of this subsection is to validate the HGM model with specific regard to hydrogen. Understanding the solubility of water in hydrogen is of paramount importance for optimizing energy storage systems. To this end, data on vapor-liquid equilibria (VLE) for hydrogen-water mixtures, obtained from various literature sources, serve as the foundation for validation. This process will critically assess the model reliability and accuracy by comparing its predictions with available experimental data. Moreover, the validation process will extend to a comparison between our model predictions and those from existing models in the literature.

2.2.3.1 Data collection

Experimental data, extracted from peer-reviewed sources, served as the basis for this validation. A total of ten sources contributed to the dataset, as summarized in Table 1.10. The

experimental data covers a range of temperatures from 273.15 to 650 K and pressures from 0.34 to 101.33 MPa. These data points provide a comprehensive spectrum for validation, encompassing conditions that have been studied since as early as 1927. To validate the HGM model, its estimations were directly compared to the compiled experimental data. Both temperature and pressure variables were matched to assess the model efficacy in replicating experimental observations of hydrogen-water VLE.

TABLE 1.10 – Experimental data for vapor-liquid equilibria (VLE) for H_2-H_2O mixtures.

No.	Reference	Temperature range (K)	Pressure range (MPa)
1	[Wiebe, 1934]	273.15-373.15	2.5-101.3
2	[Gillespie, 1980]	310.93-588.71	0.34-13.79
3	[Kling, 1991]	323.15-423.15	3.18-15.37
4	[DeVaney, 1978]	366.48-588.7	1.38-11.03
5	[Jung, 1971]	373.15-573.15	2.1-10.0
6	[Ipatev, 1934]	373.15-498.15	3.1-11.8
7	[Ugrozov, 1996]	310.95-366.45	1.38-13.79
8	[Maslennikova, 1976]	323.15-573.15	5.0-30.0
9	[Bartlett, 1927]	323.15	10.13-101.33
10	[Pray, 1952]	300-650	0.5-4.5

2.2.3.2 Comparative analysis of model predictions and experimental data

The principal aim of this analysis is to assess the accuracy and reliability of the HGM model, particularly for hydrogen. To this end, Figure 1.25 shows how the model numerical results align with experimental data points. This match provides experimental validation and confirms the model ability to accurately predict the water content in hydrogen gas under different thermodynamic conditions.

The data suggests a strong dependency of water solubility in hydrogen on temperature ; an increase in temperature is correlated with a significant rise in solubility. Conversely, increased pressure exhibits a less pronounced yet still noteworthy effect, leading to a decrease in water content. These trends are consistent with anticipated thermodynamic behavior. Consequently, this study effectively validates the numerical model and offers key insights into the thermodynamics of hydrogen-water systems.

The HGM model is particularly interesting for its ability to effectively include a wide range of temperature and pressure conditions that are relevant to hydrogen storage. In particular, the model has proven its efficiency in estimating data points at elevated pressures, reaching up to approximately 600 bar. The model ability to maintain a high degree of precision and reliability even under very challenging conditions confirms its suitability for more intricate simulations. Therefore, it can be confidently used in next chapter for simulating a salt cavern gas storage scenarios.

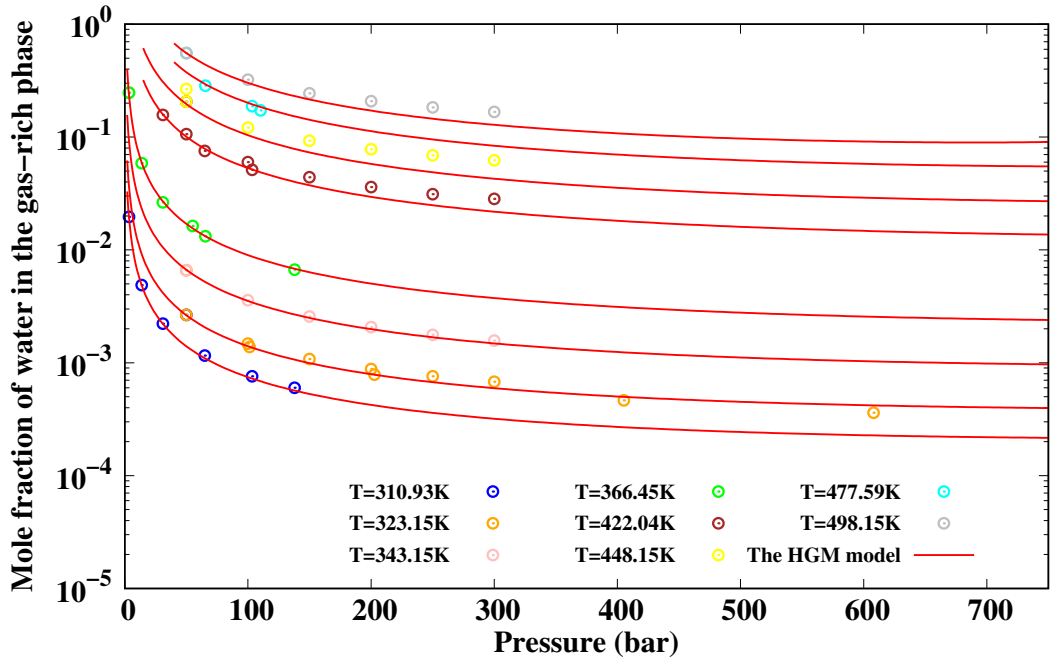

FIGURE 1.25 – Comparative analysis of model predictions and experimental data for water content in Hydrogen gas.

Validating the HGM model : A comparative analysis with existing models

The primary objective of this subsection is to further validate the HGM model, specifically in the context of hydrogen. The validation process consists of two principal components. First, our model will be rigorously compared with three existing models detailed in the work of [Rahbari, 2019]. These models, which also serve as a benchmark against experimental data, focus on the solubility of water in hydrogen over a pressure range of 0 to 800 bar and at four distinct temperatures. Therefore, this comparison will provide a comprehensive evaluation of our model efficacy in estimating water solubility in hydrogen. Second, the model's robustness will be examined by evaluating its capacity to predict key thermodynamic properties of humid hydrogen, such as Joule-Thomson coefficients, thermal expansivities, and heat capacities. This will be carried out through a comparative analysis with the models presented by [Rahbari, 2021]. Consequently, this approach aims to confirm the model efficiency for both solubility estimation and thermodynamic property prediction.

In the investigation of water content in hydrogen gas, our work presents the HGM model, delineated in Figure 1.26. This model undergoes comparative evaluation against the simulations based on TIP3P-Marx [Jorgensen, 1983 ; Marx, 1992], TIP4P/2005-Marx [Abascal, 2005 ; Marx, 1992], and TIP5P/Ew-Marx [Rick, 2004 ; Marx, 1992] force fields, as described in [Rahbari, 2019]. For a pressure range expanding over $0-800$ bar and temperatures such as 310.93, 323.15, 366.45, and 422.04 K, the HGM model demonstrates superior performance at low pressures. Specifically, the TIP3P-Marx model has been observed to slightly overpredict water content at low pressures across all isotherms, as also reported in [Rahbari, 2019]. In contrast, the TIP4P/2005-Marx model underestimates water solubility across the entire pressure spectrum. Notably, the

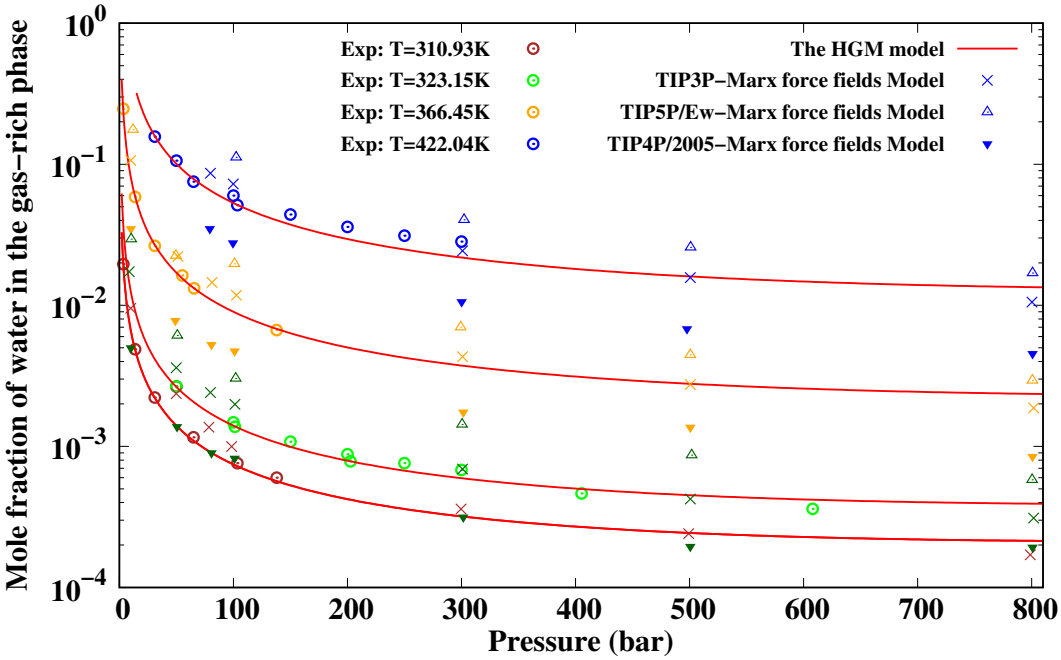

FIGURE 1.26 – Comparative analysis of model predictions and models from the literature for water content in hydrogen gas at pressure range $0 - 800$ bar and temperatures $310.93, 323.15, 366.45, 422.04$ K ; Featuring 3 models from the literature presented by [Rahbari, 2019] : TIP3P - Marx [Jorgensen, 1983 ; Marx, 1992], TIP4P/2005 - Marx [Abascal, 2005 ; Marx, 1992], and TIP5P/Ew - Marx [Rick, 2004 ; Marx, 1992] force fields models.

TIP5P/Ew-Marx model overpredicts water content for the whole pressure range. Therefore, our model offers a more accurate approximation for water content in hydrogen gas at low and high pressures compared to these models.

A comparative analysis with existing models of the impact of water content on hydrogen thermodynamic properties

This study aims to investigate the impact of water concentration on the thermodynamic properties of hydrogen. Specifically, calculations will be carried out for thermal expansivities, heat capacities, and Joule–Thomson coefficients at two distinct temperature points : 366.15 K and 423.15 K. These computations expand over a pressure range of 0 to 800 bar. Our analysis aims to establish a comparative framework with two established models in the literature, namely TIP3P-Marx [Jorgensen, 1983 ; Marx, 1992] and TIP3P-Vrabec [Jorgensen, 1983 ; Köster, 2018]. Figures 1.27, 1.28, 1.29 offer a quantitative juxtaposition between our model and these benchmark models, highlighting thermal expansivities (α), heat capacities (C_p), and Joule–Thomson coefficients (μ_{JT}), respectively. These thermodynamic proprieties are defined in the equation 1.46.

Our study outcomes align closely with the findings from previous models developed by [Rahbari, 2021]. At lower pressures below 50 bar, the thermal expansivity (α) is notably influenced by the water content, an effect that increases slightly at elevated temperatures, as can be observed by comparing the cases at $T = 366.45$ K and $T = 422.04$ K . This discrepancy between

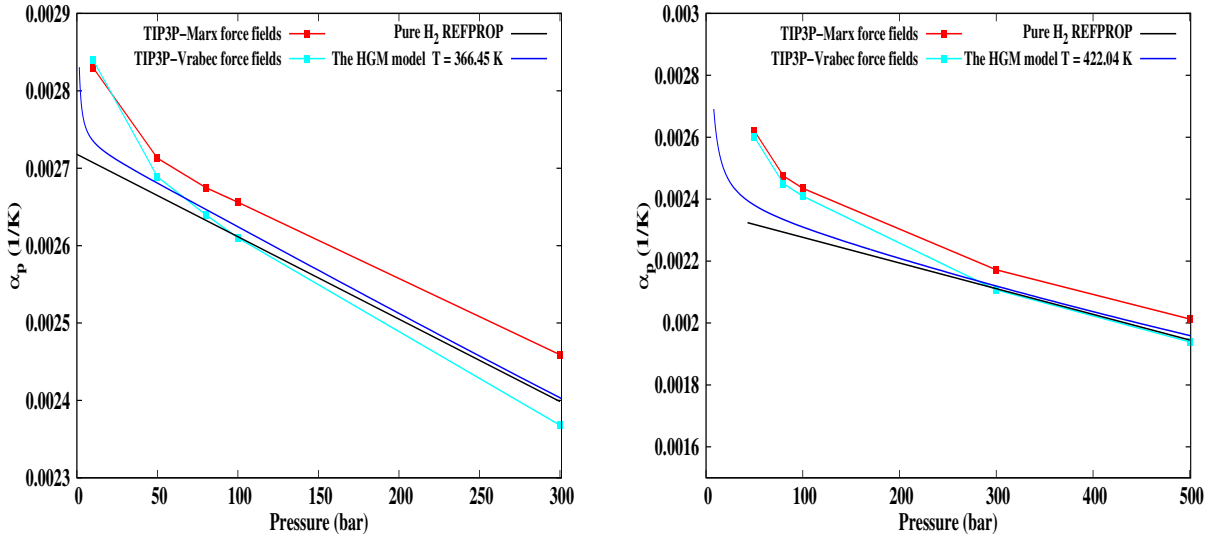

For $T = 366.45\,\mathrm{K}$ For $T = 422.04\,\mathrm{K}$

FIGURE 1.27 – Comparison of thermal expansivity values : Our HGM model vs TIP3P - Marx [Jorgensen, 1983 ; Marx, 1992] and TIP3P - Vrabec [Jorgensen, 1983 ; Köster, 2018] force fields at $T = 366.45$, and $422.04\,\mathrm{K}$ across different pressure ranges, including empirical data from REFPROP [Lemmon, 2018] for pure hydrogen presented by [Rahbari, 2021].

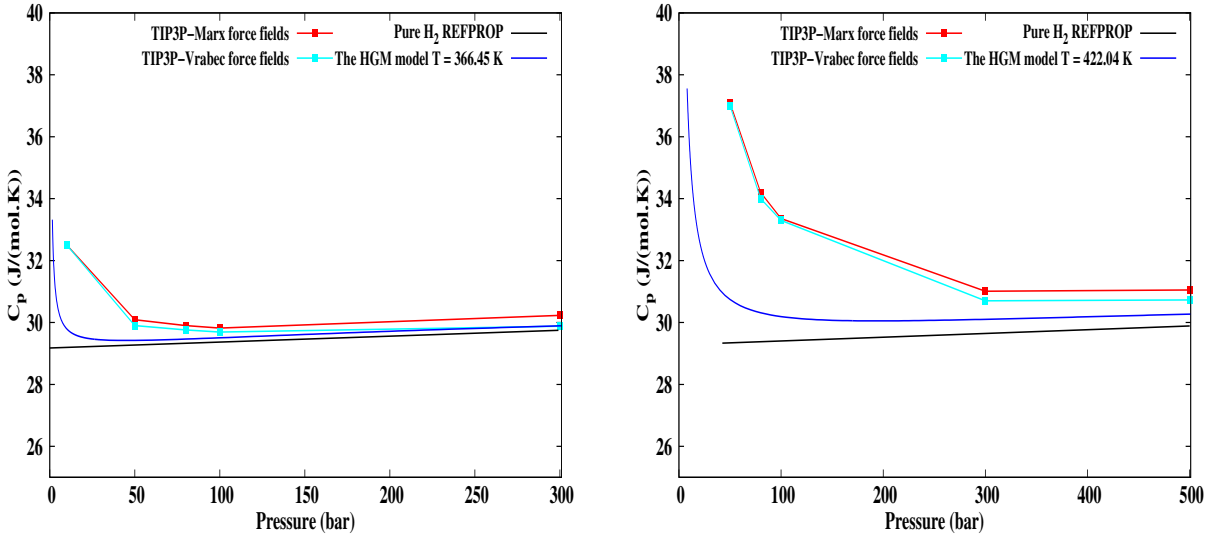

For $T = 366.45\,\mathrm{K}$ For $T = 422.04\,\mathrm{K}$

FIGURE 1.28 – Comparison of heat capacity values : Our HGM model vs TIP3P - Marx [Jorgensen, 1983 ; Marx, 1992] and TIP3P - Vrabec [Jorgensen, 1983 ; Köster, 2018] force fields at $T = 366.45$, and $422.04\,\mathrm{K}$ across different pressure ranges, including empirical data from REFPROP [Lemmon, 2018] for pure hydrogen presented by [Rahbari, 2021].

humid and dry hydrogen is evident in Figure 1.27, but it diminishes as the pressure increases, eventually aligning with the thermal expansivity of dry hydrogen at around 200 bar. In the case of the TIP3P-Marx and TIP3P-Vrabec models, the thermal expansivities also follow a similar trajectory, though with slight deviations. Transitioning to other thermodynamic parameters, si-

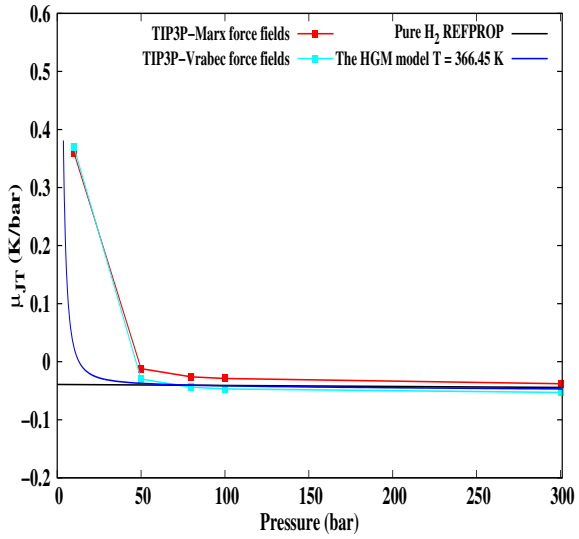

For $T = 366.45\,\mathrm{K}$

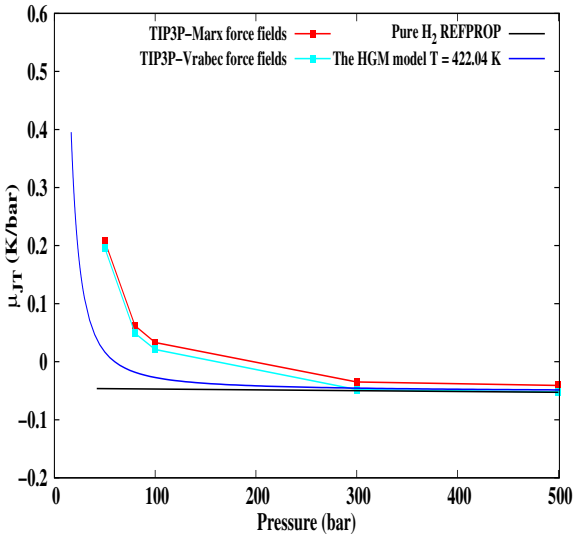

For $T = 422.04\,\mathrm{K}$

FIGURE 1.29 – Comparison of Joule – Thomson coefficients : Our HGM model vs TIP3P - Marx [Jorgensen, 1983 ; Marx, 1992] and TIP3P - Vrabec [Jorgensen, 1983 ; Köster, 2018] force fields at $T = 366.45$, and $422.04\,\mathrm{K}$ across different pressure ranges, including empirical data from REFPROP [Lemmon, 2018] for pure hydrogen presented by [Rahbari, 2021].

milar behaviors were observed for heat capacity (C_p) and the Joule–Thomson coefficient (μ_{JT}), as delineated in Figures 1.28 and 1.29. Our model yielded values for C_p and μ_{JT} that were consistently lower than the estimates generated by the TIP3P-Marx and TIP3P-Vrabec models, mirroring the trend observed for α. At lower pressures, these values become more significant.

2.2.4 Evaluation and validation of the HGM model through the helium experiment

This subsection aims to quantify the water content in the gas-rich phase by examining helium as a case study. The experimental test described in Section 1.2.3, provided a basis for this investigation in a controlled laboratory setting. So, we will use our previously developed HGM model (see section 2.2) to simulate the experimental test under storage conditions.

In fact, the experimental data included the average values of pressure, temperature, and relative humidity within the gas-rich phase (see Figures 1.10a, 1.10b, and 1.14). The model aimed to estimate the relative humidity by using temperature and pressure as inputs. The implementation of the model is divided into three parts. The HGM model was initially used to predict the relative humidity without taking into account the kinetics of humidification, as described in the equation 1.48. Following this, the equation was included to improve the model predictions. Finally, a revised equation will be introduced to further enhance the accuracy of the results.

The HGM model results without considering the kinetics of humidification

Figure 1.30 illustrates the relative humidity calculated by the HGM model without taking into account the humidification kinetics. The numerical results show a discrepancy when compa-

red to the experimental measurements of relative humidity, specifically an overestimation of the observed temporal gradual decrease of the relative humidity. In fact, before starting the cycle ($t = 2.76$ hours), we can clearly observe that the model was able to anticipate the measured relative humidity, albeit with a slight overestimation of the values. This is due to the fact that the helium-brine system was in a stabilization phase, during which it reaches its equilibrium condition, followed by a slow filling phase until $t = 2.26$ hours. Once the cycle phase begins ($t = 2.76$ hours), including the fast injection and withdrawal of helium in short intervals, the system is no longer considered to be in an equilibrium state due to the rapid cycling. The HGM model is unable to accurately anticipate the behavior of the humid gas only based on the measured temperature and pressure. Therefore, to enhance the solution, the model was modified to include the kinetics of humidification so that the water content in helium could be precisely determined over time.

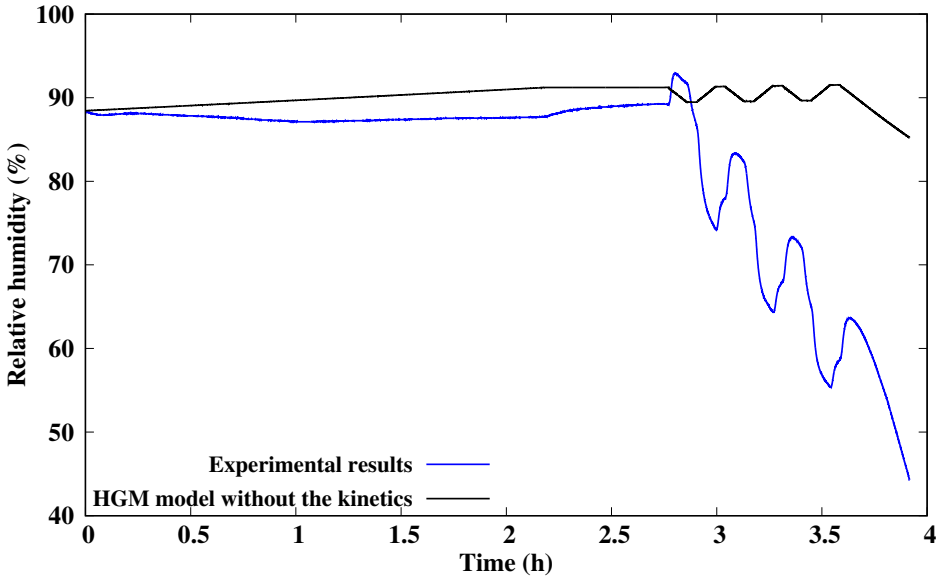

FIGURE 1.30 – Comparison between the experimental observations and the numerical estimation of relative humidity using the HGM model without taking into account the humidification kinetics.

The HGM model results considering the kinetics of humidification

The integration of humidification kinetics into the model significantly improved the accuracy of predicting relative humidity. This increase is particularly noticeable throughout the cycling process, as shown in Figure 1.31. The time constant τ for the helium test was calibrated to a value of $\tau = 85$ seconds in the equation 1.48. This calibration has resulted in a more accurate representation of relative humidity when compared to the solely thermodynamic equilibrium-based approach. Nevertheless, despite these improvements, the model still overestimates the relative humidity. Additionally, the trend of the model predictions does not align with the experimentally observed data. Consequently, the subsequent discussion will focus on the development of a nonlinear equation for humidification kinetics. The revised equation will integrate dual time

constants in order to provide a more precise replication of the experimentally observed outcomes.

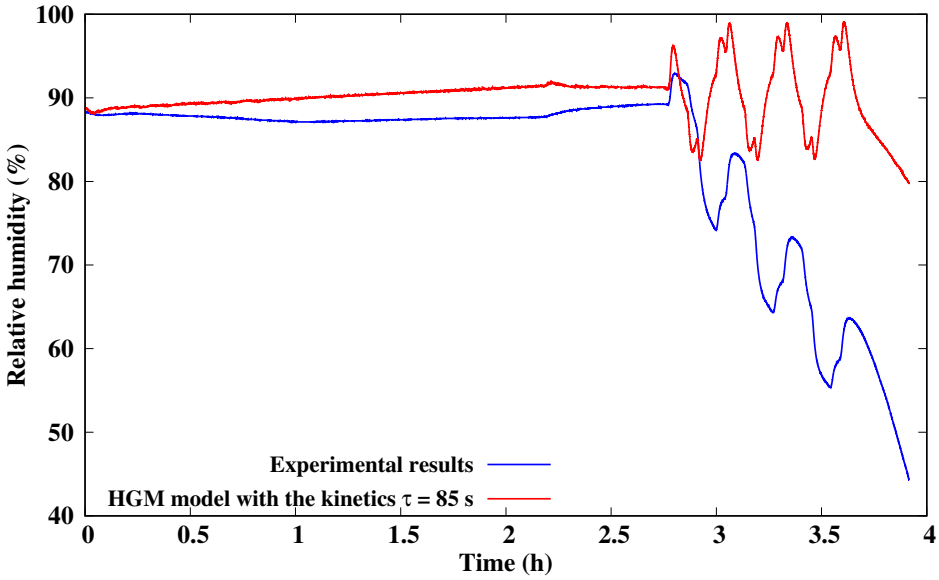

FIGURE 1.31 – Comparison between the experimental observations and the numerical estimation of relative humidity using the HGM model considering the humidification kinetics with $\tau = 85$ s.

The HGM model results using enhanced kinetics of humidification

In order to correct the overestimation of relative humidity that is observed in the calculated values of the HGM model using only one time constant during cycling, a modification has been made to the equation 1.48. This update incorporates two time constants, τ_1 and τ_2, to improve the model representation of humidification kinetics. The revised equation is presented as :

$$\begin{cases} \tau_1 \dot{c} = c^s - c, & \text{if } c \geq c^s \\ \tau_2 \dot{c} = c - c^s, & \text{if } c < c^s \end{cases} \tag{1.49}$$

After the calibration of these constants to $\tau_1 = 85$ s and $\tau_2 = 2500$ s, the HGM model showed improved agreement with the experimentally measured relative humidity values, as depicted in Figure 1.32. Although there is still a small discrepancy between the experimental and numerical data, especially at the beginning of the cycling phase, the revised model shows a notable enhancement in accurately predicting the drop in relative humidity during cycling.

In summary, the significance of this study is underscored by its contribution to the understanding of humidity kinetics in helium-brine systems. It provides a robust numerical model that has been validated through an experimental gas cycling process. The results ensure that the model predictions of relative humidity closely align with the observed data.

However, it is essential to distinguish between the controlled settings of the laboratory test and the conditions prevalent in actual salt cavern cycling scenarios. In fact, the laboratory tests involve a high rate of gas injection, with the gas in direct contact with the brine. Such conditions are not typically replicated in real-world salt cavern operations. As a result, the pronounced drop

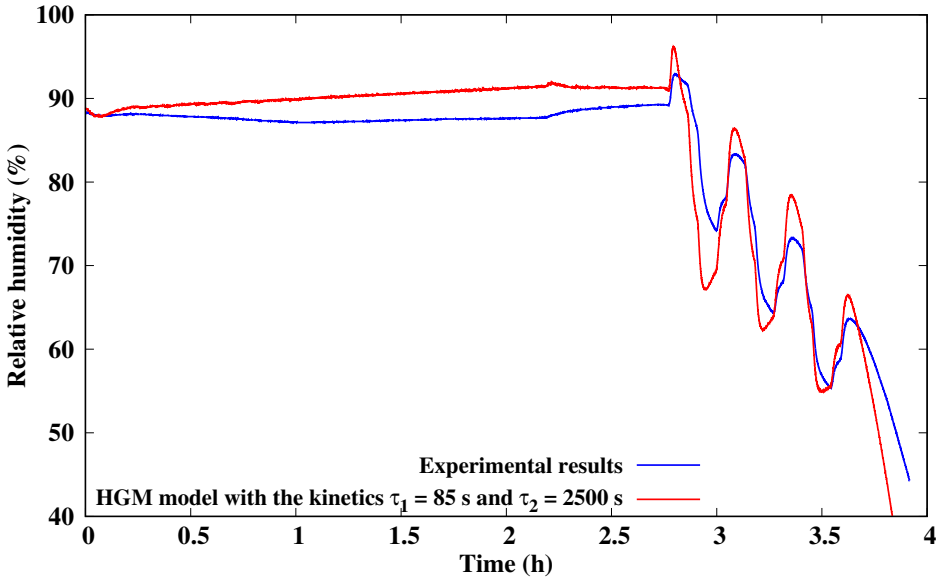

FIGURE 1.32 – Comparison between the experimental observations and the numerical estimation of relative humidity using the HGM model considering the humidification kinetics with two time constants $\tau_1 = 85$ s and $\tau_1 = 2500$ s.

in relative humidity observed in laboratory settings during cycling is not anticipated to be as significant in salt cavern conditions.

Given these considerations, the second chapter of this dissertation will focus on adapting the model to more realistically represent salt cavern scenarios. This adaptation will involve employing only the kinetics of humidification as represented in Equation 1.48. This approach ensures that the model remains relevant and applicable to practical scenarios, thereby bridging the gap between theoretical research and its practical applications in real-world settings.

2.2.5 Analysis of thermodynamic properties of humid hydrogen and helium

This subsection focuses on examining the thermodynamic characteristics of helium and hydrogen when they reach their saturation points with water in the gas-rich phase. The study encompasses variations across a diverse range of pressures and temperatures. The main goal is to not only compare the thermodynamic properties of the two gases but also to clarify the impact of water content on these properties.

The figure 1.33 elucidates the relationship between absolute humidity AH and temperature for saturation mixtures of hydrogen and helium with water vapor under various pressures. The figure introduces the Ideal Gas Model (IGM), an alternative approach for quick estimations that is not founded on robust theoretical principles, employing two key assumptions, that the gaseous phases are ideal gases and the vapor pressure of the water in the mixture is equal to the saturated vapor pressure of liquid water, denoted by $p_V = p_s(T)$. Subsequently, the concentration γ_G is formulated as $\gamma_G = (1 - p/p_s(T))/(1 - p/p_s(T) - \epsilon)$, where ϵ stands at 4.5 and 8.93 for helium and hydrogen, respectively, based on their molar mass ratios with water. At low pressures, both the HGM model and the IGM model align perfectly, confirming the applicability of the ideal

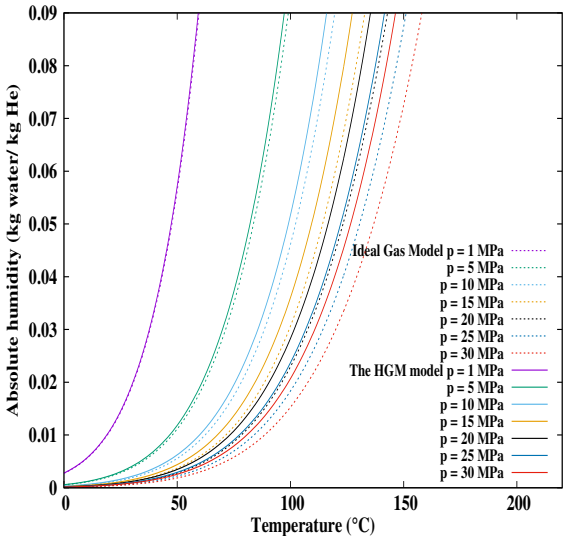

For He

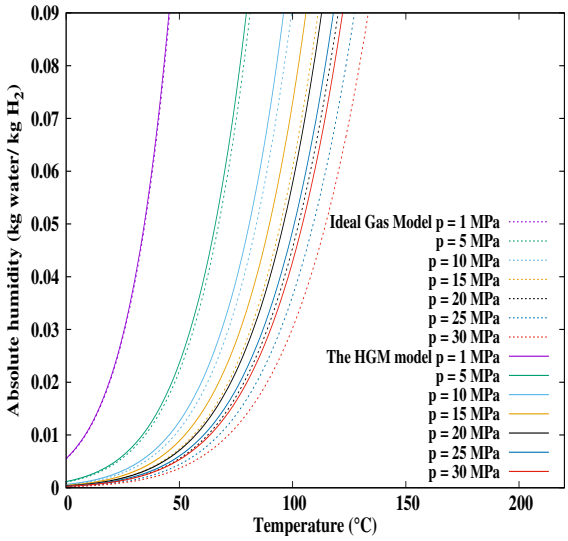

For H_2

FIGURE 1.33 – Absolute humidity as a function of temperature at the saturation of helium and H_2 with water in the gas-rich phase at varying pressures $p = \{2, 5, 10, 15, 20, 25, 30\}$ MPa.

gas assumption for low-pressure conditions. However, when the pressure increases a noticeable deviation becomes apparent between the two models for the humid hydrogen and helium. This divergence underscores the limitations of the IGM model in high-pressure. Additionally, upon maintaining a constant temperature, it is observed that the Absolute Humidity (AH) for humid hydrogen in the saturation phase is marginally greater than that of humid helium across various pressure values.

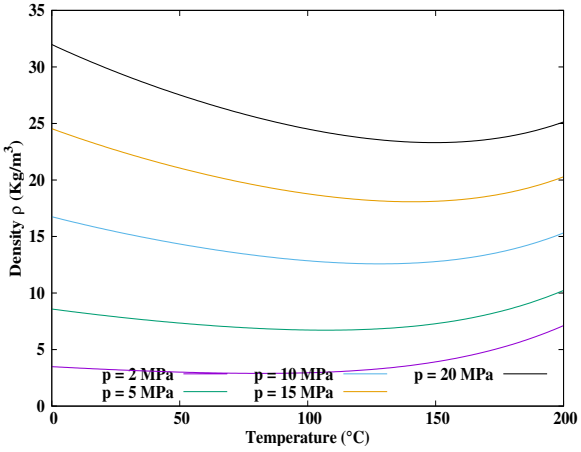

Density ρ for He

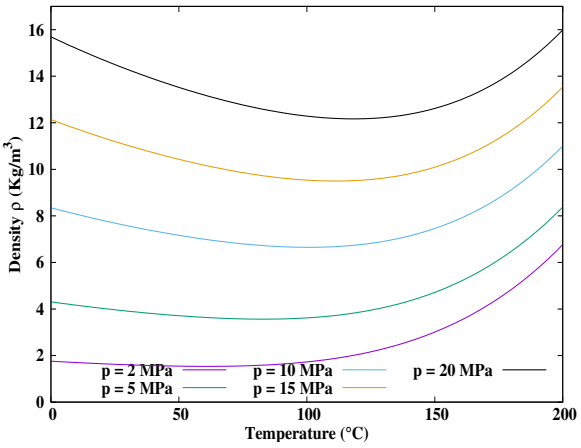

Density ρ for H_2

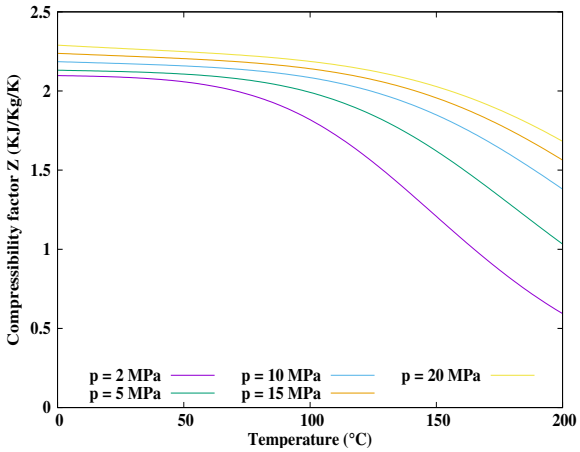

Compressibility factor Z for He

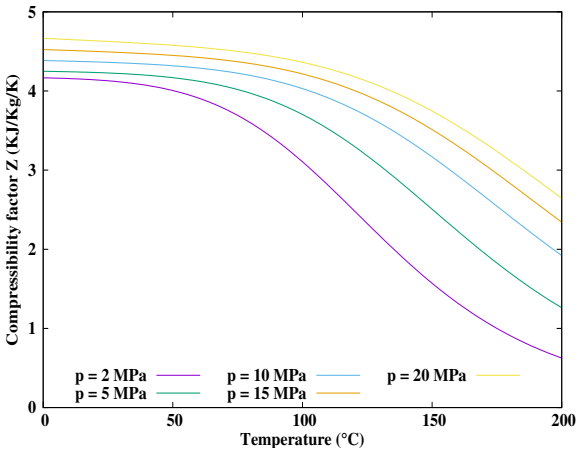

Compressibility factor Z for H_2

FIGURE 1.34 – Density ρ and compressibility factor Z as functions of temperature at the saturation of helium and H_2 with water in the gas-rich phase at varying pressures $p = \{2, 5, 10, 15, 20\}$ MPa.

To define the density ρ, we introduce the mass compressibility factor, represented as Z in the equation 1.44, and given by $\rho = p/TZ$. As depicted in Figure 1.34, the variation of Z across a range of pressure and temperature for both humid hydrogen and helium in their saturation phases is presented. Both humid gases exhibit a comparable trend of the density as a function of temperature. Specifically, the density demonstrates a consistent increase with rising pressure. Notably, the density values for humid helium are observed to be approximately twice those of humid H_2 . A similar observation can be made for Z.

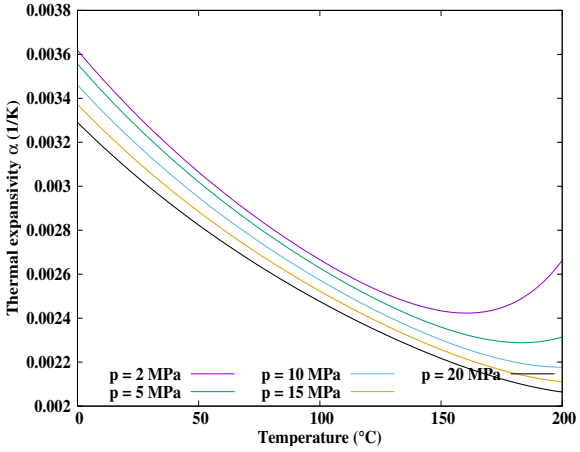

Thermal expansivity for He

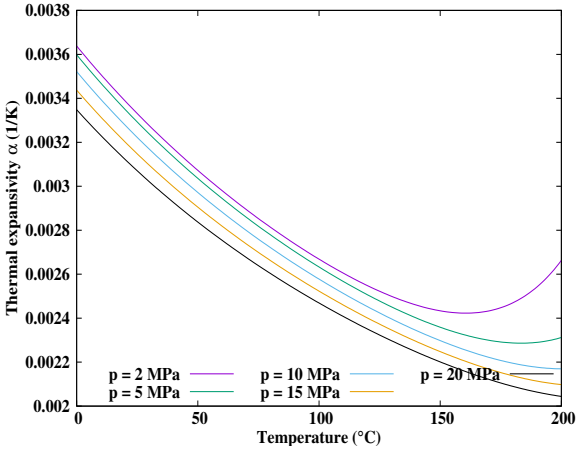

Thermal expansivity for H_2

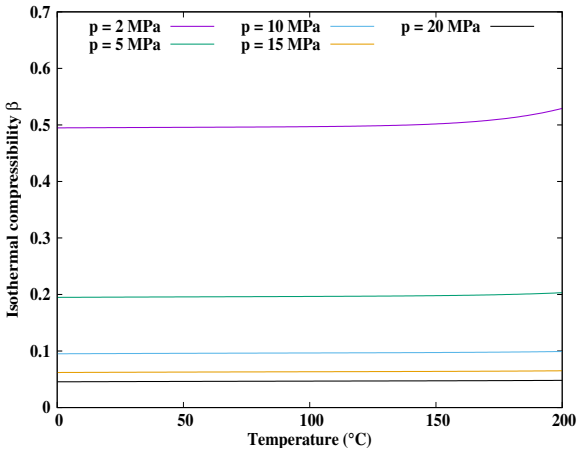

Isothermal compressibility for He

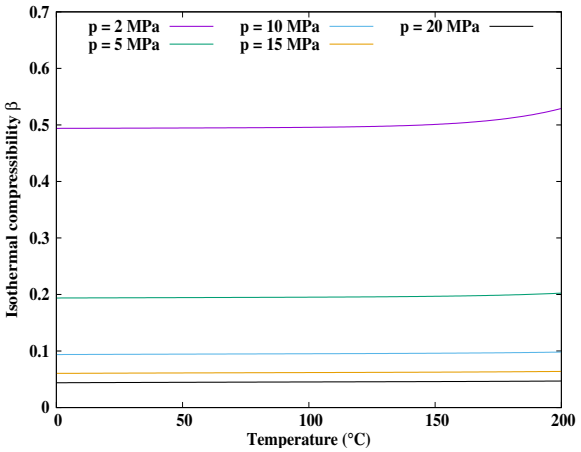

Isothermal compressibility for H_2

FIGURE 1.35 – Thermodynamic properties (thermal expansivity α, isothermal compressibility β) as a function of temperature at the saturation of helium and H_2 with water in the gas-rich phase at varying pressures $p = \{2, 5, 10, 15, 20\}$ MPa.

In Figure 1.35, the thermal expansivity α and isothermal compressibility β of humid helium and hydrogen are presented. For both gases, under varying pressures and temperatures, these coefficients exhibit similar behavior.

In Figure 1.36, the heat capacities C_p and C_v, as well as the heat capacity ratio γ, for humid helium and hydrogen are depicted. It is observed that both C_p and C_v increase as pressure increases, yet show a decrease with rising temperature. Notably, for all examined ranges of temperature and pressure, the values of C_p and C_v for humid hydrogen consistently exceed those for humid helium.

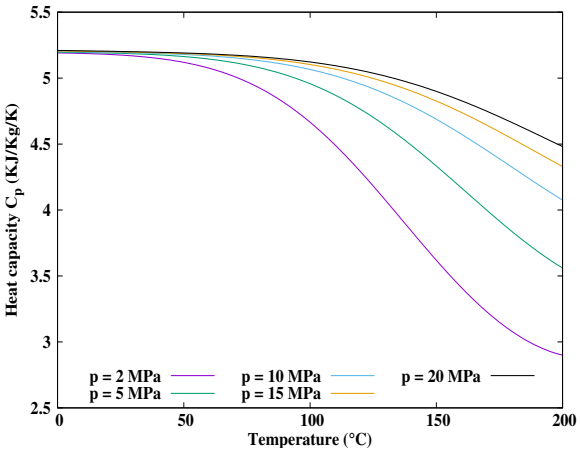

Heat capacity C_p for He

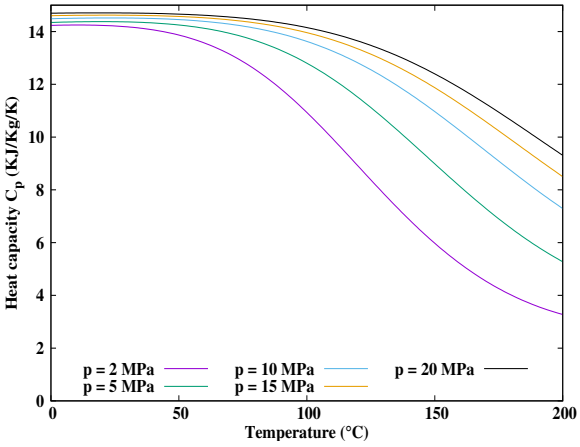

Heat capacity C_p for H_2

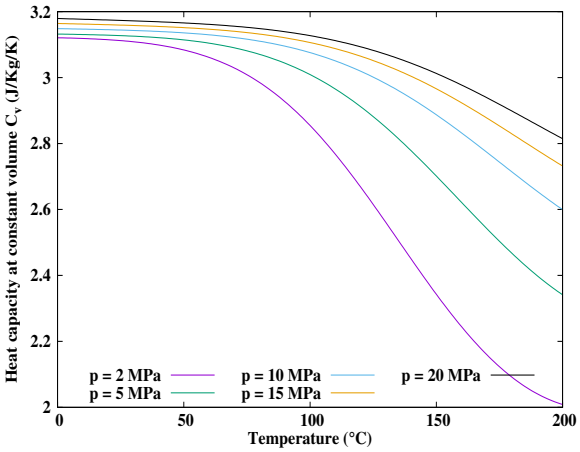

Heat capacity at constant volume C_v for He

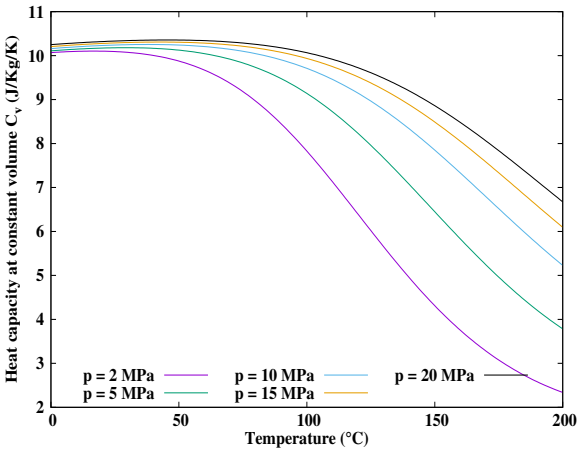

Heat capacity at constant volume C_v for H_2

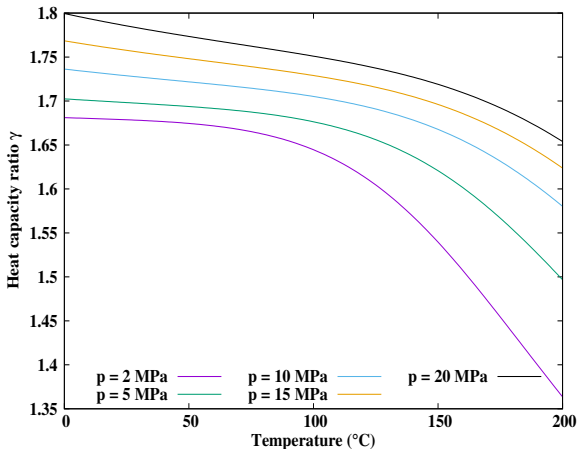

Heat capacity ratio for He

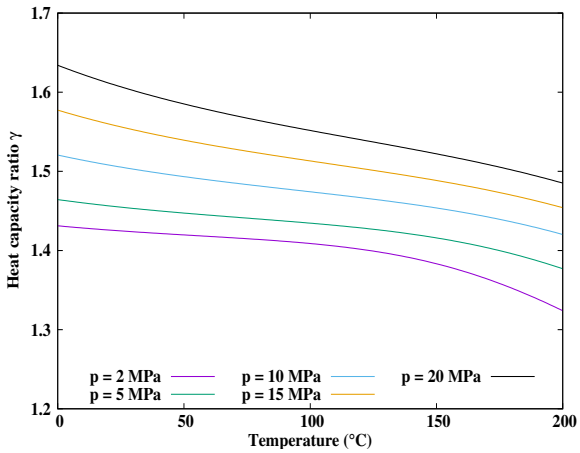

Heat capacity ratio for H_2

FIGURE 1.36 – Heat capacities C_p, C_v and heat capacity ratio γ as functions of temperature at the saturation of helium and H_2 with water in the gas-rich phase at varying pressures $p = \{2, 5, 10, 15, 20\}$ MPa.

Conclusion

To sum up, this chapter presents a comprehensive analysis of gas dissolution kinetics and gas humidification, specifically focusing on CO_2 and H_2 in aqueous solutions. This analysis incorporated both experimental and numerical approaches in order to study the phenomena under investigation.

The experimental studies, using the pressure-decay technique, have elucidated the dissolution kinetics of CO_2 and H_2 in both pure water and brine. In fact, the pressure drop observed over time during the experiment at a constant temperature represents the mass loss of gas due to its dissolution in the aqueous solutions. This mass loss is influenced by the salinity of the liquid phase as well as the volume ratio of the liquid and gas phases. As the salinity of the solution increases, the kinetics of dissolution become slower.

Additionally, the use of an innovative storage pilot for measuring gas humidity has provided valuable insights into the impact of mass transfer on the gas-rich phase. This experimental pilot, designed to replicate a salt cavern environment in a controlled laboratory setting, was used to study the water content in the gas-rich phase of the helium-brine system. A notable drop in the relative humidity was observed during cycling.

To analyze the experimental findings and accurately describe the mass exchange process, we developed mathematical and numerical models that effectively reproduced the observed physical phenomena in the experiments. These models provide a strong foundation for understanding the kinetics of gas dissolution in water and brine, as well as the behavior of humid gases under various conditions.

The dissolution experiments were simulated using two non-dimensional numerical models. The first model considers only pure diffusion and uses an apparent diffusion coefficient that is one hundred times greater than the molecular diffusion coefficient of CO_2 in aqueous solutions. To address the limitations of this approach, a second model, which incorporates all the complexities of the process, was introduced. The results from this model underscore the important role of natural convection in accelerating the kinetics of CO_2 dissolution, thereby enhancing the precision of predicting the dissolution process. On the other hand, during the study of hydrogen dissolution kinetics, we encountered difficulties arising from system leakage, which is attributed to the small molecular size of hydrogen. Thus, we incorporated a linear leakage correction into our second model to examine the experimental observations.

Moreover, we developed the HGM numerical model in order to examine the gas humidification process. The key numerical findings are :

— Accurate vapor-liquid equilibrium prediction : The model proved its ability to accurately predict the water content in the hydrogen-rich phase at thermodynamic equilibrium. It was confirmed by comparing experimental data across a wide range of temperatures and pressures with model estimations.

— Superior predictive accuracy : The HGM model shows a higher degree of accuracy of the vapor-liquid equilibrium in hydrogen-water systems.

— Prediction of thermodynamic properties : The model is capable of predicting key thermo-

dynamic properties, including the joule-thomson coefficient, thermal expansivity, and heat capacity.

— Kinetics of humidification : By including the kinetics into the model, it was able to explain the decrease in relative humidity observed during the experimental cycling test of helium.

In conclusion, the first chapter has established a solid foundation for understanding gas dissolution kinetics and gas humidification. This has been achieved through the use of both experimental and numerical approaches. Therefore, in the next chapter, we will use the developed models of gas dissolution and the HGM model along with the determined parameters, to investigate the complexities of mass exchange on the cavern scale.

Chapitre 2

Study of mass exchanges between gas and brine on the salt cavern scale

Objectifs

The objective of this chapter is to expand our understanding of gas and brine mass exchanges on the scale of salt caverns, which is pivotal for optimizing energy storage systems. This involves a detailed analysis of the dissolution rates of CO_2 and H_2 under storage conditions, considering factors such as pressure, temperature, and cavern features. Additionally, the chapter investigates the impact of humidity on the stored gases. This is achieved by using laboratory-validated models to quantify the gas loss via the dissolution process and the water content in the gas-rich phase in real-world applications.

Contents

Introduction du deuxième chapitre en français

La modélisation précise des processus thermodynamiques complexes au sein des cavités salines est indispensable pour l'utilisation efficace de ces structures dans le stockage d'énergie. Ce processus implique le transfert de chaleur et de masse entre la phase gazeuse et liquide, la cinétique de dissolution de gaz, les effets de convection, et la cinétique d'humidification des gaz. Les travaux précédents dans la littérature en matière de modélisation, basés sur l'hypothèse d'un équilibre thermodynamique instantané, ne considéraient pas un cadre global intégrant la cinétique de dissolution des gaz et leur humidification. Afin d'améliorer le stockage des gaz dans les cavités salines, il est essentiel de surmonter ces limitations.

S'appuyant sur l'étude préalable présentée dans le chapitre 1 de cette thèse, l'objectif de ce deuxième chapitre est d'élargir notre compréhension des échanges de masse entre le gaz et la saumure à l'échelle des cavités salines. L'accent est mis sur deux aspects fondamentaux de cet échange de masse à grande échelle : la dissolution des gaz dans la saumure et l'humidification des gaz dans la cavité. L'utilisation de modèles validés à l'échelle du laboratoire, dotés de paramètres calibrés, permettra d'approfondir la compréhension des interactions gaz-saumure dans les cavités salines.

Le chapitre débute par une analyse de la dissolution des gaz (CO_2, H_2) dans la cavité saline. Le processus de dissolution des gaz dans la saumure influence le comportement des cavités salines, déterminant ainsi leur capacité de stockage et leur efficacité globale. Compte tenu de la vaste surface de ces cavités, la cinétique de dissolution des gaz pourrait varier significativement par rapport à celle observée précédemment dans un environnement de laboratoire contrôlé. Une étude de dissolution des gaz sera menée pour obtenir une compréhension complète de ce processus, en se concentrant sur des facteurs clés tels que la pression, la température et les caractéristiques physiques de la cavité.

La seconde partie de ce chapitre vise à étudier les propriétés thermodynamiques des gaz humides, en particulier de l'hélium et de l'hydrogène, dans la cavité. La présence d'humidité dans le gaz peut modifier considérablement ses propriétés physiques. Il est donc essentiel de comprendre l'influence de l'humidité sur le comportement des gaz à grande échelle afin de prévoir et de contrôler la qualité du gaz stocké.

Introduction of the second chapter

The increasing use of renewable energy, motivated by the need to reduce carbon emissions in power generation, has led to a rise in interest in large-scale energy storage solutions. Renewable sources like wind and solar have intermittent characteristics, leading to discrepancies between supply and demand. Energy storage facilitates the management of oscillations in the power grid by storing surplus energy during times of excessive supply and releasing it when renewable energy production is insufficient.

Recently, underground salt caverns have emerged as a promising option for significant and long-duration energy storage. Many regions possess substantial salt deposits from a geological perspective. By using solution mining techniques to create salt caverns, it is possible to create

extremely large storage areas capable of holding millions of cubic meters. These caverns are suitable for storing pressurized gases such as CO_2 and H_2.

Precise modeling of complex thermodynamic processes within the cavern environment is crucial for effectively using salt caverns for energy storage. This includes heat and mass transfer between the gas and brine phases, dissolution kinetics, convection effects, and the kinetics of gas humidification, among others. However, prior attempts at modeling assume an immediate thermodynamic equilibrium and do not incorporate a comprehensive framework that accounts for the kinetics of gas dissolution and gas humidification in their models. To fully comprehend and optimize the storage of gases in salt caverns, it is crucial to address these limitations.

Building upon the prior examination of mass exchange between gas and brine in chapter 1 of this dissertation, this chapter extends the investigation from the laboratory scale to the cavern scale. The main focus of this chapter centers around two important aspects of this large-scale mass exchange : the dissolution of gases in the brine and the gas humidification in the cavern. Through using the validated models on the laboratory scale, this chapter will enhance the comprehension of gas-brine mass exchanges in salt caverns.

This chapter begins by examining the process of gas dissolution (section 1.1), focusing especially on CO_2 and H_2, within the salt cavern. The process of gas dissolution in brine affects the behavior of salt caverns, determining their storage capacity and overall efficiency. Due to the large surface area present in these caverns, the kinetics of gas dissolution might vary greatly compared to what is observed in a controlled laboratory environment. The dissolution rate will be investigated to get full insights into this process, focusing on key factors such as pressure, temperature, and the physical characteristics of the cavern.

The second part of this chapter (section 2) aims to elucidate the thermodynamic properties of humid gases, especially helium (He) and hydrogen (H_2), within the cavern. The presence of moisture in the gas can significantly modify its physical properties. Therefore, it is important to have a comprehensive understanding of how humidity affects gas behavior on a large scale in order to anticipate and control the quality of the stored gas.

1 Gas dissolution in salt caverns

This section investigates the dissolution process of CO_2 and H_2 in brine within salt caverns. It will be divided into two segments ; initially, the focus will be directed towards studying the geothermal effects on CO_2 dissolution kinetics in brine for underground storage in salt caverns. Subsequently, the kinetics of H_2 dissolution in salt caverns will be studied, along with the potential of employing hydrogen for tightness test within the EZ53 cavern. This analysis aims to provide a more comprehensive understanding of the mass exchange between gas and brine in salt caverns.

1.1 Dissolution of carbon dioxide in brine within salt caverns

The efficient management of CO_2 within underground salt caverns necessitates a comprehensive understanding of the dissolution kinetics of CO_2 in brine. This section establishes the

basis for a thorough examination of these kinetics, which are primarily influenced by natural convection. The natural convection appears due to changes in density caused by the concentration of dissolved CO_2 and thermal variations resulting from CO_2 cycling, which are, in addition, affected by the geothermal gradient.

By using our experimentally validated non-dimensional model described in section 2.1, this study evaluates the effect of mass and thermal variations on the kinetics of CO_2 dissolution by coupling the thermodynamics of the cavern with the dissolution processes. The model is extended to the cavern scale, addressing natural convection properties and their consequences for dissolution processes in the context of subsurface CO_2 storage. Despite the fact that the overall dissolved mass is relatively small in comparison to the initial stored mass, precise measurement of the effects of the dissolution process is nonetheless significant in order to accurately estimate the mass loss during the storage process.

This section begins with an overview of the study context. Next, the focus shifts to the mathematical model, which will include the thermodynamics of the cavern, the rock domain, and the boundary conditions into our non-dimensional model. Finally, the results and discussion of the dissolution kinetics of CO_2 within a salt cavern are presented.

1.1.1 Context of the Study

The use of underground salt caverns is recognized as a promising storage solution, primarily because of the efficiency of the solution mining process used to create them. These caverns, artificially constructed within large deposits of rock salt, have proven to be a safe storage facilities of high-pressure gases. The considerable geometric volumes and the ability to handle pressures surpassing 200 bar make them well-suited for storing significant amounts of gas [Bünger, 2016 ; Donadei, 2016]. To comprehend the problem under consideration in this work, it is essential to first understand the mechanism by which these salt caves are formed :

— **The Leaching Phase** : This phase begins with the drilling of a well into a subsurface salt deposit. This well connects the surface to salt caverns, which extend from a depth of 300 meters to 2000 meters [Berest, 2001]. The depth is determined by several factors, including the intended use of the cavern and the geological formation. After the installation of the well, the process of solution mining begins. Water is introduced into the salt formation, causing the salt to dissolve and resulting in the development of a brine solution. This brine is then extracted allowing for the gradual formation of the cavern over time. Depending on the desired size of the salt cavern, the duration of this phase might vary from one to several years.

— **The Debrining Phase** : The debrining phase begins following the cavern construction. Initially, integrity tests are conducted on the cement casing in order to verify its functionality and safety. Afterwards, the brine is removed from the cavern by injecting gas into the system. The gas is introduced via the exterior pipe, while the brine is extracted via the internal leaching pipe. At the end of this phase, the debrining pipe is carefully removed, and the cavern is ready for regular gas storage operations.

However, due to the physical limitations of the piping system, which does not reach the lowest parts of the cavern, removing the brine completely is a significant challenge. This residual brine can constitute up to 10% of the cavern volume [Soubeyran, 2019].

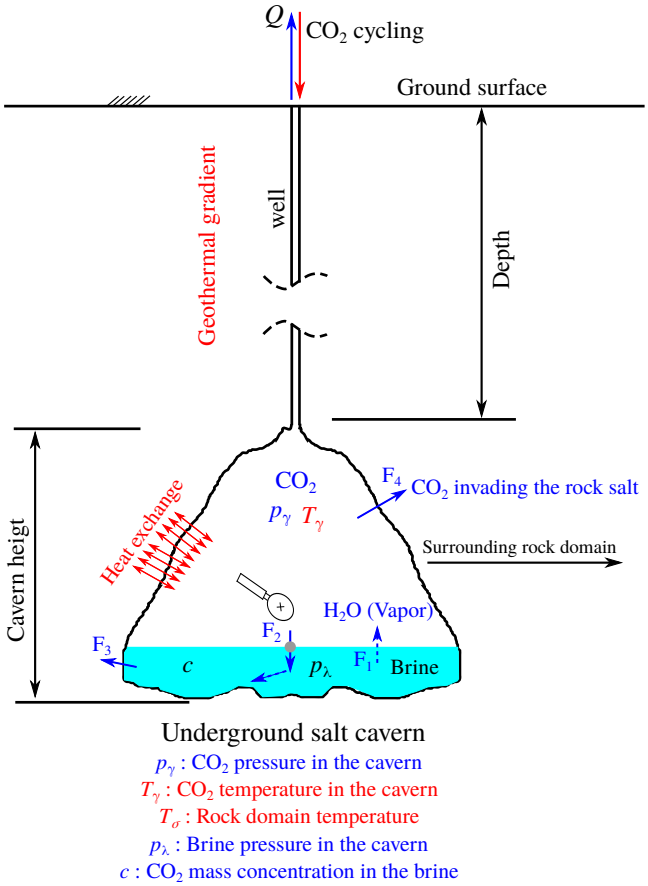

FIGURE 2.1 – Conceptual illustration of the CO_2 transport mechanisms between the different cavern phases.

Figure 2.1 illustrates the state of the cavern after the debrinning phase, revealing the coexistence of CO_2 and residual brine surrounded by the rock salt domain. During the CO_2 storage, the cavern primarily contains two distinct immiscible phases which are the brine and the stored CO_2 surrounded by salt rock domain. The three domains (stored gas, brine and the rock salt) are distinguished by specific state variables. For CO_2, these variables are pressure and temperature. For brine, the variables are pressure, temperature, salt concentration, and dissolved CO_2 concentration. Finally, for rock salt, the variables are stress and temperature.

During the operation of the cavern, the three domains interact in the following manner (see figure 2.1). The flux F_1 is the water evaporation into the stored CO_2 ; the flux F_2 is CO_2 dissolution in the brine ; the flux F_4 is CO_2 penetration into the porous rock salt ; the flux F_3 is the brine moving to the rock salt. In fact, the flux F_2 is the topic of this work.

The brine within the cavern initially has a minimal CO_2 concentration. When CO_2 is introduced, it creates a difference in concentration at the interface of the brine, causing a density gradient. As a result of these changes in the density field, convection is generated in the brine.

Furthermore, the geothermal gradient of the brine and the cycling temperature changes at the brine interface causes the development of thermal convection. The presence of both forms of convection is expected to increase the dissolution of CO_2 in the brine by generating convection vortices.

The phenomenon of CO_2 dissolution (flux F_2) has been studied in the context of water but not in brine under cavern storage conditions [Farajzadeh, 2009 ; Shi, 2018]. There were no published measurements of CO_2 dissolution in brine within salt caverns in order to compare and validate the developed model. Therefore, the gas loss due to the dissolution of CO_2 in brine necessitates a quantification process for the accurate management of cycled gas quantities. This quantification is crucial, given that it influences the study of other loss mechanisms, such as gas permeation into the surrounding rock (flux F_4) [AbuAisha, 2021].

To accurately describe the gas dissolution in brine under storage conditions and take into account the natural convection, the experimentally validated non-dimensional model in section 2 of the first chapter was used. This model was enhanced by coupling the gas dissolution process with cavern thermodynamics considering the surrounding rock domain. The goal is to develop a comprehensive model that incorporates the different complexities related to gas dissolution in salt caverns. Moreover, this model can be used to investigate the dissolution of different gases.

1.1.2 The complete mathematical model of gas dissolution

In this section, we shall extend the previously developed non-dimensional model (see section 2.1.2) to include the gas and rock domains within the context of salt caverns. The validation of the model on the laboratory scale provides a strong basis for its application on the cavern scale. This requires the development of additional equations to accurately describe the thermodynamics of the gas phase (referred to as the γ–phase) and the rock domain (referred to as the σ–phase). This section represents the continuity of the model developed in Chapter 1. First, the thermodynamics of the γ–phase within the cavern is introduced. This is followed by the presentation of the energy balance within the γ–phase. Each part presents the development of the equations in both their dimensional and non-dimensional forms.

1.1.2.1 The γ–phase domain : Cavern thermodynamics

The model development in the γ–phase will be initially presented in dimensional form, followed by its transformation into non-dimensional form.

The dimensional form

In the context of achieving a homogeneous thermodynamic environment within the gas phase in the cavern, a set of equations is applied [Abuaisha, 2023]. The equations presented here incorporate both mass and energy conservation principles, summarized as follows :

$$\begin{cases} \mathcal{M}_\gamma(-\alpha\,\dot{T}_\gamma + \beta\dot{p}_\gamma) & = Q_w - Q_{\gamma\lambda}; \\ \mathcal{M}_\gamma\, C_{p\gamma}\,\dot{T}_\gamma - \vartheta_\gamma\,\alpha\, T_\gamma\,\dot{p}_\gamma & = Q_i\, C_{p\gamma}(T_\gamma^w - T_\gamma) - \Psi_s, \end{cases} \tag{2.1}$$

Here, the mass of gas in the cavern is represented by $\mathcal{M}_\gamma$, with α and β denoting the gas thermal expansivity and compressibility respectively. The variables Q_w and Q_i are the well external flow rate (injection/ withdrawal) and the inflow rate of injection respectively. The term $Q_{\gamma\lambda}$ quantifies the mass exchange rate between gas and brine, with $C_{p\gamma}$ signifying the specific heat capacity of the gas. The cavern gas volume is $\vartheta\gamma$, while T_γ^w specifies the temperature of injected gas in the well. Lastly, the thermal power exchanged between the gas and other phases (rock and brine) is denoted as Ψ_s. The values for both Ψ_s and $Q_{\gamma\lambda}$ are considered positive when there is a loss from the gas domain. In fact, $Q_{\gamma\lambda}$ is described as :

$$Q_{\gamma\lambda} = -\int_{\Sigma_{\gamma\lambda}} \rho_\lambda \vec{v}_\lambda \cdot \vec{n}\, dA_{\gamma\lambda}, \tag{2.2}$$

where ρ_λ denotes the density of the brine, $\vec{v}_\lambda$ represents the velocity field in the λ–phase, $\Sigma_{\gamma\lambda}$ represents the gas–liquid interface with its area $A_{\gamma\lambda}$, and $\vec{n}$ is the unit normal outward vector.

The non-dimensional form

Before we start the developpement of the non-dimensional form, let us introduce the following non-dimensional variables for the gas domain :

$$\begin{cases} \tilde{p_\gamma} & = \dfrac{p_\gamma}{p_{\gamma 0}}; \\ \tilde{\rho}_\gamma & = \dfrac{\rho_\gamma}{\rho_{\gamma 0}(T_{\gamma 0},\, p_{\gamma 0})}, \end{cases} \tag{2.3}$$

where the non-dimensional gas density and gas pressure are denoted as $\tilde{\rho}_\gamma$ and $\tilde{p}_\gamma$ respectively. The initial gas density is given by $\rho_{\gamma 0}$, and the initial brine density is denoted as $\rho_{\lambda 0}$.

The dimensional forms that define the thermodynamic state of the gas in the cavern are converted to their non-dimensional equivalents by incorporating the variables from Equation 1.15 and 2.3 into the Equation 2.1. Furthermore, the temporal scaling described in Equation 1.14 is used to convert the time derivatives into non-dimensional terms. Applying this operation to the first part of Equation 2.1 yields the following expression :

$$-\tilde{\alpha}\,\dot{\tilde{T}}_\gamma + \tilde{\beta}\dot{\tilde{p}}_\gamma = \underbrace{\frac{Q_w\, L^2}{\mathcal{M}_\gamma\, D}}_{\text{Term 1}} - \underbrace{\frac{Q_{\gamma\lambda}\, L^2}{\mathcal{M}_\gamma\, D}}_{\text{Term 2}}. \tag{2.4}$$

Within this framework, $\tilde{T}_\gamma$ refers to the non-dimensional temperature of the gas and $\tilde{p}_\gamma$ signifies the non-dimensional pressure of the gas. The non-dimensional gas isobaric thermal expansivity is represented by $\tilde{\alpha}$, and $\tilde{\beta}$ is the non-dimensional isothermal compressibility of the gas.

Given the equation 2.2, Term 2 in Equation 2.4 can be expressed as,

$$\frac{Q_{\gamma\lambda}\, L^2}{\mathcal{M}_\gamma\, D} = \frac{-L^2}{\mathcal{M}_\gamma\, D} \int_{\Sigma_{\gamma\lambda}} \rho_\lambda \vec{v}_\lambda \cdot \vec{n}\, dA_{\gamma\lambda}. \tag{2.5}$$

Based on the definitions of equations 1.14 and 2.3, the non-dimensional gas mass $\tilde{\mathcal{M}}_\gamma$ and $\varepsilon_{\gamma\lambda} = \rho_\gamma/\rho_{\lambda 0}$ can be written as :

$$\begin{cases} \tilde{\mathcal{M}}_\gamma = \tilde{\vartheta}_\gamma \, \tilde{\rho}_\gamma \, \rho_{\gamma 0} \, L^3; \\ \varepsilon_{\gamma\lambda} = \dfrac{\tilde{\rho}_\gamma \, \rho_{\gamma 0}}{\rho_{\lambda 0}}, \end{cases} \tag{2.6}$$

where the non-dimensional gas volume is represented by $\tilde{\vartheta}_\gamma$.

Considering the variables in Equations 2.6, if we multiply both the top and bottom parts of equation 2.5 by $(1/\rho_{\lambda 0})$, we get :

$$\frac{Q_{\gamma\lambda} \, L^2}{\mathcal{M}_\gamma \, D} = \frac{-1}{\tilde{\vartheta}_\gamma \, \varepsilon_{\gamma\lambda}} \int_{\tilde{\Sigma}_{\gamma\lambda}} \varepsilon_\lambda \vec{\tilde{v}}_\lambda \cdot \vec{n} \, d\tilde{A}_{\gamma\lambda}, \tag{2.7}$$

The mass flux $\vec{J} \cdot \vec{n} = K(c - p_\gamma/H)$ can be expressed as $\vec{\tilde{J}} \cdot \vec{n} = \tilde{K}(\tilde{c} - p_\gamma/(H \, c^s))$, where $\tilde{K} = K \, (L/D)$ represents the non-dimensional mass transfer coefficient. By substituting the non-dimensional mass flux into equation 1.16, we obtain the following expression : $\vec{\tilde{v}}_\lambda \cdot \vec{n} = \tilde{K}(\tilde{c} - p_\gamma/(H \, c^s))/(1/c^s - \tilde{c})$ for the non-dimensional brine velocity field. Therefore, equation 2.7 can be expressed as :

$$\frac{Q_{\gamma\lambda} \, L^2}{\mathcal{M}_\gamma \, D} = \frac{-\displaystyle\int_{\tilde{\Sigma}_{\gamma\lambda}} \varepsilon_\lambda \left[\dfrac{\tilde{K}(\tilde{c} - p_\gamma/(H \, c^s))}{1/c^s - \tilde{c}} \right] d\tilde{A}_{\gamma\lambda}}{\tilde{\vartheta}_\gamma \, \varepsilon_{\gamma\lambda}}. \tag{2.8}$$

The identical procedure is employed for the second component of equation 2.1. The manipulation results in the following equation :

$$\frac{D}{L^2} \left(\dot{\tilde{T}}_\gamma + \frac{p_{\gamma 0}}{T_{\gamma 0} \, \rho_{\gamma 0} \, C_{p\gamma}} \frac{\tilde{\alpha}(\tilde{T}_\gamma + 1)}{\tilde{\rho}_\gamma} \dot{\tilde{p}}_\gamma \right) = \frac{Q_i}{\mathcal{M}_\gamma} (\tilde{T}_\gamma^w - \tilde{T}_\gamma) - \frac{\Psi_s}{T_{\gamma 0} \, \mathcal{M}_\gamma \, C_{p\gamma}}. \tag{2.9}$$

By dividing equation 2.9 by (D/L^2), we obtain the following expression :

$$\dot{\tilde{T}}_\gamma + \frac{p_{\gamma 0}}{T_{\gamma 0} \, \rho_{\gamma 0} \, C_{p\gamma}} \frac{\tilde{\alpha}(\tilde{T}_\gamma + 1)}{\tilde{\rho}_\gamma} \dot{\tilde{p}}_\gamma = \frac{Q_i \, L^2}{\mathcal{M}_\gamma \, D} (\tilde{T}_\gamma^w - \tilde{T}_\gamma) - \frac{\Psi_s \, L^2}{T_{\gamma 0} \, \mathcal{M}_\gamma \, C_{p\gamma} \, D}, \tag{2.10}$$

The gas exchanged power, denoted as Ψ_s, consists of two components.

$$\Psi_s = \int_{\Sigma_{\gamma\sigma}} -\kappa_\sigma \vec{\nabla} T_\sigma \cdot \vec{n} \, dA_{\gamma\sigma} + \int_{\Sigma_{\gamma\lambda}} -\kappa_\lambda \vec{\nabla} T_\lambda \cdot \vec{n} \, dA_{\gamma\lambda}, \tag{2.11}$$

The variables κ_σ and κ_λ represent the thermal conductivities of the σ-phase and the λ-phase, respectively. The temperatures of these phases are T_σ and T_λ. The calculations of the integrations are performed across the interfaces between these phases, denoted as $\Sigma_{\gamma\sigma}$ and $\Sigma_{\gamma\lambda}$, with surface areas $A_{\gamma\sigma}$ and $A_{\gamma\lambda}$. The definitions of $\tilde{T}_\sigma$ and $\tilde{T}_\lambda$ which are the normalized temperature differences with respect to $T_{\sigma 0}$ and $T_{\lambda 0}$ respectively, where $T_{\sigma 0}$ and $T_{\lambda 0}$ are the initial temperatures of the σ-phase and the λ-phase respectively :

$$\begin{cases} \tilde{T}_\sigma = (T_\sigma - T_{\sigma 0})/T_{\sigma 0}; \\ \tilde{T}_\lambda = (T_\lambda - T_{\lambda 0})/T_{\lambda 0}. \end{cases} \tag{2.12}$$

Based on the definitions in 2.12, we can derive the non-dimensional form of equation 2.11 :

$$\tilde{\Psi}_s = \int_{\tilde{\Sigma}_{\gamma\sigma}} -\left(\kappa_\sigma\, L\, T_{\sigma 0}\right)\, \vec{\tilde{\nabla}}\tilde{T}_\sigma \cdot \vec{n}\, d\tilde{A}_{\gamma\sigma} + \int_{\tilde{\Sigma}_{\gamma\lambda}} -\left(\kappa_\lambda\, L\, T_{\lambda 0}\right) \vec{\tilde{\nabla}}\tilde{T}_\lambda \cdot \vec{n}\, d\tilde{A}_{\gamma\lambda}, \tag{2.13}$$

The variables $\tilde{\Sigma}_{\gamma\sigma}$ and $\tilde{\Sigma}_{\gamma\lambda}$ represent the non-dimensional interfaces, while $\tilde{A}_{\gamma\sigma}$ and $\tilde{A}_{\gamma\lambda}$ represent their non-dimensional areas. By substituting equation 2.13 into equation 2.10, and taking into account the definition 2.6 of $\tilde{\mathcal{M}}_\gamma$, we can write the following formulation :

$$\frac{\Psi_s\, L^2}{T_{\gamma 0}\, \mathcal{M}_\gamma\, C_{p\gamma}\, D} = \frac{1}{\tilde{\vartheta}_\gamma\, \tilde{\rho}_\gamma}\left(\frac{T_{\sigma 0}}{T_{\gamma 0}}\frac{\kappa_\sigma}{\rho_{\gamma 0}\, C_{p\gamma}\, D}\int_{\tilde{\Sigma}_{\gamma\sigma}} -\vec{\tilde{\nabla}}\tilde{T}_\sigma \cdot \vec{n}\, d\tilde{A}_{\gamma\sigma} + \frac{T_{\lambda 0}}{T_{\gamma 0}}\frac{\kappa_\lambda}{\rho_{\gamma 0}\, C_{p\gamma}\, D}\int_{\tilde{\Sigma}_{\gamma\lambda}} -\vec{\tilde{\nabla}}\tilde{T}_\lambda \cdot \vec{n}\, d\tilde{A}_{\gamma\lambda}\right), \tag{2.14}$$

setting $A = p_{\gamma 0}/(T_{\gamma 0}\, \rho_{\gamma 0}\, C_{p\gamma})$, $B = 1/(\tilde{\vartheta}_\gamma\, \tilde{\rho}_\gamma)$, $\omega_\sigma = (T_{\sigma 0}/T_{\gamma 0})\left[\kappa_\sigma/(\rho_{\gamma 0}\, C_{p\gamma}\, D)\right]$,
and $\omega_\lambda = (T_{\lambda 0}/T_{\gamma 0})\left[\kappa_\lambda/(\rho_{\gamma 0}\, C_{p\gamma}\, D)\right]$, equation 2.10 becomes,

$$\dot{\tilde{T}}_\gamma + A\frac{\tilde{\alpha}(\tilde{T}_\gamma + 1)}{\tilde{\rho}_\gamma}\,\dot{\tilde{p}}_\gamma = \frac{Q_i\, L^2}{\mathcal{M}_\gamma\, D}(\tilde{T}_\gamma^w - \tilde{T}_\gamma) - B\tilde{\Psi}_s, \tag{2.15}$$

with,

$$\tilde{\Psi}_s = \int_{\tilde{\Sigma}_{\gamma\sigma}} -\omega_\sigma \vec{\tilde{\nabla}}\tilde{T}_\sigma \cdot \vec{n}\, d\tilde{A}_{\gamma\sigma} + \int_{\tilde{\Sigma}_{\gamma\lambda}} -\omega_\lambda \vec{\tilde{\nabla}}\tilde{T}_\lambda \cdot \vec{n}\, d\tilde{A}_{\gamma\lambda}. \tag{2.16}$$

1.1.2.2 Energy balance of the σ–phase

In order to determine the heat transfer between the fluid phases and the rock domain, we introduce the energy equation of the σ–phase :

$$\rho_\sigma C_{p\sigma}\partial_t T_\sigma - \vec{\nabla}\cdot(\kappa_\sigma \vec{\nabla} T_\sigma) = 0, \tag{2.17}$$

where $C_{p\sigma}$ and κ_σ represent the rock salt heat capacity and the rock salt thermal conductivity, respectively. Based on the equation 2.12 representing $\tilde{T}_\sigma$, the equation 2.17 in its non–dimensional form is written as follows :

$$\partial_{\tilde{t}}\tilde{T}_\sigma - \vec{\tilde{\nabla}}\cdot\left(\frac{\tilde{a}_\sigma}{D}\vec{\tilde{\nabla}}\tilde{T}_\sigma\right) = 0, \tag{2.18}$$

with $\tilde{a}_\sigma = \kappa_\sigma/\rho_\sigma C_{p\sigma}$ represents the rock salt thermal diffusivity.

1.1.2.3 Initial and boundary conditions

This section will provide the initial and boundary conditions for gas dissolution on the salt cavern scale.

Initial conditions

Initially, it is assumed that all phases (γ, λ, σ) are in thermal equilibrium equal to the geothermal gradient. Their non-dimensional temperatures are normalized with regard to the same initial temperature T_0, where $T_{\sigma 0} = T_{\gamma 0} = T_{\lambda 0} = T_0$.

The gas pressure is influenced by the operational conditions of the cavern, specifically its depth, and the initial pressure p (see equation 1.10) is $p_0 = 0$.

The boundary conditions

Gas dissolves into the brine phase at the interface between the γ and λ–phases, depending on the gas pressure. Based on the cycling program, these two phases exchange heat as well. Additionally, there is heat exchange occurring between these two phases and the surrounding rock domain (σ–phase). The dissolution of gas into the brine generates convection, which is driven by density variations and results in an intricate velocity field. Temperature variations cause also density changes and convection in the brine phase. The same boundary conditions described in the equation 1.13 are applied to the cavern scale and are expressed in their non-dimensional form in the equation 1.25. The following boundary conditions which will be specific to the cavern at the interface between the different phases are presented :

— The temperature continuity is assumed between the gas and rock phases, meaning that $\tilde{T}_\gamma(t) = \tilde{T}_\sigma(t)$ at any given time t ;

— A heat transfer coefficient $h_{\gamma\lambda}$ is introduced between the gas and brine phases, resulting in the following non-dimensional heat exchange formula : $-\vec{\tilde{\nabla}}\tilde{T}_\lambda.\vec{n} = \tilde{h}_{\gamma\lambda}\,(\tilde{T}_\gamma - \tilde{T}_\lambda)$ and $\tilde{h}_{\gamma\lambda} = h_{\gamma\lambda}\,\dfrac{L}{\kappa_\lambda}$;

— Our modeling takes into account a significantly vast rock domain to reduce the impact of far–field boundaries. The far-field temperatures are always set to be equal to the geothermal gradient.

We will employ the model parameters β_c, D, and K determined in the laboratory scale (see section 2.1.3.1) when we apply our non-dimensional model to the real salt cavern.

1.1.3 From laboratory to cavern scale : Influence of temperature variations on dissolution kinetics

While our numerical model accurately represents the kinetics of CO_2 dissolution in brine, it is challenging to extend it to the cavern scale. The challenges arise from the use of the Navier-Stokes equation (1.23). The body forces defined by the terms ($\mathrm{Ra}\,\mathrm{Pr}$) improve by a factor of three as the model dimension increases. There is a certain length beyond which numerical convergence becomes very slow. When the magnitudes of the two terms ($\vec{\tilde{\nabla}}\tilde{p}$ and $\mathrm{Ra}\,\mathrm{Pr}\,\vec{e}_z$) are comparable, the simulations run accurately. The mathematical model presented in sections 1.1.2 and 2.1.2 is general since it incorporates the influence of temperature variations on the dissolution kinetics. The effect of temperature changes on natural convection as a result of density change is shown in Equation 1.17.

While the laboratory experiments can be conducted at various temperatures, the temperature should remain constant during the test. Therefore, it is necessary to first quantify the impact of thermal effects on the dissolution of gas when a temperature gradient is applied across the cell before extending our work to the cavern scale. Due to the non-availability of the laboratory

equipment required for this application, the measurement of temperature effects on dissolution is carried out numerically.

The numerical model shown in Figure 2.2 is used to model these effects. The model illustrates a cylinder with a radius that is three times larger than the radius of the laboratory cell mentioned in Section 1.1.2. However, the same ratio of height to radius is used. In the initial scenario, a temperature gradient of 3 °C is imposed throughout the height of the model. In the second situation, the difference is set to 0.1 °C. Gas is introduced into the model via the top surface fixing $c = c^s = 10^{-5}$ at the interface. The temperature gradients are applied in the direction of gravity, whereas the sides of the model are assumed to be adiabatic. Due to axial symmetry, only one half of the model is taken into account in the simulations. The temperature is normalized with regard to $T_0 = 40$ °C. The thermo-physical properties of brine can be assigned as follows : $\kappa = 0.51$ (W/m/K) ; $C_{p\lambda} = 3300$ (J/kg/K) ; and $\beta = 45 \times 10^{-5}$ (1/K).

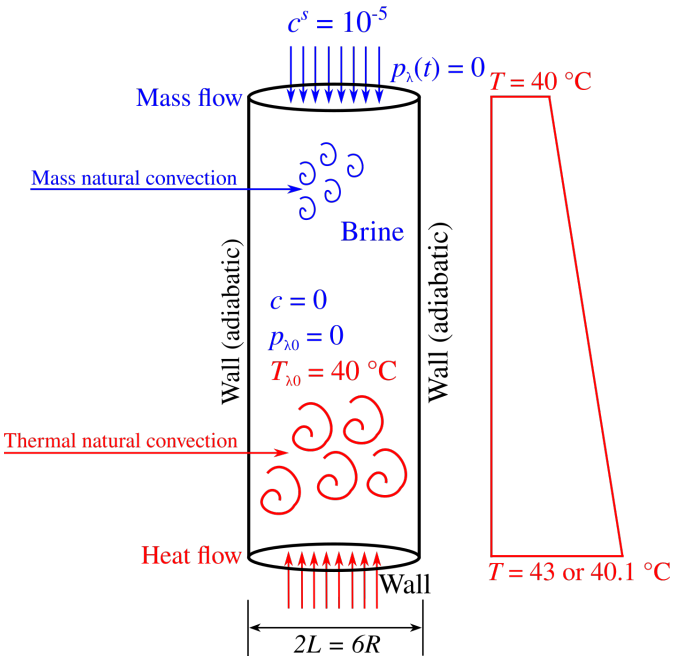

FIGURE 2.2 – Schematic representation of the model for studying thermal effects on kinetics of CO_2 dissolution in saturated brine, with tripled radius compared to laboratory cell as in section 1.1.2 maintaining the same height-to-radius ratio.

Figure 2.3 illustrates the enhanced rate of dissolution resulting from a minor temperature difference of 0.1 °C. Saturation of the model volume requires a duration of 25 days, assuming only natural convection resulting from concentration. Nevertheless, the duration is reduced to 5 days when the temperature difference is 0.1 °C, and to 2.5 days when the temperature difference is 3 °C. The relatively high thermo-physical properties of the brine are responsible for the temperature changes occurring inside the model volume. These variations result in body forces that improve the velocity field. The velocity functions as an agitation mechanism and enhances the dissolution of CO_2. This is further explained in Figure 2.4.

Figure 2.4 shows how heat begins to spread from the model bottom at early periods ($t = 4.32$ minutes), forming the velocity field. Meanwhile, the gas continues to enter the domain slowly

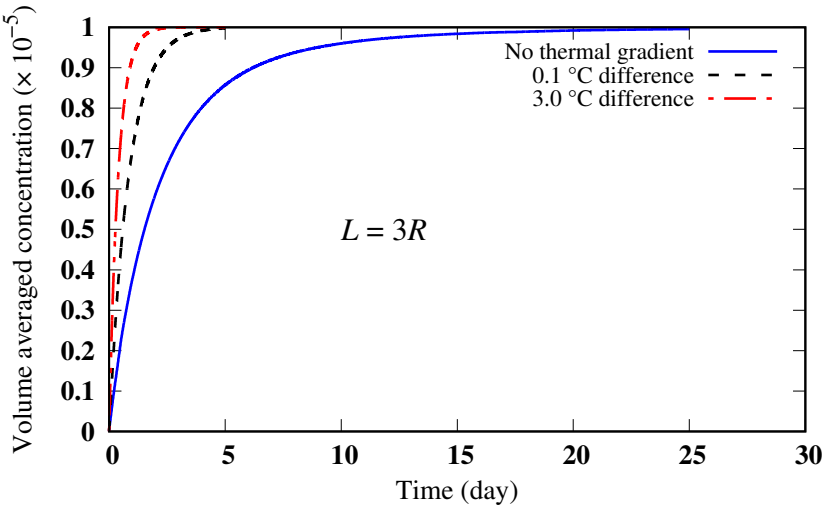

FIGURE 2.3 – Temporal variation of the volume averaged CO_2 concentration in the $L = 3R$ model : Study of the thermal effects on the dissolution process.

by Fickian diffusion.

Additionally, it can be seen in Figure 2.4 that the temperature field follows the velocity vortices, and as time passes, thermal effects become the predominant factor influencing the dissolution process. The liquid phase velocity reaches its peak at 0.25 cm/s in 12 hours (0.5 days), and the brine becomes approximately 45% saturated with CO_2. Therefore, it is evident that thermal effects have an important impact on the process of dissolution.

1.1.4 Carbon dioxide dissolution on the cavern scale

In order to study the dissolution on the salt cavern scale, we consider a cylindrical cavern with a volume of approximately 42412 m^3 inside an infinite rock salt domain (see figure 2.5). The brine inside the cavern fills about 11% of the total volume, covering a vertical distance of 1.5 meters. The cavern is supposed to be first filled with CO_2 at a pressure of 16 MPa. The surrounding rock domain is in thermal equilibrium with the gas phase of the cavern and the brine. The geothermal gradient leads to an average temperature of 44 °C across the volume of the cavern, with a temperature variation of 0.045 °C over the brine height.

To simplify the analysis, the average gas velocity over the whole volume of the cavern is overlooked. Hence, it is assumed that a uniform thermodynamic condition occurs within the cavern. This allows us to bypass the challenges associated with simulating fluid mechanics inside the cavern. Therefore, the thermodynamics of the cavern (equation 2.1) will be used only as boundary conditions for heat transfer with the rock domain, as well as for heat and mass transfer with the brine (figure 2.6).

Figure 2.6 illustrates a the discretization of the boundary value problem shown in figure 2.5. The figure shows the non-dimensional representation of the model used in the COMSOL software. A geothermal gradient of 3 °C/100 m has been established. The Dirichlet type is assumed for the far-field boundary conditions. A continuity of temperature is assumed between cavern gas and surrounding rock domain, as well as between cavern brine and surrounding rock domain.

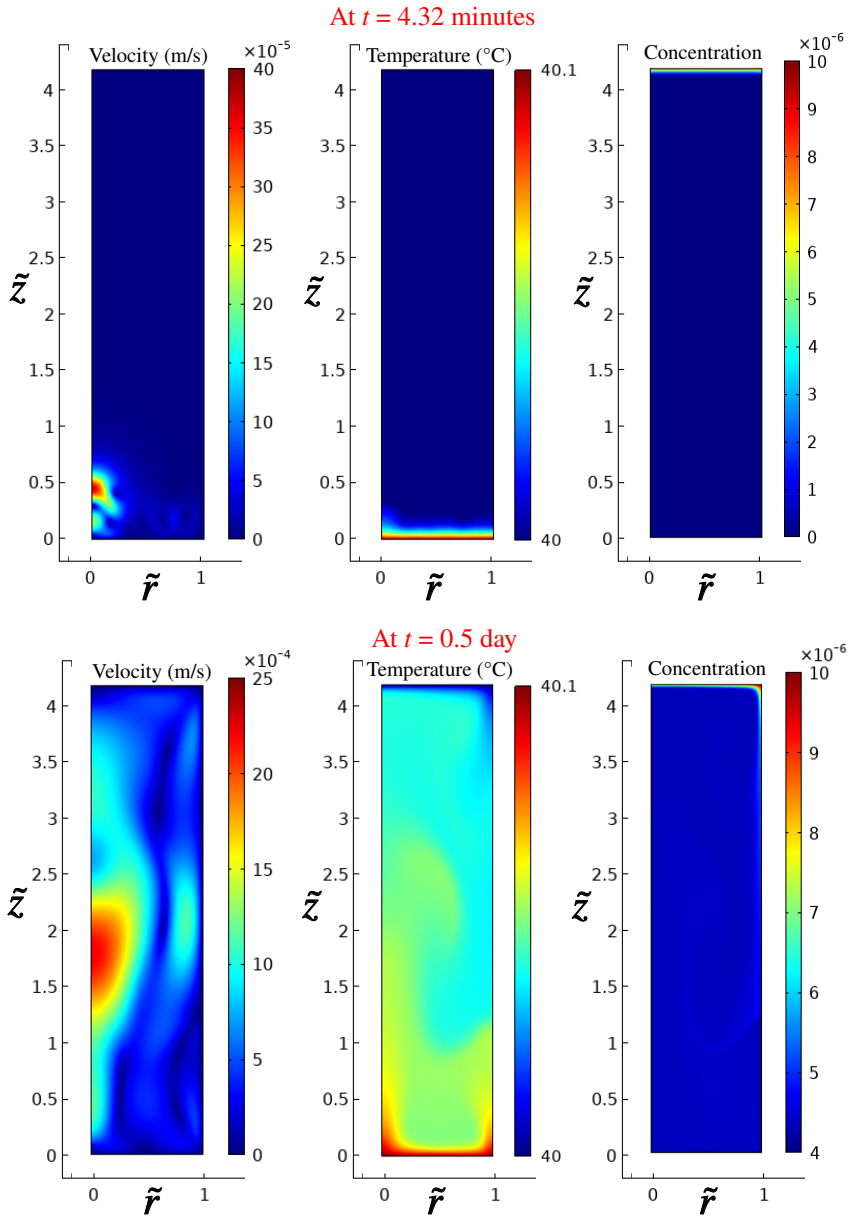

FIGURE 2.4 – Temporal evolution of CO_2 concentration, temperature, and velocity profiles at two different times for the 0.1 °C temperature difference.

A heat transfer coefficient of $h_{\gamma\lambda} = 12$ (W/m^2/K) is used to consider the thermal variations between the gas and the brine [Bourne-Webb, 2016]. Pressure continuity is maintained at all times between the two phases on the surface $\Sigma_{\gamma\lambda}$. Thus, we have $p_0 = \tilde{p}_0 = 0$ across the brine domain.

The characteristic length is defined as the height of the brine, which is equivalent to $L = 1.5$ m. For an average cycle pressure of $\langle p_\gamma \rangle = 14$ MPa, the CO_2 concentration is normalized with respect to the saturation value $c^s = 0.0188$. In order to consider the impact of the filling phase, it is assumed that the brine initially has a CO_2 concentration of $c_0 = 0.0023$ (which is about 12% of the saturation value at the average pressure of 16 MPa an average temperature of 44 °C). During cycling, it is assumed that the Henry coefficient is a function of the changing gas pressure

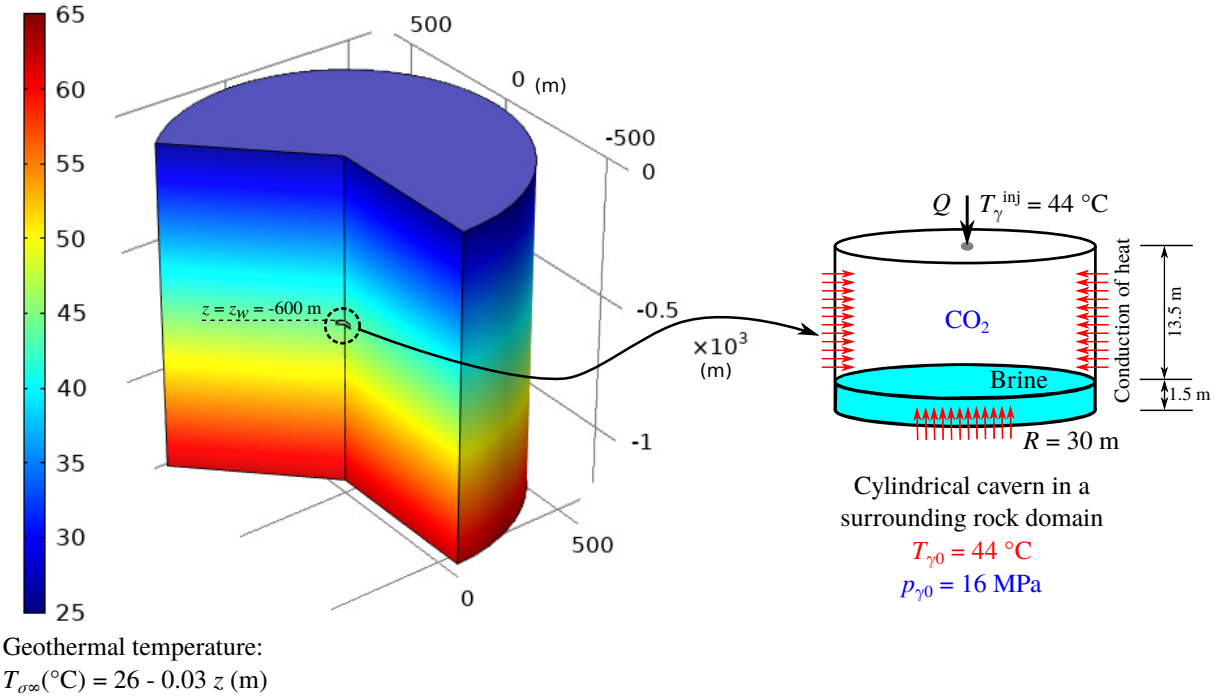

FIGURE 2.5 – Schematic representation of the boundary value problem : Illustration of a cylindrical cavern located at a depth of 600 m within rock salt domain, characterized by an average temperature of 44 °C and an initial pressure of 16 MPa.

[Chabab, 2019]. At the cavern scale, the same model parameters (β_c, D, and K) as in table 2.1 are employed. However, the scale factors of equation 1.14 are computed in consideration of the new characteristic length. The non-dimensional model parameters provided to the COMSOL are shown in Table 2.1. The temperatures of the three phases within the cavern are normalized with respect to $T_0 = 44$ °C. The thermo-physical properties of brine are employed as described in section 1.1.3.

TABLE 2.1 – The parameters of the non–dimensional model on the cavern scale.

L (m) (Brine height)	$\tilde{R}$	$\tilde{c}_0$	β_c	$\tilde{H} = f(\tilde{p}_\gamma)$	$\tilde{K}$	$\tilde{h}_{\gamma\lambda}$
1.5	20	0.12	0.212	Evolving [Chabab, 2019]	5815.38	35.29

$D = 2 \times 10^{-9}$ m^2/s, $\rho_{\lambda 0} = 1158$ kg/m^3, and $\mu_\lambda = 3.6 \times 10^{-3}$ Pa s

The CO_2 saturation concentration is $c^s = 0.0188$

$\tilde{K} = K\,(L/D)$, and $\tilde{h}_{\gamma\lambda} = h_{\gamma\lambda}(L/\Lambda_\lambda)$

Figure 2.7 shows the operation cycle program for this study. A withdrawal phase is initially identified, in which the relative mass changes $(\mathcal{M}_\gamma/\mathcal{M}_{\gamma 0} - 1) \times 100\%$ are reduced to -2.5%. Cycling begins when four cycles have been completed. The cycling program illustrates a weekly usage of the cavern, with variations occurring over a 28-day period. Although only the first four cycles are shown, this program may be performed for an extended duration.

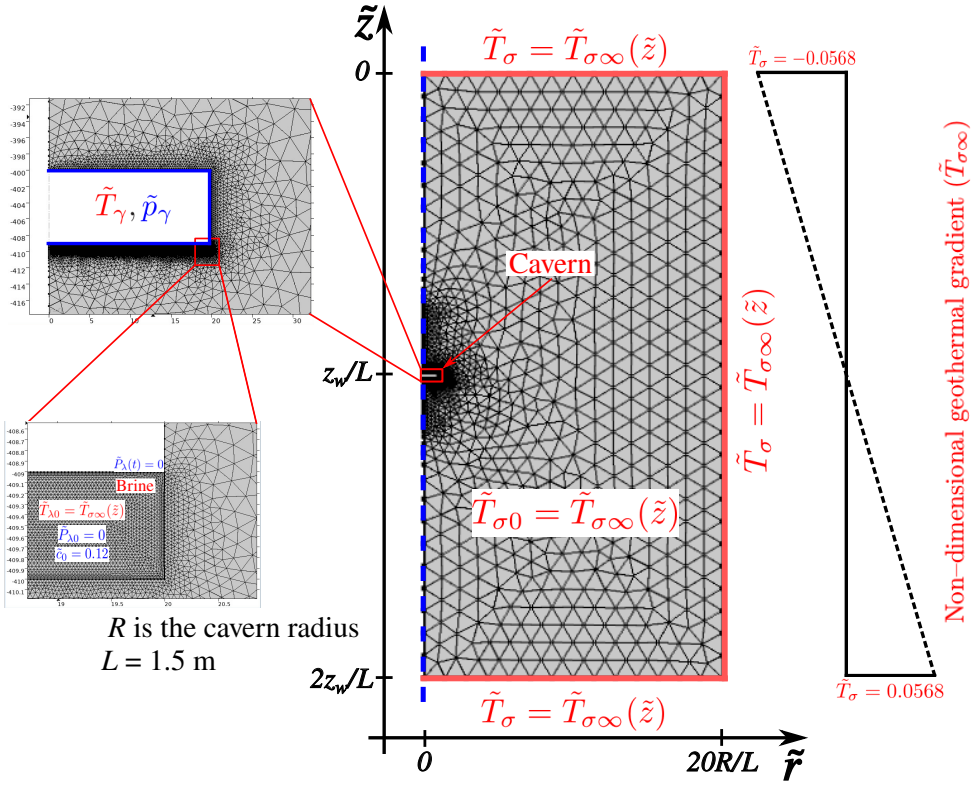

FIGURE 2.6 – Representation of the 2–D axisymmetrical discretization of the boundary value problem as illustrated in figure 2.5. A rock volume with $\tilde{r} = 20R/L$ is selected around the cavern to prevent the influence of far–field boundaries. The modeling does not take into account the gas domain, and only the brine domain is discretized. The thermodynamic properties of the cavern are applied as boundary conditions for the heat transfer with the rock domain as well as for the mass transfer with the brine. The mesh comprises 144665 elements, including 9183 quadrilateral boundary elements.

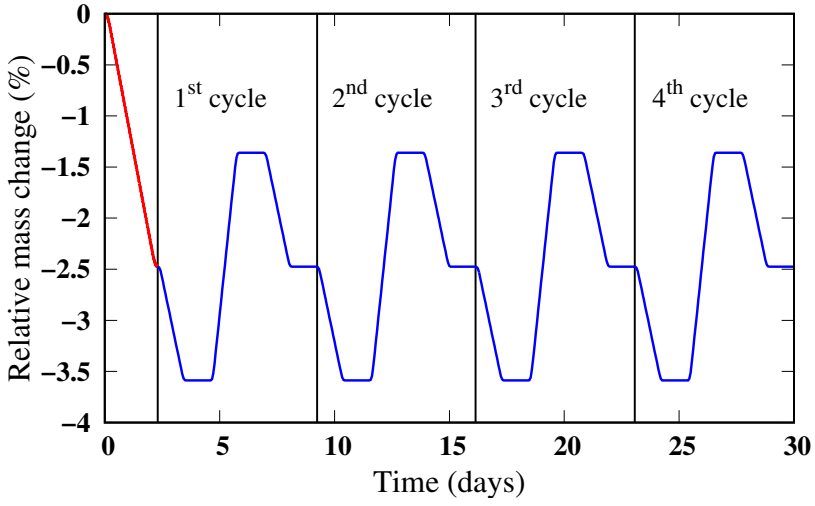

FIGURE 2.7 – The cycling program proposed for this study : Weekly operation of the cavern across approximately 28 days with four cycles. This cycling results in moderate mass changes, maintaining the cycled CO_2 consistently in its supercritical state.

1.1.5 Results and discussion

The presented non-dimensional mathematical model can be used to develop sophisticated coding. In the current investigation, the COMSOL Multiphysics software is used, leveraging its Computational Fluid Dynamics (CFD) module for resolving the Navier–Stokes and heat equations within the brine domain. The transport of species module is employed to determine the CO_2 concentration levels in the brine. The cavern thermodynamics, which serves as the boundary condition at the interface between the gas and liquid phases, is solved using the boundary Ordinary Differential Equations module. The module for heat transfer in solids is used to address the problem of heat transfer in the rock domain. Using this developed model, we will present two cases in this section to illustrate the outcomes of CO_2 dissolution on the cavern scale. In the first case, the dissolution kinetics is disregarded. Therefore, the saturation concentration of CO_2, denoted as c^s, is determined based on the pressure (p_γ) and temperature (T_γ). In this particular case, only the thermodynamics of the cavern are addressed, taking into account the heat transfer between the brine and rock domains. In the second case, the entire problem is resolved, where the thermodynamics of the cavern are coupled with the process of gas dissolution in the brine domain. This facilitates the comparison of simulations for both scenarios, providing insights into the significance of incorporating dissolution kinetics in the calculations of dissolved gas mass.

Case 1

In the first case, the cycling program depicted in Figure 2.7 will be repeated for a duration of two years. The calculation of the saturation concentration is subsequently carried out, which has been well documented in the existing literature. In our work, the saturation concentration of CO_2 in brine is depicted in Figure 2.8, illustrating its dependence on temperature and pressure within the studied range [Chabab, 2019].

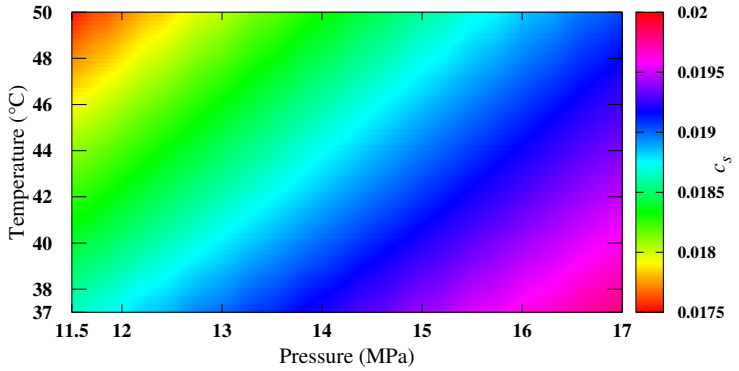

FIGURE 2.8 – The CO_2 saturation concentration in brine as a function of pressure and temperature [Chabab, 2019]. The range of c^s is observed to be relatively limited, given the scope of temperature and pressure examined in this study.

The temporal evolution of temperature and pressure within the cavern as a function of

cycling over a period of two years is depicted in Figures 2.9a and 2.9b. Cavern thermodynamics will be used as a post-treatment approach to determine the saturation concentration of CO_2 in brine, taking into account the variations of relative mass (see Figure 2.9c).

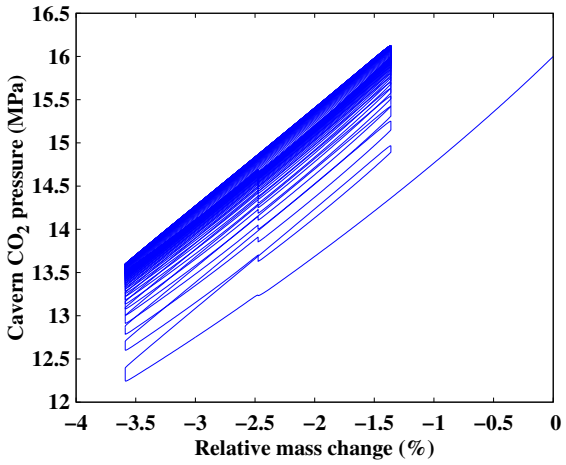

(a) Cavern CO_2 pressure

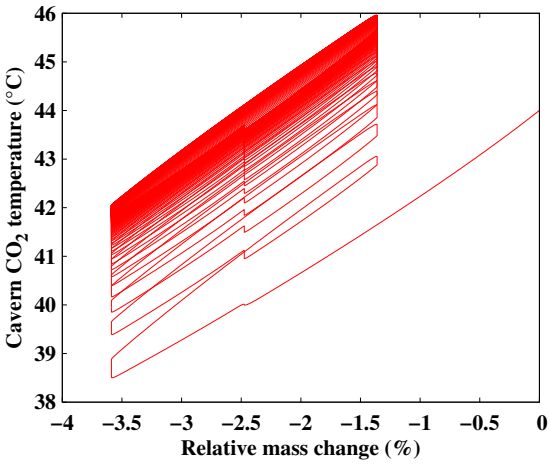

(b) Cavern CO_2 temperature

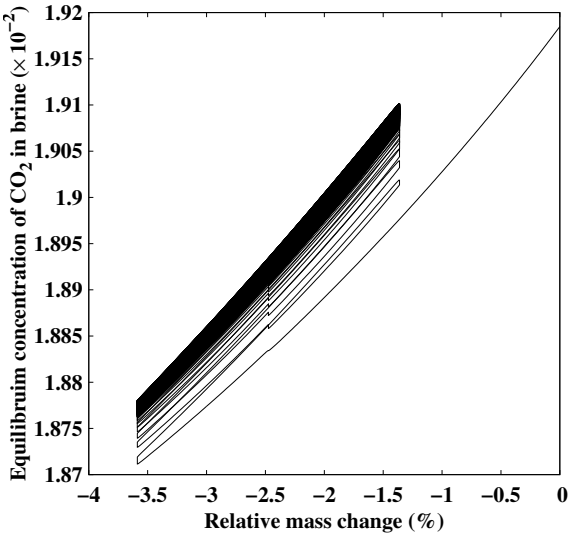

(c) Equilibrium concentration of CO_2 in brine

FIGURE 2.9 – The pressure and the temperature of CO_2 as a function of the relative mass variations over two years. A post-treatment approach using cavern thermodynamics is employed to determine the CO_2 equilibrium concentration in the brine.

The impact of heat exchange between gas and rock domains on the cavern temperature is evident in Figure 2.9b. As a result, the cavern pressure increases during cycling, which is depicted in figure 2.9a. It is important to note that an adiabatic system will exhibit superimposed pressure cycles due to the conservation of cycled mass following the first withdrawal phase (represented by the red portion in figure 2.7). The saturation concentration of CO_2 in the brine shows slight variations ($c^s \in [0.0187, 0.0192]$) within the temperature and pressure ranges investigated in this study (see figure 2.9c). The dissolved CO_2 mass can be determined from this saturation

concentration. The mass of the dissolved CO_2 ($\mathcal{M}_{\gamma\lambda}$) is measured given the brine volume (ϑ_λ) and the average density ($\rho_\lambda = 1158$ kg/m^3). In this study, the observed variations in CO_2 saturation concentration indicate that the maximum dissolved mass is estimated to be in the range of $\mathcal{M}_{\gamma\lambda} \in [91.8, 94.3]$ tons. The cavern initially contains 29283.8 tons of CO_2 stored mass. As a result, the mass lost during the dissolution process is about 0.32% of the initial stored mass.

Case 2

The second case involves the investigation and quantification of dissolution kinetics. This is accomplished by coupling the gas dissolution in the brine domain with the cavern thermodynamics. As a result, the Navier-Stockes equation in the brine domain must be considered, as well as the convection resulting from mass transfer and temperature variations. The computational time needed for such simulations is extensive. In the case of the 6.5-month cycling period addressed in this study, the simulations need 3.5 months of calculation time.

The cavern thermodynamics and brine CO_2 volume averaged concentration as a function of cycling are shown in Figure 2.10. Figure 2.10c illustrates the linear increase in brine CO_2 concentration caused by cycling. Additionally, the kinetics of dissolution are illustrated in this figure, where the concentration rises from its initial value to nearly 37% of the saturation value within 6.5 months.

Figure 2.11b illustrates the average CO_2 concentration of brine across its volume and surface. Due to the relatively short duration of the simulation (6.5 months), the majority of concentration variations occur in close proximity to the surface. Hence, the two results provide almost identical values. Nevertheless, the surface-averaged concentration clearly demonstrates the impact of cycling. This impact is not visible in the volume-averaged concentration because cycling occurs at a very quick rate compared to the characteristic time of the dissolution problem.

As depicted in Figure 2.11a, the average temperature of the brine volume is influenced by the cycling process. The initial phase of withdrawal results in a reduced temperature of the brine, which is followed by a subsequent increase in temperature that closely matches the temperature pattern of the cavern, as seen in Figure 2.10b. It is expected that these thermal variations will have an impact on the density of the brine, thus significantly influencing the dissolution process through natural convection. A little irregularity seen at $t \approx 4$ months is caused by the interruption and resuming of the simulation. The simulation software added this perturbation while trying to restore the numerical solution.

The calculation of the dissolved mass of CO_2 over time is determined by using the last equation in the system 1.25. Over the course of 6.5 months of cycling, a total of 22.11 tons of CO_2 are dissolved, constituting 0.076% of the initial stored mass.

Figure 2.12 displays the velocity contours, as well as the changes in concentration, temperature, and pressure fields during the cycling phase. The velocity field generated by convection, including both mass and thermal convection, typically has magnitudes of about 1 cm/s. The temperature, pressure, and concentration show patterns that align with the evolution of the velocity field. Pressure fluctuations caused by dissolution or thermal effects are limited to a

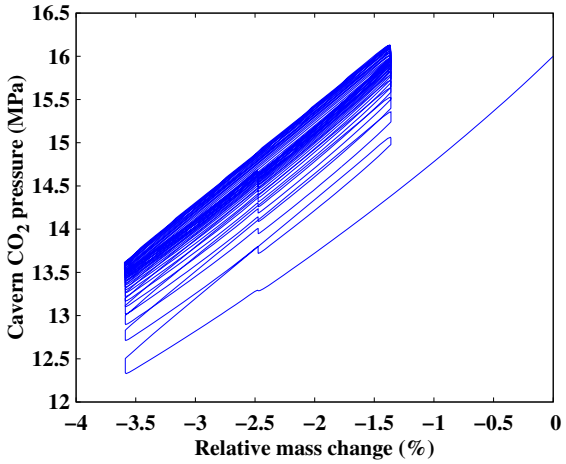

(a) Cavern CO_2 pressure

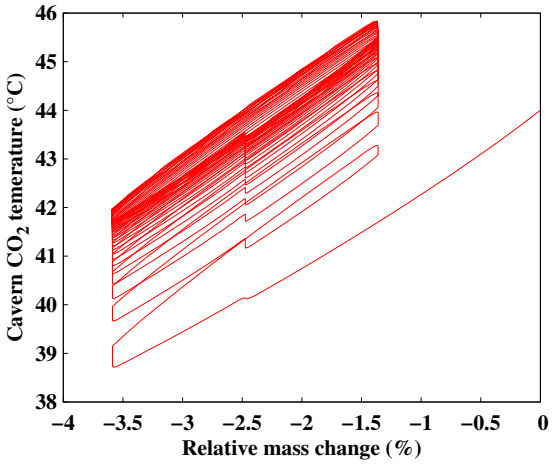

(b) Cavern CO_2 temperature

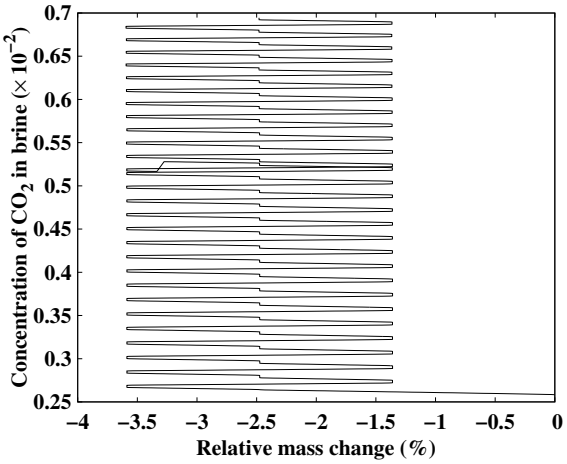

(c) Equilibrium concentration of CO_2 in brine

FIGURE 2.10 – The pressure and the temperature of CO_2 as a function of the relative mass variations over 6.5 months. The CO_2 concentration in the brine shows a linear increase, reflecting the dissolution kinetics.

maximum of 1 Pa.

1.1.6 Conclusion

Geothermal gradients have an impact on the storage of gas in underground salt caverns and the associated residual brine. The temperature variations cause thermal convection, which significantly impact the dissolution kinetics of the gases stored. The impact of these convective effects is increased throughout the gas cycling. Due to the significant thermal expansivity of brine, even small changes in temperature may cause significant changes in density. This highlights the need of including thermal convection in models of gas dissolution in underground storage scenarios.

This study differs from others in the literature because it elucidates and quantifies the impact of mass transfer and thermal convection on the gas–liquid dissolution. In fact, the simulation

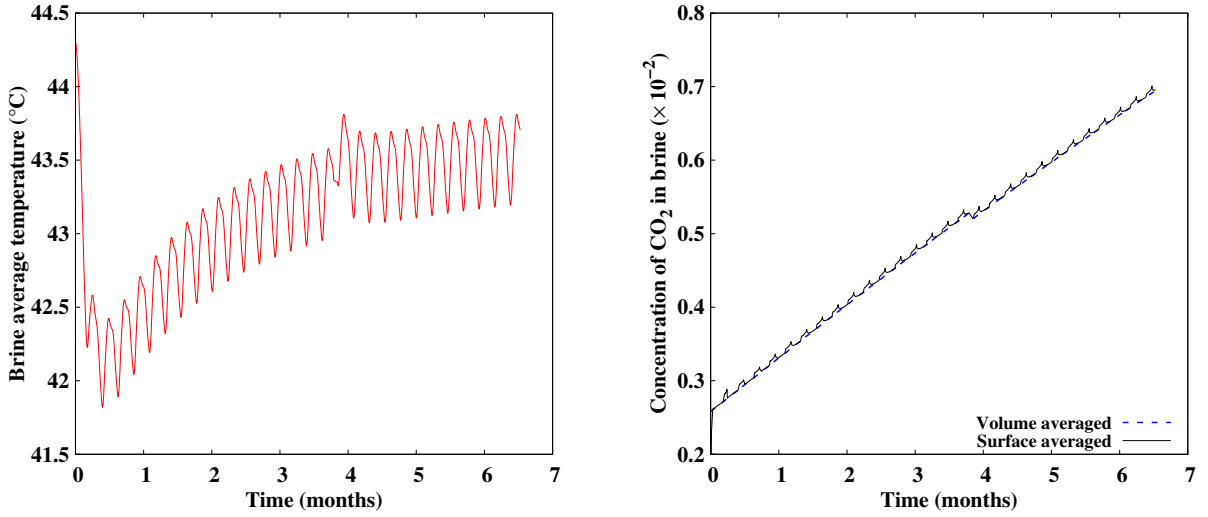

(a) Brine average temperature over time

(b) Average CO_2 concentration in brine over time

FIGURE 2.11 – The variation of the brine average temperature and CO_2 concentration (calculated across its surface and volume) during cycling.

findings suggest that the final amount of dissolved mass is about 0.32% of the initial stored quantity. The accurate measurement of this proportion over time is crucial in the context of cycling, especially when taking into account additional loss processes such gas penetration into the surrounding rock domain.

In the following section, we will study the hydrogen dissolution in brine during a tightness test in EZ53 cavern.

1.2 Dissolution of the hydrogen in brine : Application to tightness test in EZ53 cavern

The tightness test for salt caverns, especially for hydrogen storage, is essential to ensure their integrity and safety for operational use. Typically, this test is conducted using nitrogen. However, due to the smaller molecular size of hydrogen, it may exhibit higher leakage rates compared to the other commonly stored gases (CH_4,CO_2) in such caverns. Therefore, we want to study the feasibility of the tightness test using hydrogen instead of nitrogen in order to ensure a comprehensive interpretation of the test. This requires considering all involved phenomena, including the dissolution of hydrogen in brine. Therefore, we propose to examine this dissolution using the EZ53 cavern in order to quantify the mass loss of hydrogen in the brine during the tightness test.

The analysis of solubility data for hydrogen in brine, as reported in the literature [Chabab, 2020], reveals a notable finding : the total mass of hydrogen dissolved in brine at equilibrium surpasses the mass of hydrogen used during the test. This observation required the study of the dissolution kinetics. Therefore, using our calibrated and experimentally validated model (refer to Section 2.1.3.2), we will quantify the contribution of the dissolution process to the tightness test for the EZ53 cavern.

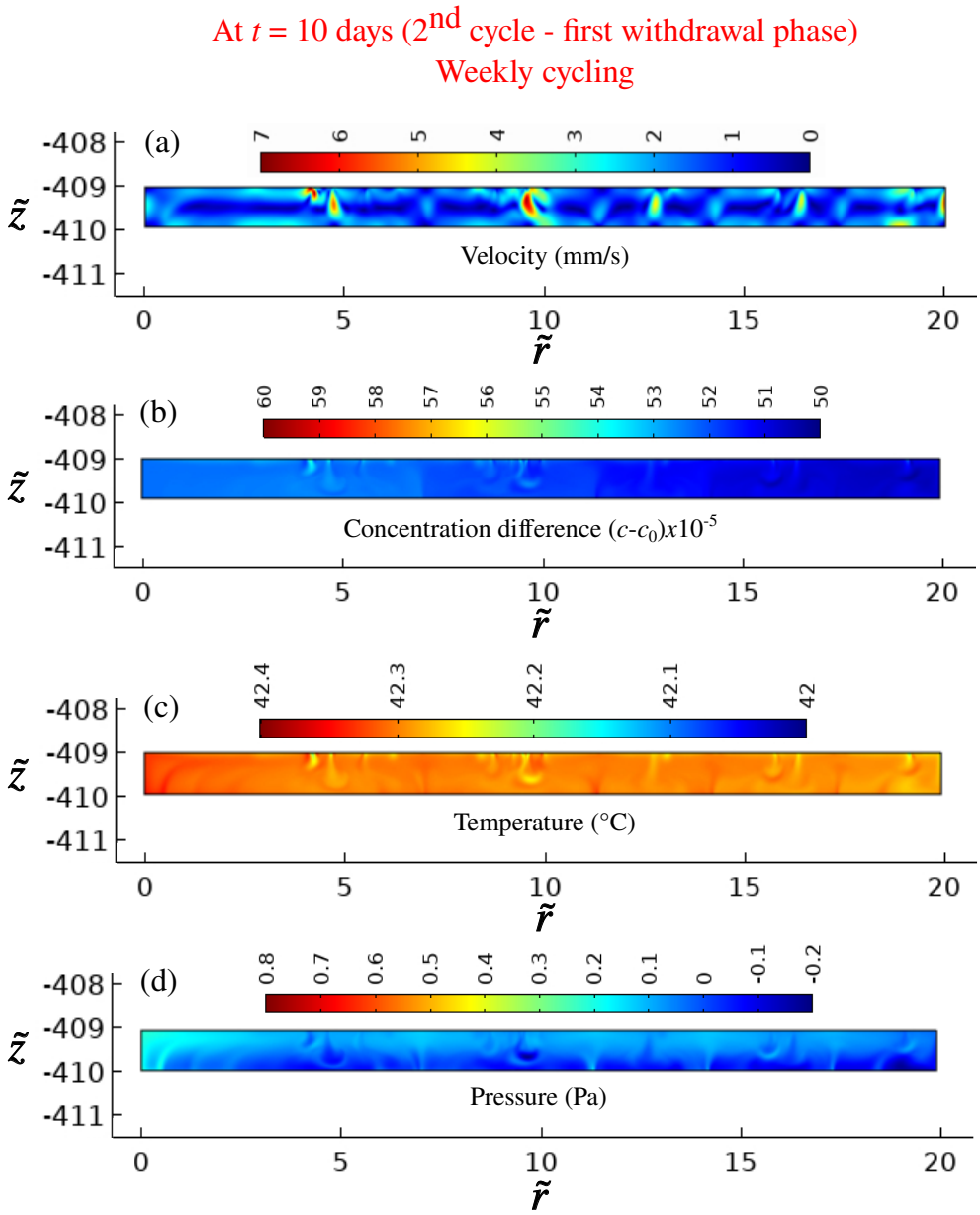

FIGURE 2.12 – The profiles of the velocity (a), the concentration difference $(c - c_0)$ (b), the temperature (c), and the pressure (d) after 10 days of weekly cycling.

In fact, we will begin with the aspects of tightness testing in salt caverns, followed by quantifying the dissolution of hydrogen in brine at thermodynamic equilibrium. Finally, we will measure the hydrogen mass loss during the test, considering the dissolution kinetics.

1.2.1 Aspects of tightness testing in salt caverns

The salt caverns provide stable and secure environments for underground storage. However, the presence of leaks may compromise the integrity of these caverns [Wei, 2023]. This leads to potential safety risks, structural damage to the caverns, and the loss of stored fluids, especially hydrogen, because of its small molecular size. In order to prevent these issues and detect all the

existing leaks, it is important to perform tightness tests. These tests are important to ensure the safety and efficiency of the storage of different fluids. The Mechanical Integrity Test (MIT) is the most widely used form of tightness testing [Berest, 2001].

In fact, there are two types of MIT illustrated in Figure 2.13 : the Nitrogen Leak Test (NLT) and the Fuel-Oil Leak Test (FLT).

(a) In this test, a nitrogen column is inserted into the annular space while the central space is filled with brine. The location of the interface between brine and nitrogen is determined by employing a logging tool. In fact, the movement of this interface indicates a potential nitrogen leakage[Albers, 1985 ; Sagi, 2016].

(b) This test consists of placing fuel oil into the annular space. It involves measuring the evolution of fuel-oil and brine pressures at the upper part of the well using pressure gauges, as shown in Figure 2.13. In fact, a pressure decline indicates the presence of leakage in the system [Berest, 2001].

Although the Nitrogen Leak Test is a commonly used method for accurately assessing the tightness of different fluids stored in salt caverns [Bérest, 2021], its reliability for hydrogen storage is still uncertain. This uncertainty arises from the minuscule size of hydrogen molecules, which are more susceptible to leakage during storage. Therefore, this study suggests using hydrogen instead of nitrogen for the tightness tests in order to evaluate its effect on leak detection. The scope of this investigation will be confined to assessing the mass loss of hydrogen in brine through the dissolution process using the EZ53 cavern as the case study. In the following section, we will represent the geometry and characteristics of this cavern.

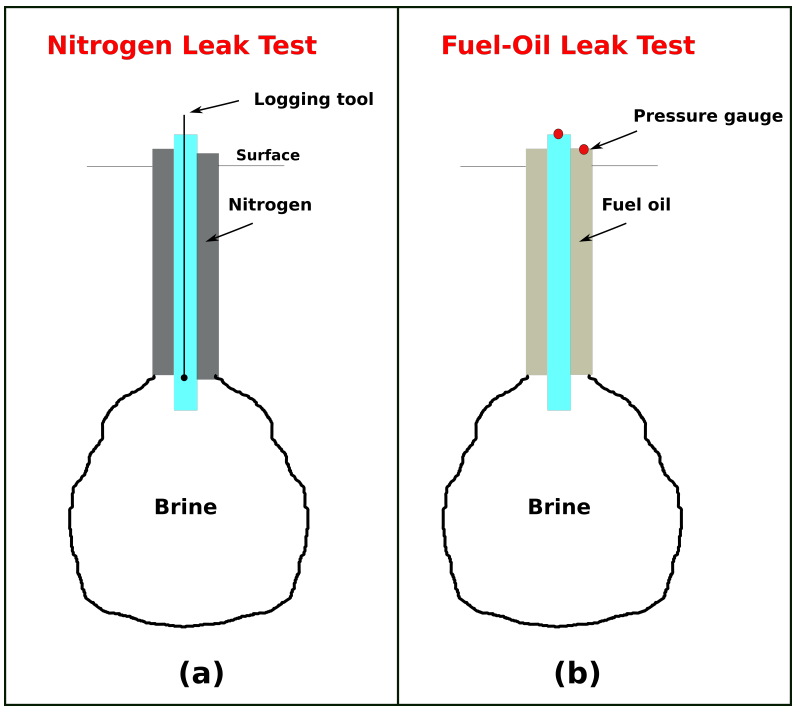

FIGURE 2.13 – Schematic representation of Mechanical Integrity Tests : (a) Nitrogen Leak Test, (b) Fuel-Oil Leak Test.

1.2.2 Geometry and characteristics of the EZ53 cavern

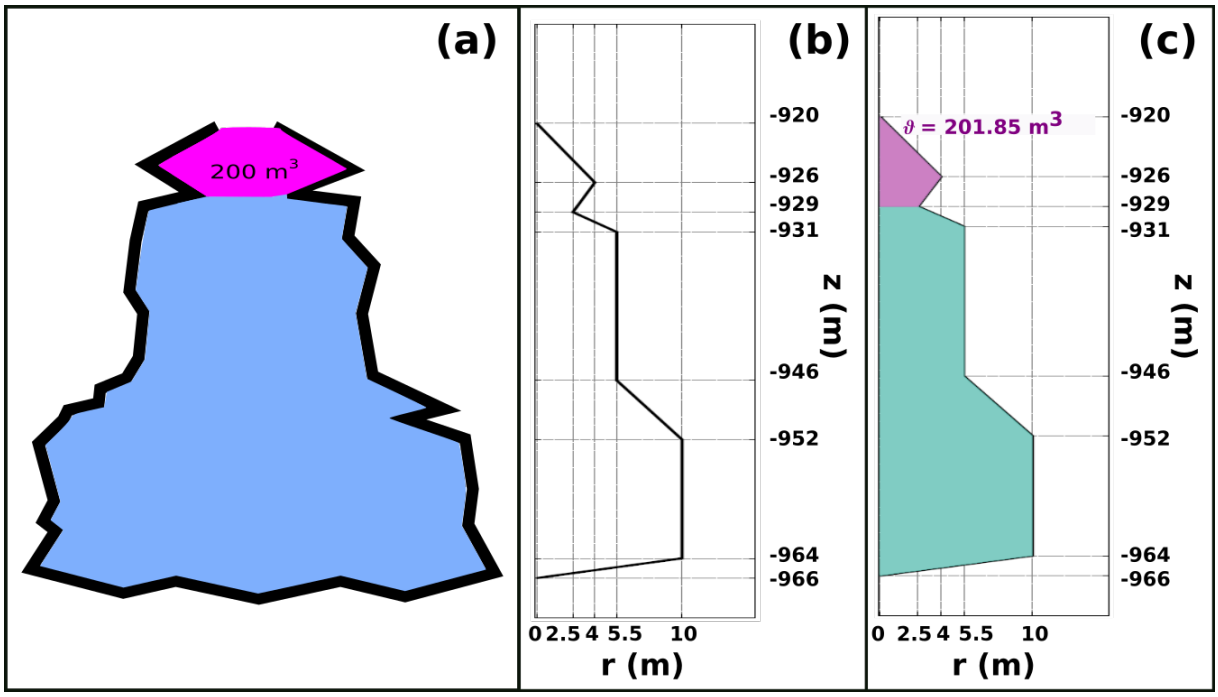

FIGURE 2.14 – (a) The geometry of the EZ53 cavern, (b) and (c) the simplified model of the EZ53 cavern geometry.

To study the hydrogen dissolution in the EZ53 cavern (Figure 2.14), the following features of the cavern are retained :

— The cavern was formed in 1982 from the Oligocene bedded salt layer in France. It was early abandoned in its development due to changes in the gas market, leaving it unused for storage but available for testing [Bérest, 2021] ;

— The volume of the cavern is around 8000 m^3, with 7400 m^3 detectable via sonar. The volume of the upper part is about 200 m^3 (see the purple volume in Figure 2.14) ;

— The cavern has an axisymmetric shape with a depth of 966 m ;

— The cavern has a narrow upper section (2 to 3 m thick) at a depth of 930 m, resulting from the presence of insoluble materials.

The geometry shown in Figure 2.14 (a) was determined based on several sonar examinations conducted on the EZ53 cavern since its creation. In order to facilitate the modeling of this cavern with the indicated geometry, Figures 2.14 (b) and (c) illustrate our simplified model of this geometry, which is designed to study the tightness test in the EZ53 cavern.

1.2.3 The dissolution of the hydrogen in brine during the tightness test

In this section, we aim to analyze the dissolution process of H_2 in brine during the tightness test. Thus, we begin with an examination of this dissolution under conditions of thermodynamic equilibrium. After that, we will add the kinetics of dissolution into the model.

1.2.4 Dissolution of the hydrogen in brine at thermodynamic equilibrium

Figure 2.15 displays the calculated saturation mass fraction of the dissolved H_2 ($c^s_{H_2}$) in saturated brine under varying pressure and temperature conditions. Using the equation 1.27, these calculated values were derived from the molar fraction data provided by the r-PR-CPA model [Chabab, 2020].

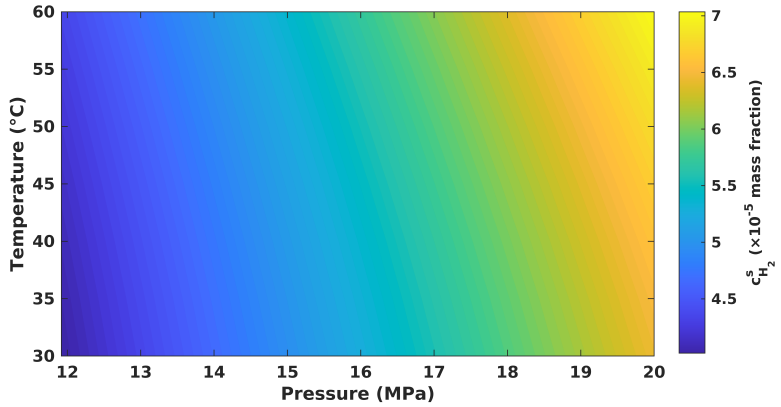

FIGURE 2.15 – The calculated saturation concentration of H_2 in saturated brine derived from [Chabab, 2020].

For a saturated brine solution, the tightness test will be conducted at a pressure of 16.5 MPa and a temperature of 50 °C, where the molar fraction is 6.22 × 10^{-4}, and the mass fraction $c^s_{H_2}$ is 5.71 × 10^{-5} (refer to Figure 2.15). Given an annular section of 5.7 L/m and a maximum depth of 920 m for this tightness test, the available volume for the hydrogen is calculated to be 5.244 m^3. At these specific temperature and pressure conditions, the density of H_2 is 11.3 kg/m^3, and the required hydrogen mass for the test is almost equal to $\mathcal{M}_{\gamma 0} = 59.25$ kg. For the EZ53 cavern with a volume of 7400 m^3 and a saturated brine density of 1158 kg/m^3, the total mass is approximately $\mathcal{M}_\lambda = 8570$ tons.

Based on the equation 2.19, the maximum dissolved hydrogen mass in this brine would be about $\mathcal{M}^s_\gamma = 489.52$ kg, a value that is higher than the used mass during the tightness test ($\mathcal{M}_{\gamma 0}$).

$$\mathcal{M}^s_\gamma = \frac{c^s_{H_2}}{1 - c^s_{H_2}} \mathcal{M}_\lambda \tag{2.19}$$

This observation indicates the necessity for a more comprehensive analysis of dissolution, particularly in terms of kinetics during the tightness test, in order to understand the impact of the dissolution process on this test.

1.2.5 Dissolution kinetics of the hydrogen in EZ53 cavern

Our experimentally validated model is used to study the dissolution kinetics during the tightness test using the EZ53 cavern. This part contains the modeling assumptions and the numerical findings.

1.2.5.1 Modeling assumptions

The hydrogen is governed by the real gas law and it is presented as boundary condition at the interface with the brine. The initial pressure of the hydrogen is 16.5 MPa. Moreover, the cavern is filled with saturated brine, considering an average temperature of 50 °C. Figure 2.16 depicts the 2D axisymmetric model of the EZ53 cavern and its corresponding mesh. This mesh is refined in the upper part of the cavern, where the boundary condition separating the gas and brine was established. It comprises 73920 elements, with 2179 being quadrilateral boundary elements. In this study, we used the same parameters determined experimentally for the mass transfer coefficient K and the diffusion coefficient of hydrogen in brine D presented in table 1.9.

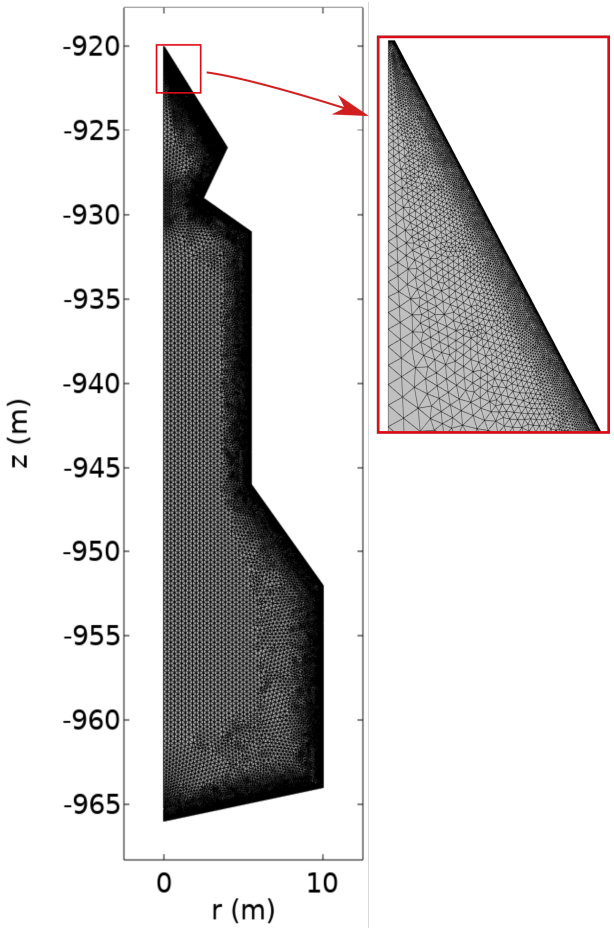

FIGURE 2.16 – The model mesh and detailed view of the upper section.

1.2.5.2 Simulations results for the tightness test

Figure 2.17 displays the ratio of the dissolved mass of the hydrogen in brine to the hydrogen present in the gaseous phase : $\xi = \mathcal{M}_{\gamma}^{\text{diss}}/\mathcal{M}_{\gamma 0} \times 100$. This ratio is represented over a period of 7 days in order to quantify the percentage of hydrogen mass loss. Actually, the average duration of the tightness test is approximately 3 days. During this period, the dissolved hydrogen constitutes

only 0.00475% of the hydrogen used in the test. Consequently, this mass loss is minimal and can be disregarded. This finding is in good agreement with the experimental results, which suggest that the hydrogen dissolution kinetics are very slow. Therefore, it requires extended simulation periods in order to observe a significant mass loss.

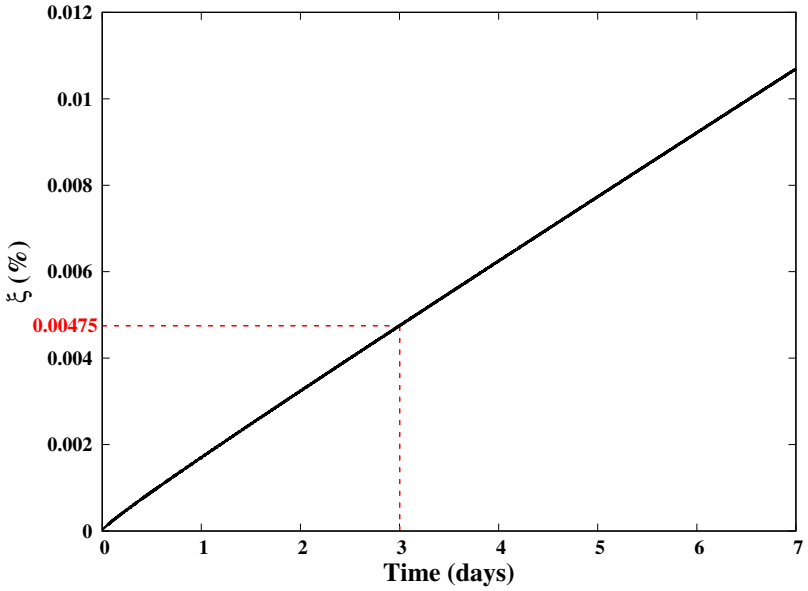

FIGURE 2.17 – Variation of the ratio ξ over time during the tightness test in the EZ53 cavern.

In Figure 2.18, we represent the 2D profile of the concentration of the dissolved hydrogen in brine at various periods : 1 day, 2 days, and 3 days. As anticipated, the depth of hydrogen dissolution within the cavern is limited, extending to approximately 0.15 meters. Moreover, given the low solubility and the gradual kinetics of hydrogen dissolution in brine, the impact of natural convection is negligible compared to that observed in the dissolution of CO_2.

To sum up, after incorporating the dissolution kinetics of hydrogen in brine to precisely determine the hydrogen mass loss during the 3 day tightness test in the EZ53 cavern, it was found that the estimated dissolved mass of hydrogen in brine during this period is minimal. As a result, the process of dissolution does not have a major impact on the initial mass of hydrogen used in this test.This leads to the conclusion that the slow dissolution kinetics of hydrogen in brine can be disregarded in this context. Therefore, conducting the tightness test with hydrogen instead of the nitrogen is feasible as there is no serious concern that the dissolution process will have a significant effect on the amount of hydrogen introduced. Nevertheless, it is essential to examine additional processes that could potentially impact this mass loss throughout the test, such as the penetration of hydrogen in the salt rock. Such an analysis will help ascertain that using hydrogen in the tightness test for hydrogen storage in salt caverns is more effective in detecting small leaks, attributed to the small size of hydrogen molecules.

In the following section, we will study another type of mass transfer process which is the humidification of gases.

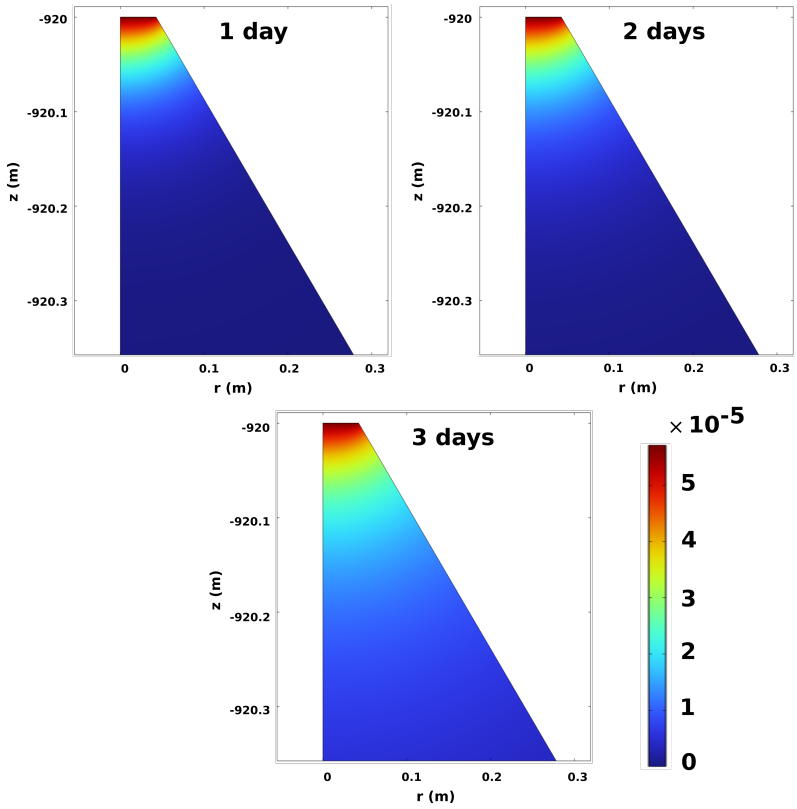

FIGURE 2.18 – Mass fraction of H_2 in salt cavern.

2 Humidity effects on stored gas behavior in salt caverns

The topic of gas storage inside salt caverns has received significant interest in the academic field of thermodynamic study. Many existing models primarily rely on the assumption of immediate thermodynamic equilibrium, which neglects the complex kinetics that govern the transfer of mass between the liquid and gaseous phases. After conducting a comprehensive investigation of the kinetics associated with the dissolution of gases into brine on the cavern scale within the previous section, it becomes necessary to investigate the amount of water present in the gas phase. Such an investigation is important, particularly given the requirement to determine the qualitative purity of the gas collected from these salt caverns before beginning the distribution process. Indeed, the presence of water vapor imposes possible obstacles. This is demonstrated by the fact that its presence can facilitate the formation of hydrates and consequent corrosion of process-related equipment. As a result, proper measurement of water content becomes essential. This chapter will focus on the analysis of the humidification process and the quantification of the water content in the gaseous phase inside the cavern.

This section will focus on measuring water content in gas-rich phases within salt caverns. Initially, we will present the importance of this study. Subsequently, the used thermodynamic model will be introduced. The section will then proceed to case studies : first, exploring the impact of humidity during helium cycling ; second, incorporating the kinetics of humidification into the model ; and finally, comparing humid helium with hydrogen.

2.1 Importance of quantifying water presence in gas-rich phase

In the realm of gas storage within salt caverns, the quantification of water content in the gas-rich phase is important. The water content in the cavern is influenced by several factors, including the unique environment of the cavern, the properties of the surrounding rock formations, and variables such as salt composition, temperature, and pressure. Furthermore, the methodologies employed in the extraction, storage, and injection of the gas directly impact its water content. In the realm of reversible underground gas and energy storage, post-withdrawal gas quality control is indispensable before the gas reaches its final users. One of the principal properties that is being evaluated is the moisture content present in the gas-rich phase.

Excessive water vapor in the gaseous phase in the salt cavern introduces a myriad of challenges, from equipment degradation to flow assurance issues. Specifically, the condensation of water vapor can lead to corrosion and complications such as ice or hydrate formation in surface facilities [Foh, 1979 ; Tarhule-Lips, 1998]. The corrosion rate, which plays a crucial role in the durability of surface installations such as compressors and pipelines, is proportionally related to water content [Kolass, 2011 ; Hua, 2015]. For instance, the CO_2, once hydrated within condensed water, evolves into carbonic acid, which is a known contributor to the corrosion process [Liu, 2021].

Furthermore, it is common for stored gases in salt caverns to exhibit saturation with water vapor. The saturation that occurs is due to the interaction between the gas and formation water present in the residual brine within salt caverns. Consequently, after the extraction process, an important step of removing water is carried out [Processors Suppliers Association, 2004]. Understanding the saturated water content under storage conditions is crucial, not only for corrosion and hydrate formation risk assessments but also for optimizing dehydration processes and ensuring that they fulfill water content standards [ISO, 2012].

In summary, the precise quantification of water presence in the gas-rich phase within salt caverns is essential. This ensures operational safety, enhances efficiency, and assists in optimizing the extraction, storage, and injection processes, thus meeting industry standards and preserving equipment longevity.

Problem of the gas hydrate formation

In the context of gas storage, especially within salt caverns, the formation of hydrates holds a distinctive significance. These solid crystal-like structures emerge when water molecules bond with gas molecules, a phenomenon further amplified under certain temperature and pressure conditions prevalent in these caverns. At its core, hydrates are formed when small molecules in vapor state, which in the context of salt caverns are primarily CO_2, hydrogen, and other gases, find themselves encased in a solid network of water molecules [Ribeiro, 2008]. This unique assembly, often described as "ice-like", is maintained in place via hydrogen bonding and Van der Waals forces, despite possessing unique characteristics compared to regular ice.

Historically, understanding hydrate formation traces back to early 20th-century research driven by the petroleum industry. The motivation was to discern the effects of water in the

operational dynamics of gas pipelines, as the inherent association between water and gases was observed to potentially lead to hydrate formations [Eslamimanesh, 2011]. Particularly in salt caverns storing these gases, the presence of water vapor, combined with specific temperature and pressure dynamics, can be conducive to hydrate formations [Liu, 2021 ; Sedaee, 2019].

When hydrate formation is left unchecked in a salt cavern environment, several repercussions can unfold. The most immediate concern is the clogging of pipelines, pumps, and other integral equipment, which is detrimental to the efficient storage and retrieval of helium and hydrogen. The presence of this obstruction not only restricts operational efficiency by decreasing the flow rate, but it can also result in equipment damage and require increased maintenance [Chatti, 2005]. Hydrates pose a significant safety risk as they have the potential to damage emergency valves and other safety mechanisms, thereby affecting the regulation of pressure and temperature in the storage caverns.

During the withdrawal of gas from these storage systems, the variations in pressure and temperature might increase the probability of hydrate development. The findings of [Hammerschmidt, 1934] in the 1930s highlighted the potential danger of gas hydrates, showing their ability to cause obstructions in transmission lines. In a couple of hours, transmission lines may be obstructed if the production, aggregation, or deposition of hydrate particles is not prevented by an effective inhibitor technology [Creek, 2011]. Such blockages can decrease pipeline cross-sectional areas, causing an increase in pressure drops and thus raising production and transportation expenses.

In light of these obstacles, proactive measures are essential. In order to prevent the development of hydrates in salt caverns, it is crucial to carefully regulate both temperature and pressure. This is accomplished by deploying heaters, refrigeration units, and other equipment to maintain optimal conditions. In addition, the use of chemicals such as methanol or glycol may be used as preventative measures to inhibit the development of hydrates [Elgibaly, 1999 ; Sun, 2001].

To sum up, the water content in gases, particularly in the context of hydrogen storage in salt caverns, requires careful attention and study. As the precursor to gas hydrate formation, understanding the implications of this water content is essential. The problems associated with gas hydrates primarily result from the initial presence of water in the gases. This makes it a major subject in the field of gas storage and processing.

2.2 Simplified solution of cavern thermodynamics

The primary objective of the present study is to investigate and quantify the water content present within the gaseous phase of underground caverns. This involves extending the HGM model, as described in the section 2.2.2, to encompass the cavern scale. This extension requires the consideration of the homogeneous thermodynamic state of the gas phase, which is assumed to consist solely of humid gas. This humid gas consists of dry gas and water (vapor and liquid).

Within the literature, there are some studies that assume that the fluid present in the cavern is incompressible and maintains a constant density [Li, 2023]. Nevertheless, considering the elevated pressure in these caverns, this assumption needs reconsideration. As a consequence, this study adopts a real gas behavior perspective, employing the GREG law [Kunz, 2007] to

articulate the fluid's state equation. The gas pressure can be written as $p = \rho T Z$, where Z stands for the compressibility factor of the gas.

In order to simplify our investigation, the current analysis primarily focuses on the thermal interactions between the fluid and rock while neglecting the mechanical behavior of the surrounding rock mass [Labaune, 2018]. The temperature distribution in the surrounding rock is governed by this heat equation :

$$\partial_t T_\sigma = a_\sigma \vec{\nabla} \cdot \left(\vec{\nabla} T_\sigma \right). \tag{2.20}$$

T_σ and a_σ are respectively representative of the rock temperature and its thermal diffusivity. In this study, it is assumed that there is a continuous temperature between the solid and fluid at the surface of the cavern.

An important property of underground caverns is their large capacity, along with their prolonged operational lifespan. Therefore, implementing a thorough computational fluid dynamics model to accurately depict the gas at every period of its existence becomes a notably time-consuming endeavor. Such numerical analyses demand considerable computational resources, largely due to the complex numerical calculations associated with a vast system of governing equations and an extensive array of elements. In order to simplify the problem, we neglect spatial variations and the velocity field inside the system. The resulting model ensures that primary variables are solely time-dependent, and notably, the time derivative remains devoid of a convective term. Such methodological decisions facilitate the simplification of the equation system governing pressure, temperature, and mass fraction of the gas (gas concentration), thereby accelerating the simulations.

In this study, we also focus on the kinetics of humidification, which is similar to the approach used to analyze the results of the helium tests done in a laboratory setting, as explained in Section 2.2.4. However, we highlighted the disparity between controlled laboratory settings and actual salt cavern scenarios. Laboratory tests involving rapid gas injection in direct contact with brine differ from typical salt cavern operations. This leads to less pronounced humidity changes in salt caverns compared to laboratory settings. Therefore, the study model was adjusted to better reflect salt cavern conditions, focusing specifically on the kinetics of humidification represented by the equation 1.48. So, the system of ordinary differential equations, represented by the pressure $p(t)$, the temperature $T(t)$, and the gas concentration $c(t)$, are defined as :

$$\begin{cases} -\alpha \dot{T} + \beta \dot{p} + \gamma_1 \dot{c} = \dfrac{\dot{\mathcal{M}}}{\mathcal{M}}; \\ \mathcal{M} C_p \dot{T} - \vartheta_c \alpha T \dot{p} + \mathcal{M} T \gamma_2 \dot{c} = Q_i C_p \left(T^{\mathrm{w}} - T \right) - \Psi_s; \\ \tau \dot{c} = c^s - c, \end{cases} \tag{2.21}$$

where $\alpha = -(1/\rho)\partial_T \rho \mid_{p,c}$ is the thermal expansion coefficient, $\beta = (1/\rho)\partial_p \rho \mid_{T,c}$ is the isothermal compressibility coefficient, $\gamma_1 = (1/\rho)\partial_c \rho \mid_{p,T}$ is the derivative of ρ considering the concentration c, $\gamma_2 = \partial_c s \mid_{p,T}$ is the derivative of the entropy considering c, $\mathcal{M}$ is the gas mass, C_p is the specific heat capacity, ϑ_c is the cavity volume, T^{w} is the well temperature, Q_i is the

inflow rate, Ψ_s is the power exchanged between gas and the surrounding rock. Moreover, we have $c^s = 1 - c^s_W$ is the concentration of the gas at saturation, which depends on the pressure and temperature, where c^s_W is the saturation concentration of water in the gas-rich phase and τ is the time constant. Additionally, the concentration c can be formulated as a function of the water concentration c_W, represented as $c = 1 - c_W$.

2.3 Applications

Our developed model will be used to study the impact of water content on the thermodynamic properties of the gas phase within a cavern under various storage scenarios. To elucidate this, we consider a spherical cavern with a volume of $\vartheta_c = 300,000\,\mathrm{m}^2$ and a radius of 67 m, carved into an infinite mass and fed by a well of length 900 m (see Figure 2.19). The surface is located at $z = 0\,\mathrm{m}$, positioning the cavern at $z = -900\,\mathrm{m}$. It is assumed that this cavern contains humid stored gas. To simplify the analysis, the rock domain surrounding the cavern is accounted for solely by its geothermal temperature, represented by $T(°\mathrm{C}) = 26 - 0.03z\,(\mathrm{m})$.

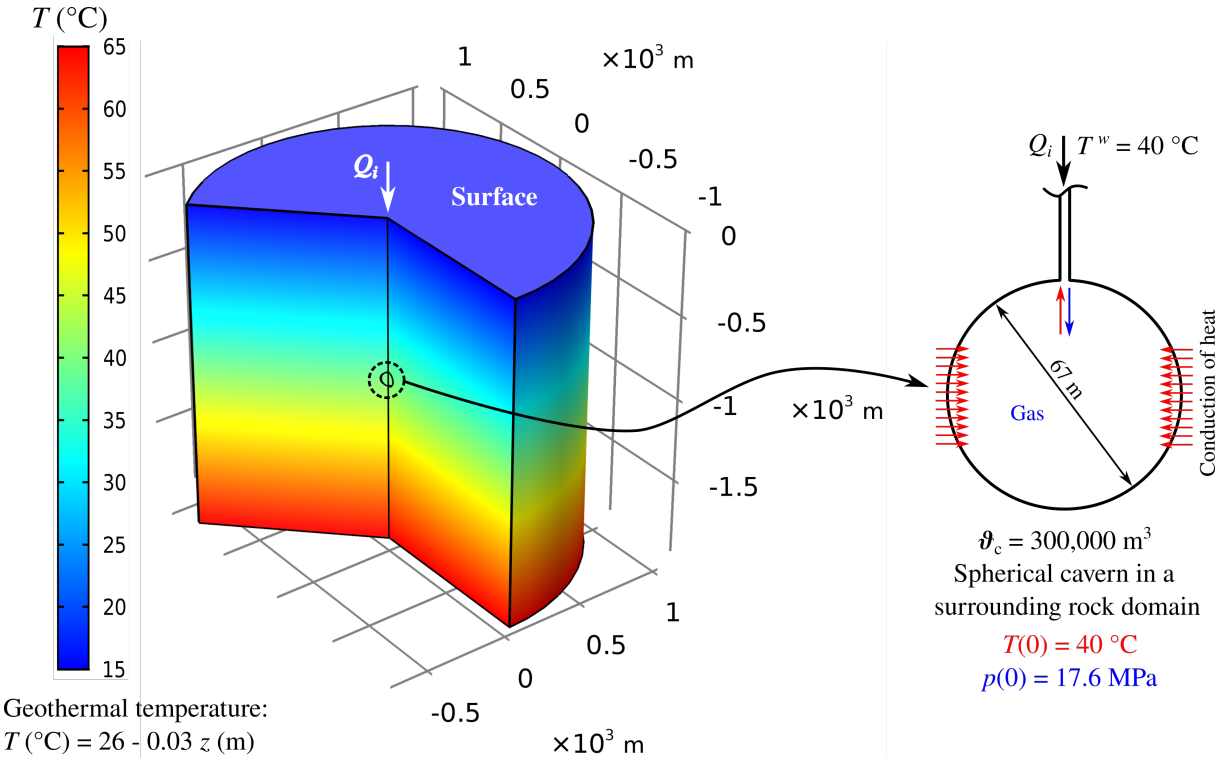

FIGURE 2.19 – 3D representation of the spherical cavern at 910 m depth, surrounded by the rock domain.

Initially (at $t = 0$), it is assumed that the cavern already contains a mass of gas under a pressure of $p = 17.6\,\mathrm{MPa}$, a temperature of $T = 40\,°\mathrm{C}$, and a gas concentration c. The cycling program used in our study, which delineates the flow rate over time, is illustrated in figure 2.20. In fact, the initial withdrawal phase is set over a period of 4 days. Following this, concerning the wellhead loading, a simple scenario is considered, comprising a total of 10 cycles, each lasting 7 days, resulting in a total of 70 days. Within these cycles, the gas undergoes an injection phase,

two withdrawal phases, and three rest phases. The injection rate is maintained at 9.7 kg/s. The withdrawal rates are calculated to preserve the gas mass in the cavern at the end of each cycle.

To model the described cavern and simulate its thermodynamic behavior, we used the COMSOL Multiphysics software. For a precise temporal resolution in our simulations, we opted for a time discretization interval of 3 seconds.

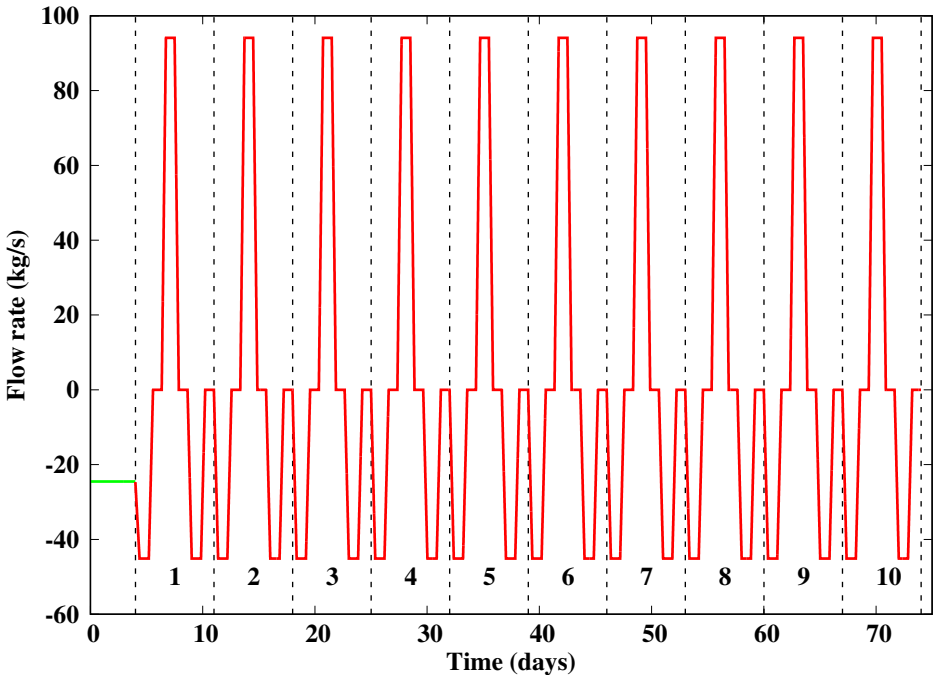

FIGURE 2.20 – Flow rate during the cycling program.

After defining the modeling approach, we will investigate various cases to examine the effect of humidity on the behavior of the stored gas in salt caverns. Initially, the study examines helium in two distinct scenarios : a highly humid gas (c = 0.9) and a almost dry gas (c = 0.99), without incorporating the kinetics of humidification. This approach involves maintaining a constant water concentration in the gas-rich phase. Subsequently, the investigation will extend to a more intricate examination, incorporating the humidification kinetics into the cycling of helium under storage conditions. Finally, the analysis will conclude with a thorough comparison of the behavior of humid helium and hydrogen during cycling.

2.3.1 Case I : Thermodynamic implications of humid helium with emphasis on temperature, pressure, and water content evolution at 1% and 10% water in the gas-rich phase

In order to better understand the behavior of stored gas, particularly helium, and to accurately quantify the various states of water (vapor and liquid) present, this first case involves examining two distinct scenarios of helium storage during cycling. The first scenario involves almost dry helium (c = 0.99), signifying a water content of 1% in the gas-rich phase. The second scenario examines highly humid helium (c = 0.9), corresponding to a water content of 10% in the gas-rich phase. The study aims to assess the impact of water quantity on gas temperature

and pressure within the cavern. Furthermore, it seeks to precisely quantify the mass of liquid water that may manifest in such conditions.

For the purpose of this specific case study, we will disregard the humidification kinetics described by the third equation in the set of equations 2.21. Instead, we will focus on two specific gas concentrations : c = 0.9 and c = 0.99, in order to analyze the impact of these two extreme scenarios on the thermodynamic behavior of the gaseous phase within the cavern.

Results and discussion

In this part, we delineate the results obtained from simulations designed to evaluate the impact of varying water content concentrations in the gas-rich phase on pressure and temperature inside the cavern. Figures 2.21 and 2.22 illustrate the evolution of pressure and temperature within the cavern during cycling. Along with the results associated with concentrations $c = 0.9$ and $c = 0.99$, these graphs also include the outcomes from the case of dry helium where the presence of water was neglected ($c = 1$). In fact, the trend observed in these plots reveals that after approximately five cycles, the pressure and temperature profiles follow the same variations.

By the end of the withdrawal phase (the black dashed line in Figures 2.21 and 2.22), the data indicates a relatively small difference between the two concentrations ($c = 0.9$ and $c = 0.99$) : specifically, a variation of 2.5 °C for temperature and 0.2 MPa for pressure. During the first cycle, we can see that the results show a discrepancy of about 4 °C and 0.45 MPa between the two humid helium cases. These differences become narrower during the injection phase. The clarity of these results is particularly evident in the temperature profiles, as illustrated in Figure 2.22. Furthermore, when we compare the dry helium and the humid helium with c =0.99, we can see that the difference in temperature can reach 1.7 °C. Therefore, even the small water content in the gas-rich phase can impact the stored helium temperature profile.

Figure 2.23 illustrates the changes in the total mass of humid helium within the gas-rich phase over time for three different gas concentrations : $c = 0.9$, $c = 0.99$, and $c = 1$ (dry helium). Upon close examination, it becomes apparent that the total mass of the humid helium with $c = 0.9$ surpasses by almost 8.3×10^5 kg that of $c = 0.99$. This elevation is due to the elevated water content, especially in its liquid state. Furthermore, the dry helium mass, indicated by a dashed line, constantly exhibits values lower than the $c = 0.99$ concentration, emphasizing their concurrent trends.

Therefore, the presence of water has a significant role in determining the overall mass of stored gas in the salt cavern. It is, thus, necessary to take into account the influence of water, considering both its quantity and state, in the assessment of the total mass in the gas-rich phase.

In the context of elucidating the behavior and composition of the gas-rich phase within the cavern, Figures 2.24 and 2.25 depict the total cavern mass and its constituents. In fact, we will present the mass of the dry helium mass, as well as the liquid and vapor water masses, for the two cases of humid gases. In Figure 2.24, the water liquid mass is observed to be approximately 8.16×10^5 kg, a markedly greater quantity when compared with the vapor water mass of almost 1.73×10^4 kg. Similarly, in the case of almost dry helium ($c = 0.99$) as shown in Figure 2.25, the liquid water mass is about 5.8×10^4 kg, with the vapor water mass being 1.7×10^4 kg, indicating

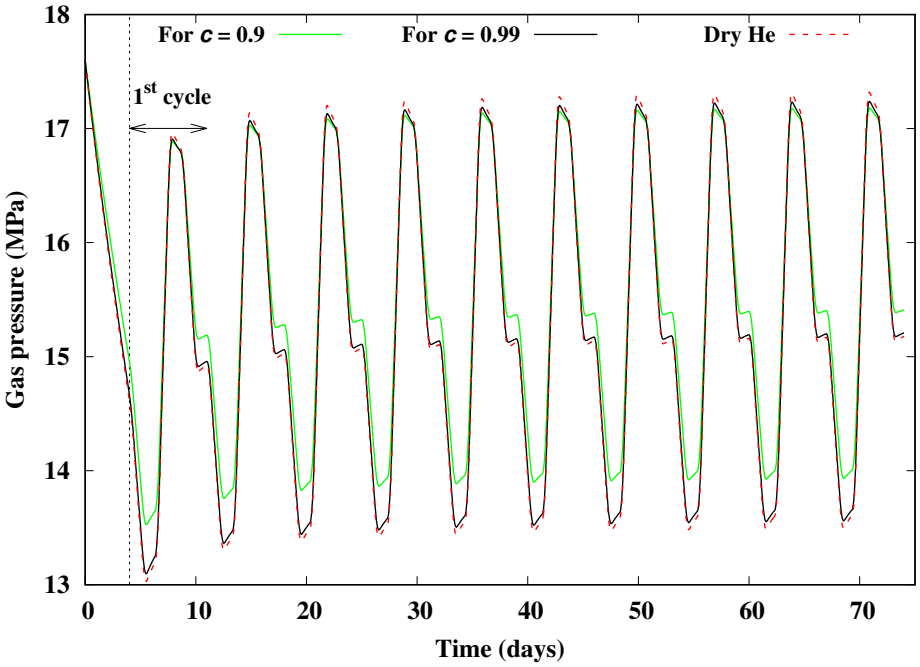

FIGURE 2.21 – Evolution of the pressure in the cavern during cycling.

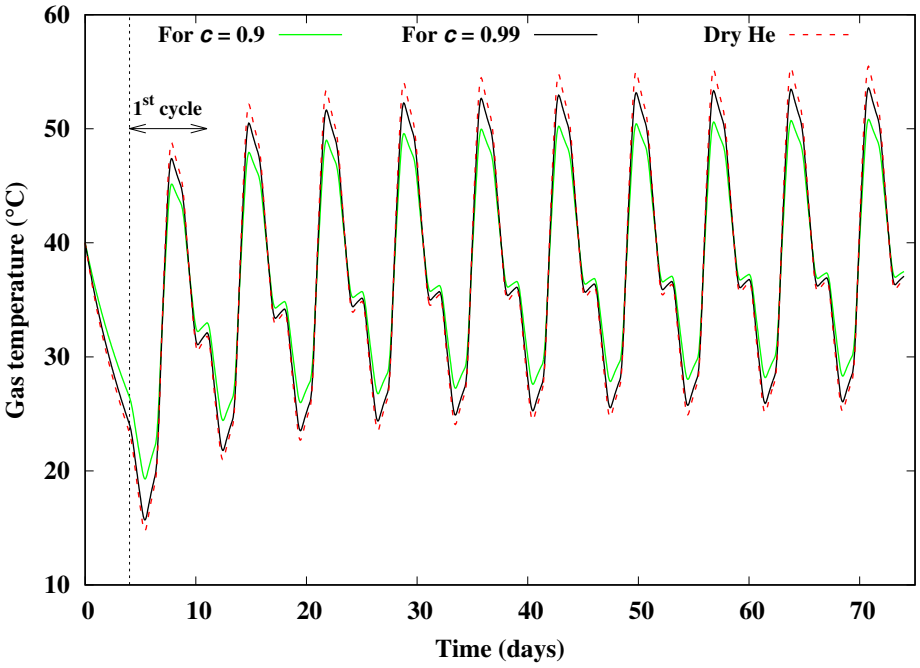

FIGURE 2.22 – Evolution of the temperature in the cavern during cycling.

that the liquid water mass is approximately 3.5 times more significant.

In fact, it is clear that the increased water content in its liquid state significantly contributes to the mass discrepancy between the two studied cases of humid helium ($c = 0.9$ and $c = 0.99$). As such, one can deduce that water in its liquid form serves as a critical component in the modulation of the mass of the stored gas. However, it is also worth noting that even though the

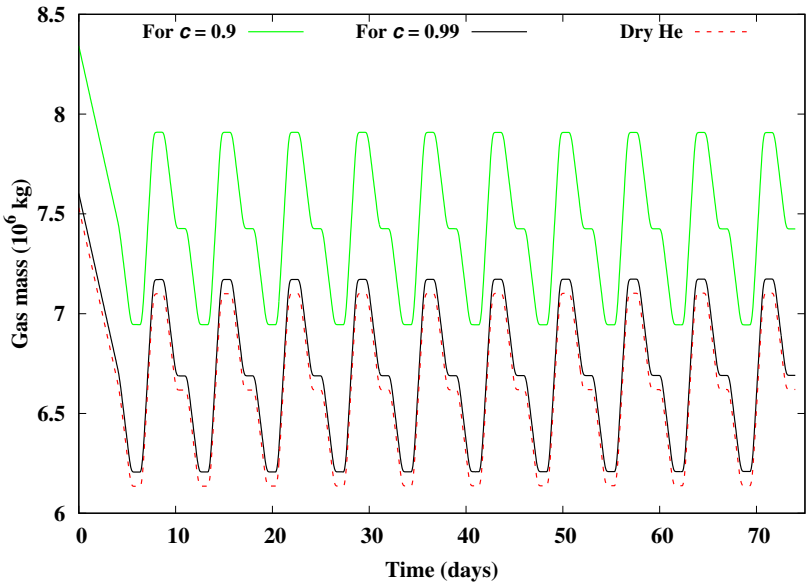

FIGURE 2.23 – Evolution of the total mass in the gas-rich phase during cycling.

liquid water contributes significantly to the mass of the humid gas, its vapor state coexists and should not be disregarded in the thermodynamic assessment of the system. This consideration becomes particularly pertinent in scenarios involving less humid gas, as the masses of vapor and liquid water in these instances become comparable.

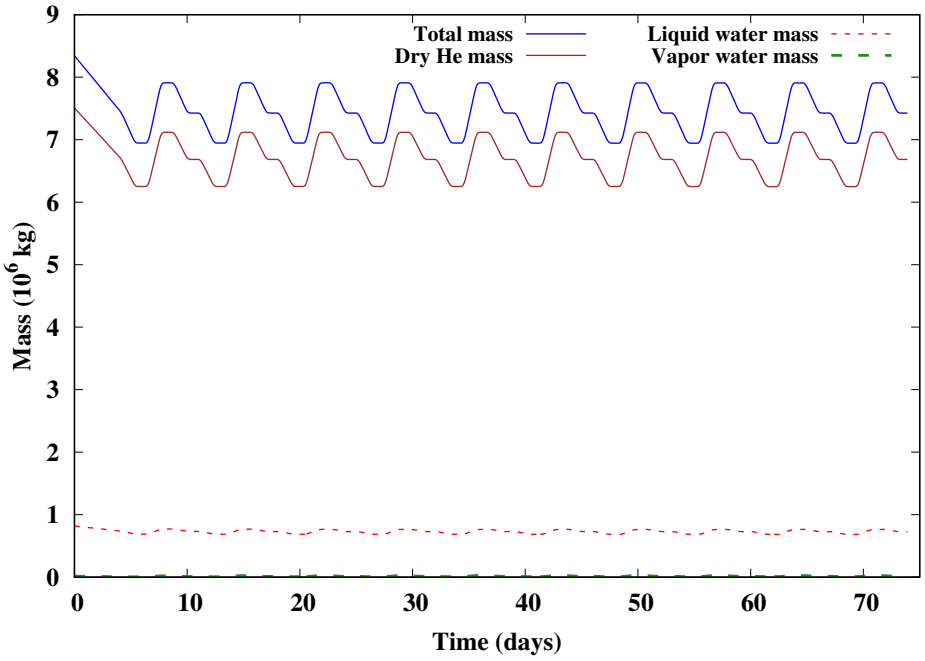

FIGURE 2.24 – Evolution of cavern mass for $c = 0.9$

Consequently, in light of these observations regarding the pivotal role of water content in modulating the gas-rich phase thermodynamics, our subsequent focus will shift to incorporating the kinetics of humidification into the model.

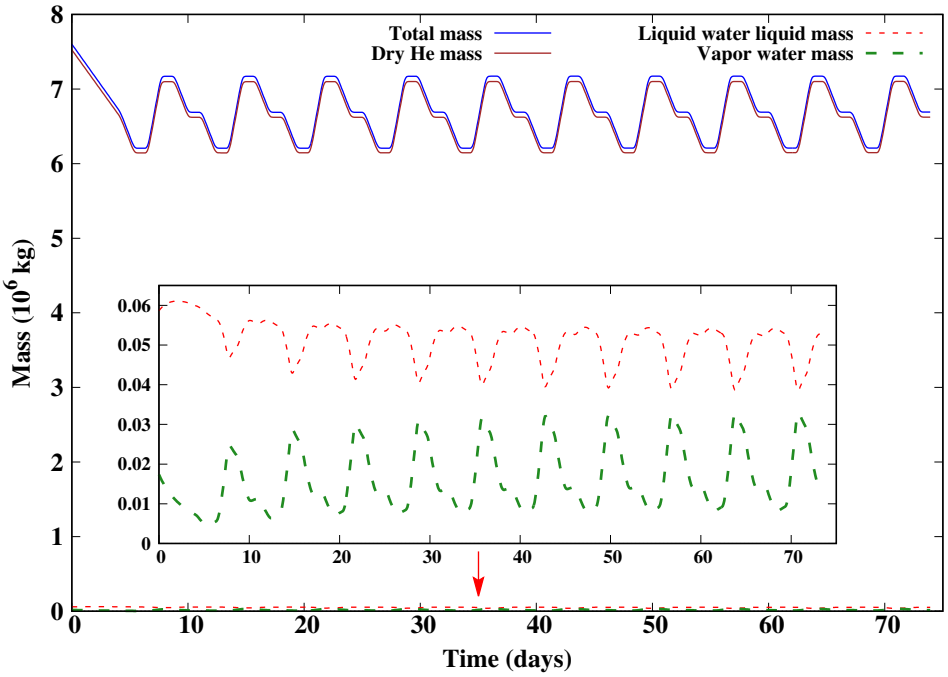

FIGURE 2.25 – Evolution of cavern mass for $c = 0.99$

2.3.2 Case II - Integration of humidification kinetics and its influence on helium storage

To advance our understanding of helium storage, it is important to examine the behavior of the stored humid helium while involving humidification kinetics. The primary focus of this case study centers on the investigation of the impact of adding these kinetics on temperature, pressure, and mass evolution over time. In contrast to the static concentration approach taken in the previous case study, here we will use the complete equation system 2.21 introducing τ, a time constant. This indicates that the attainment of thermodynamic equilibrium is not immediate. Instead, it is preceded by a transitional phase.

In fact, the time constant, denoted as τ^{exp}, was experimentally determined during the cycling of humid helium (see section 2.2.4). However, given the difference between laboratory settings and the cavern, as previously mentioned, it becomes necessary to modify this constant for application at the cavern scale. To address this, the first step involves determining τ_{min}, which represents the minimum time constant required for the gas to remain consistently saturated. Subsequently, the focus shifts to determining τ_{max}, representing the maximum time at which the concentration is no longer dependent on the equation system. The final part of this process involves calibrating the time constant under storage conditions in the salt cavern.

In this context, initial conditions significantly affect the resulting thermodynamic behavior. Specifically, for this study, we assume that the gas starts in a saturated state. We will use the same cycling program as in the previous case study, which is presented in Figure 2.20.

2.3.2.1 Identification of minimum time constant (τ_{min})

In our quest to discern the minimum time constant, we systematically varied τ as presented in the third equation of the system 2.21. Our primary objective was to pinpoint the precise value of $\tau_{\min}$ such that thermodynamic equilibrium is instantaneously achieved each time. As a foundational step in this parametric analysis, we referenced the cycle time, denoted as t_{cycle}, from our cycling program (see Figure 2.20) which stands at 7 days. This value was then divided by a series of divisors until thermodynamic equilibrium was consistently observed. Figure 2.26 depicts the water concentration (or water mass fraction) c_W and the saturation concentration c_W^s profiles for a range of τ values in the gas-rich phase during cycling. These profiles have been investigated across various τ values, calculated using the equation $\tau = t_{\text{cycle}}/n$, where $n = \{10, 100, 500\}$. It is important to note that the variations in τ directly lead to changes in both temperature and pressure, which in turn affect the saturation concentration $c_W^s(T, p)$. In the illustrated figure, each value of τ is aligned with the corresponding water concentration, shown as a continuous line, and saturation concentration, indicated by a dashed line. The figure shows that a perfect alignment between c_W and c_W^s was observed specifically for $\tau = t_{\text{cycle}}/500$. This denotes an immediate attainment of thermodynamic equilibrium, leading us to designate this specific value as $\tau_{\min}$.

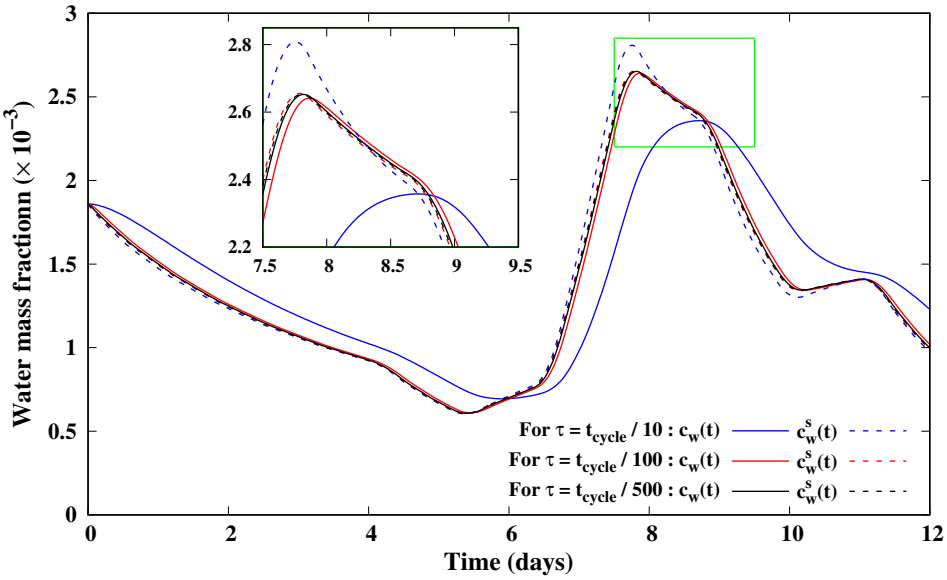

FIGURE 2.26 – Water concentration c_W and saturation concentration c_W^s profiles across diverse τ values in the cavern gas-rich phase during cycling : A study towards determining τ_{min}.

2.3.2.2 Determination of maximum time constant ($\tau_{\max}$)

Continuing our efforts to find the different time constants, we turned our focus towards the identification of the maximum time constant. Commencing this phase of our analysis, τ was systematically varied in the third equation of the system 2.21. The major objective was to determine the value of $\tau_{\max}$ at which the water concentration remains invariant and becomes entirely decoupled from the governing system of equations.

Guided by the same rigorous methodology, t_{cycle} served as our primary reference point, consistent with our earlier analysis. We then conducted an iterative process, increasing t_{cycle} using a range of factors until reaching a point where the concentration of water shows no noticeable change. A detailed illustration of the water concentration c_W and the saturation concentration c_W^s in the cavern gas-rich phase during cycling is presented in Figure 2.27. This figure compares different τ values, calculated as $\tau = t_{\text{cycle}} \times n$ where $n = \{2, 10, 50, 70, 100, 150\}$.

A main observation from our findings was that c_W remained invariant from its initial value for $\tau = t_{\text{cycle}} \times 70$. Consequently, this determined time constant is considered as $\tau_{\max}$.

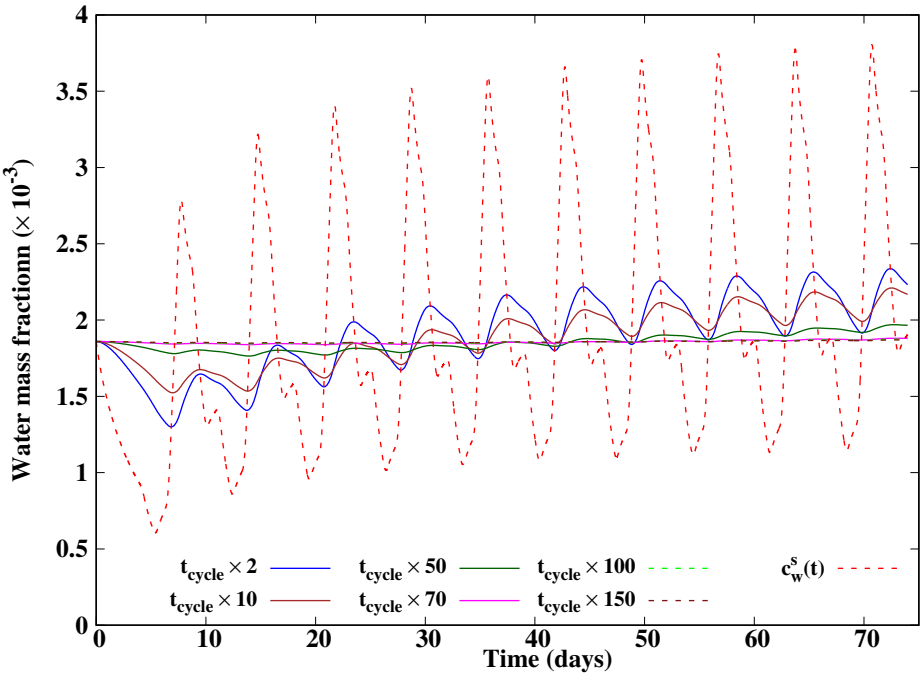

FIGURE 2.27 – Water concentration c_W and saturation concentration c_W^s profiles across diverse τ values in the cavern gas-rich phase during cycling : A study towards determining τ_{max}.

2.3.2.3 Calibration of the time constant

In the preceding parts, considerable attention was given to discern both the minimum and maximum time constants, denoted as $\tau_{\min}$ and $\tau_{\max}$, respectively. The current study aims to evaluate the value of τ_c for the humidification kinetics of helium in the gas-rich phase of the salt cavern, where this time constant τ_c is situated within the interval $[\tau_{\min}, \tau_{\max}]$. In fact, we will use the same cycling program as the earlier sections of this analysis (see Figure 2.20) with the time for one cycle denoted as t^c_{cycle}. In Section 2.2.4, we determined experimentally the time constant $\tau_{\text{exp}} = 85\,\text{s}$ for the helium humidification. However, as previously noted, controlled laboratory environments differ from salt cavern scenarios, which involve the direct interaction between the injected gas and the brine. Therefore, we will not use the same τ_{exp} on the cavern scale. Building upon these findings, an analogy was constructed to extrapolate the cavern scale time constant, τ_c :

$$\frac{\tau_c}{t^c_{\text{cycle}}} = \frac{\tau_{\text{exp}}}{t^{\text{exp}}_{\text{cycle}}}. \tag{2.22}$$

where $t^{\text{exp}}_{\text{cycle}}$ is the time for a lab-scale cycle. With known values of $t^c_{\text{cycle}} = 7$ days, $\tau_{\text{exp}} = 85$ seconds, and $t^{\text{exp}}_{\text{cycle}} = 980$ seconds, the calculation of τ_c yields a duration of 14.5 hours. Consequently, this study suggests employing this τ_c value for subsequent analyses and applications related to the humidification of helium in the gas-rich phase of salt caverns.

Using the determined τ_c, Figure 2.28 delineates the profiles of both the water concentration, c_W, and the saturation concentration, c^s_W. The saturation concentration c^s_W is influenced by the pressure and temperature conditions of the stored helium. Notably, the pressure and temperature within the cavern fluctuate substantially during cycling, as indicated in Figure 2.29, which affect the saturation concentration. The humidification kinetics play an important role in this context, rendering the water concentration c_W relatively less significant compared to the saturation concentration. This is attributed to the consideration of the transitional duration to reach equilibrium.

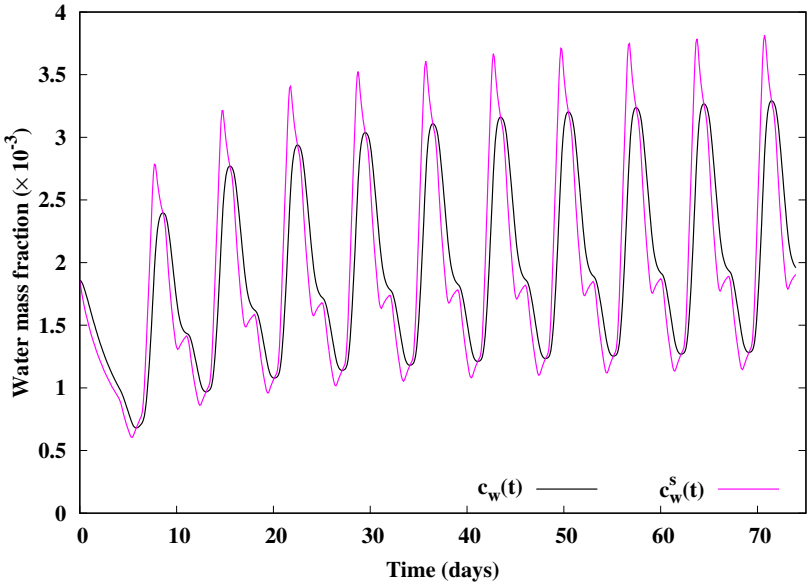

FIGURE 2.28 – Evolution of the water mass concentration (c_W) and the saturation concentration (c^s_W) over time during cycling.

For the purpose of quantifying the humidity of the stored gas, the absolute humidity, denoted as $AH = \mathcal{M}_W/\mathcal{M}_H$, is employed instead of the concentration c_W. Here, $\mathcal{M}_W$ signifies the mass of water, while $\mathcal{M}_H$ represents the mass of the helium. The relationship between AH and c_W is elucidated through the expression : $AH = c_W/(1 - c_W) \times 100$.

Figure 2.30 presents the absolute humidity within the salt cavern, juxtaposed with the flow rate over time. In this particular case study, as delineated in Figures 2.29b and 2.29a, the temperature and pressure ranges observed during the cycling process are $[16.5\,°\text{C}, 53.7\,°\text{C}]$ and $[13.1\,\text{MPa}, 17.5\,\text{MPa}]$, respectively. Under these conditions, the absolute humidity within the salt cavern remains notably low, with a maximum value recorded at 0.32%.

Despite its small values, an upward trend is observed in the absolute humidity profile with

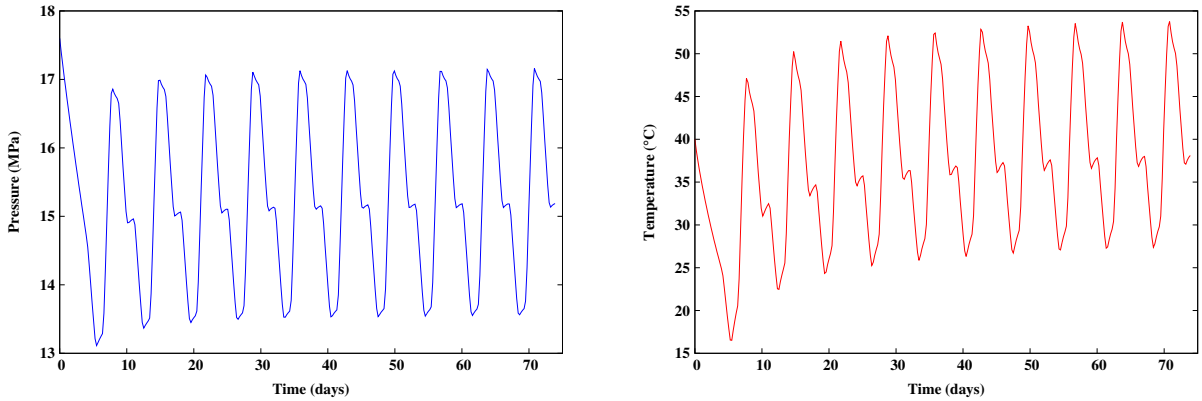

(a) Pressure (p) (b) Temperature (T)

FIGURE 2.29 – Evolution of the temperature and pressure of stored helium over time during cycling.

each cycle. This increase can be attributed to the rise in temperature and pressure of the stored gas. Consequently, this has led to more water being present in the gas-rich phase.

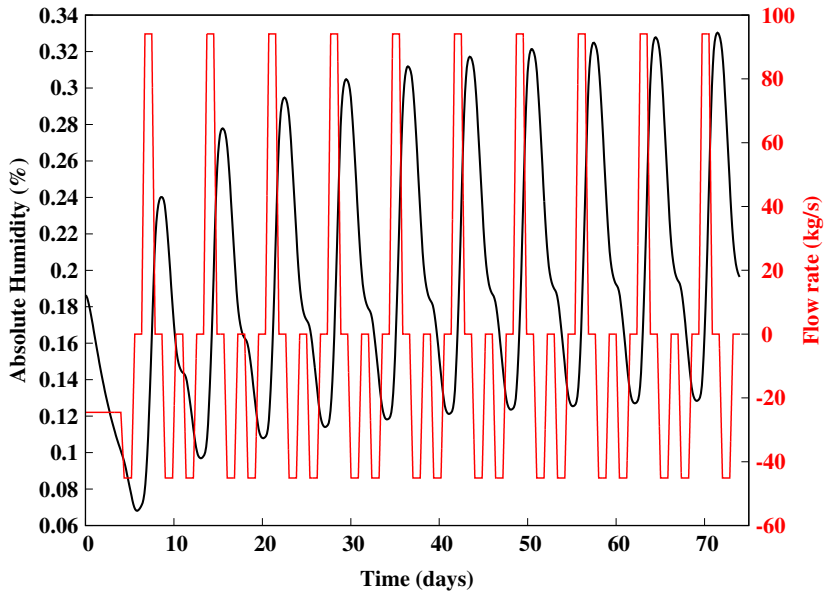

FIGURE 2.30 – Evolution of the absolute humidity during cycling.

The cavern is initially assumed to be filled with a mass of stored helium $\mathcal{M}(0)$ equal to 7.5×10^6 kg. Figure 2.31 illustrates the relative mass change $\tilde{\mathcal{M}}(t)$ during the first withdrawal phase (in green) and 10 cycles (in blue). The formula for calculating this relative mass change is given by :

$$\tilde{\mathcal{M}}(t) = \left(\frac{\mathcal{M}(t)}{\mathcal{M}(0)} - 1 \right) \times 100\%$$

The range of this relative mass change is bounded between $[-18.58\%$ to $-5.74\%]$. Indeed, the stored humid helium contains a mixture of dry helium and water. Using our model, we will quantify these two constituents within the gas-rich phase.

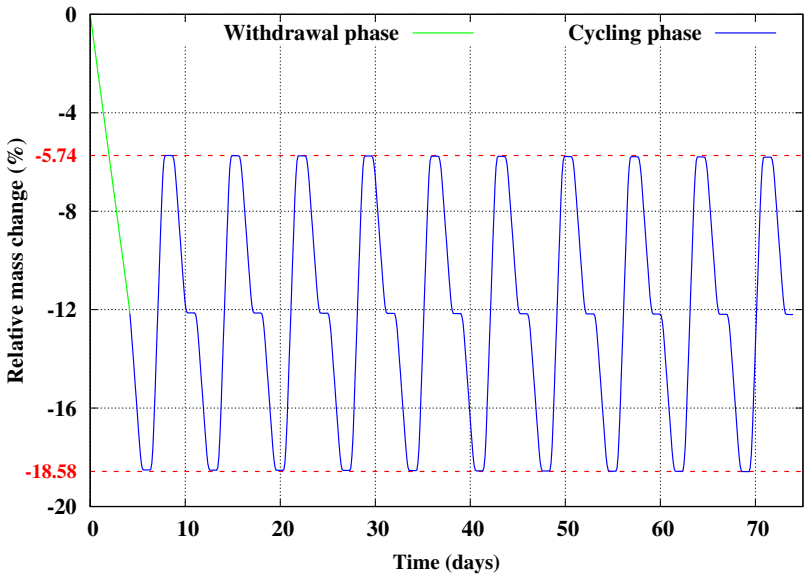

FIGURE 2.31 – Relative mass change during the first withdrawal and cycling phase.

In Figure 2.32, the composition of the humid helium within the gas-rich phase of the salt cavern is presented. The total mass of humid helium consists mainly of dry helium with a relatively small amount of water.

Despite its relatively minor proportion in comparison to the overall mass, this amount of water cannot be neglected, as it varies from nearly 6 to 23.3×10^3 kg. Notably, this mass tends to increase over time, which is attributed to the rising temperature and pressure during the cycling process, as depicted in Figures 2.29b and 2.29a. This trend is consistent with the previously conducted analysis focusing on the absolute humidity.

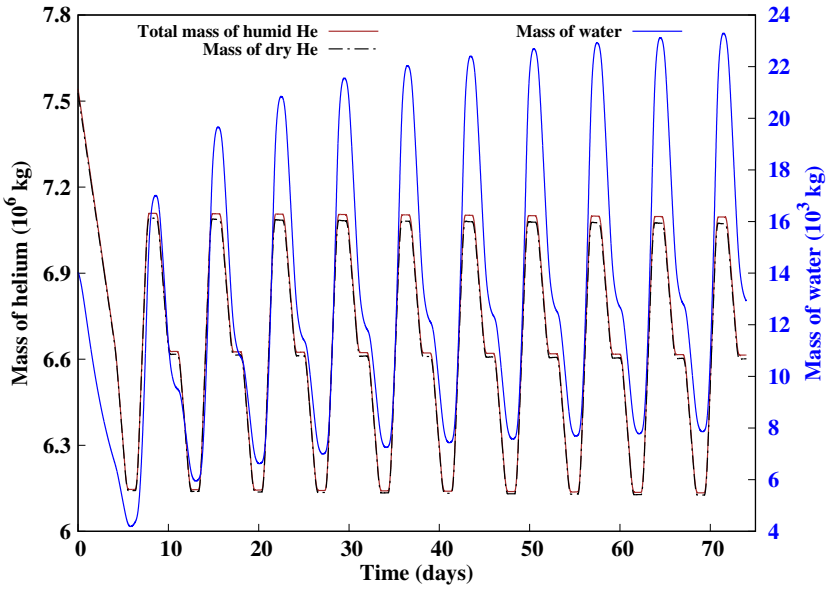

FIGURE 2.32 – Quantitative analysis of constituent masses of stored humid helium during cycling : Evolution of dry helium and water masses.

2.3.3 A comparative analysis of helium and hydrogen

This section presents a comparison analysis of the storage of humid helium and humid hydrogen in salt caverns. We will use the same cycling program and flow rate as in the case of humid helium (see Figure 2.20). This program is made to maintain the cavern temperature greater than 0 °C during cycling. This precaution is made to prevent state changes in the water present in the gas-rich phase. As previously elucidated in Section 1.2.1, due to the absence of specific data pertaining to hydrogen humidification and the similarity in properties between helium and hydrogen, the time constant τ_c, determined for helium, will be used in this study for the humidification kinetics of hydrogen.

Figure 2.33 delineates the relative mass change $\tilde{\mathcal{M}}$ for both helium and hydrogen during the first withdrawal phase (represented by a green line) and cycling phase (indicated by a brown line for helium and black for H_2). For helium, the $\tilde{\mathcal{M}}$ values are observed within the range of $[-18.58\%, -5.74\%]$. In contrast, for hydrogen, these values extend from $[-37.59\%, -11.60\%]$. The discernible difference between these ranges is attributable to the lower density of hydrogen. Consequently, employing the same rate flow program results in a greater mass of humid hydrogen being introduced into the cavern.

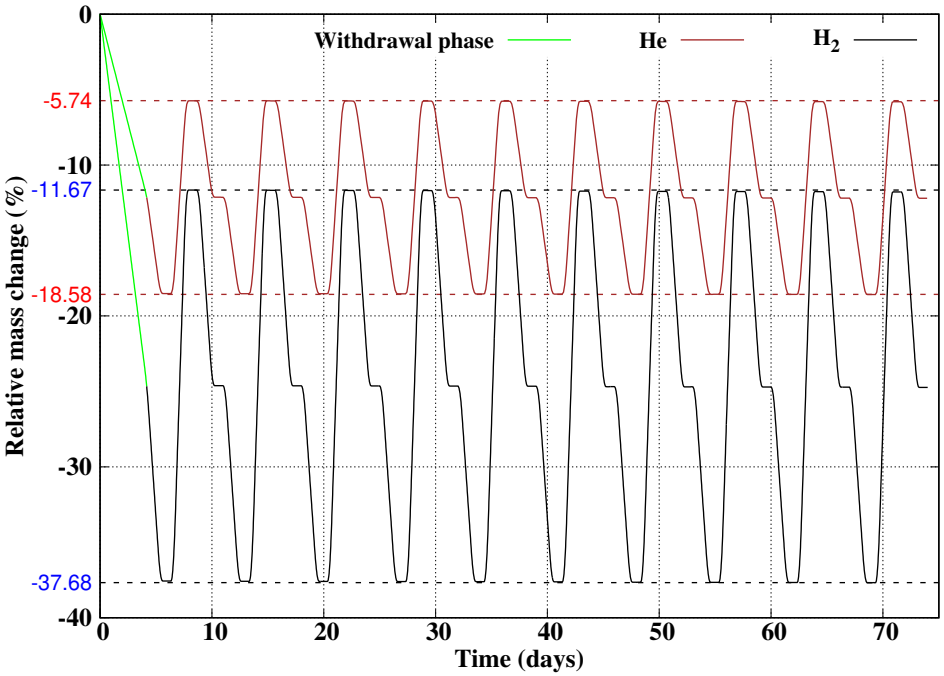

FIGURE 2.33 – Relative mass change of stored helium and hydrogen during the first withdrawal and cycling phase.

Figure 2.34 shows that there are notable differences in the temperature and pressure profiles between stored hydrogen and helium in salt caverns. The data for hydrogen cycling shows a decline in pressure and temperature to almost 9.23 MPa and 0 °C, respectively. In contrast, for helium cycling, these values do not have the same variations, with a minimum pressure and temperature recorded at 13.2 MPa and 15.7 °C.

Figure 2.35 delineates the water concentration (c_W) and the saturation concentration (c_W^s)

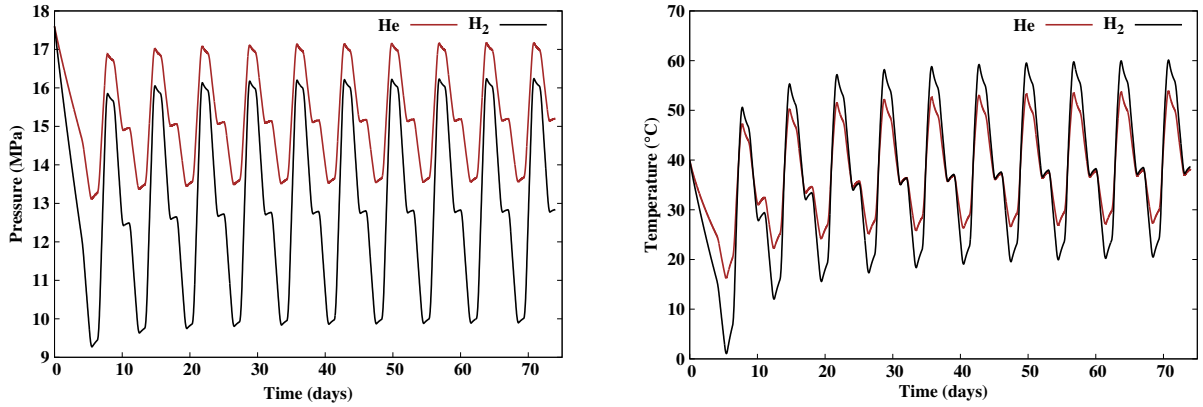

(a) Pressure (p) (b) Temperature (T)

FIGURE 2.34 – Comparison between the temperature and pressure of stored helium and hydrogen over time during cycling.

in the gas-rich phase during cycling for stored hydrogen and helium. When thermodynamic equilibrium is assumed (at saturation), it is observed that c_W^s for the two gases is more important than c_W, leading to an overestimation of the water content in the gaseous phase. Moreover, the water concentration c_W in humid hydrogen is more significant compared to that in humid helium. This difference is clearly illustrated in Figure 2.36, which represents the absolute humidity AH for both stored gases. In fact, the ratio of $AH_{\mathrm{H_2}}/AH_{\mathrm{He}}$ is increasing during cycling, ranging from almost 1.1 to 2.8.

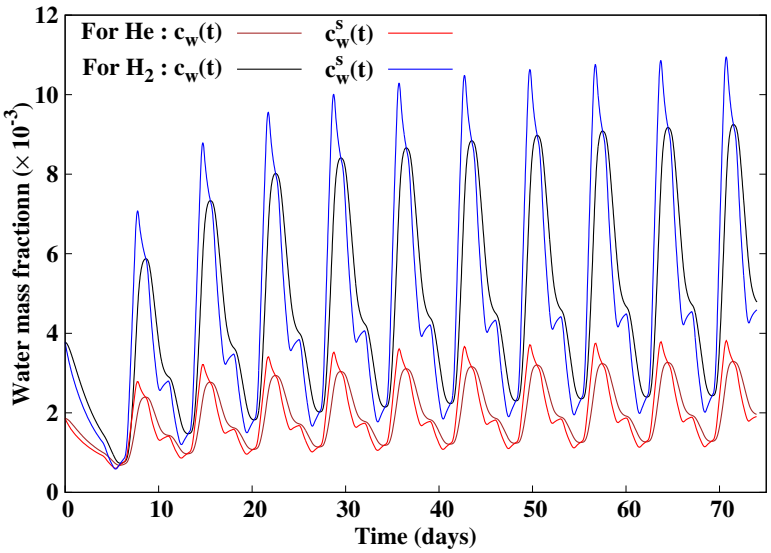

FIGURE 2.35 – Comparison between stored helium and hydrogen : Evolution of the water mass concentration (c_W) and the saturation concentration (c_W^s) over time during cycling.

In order to quantify the composition of the total mass of humid hydrogen during cycling, the mass of dry hydrogen as well as the mass of water present in the gas-rich phase are presented in Figure 2.37. It is observed that the calculated water mass ranges from approximately 2×10^3 kg to 30×10^3 kg. Comparing these results with the composition of the mass of humid helium presented

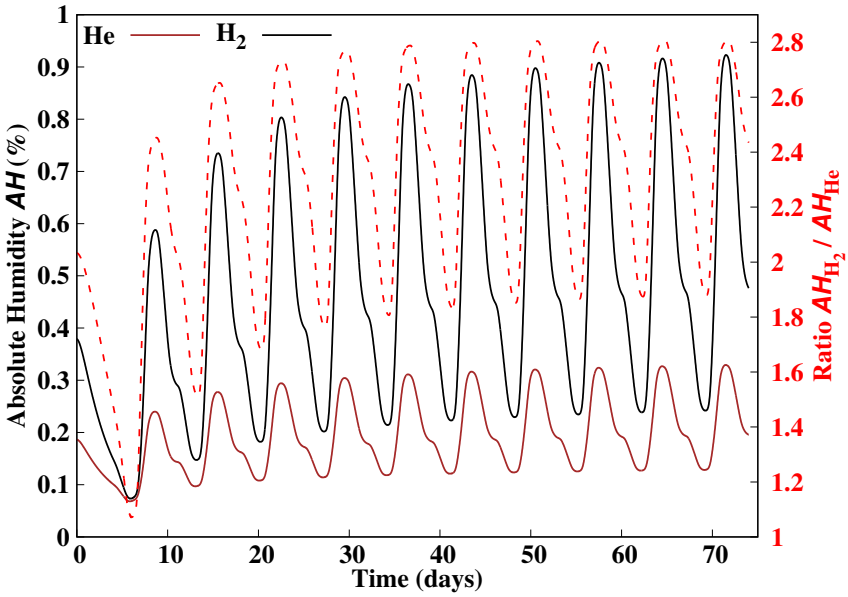

FIGURE 2.36 – Comparison between stored helium and hydroren : Evolution of the absolute humidity over time during cycling.

in Figure 2.32, it is evident that the water content in humid hydrogen is more important than in humid helium, varying between 6×10^3 kg to 23.3×10^3 kg. Thus, even though the total mass of stored helium is twice that of hydrogen, the mass of water in the gaseous phase during hydrogen cycling is found to be greater.

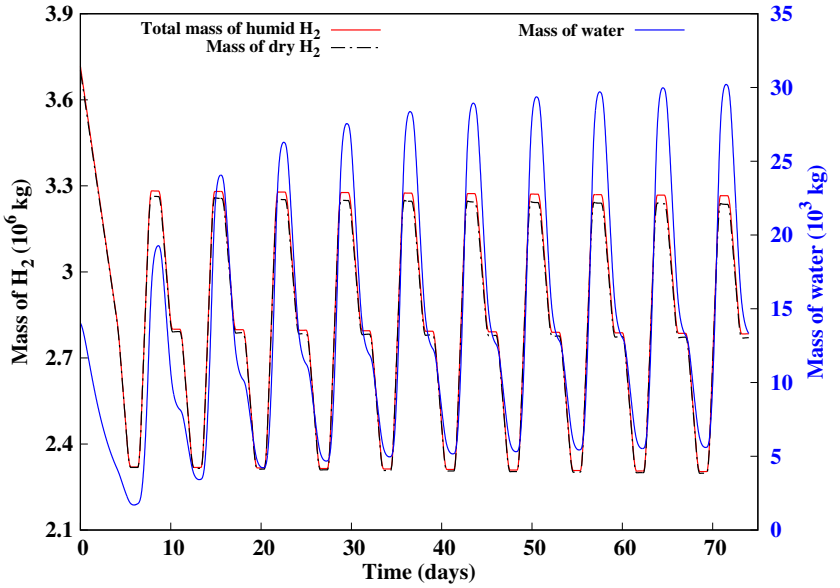

FIGURE 2.37 – Quantitative analysis of constituent masses of stored humid hydrogen during cycling : Evolution of dry hydrogen and water masses.

In summary, this section investigated the effects of humidity on stored helium and hydrogen cycling in salt caverns. Incorporating humidification kinetics into our model improved the precision of water content quantification in the gas-rich phase. Key findings include the impact

of humidity on the temperature and pressure of the cavern which affect the behavior of the stored gases. The study highlights the importance of accounting for both water states : vapor and liquid. Notably, the liquid water mass in the gas phase is more significant than the vapor mass, a factor that must be accounted for in operational protocols to prevent equipment corrosion. Furthermore, even with a lower overall mass, the study shows that the water content in hydrogen cycling is higher compared to helium. This is particularly relevant given the immense quantities of hydrogen required for energy storage, due to its low density, in order to store an amount of energy comparable to that of fossil fuels.

Conclusions and perspectives en français

Cette thèse se focalise sur l'étude des échanges de masse entre les gaz stockés et la saumure résiduelle dans les cavités salines. L'objectif est d'étudier spécifiquement la cinétique de dissolution du CO_2 et du H_2 dans la saumure, tout en explorant l'impact de l'humidité sur la thermodynamique des gaz. L'approche adoptée, combinant des études expérimentales avec le développement de modèles numériques, offre une compréhension plus approfondie de ces échanges de masse dans les conditions de stockage.

La cinétique de dissolution du CO_2 et du H_2 en solutions aqueuses (eau pure et saumure) a fait l'objet d'une étude expérimentale, en utilisant la méthode de Pressure-Decay. Ceci a été réalisé par la mesure de la pression du gaz dans une cellule PVT à température constante. La baisse de pression observée pendant le test correspond à la réduction de la masse du gaz causée par le processus de dissolution. Les résultats expérimentaux montrent que cette diminution est influencée par la salinité de la saumure, la pression initiale du gaz et le rapport de volume entre les phases liquide et gazeuse.

De plus, un pilote de stockage a été mis en œuvre, utilisant l'hélium comme cas d'étude, pour évaluer l'humidité du gaz dans les conditions de stockage. Cette étude a démontré que l'humidité impacte la thermodynamique du gaz, affectant les taux de transfert de masse et le comportement du gaz étudié. Il a été constaté aussi que l'humidité relative moyenne dans la phase gazeuse diminue avec le temps, qui a été expliqué par la cinétique d'humidification du gaz, ainsi que par l'introduction d'hélium sec et l'extraction d'hélium humide pendant le cyclage.

Par la suite, des modèles numériques ont été développés dans le but de simuler les phénomènes physiques observés lors des tests expérimentaux, puis d'utiliser ces modèles avec les paramètres ajustés pour étudier le comportement des gaz à l'échelle des cavités salines.

En fait, deux modèles numériques de dissolution de gaz ont été utilisés pour simuler les tests expérimentaux de Pressure-Decay, en mettant un accent particulier sur le CO_2 et le H_2 en solutions aqueuses. Le premier modèle, qui ne prend en compte que la diffusion pure, a réussi à estimer la baisse de pression du gaz. Cependant, il nécessite un coefficient de diffusion apparent trop élevé par rapport au coefficient moléculaire du CO_2 dans l'eau ou la saumure. Pour résoudre ce problème, un modèle plus complexe a été proposé, offrant des résultats plus précis et intégrant le processus de convection naturelle, qui accélère la dissolution du CO_2 dans la solution aqueuse.

Concernant la cinétique de dissolution de l'hydrogène, notre étude a rencontré des difficultés en raison de fuites potentielles du système, nécessitant une interprétation prudente des résultats. Par conséquent, un ajustement linéaire des fuites a été inclus dans le modèle de diffusion et de convection pour prendre en compte la fuite dans le système et analyser les résultats expérimentaux.

Ainsi, il est important de mentionner que la formulation adimensionnelle des modèles élargit leur applicabilité à diverses échelles, allant des expériences en laboratoire aux cavités souterraines.

Ce modèle inclut les processus thermodynamiques complexes existant au sein d'une cavité saline, tels que le transfert de chaleur et de masse, la cinétique de dissolution et les effets de convection. En intégrant ces variables, le modèle est capable de prédire la perte de masse liée à la dissolution et de tenir compte de l'influence de la convection naturelle, qui joue un rôle important dans la cinétique de dissolution des gaz.

La nouveauté de cette étude réside dans l'examen de l'impact de la convection thermique sur le processus de dissolution gaz-liquide. Les simulations démontrent que cette masse représente approximativement 0,32 % de la masse initialement stockée. Elles indiquent qu'environ 22.11 tonnes de CO_2 sont dissoutes pendant une période de cyclage de 6.5 mois.

D'autre part, l'étude de la cinétique de dissolution de l'hydrogène dans la saumure pour le test d'étanchéité de la cavité EZ53 sur trois jours a révélé une perte minimale d'hydrogène, représentant seulement 0.00475 % de l'hydrogène introduit pour le test. Cela suggère que la dissolution peut être considérée comme négligeable dans ce cas.

En outre, le modèle numérique HGM a été développé pour étudier l'humidification des gaz. Ce modèle prouve sa capacité à reproduire avec précision l'équilibre vapeur-liquide dans le système hydrogène-eau. Cela a été déterminé par la comparaison des données expérimentales et des prédictions du modèle. De plus, les prédictions du modèle affichent un degré de précision plus élevé par rapport aux estimations d'autres modèles existants dans la littérature. En fait, ce modèle estime aussi les propriétés thermodynamiques telles que les coefficients de Joule Thomson, les expansivités thermiques et les capacités calorifiques. En tenant compte de la cinétique d'humidification, le modèle HGM a efficacement expliqué la diminution de l'humidité relative qui s'est produite pendant le test cyclage expérimental de l'hélium.

Dans cette thèse, l'accent a été mis sur l'examen des échanges de masse entre le gaz stocké et la saumure résiduelle, en particulier la dissolution du gaz dans la saumure et l'humidification des gaz, en traitant ces phénomènes comme des problèmes séparés. Bien que cette approche ait permis d'obtenir des résultats intéressants, elle présente des limitations quant à la prise en compte simultanée de toutes les complexités des échanges de masse dans le stockage de gaz au sein des cavités salines. Par conséquent, la formulation d'un modèle qui couple tous les processus pertinents serait bénéfique. Un tel modèle améliorerait la précision de la quantification de la perte de masse lors du stockage de gaz.

De plus, il est important de noter que la cavité est entourée d'un domaine rocheux saturé de saumure. En fait, un autre aspect important des échanges de masse concernant la perméation du gaz dans la matrice solide nécessite des études supplimentairesdes. Ce phénomène peut être

plus important lorsqu'on considère les endommagements potentiels des structures de roches sur de longues périodes d'utilisation de la cavité. Actuellement, le Centre de Géosciences MINES ParisTech développe un nouvel appareil pour étudier la perméation du gaz dans le sel gemme. Comme illustré dans la Figure 4.38, l'appareil expérimental comprend un réservoir de gaz sous pression et une cellule en acier, tous deux immergés dans un bain à température contrôlée. Un système de chauffage maintient une température constante dans ce dispositif. La procédure expérimentale implique l'introduction du gaz sous pression dans l'éprouvette de sel (intact ou endommagé). Ce processus permet de mesurer la diminution de pression du gaz résultant de la perméation du gaz dans le sel. L'étude présentée dans cette thèse peut être utilisée pour quantifier les échanges de masse entre le gaz stocké et cette saumure.

Conclusions and perspectives

The study presented in this dissertation focuses on examining the mass exchange between stored gases and brine within salt caverns. It specifically investigates the kinetics of CO_2 and H_2 dissolution in brine, and also explores the impact of humidity on the thermodynamics of gases. The approach used, which combines experimental studies with the development of mathematical and numerical models, offers a more comprehensive understanding of these mass exchanges under storage conditions.

The dissolution kinetics of CO_2 and H_2 in aqueous solutions (pure water and brine) were studied experimentally using the pressure-decay method. This was achieved by the measurement of the gas pressure inside a PVT cell at a constant temperature. The observed pressure decrease during the test corresponds to the reduction in gas mass caused by the dissolution process. The experimental results show that this decrease is affected by the salinity of the brine, the initial pressure of the gas, and the volume ratio between the liquid and gas phases.

Furthermore, an innovative storage pilot was implemented using helium as a case study to assess gas humidity, providing valuable information on the influence of mass transfer on the gas-rich phase under storage conditions. These investigations have demonstrated that humidity impacts the thermodynamics of the gas, affecting the rates of mass transfer and the behavior of the studied gas. It was found that the average relative humidity in the gas-rich phase drops over time. This was explained by the gas humidification kinetics, as well as the introduction of dry helium and the extraction of humid helium during the cycling.

Subsequently, these experimental results are incorporated into the development of mathematical and numerical models. These models accurately simulate the reported physical phenomena in tests and expand the investigation to study the behavior of gases in storage conditions.

In fact, two numerical gas dissolution models were used to simulate experimental pressure-decay tests, with a special emphasis on CO_2 and H_2 in aqueous solutions. The first model, which just accounts for pure diffusion, accurately represents the decrease in pressure. However, it necessitates an apparent diffusion coefficient that is too high in comparison to the molecular diffusivity of CO_2 in water or brine. To address this issue, a more complex model was proposed that provides more precise results and incorporates the natural convection process, which speeds up the CO_2 dissolution.

Regarding the kinetics of hydrogen dissolution, our study faced challenges due to potential system leakage, which necessitated a cautious interpretation of the results. Consequently, a linear

leakage adjustment was included in the diffusion and convection model to consider the leakage in the system and analyze the experimental findings.

It is important to mention that the non-dimensional formulation of the models extends its applicability across different scales, from laboratory experiments to underground salt caverns.

This model includes the detailed complex thermodynamic processes within the cavern environment, such as heat and mass transfer, dissolution kinetics, and convection effects, which had not been incorporated in previous models in the literature. By incorporating these variables, the model can predict dissolution rates and account for the influence of natural convection, which plays a significant role in gas dissolution kinetics. In fact, temperature changes cause thermal convection, which affects the rate at which gases dissolve in brine. The importance of these convective effects becomes more noticeable during gas cycling. Due to the significant thermal expansivity of brine, even slight temperature fluctuations can result in significant changes in its density. This highlights the need to include thermal convection in models of gas dissolution under storage conditions.

Moreover, the simulations reveal that the final total dissolved mass approximates to 0.32% of the initial stored mass. Additional results show that approximately 22.11 tons of CO_2 are dissolved during a 6.5-month cycling period.

On the other hand, the study of hydrogen dissolution kinetics in brine for the EZ53 cavern tightness test over three days revealed minimal hydrogen loss, representing only 0.00475% of the introduced hydrogen for the test. This suggests that the dissolution can be deemed insignificant in this particular case. Therefore, hydrogen can be used instead of the nitrogen in tightness test, especially in hydrogen storage scenarios. However, it is essential to investigate supplementary mechanisms that might potentially influence this mass loss during this test, such as the penetration of hydrogen into the salt rock.

Furthermore, the HGM numerical model was developed to study gas humidification. It demonstrates its ability to accurately replicate the vapor-liquid equilibrium in hydrogen-water systems. This was determined through the comparison of experimental data and model predictions. Moreover, the model predictions display a higher degree of accuracy when compared to estimates from other existing models in the literature. Additionally, the HGM model has the ability to predict thermodynamic properties such as Joule Thomson coefficients, thermal expansivities, and heat capacities. As a result, it is not only used for estimating solubility but also has a much broader applicability for predicting relevant thermodynamic properties. By taking into account the kinetics of humidification, the HGM model effectively explained the decrease in relative humidity that took place during the experimental cycling test of helium.

On the cavern scale, the findings underscore the impact of humidity on the temperature and pressure which affect the behavior of stored gases. It was also highlighted that including both water states (vapor and liquid) in the humid gas models can be beneficial in order to accurately predict the water content in the gas-rich phase.

In this thesis, the focus was placed on examining the mass exchange between stored gas and residual brine, specifically the dissolution of gas in brine and gas humidification, treating these phenomena as separate problems. This approach, though providing significant insights,

presents limitations in fully understanding the complexities of mass exchange in gas storage within salt caverns. Therefore, the formulation of a model that couples all relevant processes will be beneficial. Such a model would enhance the accuracy of quantifying mass loss during gas storage.

Additionally, it is important to note that the cavern is surrounded by a rock domain saturated with brine. In fact, another important aspect of mass exchange warrants investigation : the permeation of gas into the solid matrix. This phenomenon can be more significant when considering the potential damage to rock salt structures over extended periods of cavern usage. Currently, the Geoscience Center of Paristech Fontainebleau is developing a new apparatus to study gas permeation in rock salt. As depicted in Figure 4.38, the experimental apparatus comprises a pressurized gas reservoir and a steel cell, both submerged in a temperature-controlled bath. A heating system maintains a constant temperature within this setup. The experimental procedure involves the introduction of the pressurized gas into the salt sample (intact or damaged). This process allows for the measurement of pressure decay that results from gas permeation into the sample. The study detailed in this dissertation can be used to quantify the mass exchanges between the stored gas and the brine inside pores.

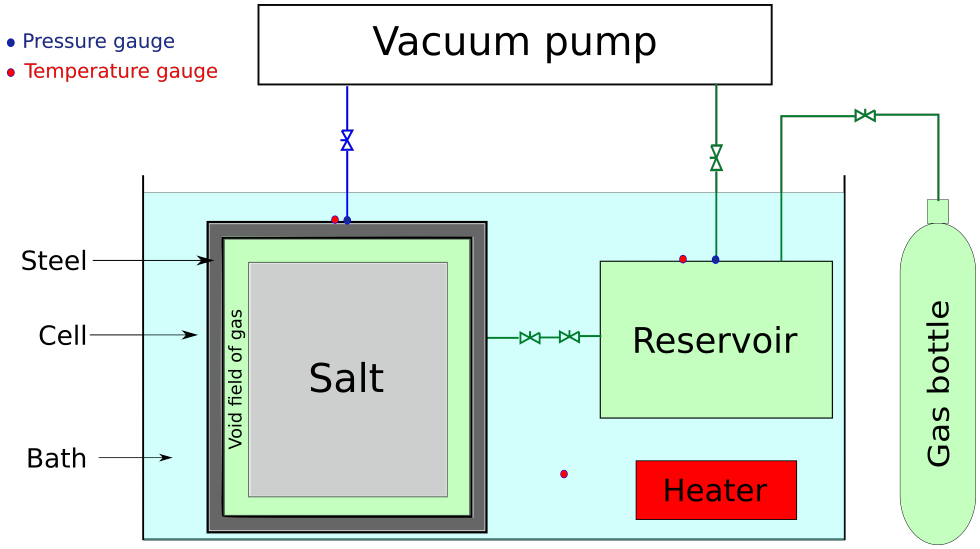

FIGURE 4.38 – Laboratory setup of the permeation device.

Appendix A

Error sources in gas dissolution device experiments

Several sources of error can be identified in experimental data, among which systematic uncertainties play a crucial role. These uncertainties are inherently linked to measurement instruments. For the pressure sensors of the PVT cell, we employed three UNIK 5000 model sensors from Druck, each suited for different pressure ranges. The first sensor is capable of measuring pressures up to 10 bar with an uncertainty of u(p) = 4 mbar, the second can measure up to 200 bar with an uncertainty of u(p) = 6 mbar, and the third is designed for pressures up to 400 bar with an uncertainty of u(p) = 8 mbar. The PVT cell's temperature probes, of the PT-100 type, which have an electrical resistance response of 100 Ω at 0 °C, were calibrated using a PT-25 type reference probe. The calibration uncertainty for these probes was estimated at u(T) = 0.03 °C for a temperature range between 5 and 70 °C. Additionally, the precision of the balance used to define the salinity of brines is ±0.1 mg ; the temperature of the bath has a set precision of approximately ±0.2 °C.

Other errors in the experimental process can arise from both the methodology employed and the actions of the experimenter. Notably, when assessing the salinity of brine, inaccuracies may stem from the precise quantity of salt dissolved in pure water, with a potential discrepancy estimated at ±0.02%. Furthermore, the evaporation of water during heating or during periods of vacuum application, along with the potential for contamination by residual traces of water, brine, or ethanol from prior experiments, can significantly affect the reliability of results.

Further operational uncertainties may result from leaks in the connections between conduits and valves, which might cause minor fluid loss if the connections aren't tightly secured. Additionally, a critical step involves vacuuming the conduits connecting the gas reserve or variable volume cell to the PVT cell, ensuring that adjustments for conduit volumes aren't needed in the volume analysis. However, if these connections aren't completely airtight, air bubbles could form, leading to inaccuracies in the measured volumes and introducing uncertainties into the experimental results.

Error sources in storage pilot experiments

In storage pilot experiments, accurately identifying and managing error sources is critical for the integrity of the data collected. One pivotal aspect involves the precision of the instruments used, such as the UNIK 5000 model pressure sensor from Druck. This sensor is essential for monitoring pressures within the system, capable of measuring up to 200 bar with an uncertainty of u(p) = 2 mbar. Temperature control is equally crucial, managed with PT-100 type probes. These probes undergo rigorous calibration, achieving an uncertainty of u(T) = 0.02 °C over a wide temperature range from 25 to 120 °C, ensuring accurate temperature monitoring essential for the storage conditions under study.

Gas purity used in the experiments

For our experimental study, the purity of gases provided by Messer is of paramount importance. The specified purity levels are as follows : Carbon Dioxide (CO2), Hydrogen (H2), and Helium (He) gases each have a purity of 99.999%. This high degree of purity is crucial for ensuring the accuracy and reliability of our experimental results.

References

[Abascal, 2005] J. L. F. Abascal et C. Vega. « A general purpose model for the condensed phases of water : TIP4P/2005 ». *The Journal of Chemical Physics* 123.23 (2005), p. 234505 (cf. p. 60, 61).

[AbuAisha, 2021] Murad AbuAisha et Joël Billiotte. « A discussion on hydrogen migration in rock salt for tight underground storage with an insight into a laboratory setup ». *Journal of Energy Storage* 38 (2021), p. 102589 (cf. p. 78).

[Abuaisha, 2023] Murad S. Abuaisha, Ahmed Rouabhi, Faouzi Hadj-Hassen, David W. Eaton, Firas Tayeb et Alain Valtz. « Thermal effects on the kinetics of gas dissolution in brine : A case study of CO2 storage in salt caverns (a non-dimensional model) ». 2023 (cf. p. 78).

[Akinfiev, 2003] Nikolay N. Akinfiev et Larryn W. Diamond. « Thermodynamic description of aqueous nonelectrolytes at infinite dilution over a wide range of state parameters ». *Geochimica et Cosmochimica Acta* 67.4 (2003), p. 613-629 (cf. p. 31, 42).

[Albers, 1985] B. Albers et H. Rose. « Nitrogen/helium leak detection used on North Rankin'A'Platform ». *The APPEA Journal* 25.1 (1985), p. 123-128 (cf. p. 94).

[Archer, 2000] Donald G. Archer et Richard W. Carter. « Thermodynamic Properties of the NaCl + H2O System. 4. Heat Capacities of H2O and NaCl(aq) in Cold-Stable and Supercooled States ». *The Journal of Physical Chemistry B* 104.35 (2000), p. 8563-8584 (cf. p. 42, 50).

[Archer, 1974] E. E. Archer et J. Hilton. « The determination of small amounts of water in gases using Karl Fischer reagent ». *Analyst* 99.1182 (1974), p. 547-550 (cf. p. 22).

[Azin, 2013] Reza Azin, Mohamad Mahmoudy, Seyed Mostafa Jafari Raad et Shahriar Osfouri. « Measurement and modeling of CO2 diffusion coefficient in Saline Aquifer at reservoir conditions ». *Central European Journal of Engineering* 3.4 (2013), p. 585-594 (cf. p. 12, 32).

[Bahar, 2008] Mohammad Mohammazadeh Bahar et Keyu Liu. « Measurement Of The Diffusion Coefficient Of CO2 In Formation Water Under Reservoir Conditions : Implications For CO2 Storage ». OnePetro, 2008 (cf. p. 12, 31).

[Bartlett, 1927] Edward P. Bartlett. « The concentration of water vapor in compressed hydrogen, nitrogen and a mixture of these gases in the presence of condensed water ». *Journal of the American Chemical Society* 49.1 (1927), p. 65-78 (cf. p. 59).

[Belgodere, 2015] Clément Belgodere, Jean Dubessy, Denis Vautrin, Marie-Camille Caumon, Jérôme Sterpenich, Jacques Pironon et al. « Experimental determination of CO2 diffusion coefficient in aqueous solutions under pressure at room temperature via Raman spectroscopy : impact of salinity (NaCl) ». *Journal of Raman Spectroscopy* 46.10 (2015), p. 1025-1032 (cf. p. 2, 6, 12, 31, 32).

[Bell, 1995] S. A. Bell. « Validation of the NPL gravimetric hygrometer ». doctoral. City University London, 1995 (cf. p. 22).

[Berest, 2001] P. Berest, B. Brouard et J. G. Durup. « Tightness Tests in Salt-Cavern Wells ». *Oil & Gas Science and Technology* 56.5 (2001), p. 451-469 (cf. p. 76, 94).

[Bérest, 2021] Pierre Bérest, Benoit Brouard, Grégoire Hévin et Arnaud Réveillère. « Tightness of salt caverns used for hydrogen storage ». OnePetro, 2021 (cf. p. 94, 95).

[Berezin, 2008] A.G. Berezin, A.I. Nadezhdinskii, Y.Y. Ponurovskii, D.B. Stavrovskii, I.E. Vyazov, A.P. Kotkov et al. « Detection of moisture content in high-purity ammonia by means of diode-laser spectroscopy ». *Applied Physics B* 90.2 (2008), p. 317-321 (cf. p. 22).

[Bignell, 1987] Noel. Bignell. « Precise density measurements of aqueous solutions of mixed nonpolar gases ». *The Journal of Physical Chemistry* 91.6 (1987), p. 1687-1690 (cf. p. 50).

[Bird, 2007] Robert Byron Bird, Warren E Stewart et Edwin N Lightfoot. *Transport phenomena*. 2 nd rev. ed. New York : Wiley, 2007 (cf. p. 46).

[Bourne-Webb, 2016] P. J. Bourne-Webb, T. M. Bodas Freitas et R. A. da Costa Gonçalves. « Thermal and mechanical aspects of the response of embedded retaining walls used as shallow geothermal heat exchangers ». *Energy and Buildings* 125 (2016), p. 130-141 (cf. p. 85).

[Bulatov, 1982] V. P. Bulatov, S. I. Zavorotnyĭ, Oleg M. Sarkisov, É A. Sviridenkov, A. I. Trostin et S. G. Cheskis. « High-sensitivity pulsed intracavity laser spectroscopy system ». *Soviet Journal of Quantum Electronics* 12.2 (1982), p. 251 (cf. p. 22).

[Bünger, 2016] U. Bünger, J. Michalski, F. Crotogino et O. Kruck. « 7 - Large-scale underground storage of hydrogen for the grid integration of renewable energy and other applications ». *Compendium of Hydrogen Energy*. Sous la dir. de Michael Ball, Angelo Basile et T. Nejat Veziroğlu. Woodhead Publishing Series in Energy. Oxford : Woodhead Publishing, 2016, p. 133-163 (cf. p. 76).

[Busse, 1971] F. H. Busse et J. A. Whitehead. « Instabilities of convection rolls in a high Prandtl number fluid ». *Journal of Fluid Mechanics* 47.2 (1971), p. 305-320 (cf. p. 40).

[Cadogan, 2014] Shane P. Cadogan, Geoffrey C. Maitland et J. P. Martin Trusler. « Diffusion Coefficients of CO2 and N2 in Water at Temperatures between 298.15 K and 423.15 K at Pressures up to 45 MPa ». *Journal of Chemical & Engineering Data* 59.2 (2014), p. 519-525 (cf. p. 2, 6, 31, 32).

[Chabab, 2020] Salaheddine Chabab, Pascal Théveneau, Christophe Coquelet, Jérôme Corvisier et Patrice Paricaud. « Measurements and predictive models of high-pressure H2 solubility in brine (H2O+NaCl) for underground hydrogen storage application ». *International Journal of Hydrogen Energy* 45.56 (2020), p. 32206-32220 (cf. p. 18, 31, 50, 51, 92, 96).

[Chabab, 2019] Salaheddine Chabab, Pascal Théveneau, Jérôme Corvisier, Christophe Coquelet, Patrice Paricaud, Céline Houriez et al. « Thermodynamic study of the CO2 – H2O – NaCl system : Measurements of CO2 solubility and modeling of phase equilibria using Soreide and Whitson, electrolyte CPA and SIT models ». *International Journal of Greenhouse Gas Control* 91 (2019), p. 102825 (cf. p. viii, 42, 86, 88).

[Chatti, 2005] Imen Chatti, Anthony Delahaye, Laurence Fournaison et Jean-Pierre Petitet. « Benefits and drawbacks of clathrate hydrates : a review of their areas of interest ». *Energy Conversion and Management* 46.9 (2005), p. 1333-1343 (cf. p. 101).

[Civan, 2001] Faruk Civan et Maurice L. Rasmussen. « Accurate Measurement of Gas Diffusivity in Oil and Brine Under Reservoir Conditions ». OnePetro, 2001 (cf. p. 12, 38).

[Connors, 1988] Kenneth A. Connors. « The Karl Fischer Titration of Water ». *Drug Development and Industrial Pharmacy* 14.14 (1988), p. 1891-1903 (cf. p. 22).

[Creek, 2011] Jefferson Louis Creek, Sivakumar Subramanian et Douglas Alexander Estanga. « New Method for Managing Hydrates in Deepwater Tiebacks ». OnePetro, 2011 (cf. p. 101).

[Crocombe, 2018] Richard A. Crocombe. « Portable Spectroscopy ». *Applied Spectroscopy* 72.12 (2018), p. 1701-1751 (cf. p. 22).

[Davies, 1975] R. J. Davies. « The determination of water in natural gas using a modified Karl Fischer titration apparatus ». *Analyst* 100.1188 (1975), p. 163-167 (cf. p. 22).

[DeVaney, 1978] W. DeVaney, J. M. Berryman, P. L. Kao et B. Eakin. *High temperature VLE measurements for substitute gas components. Gas Processors Association*. Rapp. tech. Research Report RR-30, Project 735-A, Tulsa, OK, 1978 (cf. p. 59).

[Donadei, 2016] Sabine Donadei et Gregor-Sönke Schneider. « Chapter 6 - Compressed Air Energy Storage in Underground Formations ». *Storing Energy*. Sous la dir. de Trevor M. Letcher. Oxford : Elsevier, 2016, p. 113-133 (cf. p. 76).

[Ediger, 2019] Volkan Ş. Ediger. « An integrated review and analysis of multi-energy transition from fossil fuels to renewables ». *Energy Procedia*. 5th International Conference on Power and Energy Systems Engineering (CPESE 2018) 156 (2019), p. 2-6 (cf. p. 1, 4).

[Elgibaly, 1999] Ahmed Elgibaly et Ali Elkamel. « Optimal Hydrate Inhibition Policies with the Aid of Neural Networks ». *Energy & Fuels* 13.1 (1999), p. 105-113 (cf. p. 101).

[Eslamimanesh, 2011] Ali Eslamimanesh, Amir H. Mohammadi et Dominique Richon. « Thermodynamic consistency test for experimental data of water content of methane ». *AIChE journal* 57.9 (2011), p. 2566-2573 (cf. p. 101).

[Etminan, 2010] S. Reza Etminan, Brij B. Maini, Zhangxin Chen et Hassan Hassanzadeh. « Constant-Pressure Technique for Gas Diffusivity and Solubility Measurements in Heavy Oil and Bitumen ». *Energy & Fuels* 24.1 (2010), p. 533-549 (cf. p. 11).

[Farajzadeh, 2007] R. Farajzadeh, A. Barati, H. A. Delil, J. Bruining et P. L. J. Zitha. « Mass Transfer of CO2 Into Water and Surfactant Solutions ». *Petroleum Science and Technology* 25.12 (2007), p. 1493-1511 (cf. p. 33).

[Farajzadeh, 2009] R. Farajzadeh, P. L. J. Zitha et J. Bruining. « Enhanced Mass Transfer of CO2 into Water : Experiment and Modeling ». *Industrial & Engineering Chemistry Research* 48.13 (2009), p. 6423-6431 (cf. p. 32, 33, 43, 48, 49, 78).

[Ferrell, 1967] R.T. Ferrell et D.M. Himmelblau. « Diffusion coefficients of hydrogen and helium in water ». *AIChE Journal* 13.4 (1967), p. 702-708 (cf. p. 50).

[Foh, 1979] S. Foh, M. Novil, E. Rockar et P. Randolph. *Underground hydrogen storage. Final report. [Salt caverns, excavated caverns, aquifers and depleted fields]*. Rapp. tech. BNL-51275. Brookhaven National Lab. (BNL), Upton, NY (United States), 1979 (cf. p. 100).

[Frank, 1996] Marco J. W. Frank, Johannes A. M. Kuipers et Wim P. M. van Swaaij. « Diffusion Coefficients and Viscosities of CO2 + H2O, CO2 + CH3OH, NH3 + H2O, and NH3 + CH3OH Liquid Mixtures ». *Journal of Chemical & Engineering Data* 41.2 (1996), p. 297-302 (cf. p. 32, 42).

[Funke, 2003] Hans H. Funke, Brad L. Grissom, Clark E. McGrew et Mark W. Raynor. « Techniques for the measurement of trace moisture in high-purity electronic specialty gases ». *Review of Scientific Instruments* 74.9 (2003), p. 3909-3933 (cf. p. 22).

[Gholami, 2015] Yasin Gholami, Reza Azin, Rouhollah Fatehi, Shahriar Osfouri et Alireza Bahadori. « Prediction of carbon dioxide dissolution in bulk water under isothermal pressure decay at different boundary conditions ». *Journal of Molecular Liquids* 202 (2015), p. 23-33 (cf. p. 48).

[Gillespie, 1980] P. C. Gillespie et G. M. Wilson. *Vapor-liquid equilibrium data on water-substitute gas components : N/sub 2/-H/sub 2/O, H/sub 2/-H/sub 2/O, CO-H/sub 2/O, H/sub 2/-CO-H/sub 2/O, and H/sub 2/S-H/sub 2/O*. Rapp. tech. NP-4901848. Wilco Research Co., Provo, UT (USA), 1980 (cf. p. 59).

[Gubbins, 1966] Keith E. Gubbins, Kamlesh K. Bhatia et Robert D. Walker Jr. « Diffusion of gases in electrolytic solutions ». *AIChE Journal* 12.3 (1966), p. 548-552 (cf. p. 10).

[Hammerschmidt, 1934] E. G. Hammerschmidt. « Formation of Gas Hydrates in Natural Gas Transmission Lines ». *Industrial & Engineering Chemistry* 26.8 (1934), p. 851-855 (cf. p. 101).

[Hassanzadeh, 2007] Hassan Hassanzadeh, Mehran Pooladi-Darvish et David W. Keith. « Scaling behavior of convective mixing, with application to geological storage of CO2 ». *AIChE Journal* 53.5 (2007), p. 1121-1131 (cf. p. 33, 48).

[Hirai, 1997] S. Hirai, K. Okazaki, H. Yazawa, H. Ito, Y. Tabe et K. Hijikata. « Measurement of CO2 diffusion coefficient and application of LIF in pressurized water ». *Energy*. International Symposium on CO2 Fixation and Efficient Utilization of Energy 22.2 (1997), p. 363-367 (cf. p. 12, 31, 32).

[Hua, 2015] Yong Hua, Richard Barker et Anne Neville. « The effect of O2 content on the corrosion behaviour of X65 and 5Cr in water-containing supercritical CO2 environments ». *Applied Surface Science* 356 (2015), p. 499-511 (cf. p. 100).

[IEA, 2020] IEA. *Clean Energy Innovation, IEA, Paris*. 2020 (cf. p. 1, 4).

[Ipatev, 1934] V. Ipatev et V. Teodorovich. « Equilibrium compositions of vapor-gas mixtures over solutions ». *Zh. Obshch. Khim* 4 (1934), p. 395-399 (cf. p. 59).

[Islas-Juárez, 2004] R. Islas-Juárez, F. Samaniego V., E. Luna, C. Perez-Rosales et J. Cruz. « Experimental Study of Effective Diffusion in Porous Media ». *All Days*. Puebla Pue., Mexico : SPE, 2004, SPE–92196-MS (cf. p. 10).

[ISO, 2012] ISO. *Hydrogen fuel, Product specification, Part 2 : Proton exchange membrane (PEM) fuel cell applications for road vehicles. International Standard*. Rapp. tech. 2012 (cf. p. 100).

[Jafari Raad, 2015] Seyed Mostafa Jafari Raad, Reza Azin et Shahriar Osfouri. « Measurement of CO2 diffusivity in synthetic and saline aquifer solutions at reservoir conditions : the role of ion interactions ». *Heat and Mass Transfer* 51.11 (2015), p. 1587-1595 (cf. p. 12).

[Janiga, 2020] Damian Janiga, Robert Czarnota, Edyta Kuk, Jerzy Stopa et Paweł Wojnarowski. « Measurement of Oil-CO2 diffusion coefficient using pulse-echo method for pressure-volume decay approach under reservoir conditions ». *Journal of Petroleum Science and Engineering* 185 (2020), p. 106636 (cf. p. 12).

[Johnsson, 2019] Filip Johnsson, Jan Kjärstad et Johan Rootzén. « The threat to climate change mitigation posed by the abundance of fossil fuels ». *Climate Policy* 19.2 (2019), p. 258-274 (cf. p. 4).

[Jorgensen, 1983] William L. Jorgensen, Jayaraman Chandrasekhar, Jeffry D. Madura, Roger W. Impey et Michael L. Klein. « Comparison of simple potential functions for simulating liquid water ». *The Journal of Chemical Physics* 79.2 (1983), p. 926-935 (cf. p. 60-63).

[Jung, 1971] J. Jung, O. Knacke et D. Neuschütz. « Löslichkeit von Kohlenmonoxid und Wasserstoff in Wasser bis 300°C ». *Chemie Ingenieur Technik* 43.3 (1971), p. 112-116 (cf. p. 59).

[Kalair, 2021] Anam Kalair, Naeem Abas, Muhammad Shoaib Saleem, Ali Raza Kalair et Nasrullah Khan. « Role of energy storage systems in energy transition from fossil fuels to renewables ». *Energy Storage* 3.1 (2021), e135 (cf. p. 1, 4).

[Kestin, 1981] Joseph Kestin, H. Ezzat Khalifa et Robert J. Correia. « Tables of the dynamic and kinematic viscosity of aqueous KCl solutions in the temperature range 25–150°C and the pressure range 0.1–35 MPa ». *Journal of Physical and Chemical Reference Data* 10.1 (1981), p. 57-70 (cf. p. 46).

[Kling, 1991] G. Kling et G. Maurer. « The solubility of hydrogen in water and in 2-aminoethanol at temperatures between 323 K and 423 K and pressures up to 16 MPa ». *The Journal of Chemical Thermodynamics* 23.6 (1991), p. 531-541 (cf. p. 59).

[Kolass, 2011] Rolf Kolass et Chris Parker. *Mositure measurement in natural gas*. Rapp. tech. 2011 (cf. p. 100).

[Köster, 2018] Andreas Köster, Monika Thol et Jadran Vrabec. « Molecular Models for the Hydrogen Age : Hydrogen, Nitrogen, Oxygen, Argon, and Water ». *Journal of Chemical & Engineering Data* 63.2 (2018), p. 305-320 (cf. p. 61-63).

[Kouremenos, 1988] D. A. Kouremenos et A. Stegou-Sagia]. « Use of helium instead of hydrogen in inert gas absorption refrigeration ». *International Journal of Refrigeration* 11.5 (1988), p. 336-341 (cf. p. 20).

[Kumi, 2023] Ebenezer Nyarko Kumi. « Chapter 1 - Energy storage technologies ». *Pumped Hydro Energy Storage for Hybrid Systems*. Sous la dir. d'Amos T. Kabo-Bah, Felix A. Diawuo et Eric O. Antwi. Academic Press, 2023, p. 1-21 (cf. p. 1, 4).

[Kunz, 2007] O. Kunz, R. Klimeck, W. Wagner et M. Jaeschke. *The GERG-2004 wide-range equation of state for natural gases and other mixtures*. 2007 (cf. p. 35, 54, 101).

[Kunz, 2012] O. Kunz et W. Wagner. « The GERG-2008 Wide-Range Equation of State for Natural Gases and Other Mixtures : An Expansion of GERG-2004 ». *Journal of Chemical & Engineering Data* 57.11 (2012), p. 3032-3091 (cf. p. 21, 54).

[Labaune, 2018] P. Labaune, A. Rouabhi, M. Tijani, L. Blanco-Martín et T. You. « Dilatancy Criteria for Salt Cavern Design : A Comparison Between Stress- and Strain-Based Approaches ». *Rock Mechanics and Rock Engineering* 51.2 (2018), p. 599-611 (cf. p. 102).

[Lankof, 2023] Leszek Lankof et Radosław Tarkowski. « GIS-based analysis of rock salt deposits' suitability for underground hydrogen storage ». *International Journal of Hydrogen Energy* 48.71 (2023), p. 27748-27765 (cf. p. 2, 5).

[Lemmon, 2018] E. W. Lemmon, I. H. Bell, M. L. Huber et M. O. McLinden. « REFPROP ». *NIST* (2018) (cf. p. 62, 63).

[Li, 2023] Peng Li, Yinping Li, Xilin Shi, Hongling Ma, Kai Zhao, Xiaopeng Liang et al. « Pore Structure and Brine Flow Simulation of Salt Cavern Sediments Based on X-ray Computed Tomography ». *Rock Mechanics and Rock Engineering* (2023) (cf. p. 101).

[Li, 2022] Wenjing Li, Guodong Chen, Shuanglong Ding et Yi Zhang. « A method for assessing the gas capacity based on thermodynamic state analysis for salt cavern during operation ». *Journal of Energy Storage* 50 (2022), p. 104316 (cf. p. 2, 6).

[Liu, 2023] Wei Liu, Qihang Li, Chunhe Yang, Xilin Shi, Jifang Wan, Maria Jose Jurado et al. « The role of underground salt caverns for large-scale energy storage : A review and prospects ». *Energy Storage Materials* (2023), p. 103045 (cf. p. 5).

[Liu, 2021] Xin Liu, Xilin Shi, Yinping Li, Peng Li, Kai Zhao, Hongling Ma et al. « Maximum gas production rate for salt cavern gas storages ». *Energy* 234 (2021), p. 121211 (cf. p. 100, 101).

[Lstiburek, 1996] Joseph Lstiburek et John Carmody. *Moisture control handbook : principles and practices for residential and small commercial buildings*. John Wiley & Sons, 1996 (cf. p. 23).

[Lu, 2013] Wanjun Lu, Huirong Guo, I. M. Chou, R. C. Burruss et Lanlan Li. « Determination of diffusion coefficients of carbon dioxide in water between 268 and 473K in a high-pressure capillary optical cell with in situ Raman spectroscopic measurements ». *Geochimica et Cosmochimica Acta* 115 (2013), p. 183-204 (cf. p. 2, 6, 31, 32).

[Marx, 1992] D. Marx et P. Nielaba. « Path-integral Monte Carlo techniques for rotational motion in two dimensions : Quenched, annealed, and no-spin quantum-statistical averages ». *Physical Review A* 45.12 (1992), p. 8968-8971 (cf. p. 60-63).

[Maslennikova, 1976] V. Ya Maslennikova, N. Goryunova, L. Subbotina et D. Tsiklis. « The solubility of water in compressed hydrogen ». *Russ. J. Phys. Chem* 50 (1976), p. 240-243 (cf. p. 59).

[McNair, 2019] Harold M. McNair, James M. Miller et Nicholas H. Snow. *Basic gas chromatography*. John Wiley & Sons, 2019 (cf. p. 22).

[Ministry of ecology and energy, 2009] Ministry of ecology and energy. *Accidentology involving hydrogen*. Rapp. tech. 2009 (cf. p. 20).

[Moghaddam, 2012] R. Nazari Moghaddam, B. Rostami, P. Pourafshary et Y. Fallahzadeh. « Quantification of density-driven natural convection for dissolution mechanism in CO 2 sequestration ». *Transport in Porous Media* 92.2 (2012) (cf. p. 12).

[Mohammadi, 2004] Amir H. Mohammadi, Antonin Chapoy, Dominique Richon et Bahman Tohidi. « Experimental Measurement and Thermodynamic Modeling of Water Content in Methane and Ethane Systems ». *Industrial & Engineering Chemistry Research* 43.22 (2004), p. 7148-7162 (cf. p. 21).

[Mutoru, 2011] J. Wambui Mutoru, Alana Leahy-Dios et Abbas Firoozabadi. « Modeling infinite dilution and Fickian diffusion coefficients of carbon dioxide in water ». *AIChE Journal* 57.6 (2011), p. 1617-1627 (cf. p. 31).

[Navaid, 2023] Humza Bin Navaid, Hossein Emadi et Marshall Watson. « A comprehensive literature review on the challenges associated with underground hydrogen storage ». *International Journal of Hydrogen Energy* 48.28 (2023), p. 10603-10635 (cf. p. 6).

[Nguyen, 1998] T.A. Nguyen et S.M. Farouq Ali. « Effect of Nitrogen On the Solubility And Diffusivity of Carbon Dioxide Into Oil And Oil Recovery By the Immiscible WAG Process ». *Journal of Canadian Petroleum Technology* 37.02 (1998) (cf. p. 10).

[Pray, 1952] H. A. Pray, C. E. Schweickert et B. H. Minnich. « Solubility of Hydrogen, Oxygen, Nitrogen, and Helium in Water at Elevated Temperatures ». *Industrial & Engineering Chemistry* 44.5 (1952), p. 1146-1151 (cf. p. 59).

[Processors Suppliers Association, 2004] Gas Processors Suppliers Association. *Suppliers Association Engineering Data Book*. Tulsa, Oklahoma, USA, 2004 (cf. p. 100).

[Rahbari, 2019] Ahmadreza Rahbari. « Solubility of Water in Hydrogen at High Pressures : A Molecular Simulation Study ». *Journal of Chemical & Engineering Data* 64 (2019) (cf. p. 60, 61).

[Rahbari, 2021] Ahmadreza Rahbari, Julio C. Garcia-Navarro, Mahinder Ramdin, Leo J. P. van den Broeke, Othonas A. Moultos, David Dubbeldam et al. « Effect of Water Content on Thermodynamic Properties of Compressed Hydrogen ». *Journal of Chemical & Engineering Data* 66.5 (2021), p. 2071-2087 (cf. p. 60-63).

[Renner, 1988] T. A. Renner. « Measurement and Correlation of Diffusion Coefficients for CO2 and Rich-Gas Applications ». *SPE Reservoir Engineering* 3.02 (1988), p. 517-523 (cf. p. 11, 32, 33).

[Reza Etminan, 2013] S. Reza Etminan, Mehran Pooladi-Darvish, Brij B. Maini et Zhangxin Chen. « Modeling the interface resistance in low soluble gaseous solvents-heavy oil systems ». *Fuel* 105 (2013), p. 672-687 (cf. p. 38, 42).

[Rezk, 2022] Mohamed Gamal Rezk, Jalal Foroozesh, Ahmed Abdulrahman et Jebraeel Gholinezhad. « CO2 Diffusion and Dispersion in Porous Media : Review of Advances in Experimental Measurements and Mathematical Models ». *Energy & Fuels* 36.1 (2022), p. 133-155 (cf. p. 33).

[Riaz, 2014] Amir Riaz et Yildiray Cinar. « Carbon dioxide sequestration in saline formations : Part I—Review of the modeling of solubility trapping ». *Journal of Petroleum Science and Engineering* 124 (2014), p. 367-380 (cf. p. 48).

[Riazi, 1996] Mohammad Riazi. « A new method for experimental measurement of diffusion coefficients in reservoir fluids ». *Journal of Petroleum Science and Engineering* 14.3 (1996), p. 235-250 (cf. p. 11, 13).

[Ribeiro, 2008] Cláudio P. Ribeiro et Paulo L. C. Lage. « Modelling of hydrate formation kinetics : State-of-the-art and future directions ». *Chemical Engineering Science* 63.8 (2008), p. 2007-2034 (cf. p. 100).

[Rick, 2004] Steven W. Rick. « A reoptimization of the five-site water potential (TIP5P) for use with Ewald sums ». *The Journal of Chemical Physics* 120.13 (2004), p. 6085-6093 (cf. p. 60, 61).

[Rowley, 1997] Richard L. Rowley, Michael E. Adams, Tonya L. Marshall, John L. Oscarson, W. Vincent Wilding et Darin J. Anderson. « Measurement of Diffusion Coefficients Important in Modeling the Absorption Rate of Carbon Dioxide into Aqueous N-Methyldiethanolamine ». *Journal of Chemical & Engineering Data* 42.2 (1997), p. 310-317 (cf. p. 33).

[Sagi, 2016] Hemi Sagi. « Advanced leak test methods ». *no date, ATC Inc* (2016), p. 1-6 (cf. p. 94).

[Sankar, 2011] M. Sankar, Youngyong Park, J. M. Lopez et Younghae Do. « Numerical study of natural convection in a vertical porous annulus with discrete heating ». *International Journal of Heat and Mass Transfer* 54.7 (2011), p. 1493-1505 (cf. p. 40).

[Scholz, 2012] Eugen Scholz. *Karl Fischer titration : determination of water*. Springer Science & Business Media, 2012 (cf. p. 22).

[Sedaee, 2019] B. Sedaee, M. Mohammadi, L. Esfahanizadeh et Y. Fathi. « Comprehensive modeling and developing a software for salt cavern underground gas storage ». *Journal of Energy Storage* 25 (2019), p. 100876 (cf. p. 101).

[Sell, 2013] Andrew Sell, Hossein Fadaei, Myeongsub Kim et David Sinton. « Measurement of CO2 Diffusivity for Carbon Sequestration : A Microfluidic Approach for Reservoir-Specific Analysis ». *Environmental Science & Technology* 47.1 (2013), p. 71-78 (cf. p. 12, 32).

[Sheikha, 2005] Hussain Sheikha, Mehran Pooladi-Darvish et Anil K. Mehrotra. « Development of Graphical Methods for Estimating the Diffusivity Coefficient of Gases in Bitumen from Pressure-Decay Data ». *Energy & Fuels* 19.5 (2005), p. 2041-2049 (cf. p. 10).

[Shi, 2018] Z. Shi, B. Wen, M. A. Hesse, T. T. Tsotsis et K. Jessen. « Measurement and modeling of CO2 mass transfer in brine at reservoir conditions ». *Advances in Water Resources* 113 (2018), p. 100-111 (cf. p. 31, 32, 48, 78).

[Sigmund, 1976] Phillip M. Sigmund. « Prediction of molecular diffusion at reservoir conditions. Part 1-Measurement and prediction of binary dense gas diffusion coefficients ». *Journal of Canadian Petroleum Technology* 15.02 (1976) (cf. p. 10).

[Skjold, 2017] T. Skjold, D. Siccama, H. Hisken, A. Brambilla, P. Middha, K. M. Groth et al. « 3D risk management for hydrogen installations ». *International Journal of Hydrogen Energy*. Special issue on The 6th International Conference on Hydrogen Safety (ICHS 2015), 19-21 October 2015, Yokohama, Japan 42.11 (2017), p. 7721-7730 (cf. p. 20).

[Soeder, 2021] Daniel J. Soeder. « Fossil Fuels and Climate Change ». *Fracking and the Environment : A scientific assessment of the environmental risks from hydraulic fracturing and fossil fuels*. Sous la dir. de Daniel J. Soeder. Cham : Springer International Publishing, 2021, p. 155-185 (cf. p. 4).

[Soubeyran, 2019] A. Soubeyran, A. Rouabhi et C. Coquelet. « Thermodynamic analysis of carbon dioxide storage in salt caverns to improve the Power-to-Gas process ». *Applied Energy* 242 (2019), p. 1090-1107 (cf. p. 2, 6, 33, 38, 77).

[Sun, 2001] Zhi-Gao Sun, Shuan-Shi Fan, Lei Shi, Yan-Kun Guo et Kai-Hua Guo. « Equilibrium Conditions Hydrate Dissociation for a Ternary Mixture of Methane, Ethane, and Propane in Aqueous Solutions of Ethylene Glycol and Electrolytes ». *Journal of Chemical & Engineering Data* 46.4 (2001), p. 927-929 (cf. p. 101).

[Tamimi, 1994] A. Tamimi, Edward B. Rinker et Orville C. Sandall. « Diffusion Coefficients for Hydrogen Sulfide, Carbon Dioxide, and Nitrous Oxide in Water over the Temperature Range 293-368 K ». *Journal of Chemical & Engineering Data* 39.2 (1994), p. 330-332 (cf. p. 31, 32).

[Tan, 1992] K. K. Tan et R. B. Thorpe. « Gas diffusion into viscous and non-Newtonian liquids ». *Chemical Engineering Science* 47.13 (1992), p. 3565-3572 (cf. p. 31).

[Tarhule-Lips, 1998] ROZEMARIJN FA Tarhule-Lips et Derek C. Ford. « Condensation corrosion in caves on Cayman Brac and Isla de Mona ». *Journal of caves and karst studies* 60 (1998), p. 84-95 (cf. p. 100).

[Tayeb, 2023] Firas Tayeb, Ahmed Rouabhi, Murad AbuAisha et Alain Valtz. « Kinetics of CO2 dissolution for underground applications ». *Geoenergy Science and Engineering* 230 (2023), p. 212061 (cf. p. 17, 33).

[Ugrozov, 1996] V. V. Ugrozov. « Equilibrium compositions of vapor-gas mixtures over solutions ». *Russian journal of physical chemistry* 70.7 (1996), p. 1240-1241 (cf. p. 59).

[Upreti, 2000] Simant R. Upreti et Anil K. Mehrotra. « Experimental Measurement of Gas Diffusivity in Bitumen : Results for Carbon Dioxide ». *Industrial & Engineering Chemistry Research* 39.4 (2000), p. 1080-1087 (cf. p. 33).

[Upreti, 2002] Simant R. Upreti et Anil K. Mehrotra. « Diffusivity of CO2, CH4, C2H6 and N2 in athabasca bitumen ». *The Canadian Journal of Chemical Engineering* 80.1 (2002), p. 116-125 (cf. p. 33).

[Visscher, 1999] Gert J W Visscher. « Humidity and Moisture Measurement » (1999) (cf. p. 22).

[Wang, 2013] S. Wang, J. Hou, B. Liu, F. Zhao, G. Yuan et G. Liu. « The Pressure-decay Method for Nature Convection Accelerated Diffusion of CO2 in Oil and Water Under Elevated Pressures ». *Energy Sources, Part A : Recovery, Utilization, and Environmental Effects* 35.6 (2013), p. 538-545 (cf. p. 32, 43).

[Wei, 2023] Xinxing Wei, Xilin Shi, Wei Hu, Shengnan Ban, Yinping Li, Hongling Ma et al. « Dynamic tightness evaluation of salt cavern energy storage ». *Journal of Energy Storage* 57 (2023), p. 106313 (cf. p. 93).

[Wiebe, 1934] R. Wiebe et V. L. Gaddy. « The Solubility of Hydrogen in Water at 0, 50, 75 and 100° from 25 to 1000 Atmospheres ». *Journal of the American Chemical Society* 56.1 (1934), p. 76-79 (cf. p. 59).

[Wilke, 1993] R. J. Wilke, D. W. R. Wallace et K. M. Johnson. « Water-based, gravimetric method for the determination of gas sample loop volume ». *Analytical Chemistry* 65.17 (1993), p. 2403-2406 (cf. p. 22).

[Witherspoon, 1965] P. A. Witherspoon et D. N. Saraf. « Diffusion of Methane, Ethane, Propane, and n-Butane in Water from 25 to 43° ». *The Journal of Physical Chemistry* 69.11 (1965), p. 3752-3755 (cf. p. 10).

[Wuebbles, 2001] Donald J. Wuebbles et Atul K. Jain. « Concerns about climate change and the role of fossil fuel use ». *Fuel Processing Technology*. Fuel science in the year 2000 : Where do we stand and where do we go from here ? 71.1 (2001), p. 99-119 (cf. p. 4).

[Yan, 2011] Wei Yan, Shengli Huang et Erling H. Stenby. « Measurement and modeling of CO2 solubility in NaCl brine and CO2–saturated NaCl brine density ». *International Journal of Greenhouse Gas Control* 5.6 (2011), p. 1460-1477 (cf. p. 40, 46).

[Yang, 2006] Chaodong Yang et Yongan Gu. « Accelerated Mass Transfer of CO2 in Reservoir Brine Due to Density-Driven Natural Convection at High Pressures and Elevated Temperatures ». *Industrial & Engineering Chemistry Research* 45.8 (2006), p. 2430-2436 (cf. p. 11, 31, 32, 43).

[Yang, 2008] Daoyong Yang et Yongan Gu. « Determination of Diffusion Coefficients and Interface Mass-Transfer Coefficients of the Crude OilCO2 System by Analysis of the Dynamic and Equilibrium Interfacial Tensions ». *Industrial & Engineering Chemistry Research* 47.15 (2008), p. 5447-5455 (cf. p. 11).

[Zarghami, 2017] Shahin Zarghami, Fathi Boukadi et Yahya Al-Wahaibi. « Diffusion of carbon dioxide in formation water as a result of CO2 enhanced oil recovery and CO2 sequestration ». *Journal of Petroleum Exploration and Production Technology* 7.1 (2017), p. 161-168 (cf. p. 17, 32).

[Zhang, 2015] Weidong Zhang, Shuangliang Wu, Shaoran Ren, Liang Zhang et Juntao Li. « The modeling and experimental studies on the diffusion coefficient of CO2 in saline water ». *Journal of CO2 Utilization*. The assessment of CO2 utilization technology in China 11 (2015), p. 49-53 (cf. p. 12, 32, 33).

[Zhang, 2000] Y. P. Zhang, C. L. Hyndman et B. B. Maini. « Measurement of gas diffusivity in heavy oils ». *Journal of Petroleum Science and Engineering* 25.1 (2000), p. 37-47 (cf. p. 11, 33).

[Zhang, 2022] Yi Zhang, Wenjing Li et Guodong Chen. « A Thermodynamic Model for Carbon Dioxide Storage in Underground Salt Caverns ». *Energies* 15.12 (2022), p. 4299 (cf. p. 2, 6).

[Zhao, 2022] Kai Zhao, Yuanxi Liu, Yinping Li, Hongling Ma, Wei Hou, Changfu Yu et al. « Feasibility analysis of salt cavern gas storage in extremely deep formation : A case study in China ». *Journal of Energy Storage* 47 (2022), p. 103649 (cf. p. 5).

RÉSUMÉ

L'usage croissant des énergies renouvelables nécessite des solutions avancées pour le stockage de l'énergie pour aborder efficacement les difficultés causées par leur approvisionnement fluctuant et intermittent. Cette étude se concentre sur le stockage souterrain de gaz dans les cavités salines, une solution prometteuse pour répondre à ces défis. Dans une première étape, des études expérimentales sont menées pour étudier la cinétique de dissolution du CO_2 et du H_2 dans l'eau pure et la saumure en utilisant la méthode de Pressure-decay. Ces études incluent également la mesure de l'humidité des gaz à travers un pilote de stockage innovant, permettant d'évaluer l'influence du transfert de masse sur la phase gazeuse. Par la suite, des modèles mathématiques et numériques ont été développés pour modéliser ces phénomènes physiques permettant l'analyse du comportement des gaz dans les conditions de stockage. Dans une deuxième étape, ces modèles sont utilisés pour évaluer la cinétique de dissolution du CO_2 et du H_2 dans la saumure, ainsi que le comportement des gaz humides dans les cavités salines. Cette approche améliore notre compréhension des échanges de masse entre les gaz et la saumure dans les conditions de stockage souterrain.

MOTS CLÉS

Stockage souterrain du gaz, cinétique de dissolution, gaz humide, convection naturelle, cavités salines.

ABSTRACT

The increasing integration of renewable energy sources into the power grid requires the development of sophisticated energy storage technologies to efficiently address the difficulties caused by their fluctuating and intermittent supply. This study delves into the underground storage of gases in salt caverns, which has emerged as a promising solution for overcoming these challenges. The work begins with laboratory-scale experimental studies to elucidate the CO_2 and H_2 dissolution kinetics in aqueous solutions (pure water and brine) using the pressure decay method, while also measuring gas humidity through an innovative storage pilot to assess the influence of mass transfer on the gas-rich phase. Building on these experimental studies, the work proceeds towards the development of mathematical and numerical models that simulate these processes, allowing for a deeper analysis and comprehension of gas behavior under storage conditions. The latter part of the study extends these models to a real cavern environment, assessing CO_2 and H_2 dissolution in brine and the behavior of humid gases within the salt caverns.

KEYWORDS

Underground gas storage, kinetics of dissolution, gas humidification, natural convection, salt caverns.